Search for the permanent electric dipole moment of 129Xe

Grasdijk, Jan Olivier

Search for the Permanent Electric Dipole Moment of ^{129}Xe

university of groningen

faculty of mathematics and natural sciences

van swinderen institute for particle physics and gravity

This work is part of the research program of the Foundation for Fundamental Research on Matter (FOM), which is part of the Netherlands Organizations for Scientific Research (NWO). This thesis has been conducted in the framework of and with the resources of the FOM program Broken Mirrors and Drifting Constants. This work was performed in the framework of the MIXed collaboration between the University of Mainz, University of Heidelberg, University of Groningen and research center FZ Jülich.

ISBN: 978-94-034-0872-9
ISBN (digital): 978-94-034-08710-2
Printing: Gildeprint - Enschede

university of groningen

Search for the Permanent Electric Dipole Moment of ^{129}Xe

PhD Thesis

to obtain the degree of PhD at the
University of Groningen
on the authority of the
Rector Magnificus Prof. E. Sterken
and in accordance with
the decision by the College of Deans

This thesis will be defended in public on

Friday 19 October 2018 at 12.45 hours

by

Jan Olivier Grasdijk

born on 21 February 1990
in Groningen

Supervisor
Prof. Dr. K.H.K.J. Jungmann

Co-Supervisor
Dr. L. Willmann

Assessment committee
Prof. Dr. A. Pellegrino
Prof. Dr. B.E. Sauer
Prof. Dr. R.G.E Timmermans

Abstract

The goal of the MIXed experiment is to measure the permanent electric dipole moment (EDM) of ^{129}Xe. The experiment uses differential free spin precession of ^{3}He and ^{129}Xe, co-occupying the same fiducial volume, to search for a finite permanent electric dipole moment of ^{129}Xe.

A non-zero EDM implies breakdown of P (parity) and T (time reversal) symmetries. Provided CPT invariance holds, this also implies CP violation. Observation of an EDM at achievable experimental sensitivity would provide unambiguous evidence for physics beyond the Standard Model of particle physics. It could also provide a solution to the matter-antimatter asymmetry puzzle in the universe.

An EDM experiment requires homogeneous magnetic and electric fields. The magnetic field strength and homogeneity are monitored in-situ with the ^{3}He precession frequency and it's polarization decay rate. In experiments to date the presence of an electric field is achieved by applying a voltage difference between two electrodes. During an experimental run it is challenging to monitor or determine the actual voltage difference. Conventional electric field measurement methods disturb high precision EDM experiments. We have designed an electro-optic field sensor, using a non-linear optical crystal sensor, to non-invasively monitor the DC electric field real-time in-situ.

The experiment resides in a magnetically shielded room (MSR), consisting of two layers of μ-metal and one layer of aluminum. An additional cylindrical μ-metal shield surrounds the experiment's magnetic field coil system and fiducial volume. The magnetic coil system generates a homogeneous magnetic holding field of $\sim$400 nT, in which the spins precess. The spin precession is picked up with low temperature DC-SQUID magnetometers as low noise magnetic flux detectors. The phase evolution is extracted from the precession signals and correlated with switching of electric field polarity.

From a series of six measurements of several hours length each, a *preliminary* value for the EDM of ^{129}Xe of $d_{\mathrm{Xe}} = (-1.6 \pm 0.9) \times 10^{-27}$ $e$cm is extracted. This value corresponds to an upper limit of $|d_{\mathrm{Xe}}| < 3.1 \times 10^{-27}$ $e$cm (90% C.L.).

Contents

List of Figures

1. Introduction

The Standard Model (**SM**) of particle physics describes all known and confirmed effects in the field to sufficent accuracy. Together with General Relativity (**GR**) it provides a framework for describing all experimental results to date and it provides for accurate predictions. The SM and GR have been tested to high precision on a wide range of energy scales.

The SM describes all known fundamental forces in nature, with the exception of gravity. The fundamental forces are the electromagnetic, weak and strong interactions as well as gravity. The SM also classifies all known elementary particles. The elementary particles are split into two distinct groups (see Fig. 1.1), which are together 24 fundamental fermions and 13 force-carrier bosons. The fundamental fermions are grouped into three generations of leptons (electron, muon, tauon) and the associated neutrinos, and three generations of quarks (up/down, charm/strange and top/bottom). The bosons fall into two groups, with 12 gauge bosons and 1 scalar boson. The gauge bosons are the photon, for the electromagnetic interaction, the Z^0 and $W^{\pm}$ bosons for the weak interaction, and 8 gluons for the strong interaction. The scalar boson is the Higgs boson, which gives mass to fundamental particles.

From several observations, both theoretical and experimental, it has been shown that the SM and GR are a complete description of nature, however they lack in many cases a deeper explanation of the findings. It has become clear that a new model is required to explain all such observations, which is colloquially called the "Physics beyond the Standard Model" model.

Searches for new physics are mainly concentrated in two areas: high-energy physics at colliders, such as at the LHC at CERN, or high-precision experiments at low energy, such as in atomic systems.

1.1. Physics beyond the Standard Model

CPT symmetry is a fundamental symmetry of physical laws under simultaneous C, P and T transformations. It was first derived explicitly by Gerhart Lüders and Wolfgang Pauli [1, 2]. CPT is preserved in the SM.

Charge symmetry (**C**) is the assumption that physical laws are invariant under charge-conjugation transformations. Under this transformation particles are conjugated to their respective anti-particles. Parity symmetry (**P**) is the assumption that physical laws are

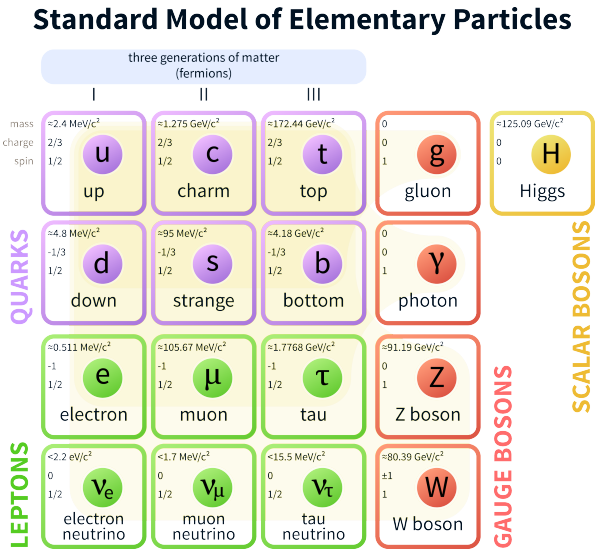

Figure 1.1.: The Standard Model of particle physics, with the three generations of matter fermions in the first three columns, gauge bosons in the fourth column, and the Higgs boson in the fifth. Figure from wikimedia commons.

invariant under spatial inversion transformations. Finally, Time reversal symmetry (**T**) is the assumption that physical laws are invariant under time reversal transformation. In physics the combined Charge and Parity symmetry (**CP**) is often used, implying that physical laws are invariant when a particle is exchanged for its anti-particle while concurrently spatial inversion is applied.

P symmetry is conserved in electromagnetism, strong interactions and gravity, but in weak interactions it can be violated. It is incorporated in the SM by expressing the weak interaction as a chiral gauge interaction. P violation was found experimentally in the weak interaction by Wu et al. [3] in 1957 through spatial anisotropy in the β-decay of polarized ^{60}Co.

CP violation can be described by a complex phase in the quark mixing matrix (CKM matrix) or in the neutrino mixing matrix (PMNS matrix). The complex phases are only present in the SM if there are at least three generations of quarks, and subsequently also at least three generations of leptons. In 1964 CP violation was first observed experimentally in kaon (K^0) decay [4], and later also in the heavier neutral B-meson decay channels [5].

An additional problem of the SM is the baryon asymmetry of the universe, or in other words why the observable universe consists mostly of matter. The Big Bang should have

produced matter and anti-matter in similar quantities, however, current observations do not support this. The currently observed asymmetry is $\eta = \frac{n_B - n_{\bar{B}}}{n_\gamma} \sim 10^{-10}$, where n_B is the matter density, $n_{\bar{B}}$ the anti-matter density and n_γ the photon density. Sakharov formulated conditions that, if CPT holds, could explain the imbalance [6]:

- Baryon number (**B**) violation
- C and CP violation
- Interactions out of thermal equilibrium

CP violation implies that a process occurs at different rates for a particle and its anti-particle. In other words, CP violation is required to explain the imbalance. However, the CP violation presently known in the SM is insufficient to explain the observed imbalance. Additional sources of CP violation are necessary, requiring physics beyond the Standard Model.

A second suggested possibility to generate the baryon asymmetry would be a violation of CPT symmetry [7].

1.2. Permanent Electric Dipole Moments

Electric dipole moments, **d**, quantify the separation of charges in a system. Positive and negative elementary charges seperated by distance **r** generate an electric dipole moment (**EDM**)

$$\mathbf{d} = e \cdot \mathbf{r}. \tag{1.1}$$

A fundamental particle can also have a permanent EDM, which must be aligned parallel to the spin **I**, as it is the only vector for an eigenstate of the isolated particle. Any other direction of a permanent EDM would require additional quantum numbers leading to additional states that do not exist. Hence the permanent EDM of a fundamental particle is described by:

$$\mathbf{d} = d \cdot \frac{\mathbf{I}}{|\mathbf{I}|}. \tag{1.2}$$

A non-zero permanent EDM violates both P and T symmetries, and by extension, also CP symmetry if the CPT theorem holds. P symmetry is violated since the EDM **d** is a polar vector, reversing sign under P, while the spin **I** is an axial vector, which is invariant under P

$$\mathrm{P}\left(\mathbf{d} = d\frac{\mathbf{I}}{|\mathbf{I}|}\right) \rightarrow -\mathbf{d} = d\frac{\mathbf{I}}{|\mathbf{I}|}. \tag{1.3}$$

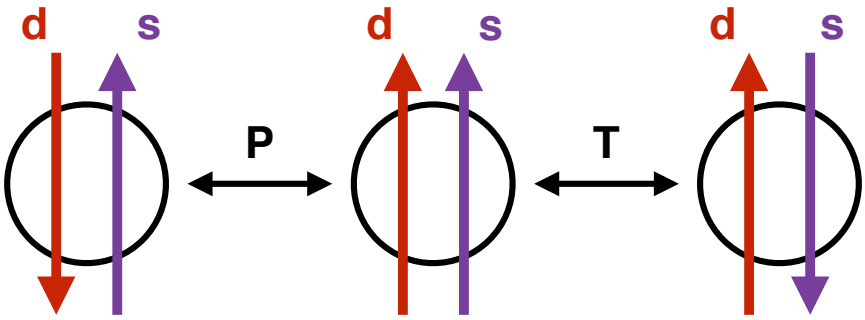

Figure 1.2.: A non-zero permanent Electric Dipole Moment (**EDM**) violates for a particle with spin **S** both Parity (**P**) and Time (**T**) symmetries, and by extension also CP symmetry, if the CPT theorem holds.

T symmetry is also violated by a non-zero permanent EDM, since **d** is invariant under T whereas **I** reverses sign under T

$$\mathrm{T}\left(\mathbf{d} = d\frac{\mathbf{I}}{|\mathbf{I}|}\right) \rightarrow \mathbf{d} = -d\frac{\mathbf{I}}{|\mathbf{I}|}. \tag{1.4}$$

Therefore, for a particle with a permanent EDM, under preservation of CPT, CP symmetry also has to be violated. This could provide one of the sources of additional CP violation required to explain the observed baryon asymmetry in the observable universe.

The SM predictions for EDMs are very small, contributing only at three-loop level for quarks, and even four-loop level for the electron [8]. For example, SM contributions to the the neutron EDM are at least of second order in the weak interaction coupling constants, resulting in a neutron EDM of order $d_n \sim 10^{-31}$ $e$cm to 10^{-33} $e$cm [9]. The SM prediction the electron EDM is even smaller, $d_e \sim 10^{-37}$ $e$cm to 10^{-40} $e$cm, because it requires at least a three-loop process. Many Physics beyond the Standard Model models predict larger EDMs than the SM, making EDM experiments excellent probes for Physics Beyond the Standard Model. Constraints on EDMs can directly rule out new physics models. In Figure 1.3 various Physics Beyond the Standard Model models are shown, some already excluded due to the current experimentally found electron EDM upper limit.

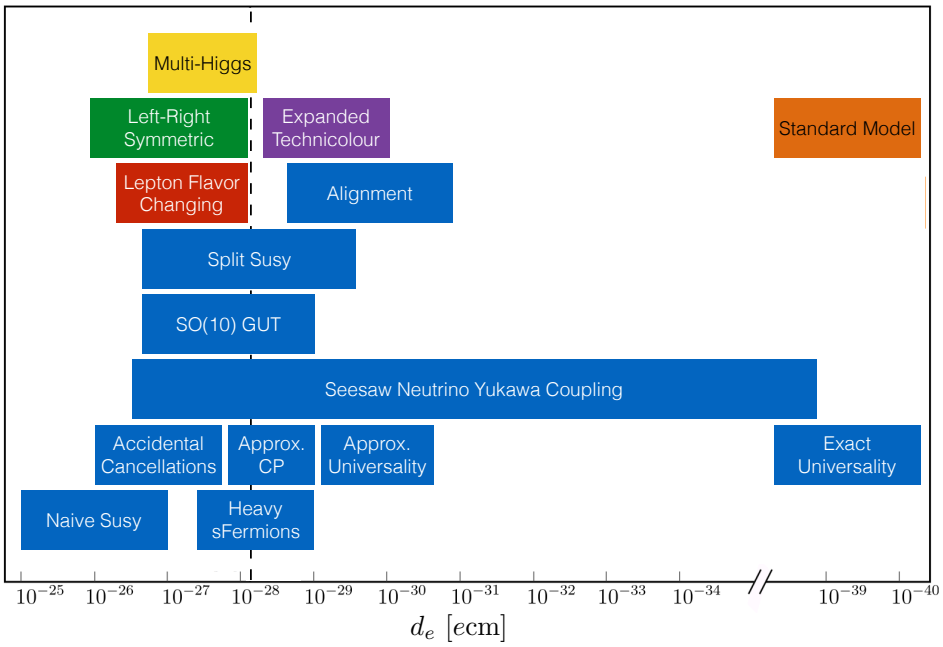

Figure 1.3.: Predictions of the electron EDM d_e for various suggested theoretical approaches to Physics Beyond the Standard Model. The current experimentally determined electron EDM limit is indicated by the dashed line, found by the ACME collaboration [10], already disavowing strongly many models. The blue bars indicate different versions of supersymmetry. Figure adapted from [11].

1.3. Atomic Electric Dipole Moments

Permanent EDMs of fundamental particles, in addition to interactions between the constituents, can lead to induced electric dipole moments in composite systems such as nucleons, atoms or molecules [12].

In a neutral atom a naive expectation would be that the constituents are shielded from the external electric field by the atomic electron cloud. However, this is only partially true, since we have to contend with non electro-static forces, finite-size effects and relativistic corrections, generating an electric field inside the atom large enough to be of use in EDM searches.

The contributions to the atomic EDM come from several sources:

- A permanent EDM of the electron (d_e). This contribution is largest in paramagnetic atoms, atoms with an unpaired electron, such as thallium or rubidium.
- A permanent EDM of the neutron (d_n) or proton (d_p).
- CP and P violating electron-nucleon interactions, characterized in models by three dimensionless parameters: C_{T} describes the strength of the tensor-pseudotensor interactions, C_{SP} the strength of the scalar-pseudoscalar interactions and C_{PS} describes the strength of the pseudoscalar-scalar interactions.
- CP and P violating nucleon-nucleon interactions, characterized by the dimensionless parameter η describing the strength of the interaction.

Paramagnetic atoms can generate an EDM due to the interaction between the electron EDM and the internal atomic electric field, scaling as [13]

$$Z^3\alpha^2, \tag{1.5}$$

favouring searches in heavier atoms.

For diamagnetic atoms, which have only paired electrons, most of the EDM contribution comes from the nucleus. As with the paramagnetic atoms, the atomic nucleus is shielded from external electric fields, but finite-size effects and relativistic corrections partially circumvent the shielding. The finite-size effects dominate in heavier atoms, resulting in an EDM contribution that scales with [13]

$$RZ^2\left(\frac{r_0}{a_0}\right)^2 d_N, \tag{1.6}$$

where R is a relativistic enhancement factor, r_0 is the nuclear radius, a_0 the Bohr radius and d_N is the nuclear EDM. This scaling factor is rather small, for example the scaling factor for xenon is about 10^{-3}.

From the scaling factors shown for para- and diamagnetic atoms one would expect the paramagnetic atoms to be much more suited for atomic EDM searches. However, due to experimental constraints, the current most sensitive EDM measurements have been performed on diamagnetic atoms.

Calculations for several atomic EDMs have been carried out, for instance for xenon and mercury in $e$cm [14, 15]

$$d(^{129}\mathrm{Xe}) = 10^{-3}d_e + 5.2\times10^{-21}C_{\mathrm{T}} + 5.6\times10^{-23}C_{\mathrm{SP}} + 1.2\times10^{-23}C_{\mathrm{PS}} + 6.7\times10^{-26}\eta, \tag{1.7}$$

$$d(^{199}\mathrm{Hg}) = 10^{-2}d_e + 2.0\times10^{-20}C_{\mathrm{T}} + 5.9\times10^{-22}C_{\mathrm{SP}} + 6\times10^{-23}C_{\mathrm{PS}} + 3.9\times10^{-25}\eta. \tag{1.8}$$

Combined with measurements on the EDMs of ^{129}Xe and ^{199}Hg, these equations can be used to give bounds on the parameters inducing atomic EDMs.

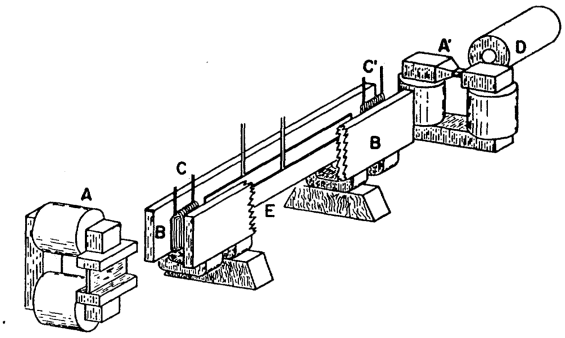

Figure 1.4.: Smith, Purcell and Ramsey neutron EDM experiment. A is a magnetized iron mirror polarizer, A′ a magnetized iron transmission analyzer, B the pole faces of the homogeneous magnetic field, C and C′ are the RF magnetic field coils and D is a BF_3 neutron counter. Finally E generates an electric field [16].

1.4. Experimental Searches

Experimental searches are performed in various systems; atomic, ionic, molecular and on fundamental and composite particles. In this section some of the systems are discussed along with their benefits and disadvantages.

1.4.1. Fundamental and Composite Particles

Searches in fundamental and composite particles include among the leptons the muon, tauon and among the hadrons the neutron. The first EDM search was performed on the neutron by Smith, Purcell and Ramsey [16] in 1957, where a limit of $|d_n| < 5 \times 10^{-20}$ $e$cm (95% C.L.) was found.

Composite and fundamental particles can be trapped with an electric and magnetic fields in a suited geometry with an appropriate time structure [17] if they are electrically charged, and the neutral ones can be trapped by exploiting their magnetic dipole moment [17]. An EDM measurement requires homogeneous electric and magnetic fields in the frame of the particle, which makes it very difficult to create a trapping potential. Hence these types of experiments are performed in beam, storage ring and magnetic bottle configurations.

In beam configuration the interaction time of a particle with the magnetic and electric field is limited, limiting the sensitivity. Additionally, the beam velocity brings specific systematic effects with it, which are discussed in detail in Chapter 5. The interaction time is

extended in a storage ring type experiment, however the beam velocity remains a source of systematics.

Beam type EDM experiments, such as the neutron EDM started with the aforementioned Smith, Purcell and Ramsey [16] experiment. A polarized thermal neutron beam was injected into a region with a homogeneous magnetic field. A radiofrequency (RF) magnetic field applied to the neutrons causes a $\pi/2$ spin flip. The neutrons then then passed through a homogeneous electric field region, before passing through a second RF magnetic field region for another $\pi/2$ flip. A gradient magnetic field was then used to split the two spin states spatially after which the spin state of interest was detected using a neutron counter. The two RF fields together with the state selection at the end of the beamline form a Ramsey interferometer, giving maximum signal when the RF field frequency is tuned to the precession frequency. An applied electric field together with a permanenet EDM would change the resonance frequency, resulting in a change of signal from which the EDM limit can be extracted. A schematic overview of the experiment is shown in Figure 1.4.

Most of the subsequent gain in beam type experiments has been achieved by slowing down the beam. For example the neutron EDM experiments have improved the EDM limit by moving to cold neutrons. However, this leads to reduced beam intensities in the interaction region. The latest experiments use stored ultra cold neutrons, greatly increasing the interaction time. The current best limit for the neutron has been established at the Intitute Laue-Langevin, Grenoble, France in 2015 [18, 19, 20], where a limit of $|d_n| < 3 \times 10^{-26}$ $e$cm (90% C.L.) was found.

In storage ring type experiments, such as the muon $g-2$ collaboration [22], particles are shot into the storage ring volume where a magnetic field keeps the particles in the horizontal plane of the ring. An electric quadrupole field is added to provide vertical focusing of the beam.

The muon $g-2$ collaboration was primarily established to measure the anomalous magnetic moment of the muon (a_μ). The muons are shot into the storage ring and they are polarized along the momentum direction. They start precessing in the magnetic and electric fields. The precession frequency of a_μ is given by

$$\boldsymbol{\omega}_a = -\frac{q}{m}\left[a_\mu \mathbf{B} + \left(-a_\mu + \frac{1}{\gamma^2-1}\right)\boldsymbol{\beta} \times \frac{\mathbf{E}}{c}\right], \tag{1.9}$$

where q is the particle charge, m the particle mass, $\gamma = \sqrt{\frac{1}{1-\frac{v^2}{c^2}}}$ the relativistic gamma factor and $\beta = v/c$ the velocity. By tuning the momentum of the beam to the "magic" gamma factor, $\gamma_\mu = 29.3$, the second term in the brackets disappears (the motional electric magnetic term), leaving only the $a_\mu \mathbf{B}$ term. The resulting precession is in the horizontal plane of the storage ring.

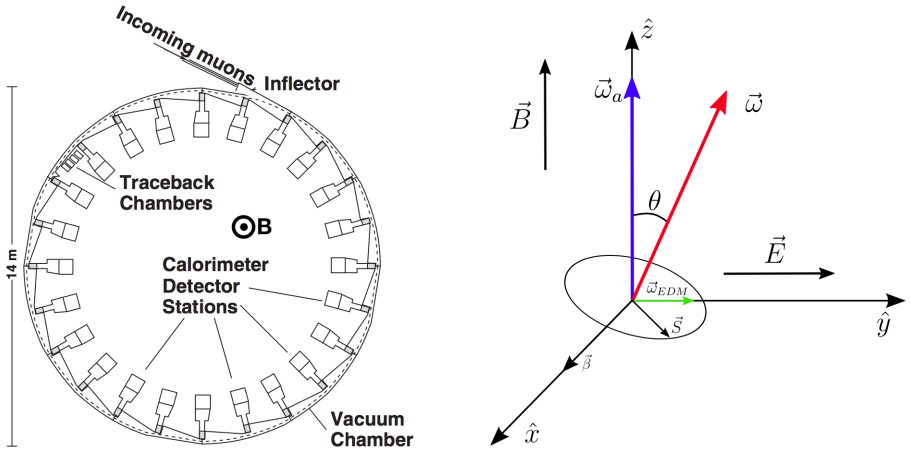

(a) (b)

Figure 1.5.: Schematic overview of the Brookhaven (E821) muon $g-2$ EDM experiment. (a) The muon g-2 ring in which the muons are trapped. (b) The tilting of the spin precession as a result of a permanent electric dipole moment, with the angle being exaggerated for illustrative purposes. Here x is the direction of the muon beam, and the magnetic field **B** is pointing out of the page in (a) [11, 21].

If the muon possesses a permanent EDM, an additional precession frequency appears

$$\boldsymbol{\omega}_{\text{EDM}} = -\eta \frac{q}{2m}\left[\boldsymbol{\beta} \times \mathbf{B} + \frac{\mathbf{E}}{c}\right], \tag{1.10}$$

where η is the muon EDM in units of $\frac{e\hbar}{4mc}$. Due to the magic gamma factor of 29.3, the motional electric field is vastly larger than the applied electrostatic field used for vertical focusing of the beam, which can subsequently be ignored. The additional EDM frequency causes a radial tilt of the rotational precession plane (see Figure 1.5). By measuring the angle the muon EDM can be extracted, resulting in [21]:

$$\left|d_{\mu^+}\right| \leq 2.1 \times 10^{-19}\ e\text{cm (95\% C.L.)}, \tag{1.11}$$

$$\left|d_{\mu^-}\right| \leq 1.5 \times 10^{-19}\ e\text{cm (95\% C.L.)}. \tag{1.12}$$

Assuming CPT is valid, the EDM of the μ^+ should be equal to the negative EDM of the

μ^-, i.e. $d_{\mu^+} = -d_{\mu^-}$. This gives a combined muon EDM limit of

$$\left|d_\mu\right| \leq 1.8 \times 10^{-19}\ e\text{cm (95\% C.L.)}, \tag{1.13}$$

approximately a factor 5 improvement over the previous best limit.

1.4.2. Molecular Systems

Heavy molecular polar systems have a very large enhancement factor for the external electric field, several orders of magnitude larger than heavy atomic systems. Past experiments have not been able to trap these molecules yet, necessitating beam type experiments to measure the EDM. These paramagnetic dipolar molecules are difficult to obtain, especially in the right state which is suited for an EDM measurement.

Recent measurements have been performed on ytterbium fluoride (YbF) by Hinds et al [23], and in thorium monoxide (ThO) by the ACME collaboration [10]. Both experiments create a cold beam which is shot through the interaction region. Hinds et al. found an upper limit on the electron EDM

$$|d_e| < 10.5 \times 10^{-28}\ e\text{cm (90\% C.L.)} \tag{1.14}$$

and the ACME collaboration found

$$|d_e| < 8.7 \times 10^{-29}\ e\text{cm (90\% C.L.)}. \tag{1.15}$$

The ThO electron EDM limit (Eq. 1.15) was extracted using an effective internal electric field of 84 GV/cm. Newer calculations result in an effective internal electric field of 79.9 GV/cm [24].

Molecular EDM experiments in general start with preparing the molecules in a state suited for an EDM measurement and polarizing them. Subsequently the molecules travel through the interaction region with a homogeneous electric and a magnetic field, where they undergo free precession. After the interaction zone the molecular state is determined, from which an EDM limit can be extracted. For example, in the ThO experiment by the ACME collaboration the ThO molecules are created from a cryogenic buffer gas source and are shot into a region with parallel magnetic and electric fields. The molecules are pumped with laser light from the electronic ground state into the lowest rotational level of the $H^3\Delta_1$ state. A second laser beam is used to select to desired state of $H^3\Delta_1$ for the EDM measurement. After free spin precession when the molecules pass through the interaction region the state is read out. From this the EDM limit is extracted (see also Figure 1.6).

The YbF experiment is working on slowing down the molecular beam even further, and aim to eventually trap the molecules in order to increase the interaction time and to decrease systematic effects which arises from the finite velocity of the beam. The

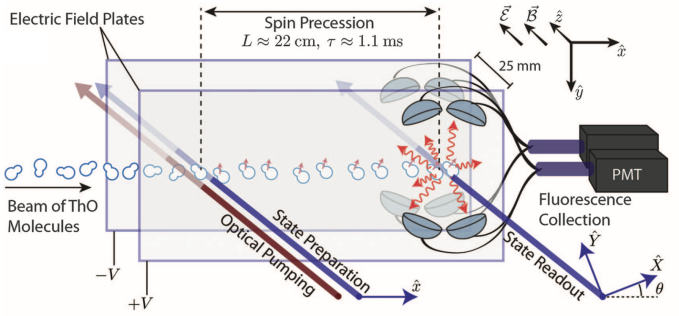

Figure 1.6.: Schematic overview of the ACME collaboration electron EDM experiment. A beam of ThO molecules is shot into a region with parallel magnetic and electric fields, where they prepared in the desired state for the EDM measurement. After free spin precession the current state is read out, and from this an EDM limit can be extracted. [10]

ThO (ACME) experiment is now using STIRAP to increase the efficiency of state preparation [25].

An EDM experiment with BaF is currently starting up in the Netherlands [26], aiming at an electron EDM sensitivity of 5×10^{-30} $e$cm by employing a traveling wave Stark decelerator.

Molecular Ions

Recently a measurement on an EDM on a molecular ion has been performed by the University of Colorado. The molecular ion, $^{180}Hf^{19}F^{+}$, is trapped in an RF trap and for an EDM measurement brought into the preferred state. The trapping of the ions results in a longer interrogation time compared to the molecular beam experiments, increasing by some 3 orders of magnitude. An electron EDM limit of [27]

$$|d_e| < 1.3 \times 10^{-28}\ e\text{cm (90\% C.L.)}, \tag{1.16}$$

has been found which is consistent with the limit established by the ACME experiment.

1.4.3. Atomic Systems

Atomic systems generally have rather long coherent interaction times as an advantage. The interaction times are far in excess of what can be achieved with composite and fundamental particles and with molecules. In contrast with to molecular EDM searches however, the enhancement factor is significantly diminished. The number of particles is in

general larger than in other EDM experiments. A further advantage of atomic systems is the use of spin clocks, where a second, different species is used in situ to monitor the magnetic field in real time, thereby gaining precision. This is also called co-magnetometry, and it is explained in more detail in Section 2.4.

The atomic EDM experiments generally work by polarizing the atoms, which is equivalent to the state preparation of the molecular EDM experiments. The polarized atoms are then put into a cell which resides inside parallel and anti-parallel homogeneous electric and magnetic fields, where they undergo free spin precession. The spin precession of both species is subsequently read out and an EDM limit can be extracted.

Recent atomic EDM experiments include projects on mercury (^{199}Hg) [28], xenon (^{129}Xe) [29] and radium (^{225}Ra) [30]. For each species an EDM limit was extracted to be

$$\left|d_{\mathrm{Hg}}\right| < 7.4 \times 10^{-30}\ e\mathrm{cm}\ (95\%\ \mathrm{C.L.})\ \text{for}\ ^{199}\mathrm{Hg}\ [28], \tag{1.17a}$$

$$|d_{\mathrm{Xe}}| < 4.1 \times 10^{-27}\ e\mathrm{cm}\ (90\%\ \mathrm{C.L.})\ \text{for}\ ^{129}\mathrm{Xe}\ [29], \tag{1.17b}$$

$$|d_{\mathrm{Ra}}| < 1.4 \times 10^{-23}\ e\mathrm{cm}\ (95\%\ \mathrm{C.L.})\ \text{for}\ ^{225}\mathrm{Ra}\ [30]. \tag{1.17c}$$

The radium EDM experiment differs in several respects from the mercury and xenon experiments. The Ra enhancement factor is much larger [31] than those of Hg and Xe, and in addition Ra is radioactive, whereas Hg and Xe are noble gases. As a result, the interrogation times of Hg and Xe are longer than those of Ra.

1.4.4. Overview

In Figure 1.7 an overview is given of the EDM searches as a function of time, where it appears that the current numerically lowest EDM limit is in the atomic system of ^{199}Hg, although the molecular systems sensitivity has been increased significantly recently.

Each of the systems has its own merits, as discussed in more detail in sections 1.4.1, 1.4.2 and 1.4.3. In summary we have for the different systems as their main features:

- Fundamental and composite particles:
  - direct limit on the particle EDM
- Molecular Systems:
  - large enhancement factor for the electron EDM
- Atomic Systems:
  - long coherent interaction times
  - large amount of particles
  - co-magnetometry

While the limits that can be currently experimentally reached for atomic systems are less stringent than those of molecular systems, the diamagnetic atomic systems require complicated theoretical work (see Sec. 1.3) to calculate the couplings to the total atomic EDM, whereas in molecular systems, due to the large enhancement factor, essentially only the electron EDM contributes.

Any EDM found at the current limit would imply Physics Beyond the Standard Model, making the atomic systems, due to their current experimentally reachable limits, excellent systems for an EDM search.

Recently it has been suggested to look for time-varying EDMs which could be the result of axion-like dark matter [32, 33].

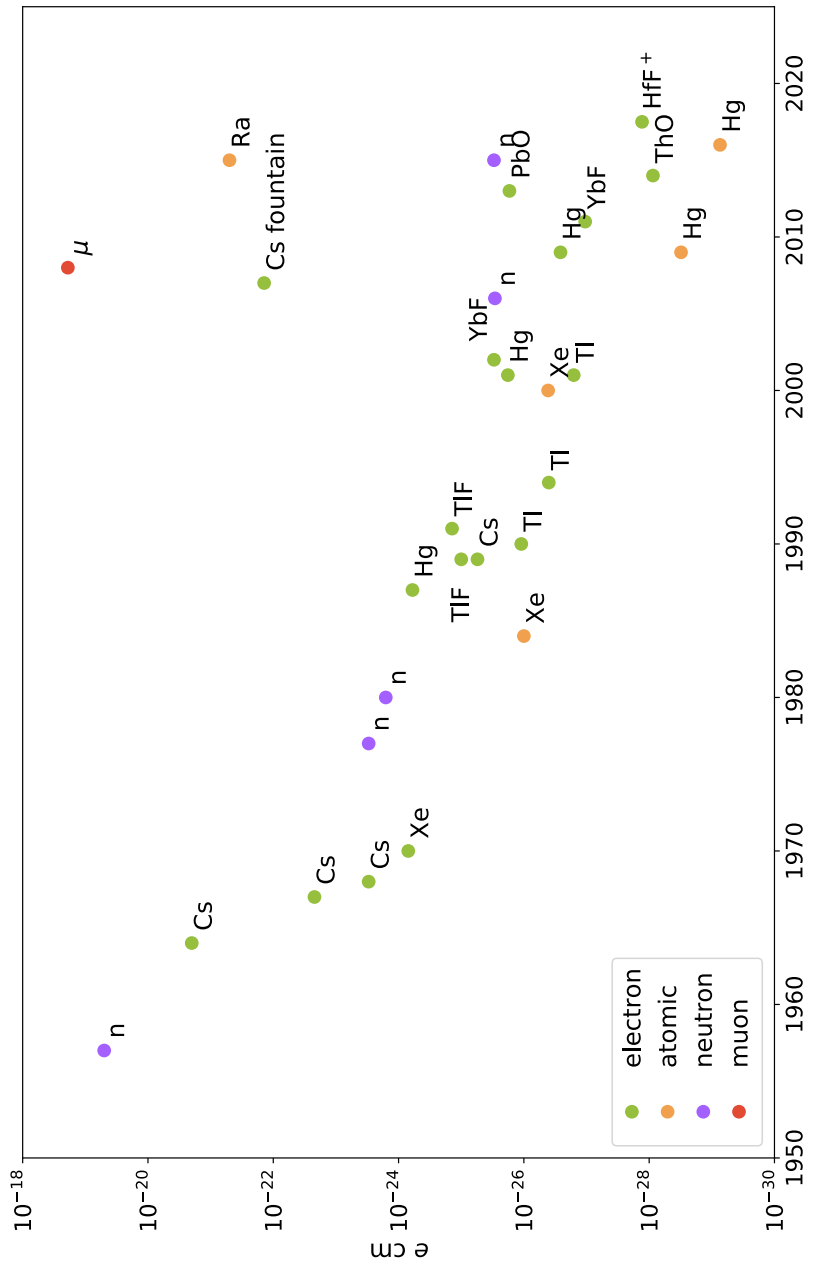

Figure 1.7.: Overview of EDM searches throughout the years, starting at the original neutron EDM experiment in 1953. Plotted are upper limits for various EDM experiments [11, 21, 30, 27, 28, 20, 34], with the systems investigated given with their respective limits. Note that for systems such as the muon (μ), Ra atoms and Cs fountains significant improvements need to follow the recently reported proofs of principle.

2. Experimental Principle

EDM measurements require the polarization of a species, the proper orientation of the polarization with respect to an electric field (**E**) and magnetic field (**B**) and the possibility to observe the spin precession of the system. This chapter will focus on the spin precession the noble gases helium and xenon, which can be polarized efficiently by laser light, and the observation of the spin precession by Superconducting Quantum Interference Devices (SQUID) gradiometers [35]. The mechanisms leading to spin de-coherence will also be discussed.

2.1. Spin Precession

An atom with a nuclear spin **I**, where $|\mathbf{I}| = \sqrt{I(I+1)}\hbar$, has an associated magnetic moment

$$\boldsymbol{\mu} = \gamma \mathbf{I}, \tag{2.1}$$

where γ is the gyromagnetic ratio, given by $\gamma = \frac{g\mu_N}{\hbar}$. g is the nuclear g-factor and $\mu_N = \frac{e\hbar}{2m_p}$ the nuclear magneton. Quantifying the spin along the z axis, the z-component of the magnetic moment is

$$\mu_z = \gamma \hbar m_I, \tag{2.2}$$

with m_I the projection of **I** on the z axis, running from $-I$ to I in integer increments. An externally applied magnetic field (B_0) interacts with the magnetic moment, causing a splitting in the energy sub levels. This is called the Zeeman effect where the additional energy levels are given through

$$E_{\text{Zeeman}} = -\mu_z B = -\gamma \hbar m_I B \text{ [17]}. \tag{2.3}$$

In the case of spin-1/2 particles, such as the noble gasses ^{3}He and ^{129}Xe, there are only two projections of the nuclear spin along the z axis, namely -1/2 (spin down) and +1/2 (spin up).

The magnetic moment can also be expressed in terms of spin, $\boldsymbol{\mu} = \gamma \boldsymbol{\sigma}$. The Hamiltonian for a particle with spin $\boldsymbol{\sigma}$ is given by

$$H = -\gamma \boldsymbol{\sigma} \cdot \mathbf{B}, \tag{2.4}$$

where γ is the gyromagnetic ratio. Here $\boldsymbol{\sigma}$ are given in form of the Pauli spin matrices

$$\sigma_x = \begin{pmatrix} 0 & 1 \\ 1 & 0 \end{pmatrix},\ \sigma_y = \begin{pmatrix} 0 & -i \\ i & 0 \end{pmatrix},\ \sigma_z = \begin{pmatrix} 1 & 0 \\ 0 & -1 \end{pmatrix}, \tag{2.5}$$

where $\boldsymbol{\sigma} = \frac{\hbar}{2}\left(\sigma_x,\ \sigma_y,\ \sigma_z\right)$. $|\psi\rangle$ is the two-component spinor wavefunction, given by

$$|\psi\rangle = \begin{pmatrix} \psi_+ \\ \psi_- \end{pmatrix}, \tag{2.6}$$

where ψ_+, ψ_- are the spin up and spin down states, respectively, with respect to the magnetic field direction. The time evolution can then be calculated using the time-evolution operator $U(t)$

$$U(t) = e^{-iHt/\hbar}. \tag{2.7}$$

With the given Hamiltonian in Eq. 2.4, the time-evolution of spin becomes

$$|\psi(t)\rangle = U(t)|\psi(0)\rangle = e^{i\gamma\boldsymbol{\sigma}\cdot\mathbf{B}t/\hbar}|\psi(0)\rangle, \tag{2.8}$$

generating a spatial rotation around $\mathbf{B}$ with an angle $-\gamma\,|\mathbf{B}|\,t$. In other words, for a constant magnetic field the spin precesses around the magnetic field vector with a frequency

$$\omega_L = -\gamma\,|\mathbf{B}|\,, \tag{2.9}$$

with ω_L the Larmor frequency.

A general solution for spin precession can be found using the Schrödinger equation to solve for the expectation value of the magnetic moment $\boldsymbol{\mu}$ with the Hamiltonian given in Eq. 2.4, substituting $\boldsymbol{\mu}$ for $\gamma\boldsymbol{\sigma}$. The solution for the expected value for the magnetic moment follows the classical Euler equation for rigid bodies

$$\frac{d\langle\boldsymbol{\mu}(t)\rangle}{dt} = \gamma\langle\boldsymbol{\mu}(t)\rangle \times \mathbf{B}(t). \tag{2.10}$$

This can also be described classically. Any particle with a magnetic moment $\boldsymbol{\mu}$ starts precessing in an external magnetic field due to the torque the external magnetic field exerts onto the magnetic moment. Macroscopically the magnetization of an ensemble is given by

$$\mathbf{M} = \frac{N}{V}\,\langle\boldsymbol{\mu}\rangle\,, \tag{2.11}$$

where N is the total number of spins and V the volume over which they are spread. $\langle\boldsymbol{\mu}\rangle$ represents the ensemble average of the magnetic moments. Using the Bloch equations the time evolution of the magnetization of the ensemble can be given as:

$$\frac{d\mathbf{M}(t)}{dt} = \gamma\mathbf{M}(t) \times \mathbf{B}(t). \tag{2.12}$$

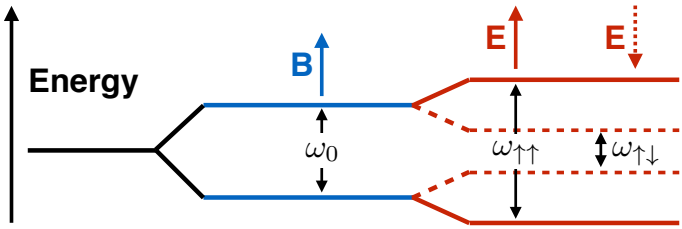

Figure 2.1.: Energy levels of a spin-1/2 system with a magnetic moment and an electric dipole moment in magnetic and electric fields.

For a magnetic holding field in the z direction and a magnetization perpendicular to the holding field in the xy plane, this gives the classical spin precession in the xy plane

$$\mathbf{M}(t) = \mathbf{M} \cdot [\cos(\omega_L t), \sin(\omega_L t), 0]\,. \tag{2.13}$$

Spin relaxation terms can also be included in the Bloch equations, resulting in the following equation assuming the magnetic holding field is still oriented parallel to z:

$$\frac{d\mathbf{M}(t)}{dt} = \gamma \mathbf{M}(t) \times \mathbf{B}(t) + \begin{bmatrix} -M_x/T_2^* \\ -M_y/T_2^* \\ (M_0 - M_z)/T_1 \end{bmatrix}. \tag{2.14}$$

T_2^* is a time constant characterizing the transverse magnetization decay, T_1 a time constant characterizing the longitudinal magnetization decay and M_0 is the magnetization at thermal equilibrium, i.e. where the ensemble magnetization ends up as $t \to \infty$.

2.1.1. Spin Precession with an Electric Dipole Moment

Adding an EDM to a particle simply extends the Hamiltonian with another term, corresponding to the interaction with the electric field

$$\mathbf{H} = -(\mu \mathbf{B} + d\mathbf{E}) \frac{\mathbf{I}}{|\mathbf{I}|}, \tag{2.15}$$

creating a splitting of the energy levels dependent on the electric field, in addition to the Zeeman effect, dependent on the magnetic field. The splitting in energy levels is shown schematically in Figure 2.1. Atoms in parallel or anti-parallel magnetic and electrics fields then start precessing around the magnetic and electric fields with a frequency depending

on the relative orientation between the fields (parallel or anti-parallel)

$$\omega_{\uparrow\uparrow} = -\frac{(\mu B + dE)}{I\hbar}, \tag{2.16a}$$

$$\omega_{\uparrow\downarrow} = -\frac{(\mu B - dE)}{I\hbar}. \tag{2.16b}$$

However, since the electric dipole moment d is very small compared to the magnetic dipole moment μ, the shift in frequency due to d is correspondingly small. An EDM at the current limit, 10^{-29} $e$cm, in an electric field of 2 kV/cm would result in a spin precession frequency of 4×10^{-10} Hz, i.e. one full precession in 80 years.

Switching the relative orientation of the electric and magnetic fields during a measurement and measuring the frequency difference $\Delta\omega$ then gives

$$\Delta\omega = \omega_{\uparrow\uparrow} - \omega_{\uparrow\downarrow} = -\frac{2dE}{I\hbar}. \tag{2.17}$$

2.2. Polarized Spins

For measuring spin precession accurately, maximal polarization is required. The degree of polarization represents how much the spin, or angular momentum, is aligned with a certain direction. In the case of a spin-1/2 particle, such as ^{3}He or ^{129}Xe, a magnetic field creates two Zeeman states, with spin projection quantum numbers $S_z = \pm 1/2$ (spin up/down), with populations N_+ and N_-, respectively. The energy difference between the two states is $\Delta E = \gamma\hbar B$, as shown in Section 2.1. In thermal equilibrium, at temperature T and a magnetic field B_0 the population ratio between the two states is

$$\frac{N_-}{N_+} = e^{-\frac{\Delta E}{kT}} = e^{-\frac{\gamma\hbar B_0}{kT}}, \tag{2.18}$$

where k is the Boltzmann constant. The definition of spin polarization for an atom with spin $\mathbf{F} = \mathbf{I} + \mathbf{J}$, where $\mathbf{F}$ is the spin polarization of the atom, $\mathbf{I}$ is the nuclear polarization and $\mathbf{J}$ is the electronic polarization. The polarization of an atomic ensemble is defined as

$$P = \frac{1}{|\mathbf{F}|} \frac{\sum_F m_F N(m_F)}{\sum_F N(m_F)}, \tag{2.19}$$

with $N(m_F)$ the population number of the state with the magnetic quantum number m_F. ^{3}He and ^{129}Xe both have nuclear spin I 1/2 and electronic spin 0, resulting in the polarization

$$P = \frac{N_- - N_+}{N_- + N_+}. \tag{2.20}$$

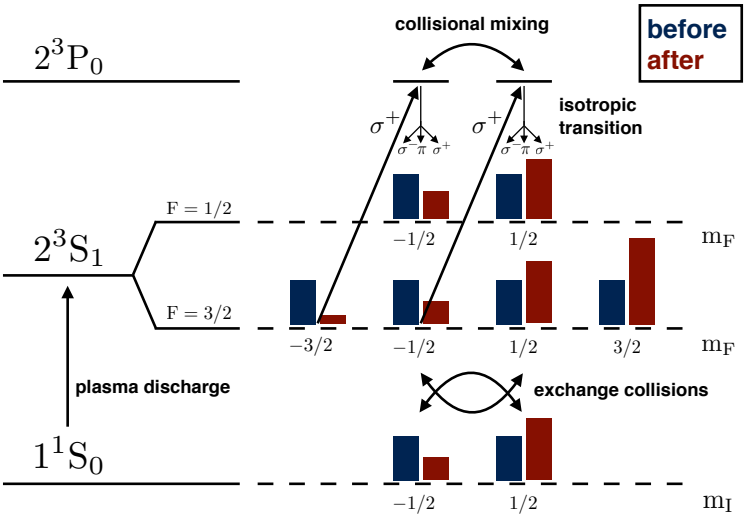

Figure 2.2.: Schematic overview of metastability exchange optical pumping (MEOP) of ^{3}He (adapted from [36]). Through collisions via gas discharge the metastable 2^3S_1 state is populated and with circular polarized laser light at 1083.03 nm wavelength optical pumping is possible.

At thermal equilibrium this gives a polarization of $\tanh\left(-\frac{\Delta E}{2kT}\right)$. At large magnetic fields ($\sim$ 1T) at room temperature the polarization of ^{129}Xe would be $\sim 10^{-8}$. In the MiXeD experimental setup, with a magnetic holding field of 400 nT at room temperature, the polarization would be $\sim 4 \times 10^{-13}$, insufficient for performing high precision EDM measurements. Thus a different method is required for polarizing the atoms. Using a different technique, optical pumping, ^{3}He and ^{129}Xe can be polarized such that several 10 percent polarization can be achieved.

2.2.1. Optical Pumping of ^{3}He

^{3}He can be polarized using two different methods; namely through spin-exchange optical pumping with rubidium (SEOP) [37, 38], or through metastability exchange optical pumping (MEOP) [39, 40]. Our experiment uses MEOP, which uses optical pumping between two excited states of helium. In MEOP the metastable state, 2^3S_1, is populated from the ground state (1^1S_0) by electron collisions resulting from a plasma discharge maintained in a gas at a pressure up to a few millibars. The 2^3S_1 metastable state is

pumped optically to the 2^3P_0 state. Due to angular momentum conservation, transitions from the metastable state to the ground state are forbidden, but collisions with the glass of the pumping cell can give rise to transitions back to the ground state. This causes the lifetime of the metastable state to be of order 1 ms.

Spin polarization requires a magnetic field, which results in a splitting of the hyperfine levels. σ^+ photons with 1083.03 nm wavelength are used to pump ^{3}He atoms in the 2^3S_1 state to the 2^3P_0 state, thereby transferring the angular momentum of the photons to the atoms. The lifetime of the 2^3P_0 state is 10^{-7} s, sufficient for atomic collisions leading to radiationless transitions to the 2^3P levels (collisional mixing). Transitions of the 2^3P levels back to the Zeeman levels in the stable 2^3S_1 state are isotropic, resulting in no net angular momentum transfer during the de-excitation. Many pumping cycles lead to a redistribution of the population into the higher Zeemann (m_F) states, polarizing the electron spins of the atoms in the 2^3S_1 state.

The hyperfine interaction couples the electron spin to the nuclear spin, which means that the polarized 2^3S_1 ^{3}He atoms are also nuclear polarized. Collisions with unpolarized ^{3}He atoms in the 1^1S_0 ground state can lead to an exchange of excitation energy while maintaining nuclear polarization, leading to nuclear polarized ^{3}He atoms in the 1^1S_0 ground state.

The polarized ^{3}He sample used in this work was build and operated in Mainz [41, 42], and polarizations of $\sim 90\%$ have been reached.

2.2.2. Optical Pumping of ^{129}Xe

^{129}Xe can be polarized using spin-exchange optical pumping (SEOP), where the spin of an alkali atom is polarized using optical pumping, and subsequently the electron polarization of the alkali atom is then transfered to the ^{129}Xe nucleus. Typically rubidium is used. The electron polarization of Rb is exchanged with ^{129}Xe by dipole-dipole interactions. This exchange is possible through two different mechanisms: through sudden binary collisions and through Rb-Xe van der Waals molecules that result from three body collisions. The nuclear spin-exchange interaction that couples the nuclear spin $\mathbf{I}$ of the atom to the electron spin $\boldsymbol{\sigma}$ of the alkali atom is

$$V = \alpha \mathbf{I} \cdot \boldsymbol{\sigma}, \tag{2.21}$$

where α is a coupling constant which depends on the distance between the atom and the alkali atom. The binary collisions are pressure independent and dominate at high pressure, while the van der Waals molecules dominate at low pressure.

Rubidium is polarized using a mixture of rubidium vapor, N_2 and ^{4}He, where the Rb D_1 transition is used for optical pumping [43, 44]. ^{4}He is used to pressure broaden the Rb D_1 line to increase absorption from relatively broad laser diodes. N_2 prevents radiation trapping by quenching excited rubidium atom.

2.3. Spin Relaxation

The polarization of an ensemble is not constant, several mechanisms cause the polarization to decay exponentially towards the Boltzmann polarization, i.e. thermal equilibrium. Two characteristic decays exist, namely longitudinal magnetization decay, characterized by a time constant T_1 and a transverse magnetization decay, characterized by a time constant T_2^*. Longitudinal refers to the decay of the magnetic moment parallel to the magnetic field, while transverse magnetization decay refers to the decay of the magnetic moment perpendicular to the magnetic field.

2.3.1. Longitudinal Relaxation

Longitudinal relaxation mechanisms are the magnetic field gradient relaxation, wall relaxation, binary collisions and van der Waals collisions. The total longitudinal relaxation time is then given by

$$\frac{1}{T_1} = \frac{1}{T_{1,\text{grad}}} + \frac{1}{T_{1,\text{wall}}} + \frac{1}{T_{1,\text{bin}}} + \frac{1}{T_{1,\text{vdW}}}. \tag{2.22}$$

All separate contributions have the same mechanism causing spin decoherence: spin flips are induced by the interactions of the magnetic moment with the environment.

The gradient relaxation is caused by gradients in the magnetic holding field, inducing spin flips. Nuclear polarized atoms in a cell move randomly throughout the volume, which means, because the magnetic field is not homogeneous, the strength of the magnetic field for each atom at every point in time varies. The time variation of the fluctuating magnetic fields can induce spin flips, which is described in detail in [45]. In [46] an analytical expression is derived for the longitudinal gradient relaxation. Only two simplified scenarios are shown here; the regime of motional narrowing, with low pressure and low magnetic field, and the high pressure, high magnetic field regime. First for the motional narrowing regime

$$\frac{1}{T_1} \approx \frac{8R^4\gamma^2}{175D}\left(\left|\nabla B_y\right|^2 + \left|\nabla B_z\right|^2\right) \tag{2.23}$$

and finally for the high pressure, high magnetic field regime

$$\frac{1}{T_1} \approx \frac{D}{B^2}\left(\left|\nabla B_y\right|^2 + \left|\nabla B_z\right|^2\right). \tag{2.24}$$

When the polarized gas is being produced and transported, the high pressure, high magnetic field regime is applicable, i.e. Eq. 2.24, whereas during the measurements the motional narrowing regime applies, i.e. Eq. 2.23.

Wall relaxation is caused by interaction of the nuclear polarized atoms with the surface of the containment cell, usually glass. Atoms colliding with the the cell surface can be

adsorbed or diffuse into the glass. Interactions with the ferromagnetic and paramagnetic impurities on in the cell material causes spin flips, i.e. loss of spin coherence [47, 48, 49]. The wall relaxation is independent of pressure but depends on the surface to volume ratio of the containment cell

$$\frac{1}{T_{1,\mathrm{Wall}}} \propto \frac{A}{V}. \tag{2.25}$$

During collisions between atoms there are two mechanisms causing polarization loss, through short lifetime molecules being formed and through longer lifetime van der Waals molecules being formed. For lighter atoms the short lifetime molecules are a more dominant spin loss mechanism, while for heavier atoms the van der Waals molecules are. These molecules have rotational and vibrational degrees of freedom in addition to the translational degrees of freedom. The rotational angular momentum of the molecules is coupled to the nuclear spin, transferring some of the nuclear polarization to the orbital angular momentum. The relaxation times due to binary collisions for ^{3}He and ^{129}Xe were determined by [50] and [51]

$$T_{1,\mathrm{bin}}^{\mathrm{He}} = 744 \qquad \frac{p_0}{p_{\mathrm{He}}}\frac{T}{T_0}\ \mathrm{h}, \tag{2.26}$$

$$T_{1,\mathrm{bin}}^{\mathrm{Xe}} = (56.3 \pm 2.6)\frac{p_0}{p_{\mathrm{Xe}}}\frac{T}{T_0}\ \mathrm{h}. \tag{2.27}$$

Here p is the pressure and T the temperature and the factors p_0 and T_0 are 1013 mbar and 273.15 K respectively. The He value is numerically calculated and no error is given.

The van der Waals molecules cause a larger spin relaxation due to the longer lifetimes. In [52] it was found the relaxation times for xenon van der Waals molecules is given by

$$T_{1,\mathrm{vdW}}^{\mathrm{Xe}} = (4.1 \pm 0.06)\left(1 + r\frac{p_N}{p_{\mathrm{Xe}}}\right)\ \mathrm{h}, \tag{2.28}$$

where p_N and p_{Xe} are the partial pressures of the buffer gas and the xenon and r is the relative breakup rate coefficient, with some examples in Table 2.1. The addition of a buffer gas improves the relaxation rate.

Table 2.1.: Relative breakup coefficients r from Eq. 2.28 for various buffer gases taken from [52].

buffer gas	r
He	0.25 ± 0.08
Ar	0.49 ± 0.06
N_2	1.05 ± 0.08

2.3.2. Transverse Relaxation

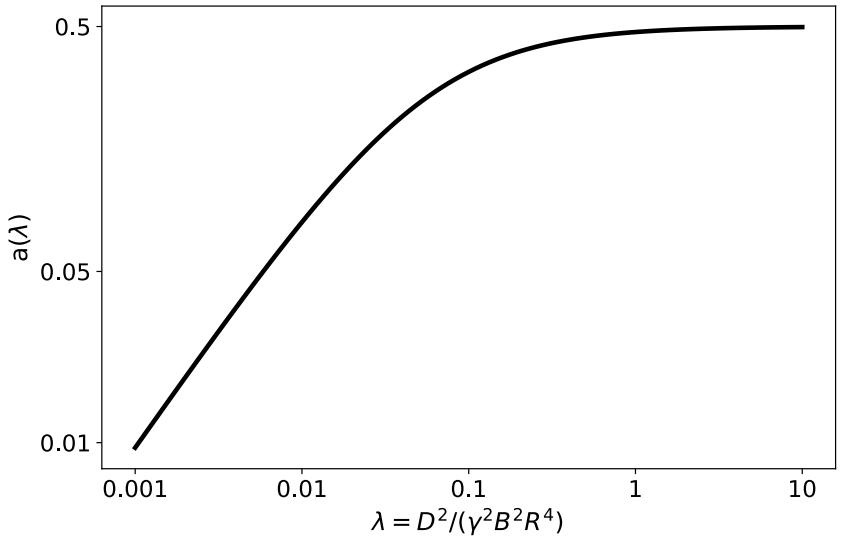

Figure 2.3.: The factor a(λ) of Eqs. 2.29 and 2.30. By varying λ, e.g. by changing the pressure, the contributions of the transverse gradients of the magnetic field to the transverse relaxation time T_2^* can be modified.

A magnetic moment precessing perpendicular to an external magnetic field decays exponentially with the time constant T_2^*. This relaxation is caused by a loss of coherence between the magnetic moments of the ensemble due to collisions and magnetic field gradients. Analytical expressions for T_2^* in case of spherical and cylindrical cells have been found [46, 53]. Due to spherical symmetry a spherical cell is easier to describe and has a longer coherence time. The transverse relaxation rate for spherical cell is given by

$$\frac{1}{T_2^*} = \frac{1}{T_1} + \frac{8R^4\gamma^2}{175D}\left(|\nabla B_z|^2 + a(\lambda)\left[|\nabla B_x|^2 + \left|\nabla B_y\right|^2\right]\right), \tag{2.29}$$

with

$$a(\lambda) = \frac{175}{8}\lambda \sum_n \frac{1}{\left(x_{0,n}^2 - 2\right)\left(1 + x_{0,n}^4\lambda\right)} \tag{2.30}$$

and (see also Figure 2.3)

$$\lambda = \frac{D^2}{\gamma^2 B^2 R^4}, \tag{2.31}$$

where the external magnetic field B is in the z direction. D represents the diffusion coefficient. At $x_{0,n}$ the derivatives of the spherical Bessel function $j_1(x)$ are zero. γ is the gyromagnetic ratio and R is the radius of the spherical cell. Further, T_2^* depends on T_1.

In the regime of motional narrowing, at low pressures and low magnetic field strengths, this equation simplifies to

$$\frac{1}{T_2^*} = \frac{1}{T_1} + \frac{4R^4\gamma^2}{175D}\left(2\left|\nabla B_z\right|^2 + \left[\left|\nabla B_x\right|^2 + \left|\nabla B_y\right|^2\right]\right). \tag{2.32}$$

At higher pressures, λ approaches zero, making the magnetic gradient relaxation only sensitive to gradients in the z direction

$$\frac{1}{T_2^*} = \frac{1}{T_1} + \frac{8R^4\gamma^2}{175D}\left|\nabla B_z\right|^2. \tag{2.33}$$

2.4. Co-magnetometry

In order to do precision measurements on EDMs precise control and monitoring of the external fields is needed. The easiest way to accomplish this is by monitoring the precession of two species in the same setup, where only one of the species exhibits the effect you are interested in. Then the influence of temporal and spatial variations of external fields can be suppressed.

The spin precession of noble gases is well suited for this application. The noble gases have minimal interactions and thus the two polarized species can be confined in the same volume, giving real time in-situ monitoring of the magnetic field. Due to the Z^2 scaling of EDMs in atoms with a closed electron shell (see Sec. 1.3, Eq. 1.6), the EDM contribution of one of the species can be minimized by using a lighter species. In this experiment ^{3}He and ^{129}Xe were chosen, due to their excellent polarisability.

Because the precession frequencies fluctuate with the magnetic and electric field, measuring the phase instead of the frequency gives makes it much more accurate. The phases as a function of time for ^{3}He and ^{129}Xe can be expressed as

$$\varphi_{\mathrm{He}} = \frac{2}{\hbar}\left(\mu_{\mathrm{He}}B + d_{\mathrm{He}}E\right)t \text{ and} \tag{2.34}$$

$$\varphi_{\mathrm{Xe}} = \frac{2}{\hbar}\left(\mu_{\mathrm{Xe}}B + d_{\mathrm{Xe}}E\right)t. \tag{2.35}$$

Taking the weighted phase difference between φ_{Xe} and φ_{Xe} gives for the weighted phase difference

$$\Delta\varphi = \varphi_{\mathrm{Xe}} - \frac{\gamma_{\mathrm{Xe}}}{\gamma_{\mathrm{He}}}\varphi_{\mathrm{He}} = \frac{2}{\hbar}\left(d_{\mathrm{Xe}}E - \frac{\gamma_{\mathrm{Xe}}}{\gamma_{\mathrm{He}}}d_{\mathrm{He}}E\right)t. \tag{2.36}$$

Taking into account that d_{He} is much smaller than d_{Xe}, using the fact that the atomic EDM scales with Z^2 (Eq. 1.6), results in the time dependent weighted phase difference

$$\Delta\varphi(t) \approx \frac{2}{\hbar}(d_{Xe}E)\,t. \tag{2.37}$$

The magnetic field term is completely removed from the resulting equation. Having both species in the same volume assures the magnetic field measured by helium is the same magnetic field experienced by xenon. Other experiments have used co-magnetometry but only in adjacent volumes, giving an approximation of the magnetic fields at the location of the EDM measurement. To gain higher orders of precision for the EDM measurement better control over magnetic fields is required, necessitating in-situ co-magnetometry.

Integrated over time the total accumulated weighted phase difference is then

$$\Delta\Phi = \Phi_{Xe} - \frac{\gamma_{Xe}}{\gamma_{He}}\Phi_{He}. \tag{2.38}$$

2.5. Sensitivity

The Cramer-Rao Lower Bound (CRLB) gives a lower bound on the variance of an unbiased estimator of a deterministic parameter, giving a means to estimate the best possible sensitivity reachable in the MiXeD experiment. The precession signal, assuming white noise, picked up by the SQUIDs can be described by

$$x[n] = A\exp\left[-\frac{n}{r_s T_2^*}\right]\cos(2\pi(f/r_s)n+\phi) + w[n] \text{ for } n = 0,1,...,N-1 \tag{2.39}$$

where n indicates the nth data point, r_s the sampling ratio and $w[n]$ white noise. With the CRLB (see Appendix C) it can be shown that the lower limit of the variance of the frequency is given by

$$\sigma_f^2 \geq \frac{12}{(2\pi)^2 \mathrm{SNR}^2 f_{BW} T^3} C(T;T_2^*), \tag{2.40}$$

where C is a term accounting for the exponential decay of the signal, SNR is the signal-to-noise ratio, f_{BW} is the Nyquist frequency and T is the total measurement time. The uncertainty of the phase determination, assuming constant frequency, is then

$$\sigma_\Phi \geq \frac{\sqrt{3}}{\pi \mathrm{SNR}\sqrt{f_{BW}T}}\sqrt{C(T;T_2^*)}. \tag{2.41}$$

The contribution of the EDM to the weighted phase difference (in radians) using co-magnetometry (see Sec. 2.4) is given by

$$\Delta\varphi \approx \frac{2}{\hbar}(d_{Xe}E)\,t. \tag{2.42}$$

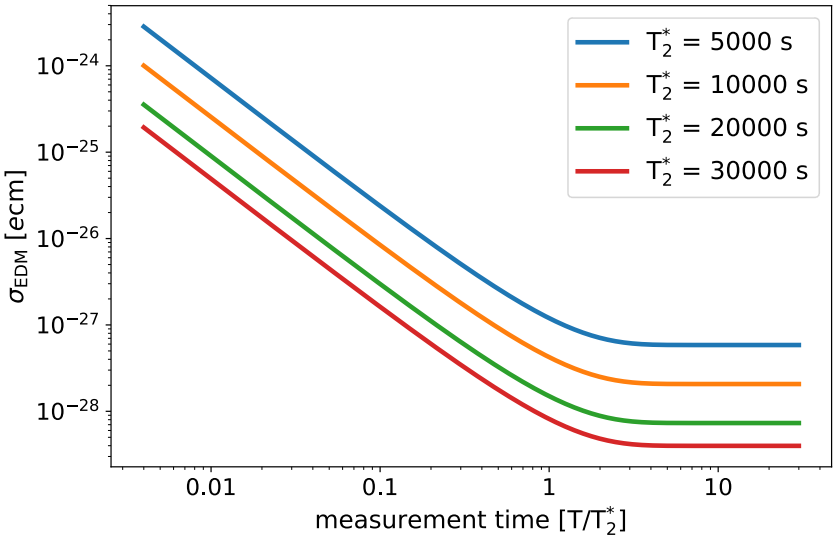

Figure 2.4.: The sensitivity to the EDM of ^{129}Xe as given in Eq. 2.43 as a function of measurement time for varying T_2^*. For this plot the SNR was set to 500, E to 800 V/cm and the sampling rate r_s to 250 Hz.

Naively, the EDM sensitivity would then scale as

$$\sigma_{\mathrm{EDM}} \geq \frac{\sqrt{3}h}{2\pi \mathrm{SNR} E \sqrt{f_{\mathrm{BW}}} T^{3/2}} \sqrt{C(T; T_2^*)}. \tag{2.43}$$

However, in order to distinguish between the EDM and other linear effects, the electric field orientation is switched periodically, resulting in a triangular EDM phase pattern for a non-zero EDM.

2.6. Superconducting Quantum Interference Device

Superconducting Quantum Interference Devices (SQUIDs) [35, 54] are employed to pick up the macroscopic magnetic fields generated by the precessing magnetic moments of the spin polarized gases. DC-SQUIDs consist of two Josephson junctions in a superconducting loop. A bias current fed into the SQUID module splits equally between the two sections of the superconducting loop. An increasing magnetic field induces a screening current resulting in an asymmetric current between the two branches such that the magnetic

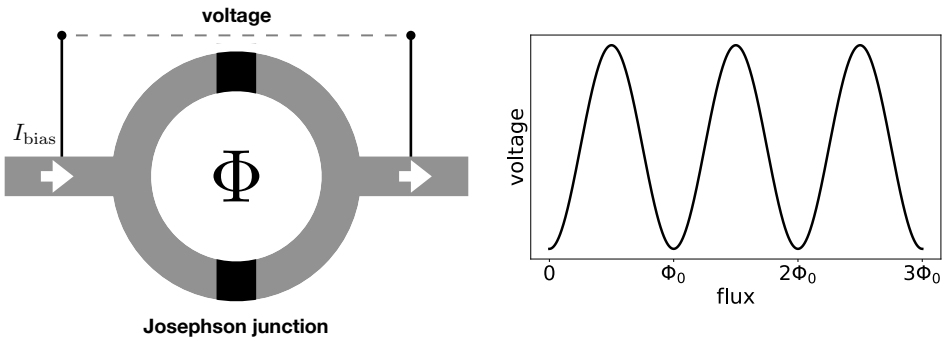

Figure 2.5.: DC SQUID with constant bias current. A change in flux through the loop generates an imbalance between the current between the paths via a screening current, generating a voltage differential. The screening current increases the SQUID flux to the nearest integer multiple of a flux quanta Φ_0, generating a periodic voltage.

flux through the module is a multiple of a magnetic flux quantum $\Phi_0 = h/(2e)$. For an external flux below $\Phi_0/2$ the current generates a magnetic field canceling the flux enclosed by the module, otherwise it it increases it to Φ_0. In other words, the screening current increases the SQUID flux to the nearest integer multiple of a flux quanta Φ_0. With an appropriate bias current a linear change in magnetic flux generates a periodic change in the voltage across the junctions with a period Φ_0. With resistive shunts the modulation becomes smooth (see Figure 2.5). To optimally measure small changes in the applied flux a bias current is chosen to maximize the amplitude of voltage modulation and off-set flux, maximizing $\delta V/\delta\Phi$. To generate the required superconductivity the SQUIDs are put into a cryostat, filled with liquid helium.

SQUIDs operated in flux-locked loop (FLL) mode are set at the optimal working point to achieve maximal sensitivity and a linear response function, i.e. where $\delta V/\delta\Phi$ is maximal. A feedback coil is placed next to the SQUID to generate a flux. Any change in the working point of the SQUID voltage is amplified and integrated, feeding back current to the feedback coil through a feedback resistor, compensating the flux change through the SQUID.

The signal of SQUIDs is limited by the amout of flux, i.e. the surface area of the superconducting loop. Utilizing larger pickup coils feeding back flux to the SQUIDs increases the effective surface area and thus the signal. To incorporate pickup coils the SQUIDs are encased in a niobium shield, providing shielding of external magnetic fields. A pickup loop is situated outside of the niobium shield, but still inside of the cyrostat, and is connected to a feedback coil next to the SQUIDs. The feedback coil flux-couples the pickup

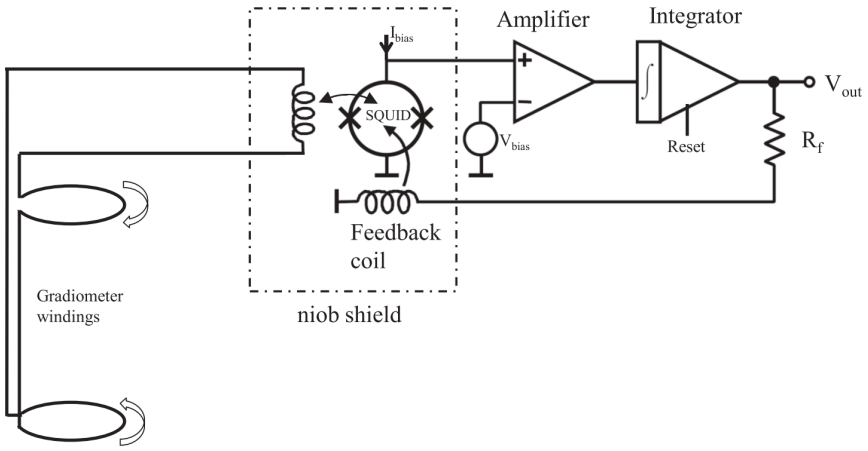

Figure 2.6.: Schematic overview of a flux-locked loop (FLL) with a SQUID as a current detector. The SQUID, niobium shield and pickup coil are at liquid helium temperature. An external pickup coil, in gradiometer configuration, is flux coupled to the SQUID loop. A change in external field generates a current in the pickup coil, which is coupled to the SQUID via a coil. A deviation from the working point is amplified, integrated and fed back to a feedback coil via a resistor. This feedback loop sets the SQUID back to the optimal working point, canceling out the flux change from the pickup coil. Figure from [55].

loop to the SQUIDs, effectively utilizing the SQUIDs as current detectors. Because the pickup loop can be of greater size than the SQUIDs, the flux picked up is larger, whereas the noise level of the SQUID remains the same. Figure 2.6 depicts a SQUID system in this configuration.

3. Electric Field Sensor

The fiducial volume in this experiment is completely enclosed by magnetic field coil systems, a μ-metal magnetic shielding cylinder and the magnetically shielded room. The electric field is generated over the fiducial volume with two silicon wafers connected to a high voltage power supply residing outside of the magnetically shielded room. The presence of an electric field over the fiducial volume is verified by an electro-optical measurement of the electric field inside of the glass cell for gas mixtures of He and Xe at different pressures.

In electro-optically active crystals the polarization of light passing through the crystal changes as a function of the applied electric field [56]. The change of polarization is determined by passing through a polarizer and measurement the intensity of the two components.

On a slow time scale the external electric field is compensated by an internal crystal field which results in a decrease of the induced electro-optical rotation of the polarization. The accumulated charge slowly balances out the external electric field, causing the internal electric field to eventually drop to zero. The internal electric field is essentially the output of a high pass filter of the applied external electric field. The associated time constant is proportional to the crystal conductivity [57]. A corresponding time τ_c constant can be defined as

$$\tau = \frac{\epsilon_0 \epsilon_r}{G}, \tag{3.1}$$

where ϵ_0 and ϵ_r are the vacuum and relative crystal permittivities, and G is the specific conductivity of the crystal. Under application of an external electric field, the internal electric field then exhibits the exponential behavior

$$E_{\text{crystal}}(t) = E_{\text{crystal}}(0) e^{-t/\tau}, \tag{3.2}$$

where $E_{\text{crystal}}(0)$ is the internal electric field at $t = 0$. Additionally, photoconductivity can accelerate this process [57]. We have identified a crystal for which the time scale τ_c is of order 1.4 h and the measurement on the time scale for the electric field in the ^{129}Xe EDM experiment becomes possible. Electro-optic crystals which are most suitable for DC measurements are Lithium Niobate ($LiNbO_3$) and Bismuth Germanate ($Bi_4Ge_3O_{12}$). Charge relaxation constants of 7×10^7 s and 248 s, respectively, have been estimated [57]. Care has to be taken about the temperature dependence of the crystal properties when using a crystal as an electric field sensor [58].

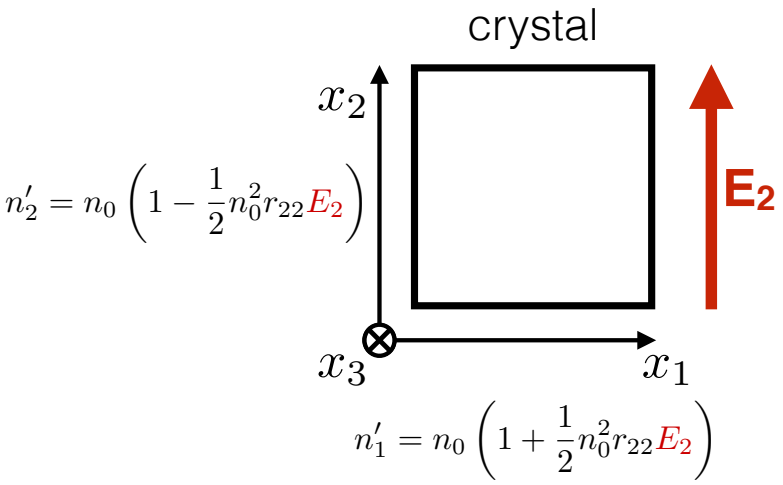

Figure 3.1.: Schematic overview of the two principal axes of the electro-optic Lithium Niobate crystal for an electric field applied along x_2, assuming a light wave propagating along x_3 The principal axes then coincide with x_1, x_2, the optical axes. The birefringence of such a configuration as a function of the applied electric field is $\Delta n = -n_0^3 r_{22} E_2$.

3.1. Electro-Optical Properties of Crystals

In order to use an electro-optic crystal as an electric field sensor several requirements have to be met. Firstly, the time dependence of the internal field (see Eq. 3.2) should be minimized and secondly the temperature dependence should also be minimal. To meet these constraints a Lithium Niobate crystal was chosen.

In Appendix A the properties of electro-optic crystals are derived, specifically for $LiNbO_3$, which is an uniaxial crystal if no external electric field is applied (see Sec. A.1). The index ellipsoid in the principal coordinate system x_1, x_2, x_3 yields the refractive indices,

$$n_1 = n_0,\ n_2 = n_0 \text{ and } n_3 = n_e. \tag{3.3}$$

For an electro-optic crystal under influence of an external applied electric field index ellipsoid is modified (see Sec. A.2), yielding refractive indices with electric field dependence. The derivation of the refractive indices under an external applied electric field for $LiNbO_3$ is shown in Section A.3. For light propagating along x_3 the refractive indices in

the principal coordinate system are

$$n_1' = n_0\left(1+\frac{E_3 n_0^2 r_{13} - n_0^2 r_{22} E_{12}}{2}\right),\ n_2' = n_0\left(1+\frac{E_3 n_0^2 r_{13} + n_0^2 r_{22} E_{12}}{2}\right). \tag{3.4}$$

Here n_1', n_2' are the refractive indices in the principal coordinate system x_1', x_2', which is rotated with respect to the principal coordinate system in zero external applied electric field (the optical axes x_1, x_2). r_{13}, r_{33} are the electro-optic coefficients for $LiNbO_3$ and E_{12} is the electric field in the x_1x_2 plane (see Secs. A.2, A.3). The rotation along x_3 with respect to x_1 is

$$\theta = \frac{\pi/2 - \phi}{2}, \tag{3.5}$$

where ϕ is the angle of the external applied electric field in the x_1x_2 plane with respect to x_1. The indices of refraction in Eq. 3.4 yield

$$\Delta n = -n_0^3 r_{22} E_{12}, \tag{3.6}$$

where E_{12} is the electric field magnitude in the x_1x_2 plane. Figure 3.1 shows the refractive indices for propagation along x_3 and an external electric field along x_2. The phase retardation is given by

$$\Gamma = \frac{2\pi \Delta n L}{\lambda}, \tag{3.7}$$

where L is the path length the light travels through the electro-optic medium and λ is the light wavelength.

In conclusion we have chosen a Y-cut Z-propagation $LiNbO_3$ crystal for which the temperature dependence is minimized. The birefringence then only depends on the r_{22} electro-optic coefficient, which has a small temperature coefficient [59]. Under $Z = x_3$ propagation the crystal shows no natural birefringence (see Eq. 3.6) and has an induced birefringence independent of the orientation of the electric field vector in the x_1x_2 plane.

3.2. Electro-Optic Electric Field Sensor

The electro-optic crystal is deployed as a phase retarder and the phase retardation is a measurement of the applied electric field. Measuring phase retardation is accomplished using a linear polarizer as an analyzer. A linear polarizer picks a polarization of light to let through, removing other polarizations. Any change in phase retardation changes the polarization of outgoing light, thus changing the light intensity after the polarization analyzer. A schematic overview of the electro-optic electric field sensor is shown in Figure 3.2.

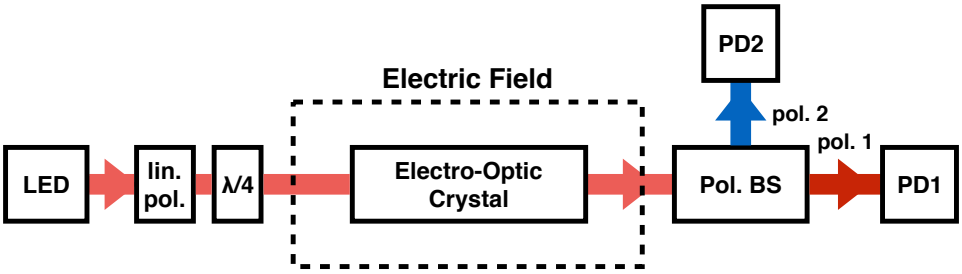

Figure 3.2.: Schematic overview of an electro-optic electric field sensor. The light is generated with a Light Emitting Diode (LED), which is circularly polarized by means of a linear polarizer followed by a quarter waveplate at 45°. The circularly polarized light subsequently enters the electro-optic crystal, which acts as a wave retarder with retardation as a function of the applied electric field strength. The amount of retardation is measured using a polarizing beamsplitter (the analyzer) in combination with two photodiodes (PD), which measures the intensities of perpendicular polarizations of light exiting the sensor.

First linearly polarized light is made circular using a quarter waveplate at an angle of 45° to the optic axis. In Jones calculus Left Handed Circular Polarized light (LHCP) is written as

$$\frac{1}{\sqrt{2}}\begin{bmatrix}1\\+i\end{bmatrix}. \tag{3.8}$$

The circular polarized light is transformed to the principal axes of the electro-optic crystal, before being transformed back to the laboratory frame. Assuming LHCP light propagating in x_3 direction through a $LiNbO_3$ crystal, the light exiting the crystal is described by

$$\mathbf{L}_{\text{crystal}} = \frac{1}{\sqrt{2}}\begin{bmatrix}\cos\theta & -\sin\theta\\ \sin\theta & \cos\theta\end{bmatrix}\begin{bmatrix}e^{i\frac{\Gamma}{2}} & 0\\ 0 & e^{-i\frac{\Gamma}{2}}\end{bmatrix}\begin{bmatrix}\cos\theta & \sin\theta\\ -\sin\theta & \cos\theta\end{bmatrix}\begin{bmatrix}1\\ i\end{bmatrix}, \tag{3.9}$$

where θ is the angle of the principal axes with respect to the x_1 axis. The phase retardation can then be measured using a linear polarizer as an analyzer and measuring the light intensity with a photodiode. For ease of explanation a linear polarizer with the axis of transmission along x_1 will used, resulting in a transmission of light through the sensor of

$$\mathbf{L}_{\text{sensor}} = \frac{1}{\sqrt{2}}e^{i\frac{\Gamma}{2}}\begin{bmatrix}\left(\cos^2\theta + i\cos\theta\sin\theta\right) - e^{i\Gamma}\left(-\sin^2\theta\, i\cos\theta\sin\theta\right)\\ 0\end{bmatrix}. \tag{3.10}$$

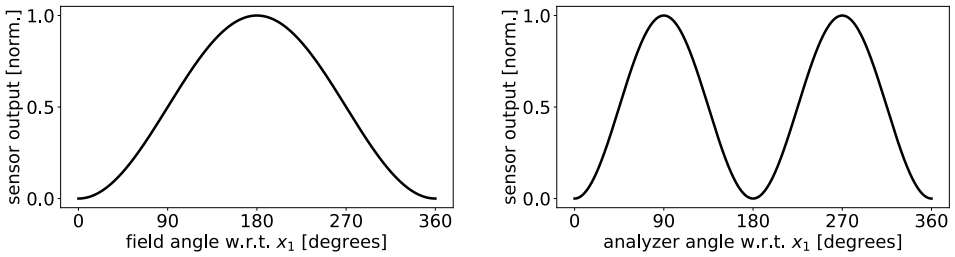

(a) (b)

Figure 3.3.: (a) Simulated response of the output of an electro-optic electric field sensor constructed out of a Y-cut Z-propagating $LiNbO_3$ crystal as a function of the electric field angle with respect to the x_1 axis, with a horizontal axis of transmission for the analyzer. (b) Electric field fixed parallel to the x_1 axis, and the simulated response as a function of the analyzer angle in the x_1x_2 plane with respect to x_1 is plotted.

The light intensity exiting the sensor is given by the $\mathbf{L}_{\text{sensor}}\mathbf{L}_{\text{sensor}}^{\dagger}$, the product of $\mathbf{L}_{\text{sensor}}$ and its complex conjugate

$$I = \frac{1}{2}(1 - \Gamma \cos\phi), \tag{3.11}$$

where θ has been transformed to ϕ, the angle of the electric field vector rotating along x_3 with respect to the x_1 axis (see Eq. 3.5). An electric field vector parallel to the x_1 axis results in the sensor output as a function of applied electric field strength

$$I = \frac{1}{2}\left(1 - \frac{2\pi}{\lambda} n_0^3 r_{22} E_1\right). \tag{3.12}$$

The linear polarizer in combination with the quarter waveplate behind the LED generate circularly polarized light. The photodiode (PD) after the analyzer measures the intensity of the light exiting in one particular polarization.

The normalized response of an electro-optic sensor in this configuration is shown in Figure 3.3a. In absence of an externally applied electric field the sensor output is equal to half the incoming light (see Eq. 3.11). The rotation of light polarization inside the electro-optic crystal is maximal for an externally applied electric field parallel or anti-parallel to the x_1 axis.

Any arbitrary orientation of the electric field vector in the x_1x_2 plane can be measured by choosing an appropriate orientation of the analyzer in the x_1x_2 plane. A linear analyzer with an arbitrary angle α with respect to x_1 in the x_1x_2 plane is described by

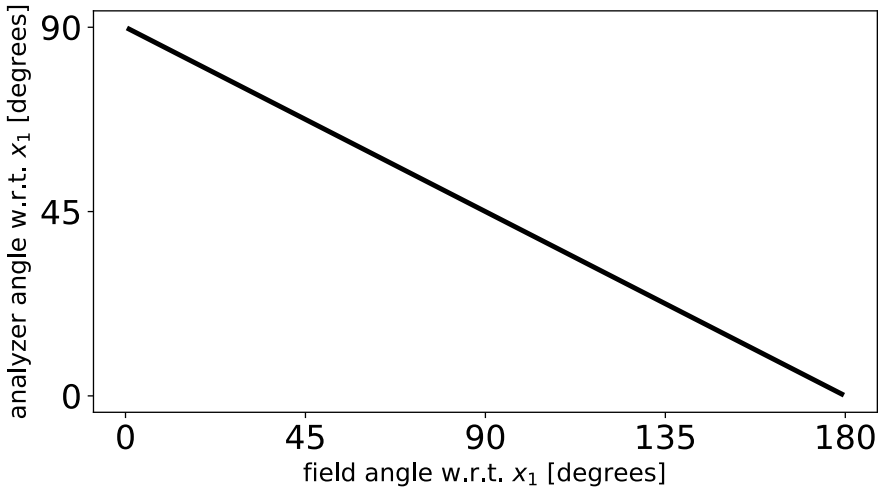

Figure 3.4.: Electric field angle with respect to x_1 in the x_1x_2 plane versus the optimum analyzer angle with respect to the x_1 axis, as given in Eq. 3.13. As can be seen in Figure 3.3b, the sensor response is degenerate for increments of ±90°, meaning that for any given electric field angle there are 4 optimal analyzer angles.

$$\begin{bmatrix} \cos\alpha & -\sin\alpha \\ \sin\alpha & \cos\alpha \end{bmatrix} \begin{bmatrix} 1 & 0 \\ 0 & 0 \end{bmatrix} \begin{bmatrix} \cos\alpha & \sin\alpha \\ -\sin\alpha & \cos\alpha \end{bmatrix}. \tag{3.13}$$

An electric field in the x_2 direction, E_2, can be measured by rotating the linear analyzer 45° (See Figure 3.4). Maximal sensitivity is reached when the analyzer is at 45° with respect to the principal axes, resulting in 4 possible orientations for the analyzer.

Figure 3.4 plots the simulated optimal analyzer angle with respect to the x_1 axis against the applied electric field angle in the x_1x_2 plane. These optima are degenerate for multiples of ±90°, as can be seen in Figure 3.3b, meaning there are 4 optimal analyzer angles for each applied electric field angle.

From Figure 3.3b it is apparent that measuring the intensity for polarizations perpendicular to each other gives the same response amplitude, but differing in sign. This can be applied by incorporating a polarizing beamsplitter as the analyzer and measuring the intensity of both perpendicular polarizations as a function of the electric field, essentially using the electro-optic electric field sensor as a polarimetric interferometer [60]. By measuring the differential between the two intensities any fluctuations of the light source are

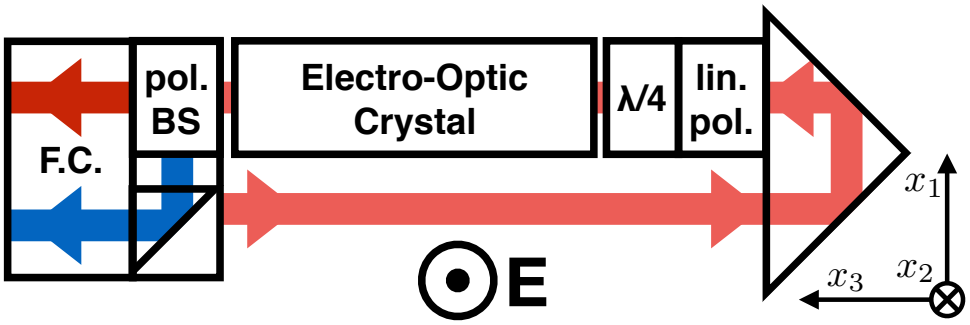

Figure 3.5.: Schematic overview of the fiber-coupled electro-optic electric field sensor. Light is coupled in through a fiber coupling (F.C.), subsequently reflected by 180° with a prism before being circularly polarized by a linear polarizer followed by a quarter waveplate at 45°. It then enters a Lithium Niobate electro-optic crystal configured to measure an electric field in the x_2 direction. The analyzer, a polarizing beamsplitter (pol. BS), then has to be at 45° in the x_1x_2 plane w.r.t. the crystal optical axis x_1. Both orthogonal polarizations are then fiber coupled, where one requires an additional prism to reflect the light by towards the fiber coupling.

removed from the output, and the signal with respect to the electric field is increased by a factor two. This setup is shown schematically in Figure 3.2, where the intensity of both perpendicular polarizations is also plotted.

3.3. Integrated Sensor

To isolate the light source from the magnetic shielding a fiber coupled solution was chosen. A fiber coupled Thorlabs LED generated light outside of the magnetically shielded setup and transmits it through a fiber to the sensor. To prevent run-to-run polarization changes from movement of the fiber, it was chosen to place the polarization optics next to the electro-optic crystal. Apart from the optic components, the sensor is manufactured out of macor.

Figure 3.5 shows a schematic overview of the integrated electro-optic electric field sensor. The light enters through the fiber coupling (F.C.), where the fiber is glued in front of a lens embedded into a macor holder. The macor holder has 3 fiber couplings, one for light entering the sensor and two for the two orthogonal polarization directions leaving the sensor as discussed in Section 3.2 and shown in Figure 3.2. The fiber coupling all

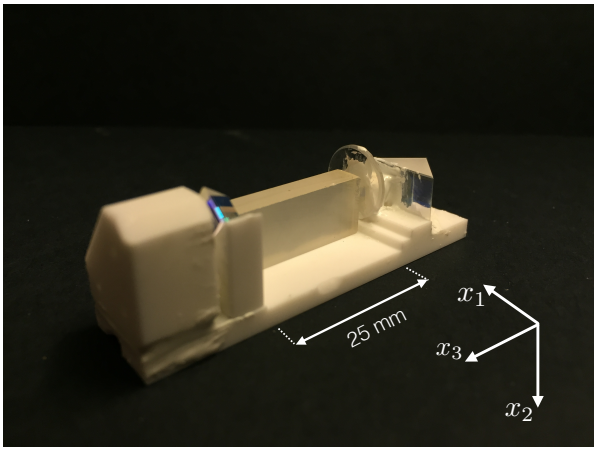

Figure 3.6.: Photograph of the fiber-coupled electro-optic electric field sensor exploiting a Lithium Niobate crystal, without the fibers attached.

consist of a fiber embedded into the macor, with the fiber glued in front of the lens.

The light subsequently travels to a prism, which reflects the light by 180°, upon which it travels through a linear polarizer followed by a quarter waveplate at 45° with respect to the linear polarizer, circularly polarizing the light. The prism, linear polarizer and quarter waveplate are all glued to a macor baseplate and to each other. The circularly polarized light then travels through the Lithium Niobate electro-optic crystal, acting as a wave retarder under influence of an applied electric field unequal to zero.

A polarizing beamsplitter is used as an analyzer. The sensor is configured in order to measure an electric field in the x_2 direction for light propagating through the crystal in the x_3 direction, as shown in Figure A.2. For Figure 3.5 this means the applied electric field is either pointing out of, or into, the page. From Figure 3.4 it is clear that for an applied electric field angle of 90° (x_2 direction), the analyzer should be at an angle 45°, both with respect to the x_1 axis in the x_1x_2 plane. Subsequently the light of both orthogonal polarization directions is coupled into two fibers, and read out by two photodiodes situated outside of the magnetic shielding. One of the orthogonal polarizations requires an additional prism reflecting the light towards the fiber coupling.

A photograph of the constructed fiber coupled sensor is shown in Figure 3.6, without the fibers attached.

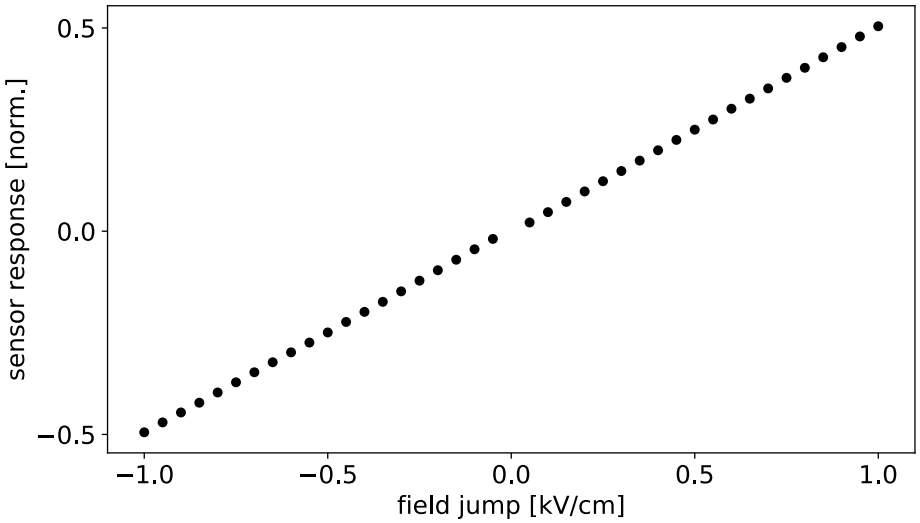

Figure 3.7.: Sensor response for field jumps up to 1 kV/cm.

3.4. Performance of Electro-Optic Field Sensor

The sensor was calibrated with light from a LED at 740 nm as a light source. The Lithium Niobate electro-optic crystal was placed between two copper electrodes separated by 2 cm and a potential difference was applied. A polarizing beamsplitter was used as an analyzer, with both beam directions measured by photodiodes. The sensor output is given by

$$S_{\text{output}} = \frac{a_1\,(\text{PD}_1 - c_1) - a_2\,(\text{PD}_2 - c_2)}{a_1\,(\text{PD}_1 - c_1) + a_2\,(\text{PD}_2 - c_2)}, \tag{3.14}$$

where PD_1, PD_2 are the photodiode signals, c_1, c_2 the respective photodiode offsets and a_1, a_2 calibration constants between the photodiodes, determined by measuring the photodiode response for an electric field change.

The high voltage power supply unit (HV PSU) used to generate the voltage differential over the electrodes was switchable externally, allowing for an automated measurement procedure. With the HV PSU it is possible to generate an electric field up to 1 kV/cm, but the directionality of the electric field was not switchable without swapping cables.

Figure 3.7 shows the response of the sensor for field jumps up to 1 kV/cm.

A short term measurement is shown in Figure 3.10, where the electric field was switched on/off every 10 minutes. From these measurements it was not possible to determine the

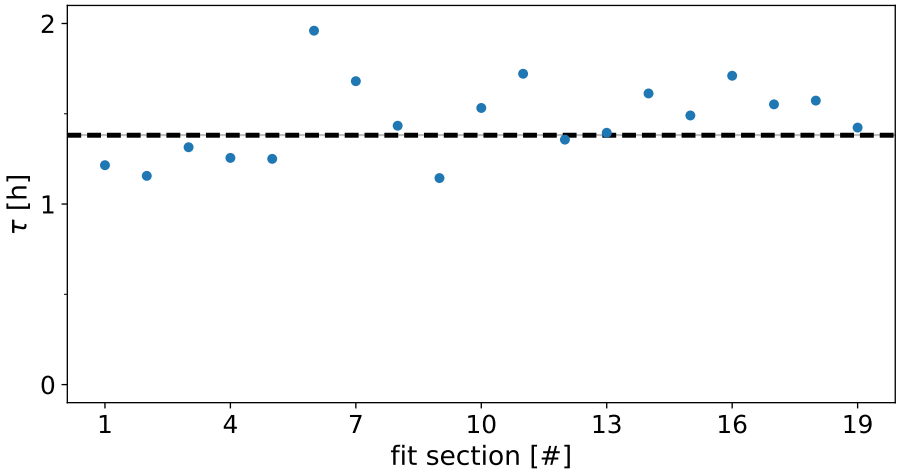

Figure 3.8.: Measurements of the characteristic time constant τ_c of a Lithium Niobate electro-optic crystal between bare electrodes on a glass plate. Extracted from recorded electric field stepwise changes $\tau_c = 1.4(1)$ h, indicated by the dashed black line. Measurement data shown in Figure 3.11.

time constant of the crystal, 10 minutes switching time was not sufficient. To that end a measurement run over the course of several days was performed, shown in Figure 3.11. The electric field was switched between in a sequence between [0, 0.5, 0, 1] kV/cm alternating between 6 and 12 hours every complete cycle. Now an exponential decay in signal from the electro-optic crystal is clearly visible. The accompanying time constant was $\tau_c = 1.4(1)$ hours, sufficient for the MiXeD experiment. The time constant for each electric field switch is shown in Figure 3.8. The time constant is determined by an exponential fit, resulting in errors for τ_c that are significantly smaller than the scatter of τ_c in Fig. 3.8. The decay of signal is not purely exponential. Environmental effects such as temperature also generate birefringence in the electro-optic crystal, distorting the exponential decay caused by the electric field. Another possibility is the presence of different processes through which the external electric field is shielded in the electro-optic crystal. Each process could have its own characteristic time constant. This has not been further investigated in the course of this work.

The signal from the integrated sensor described in Section 3.3 is shown in Figure 3.9a. The time constant of the integrated sensor is shown in Figure 3.9b, from which $\tau_c = 1.7(1)$ h was found.

The integrated sensor was a first proof of principle build with significantly lower SNR (factor 10 to 30 smaller) than achieved in the free space setup described in the beginning of this section. With better alignment of the crystal and optical components the integrated sensor should be able to approach the SNR achieved previously with the free space setup.

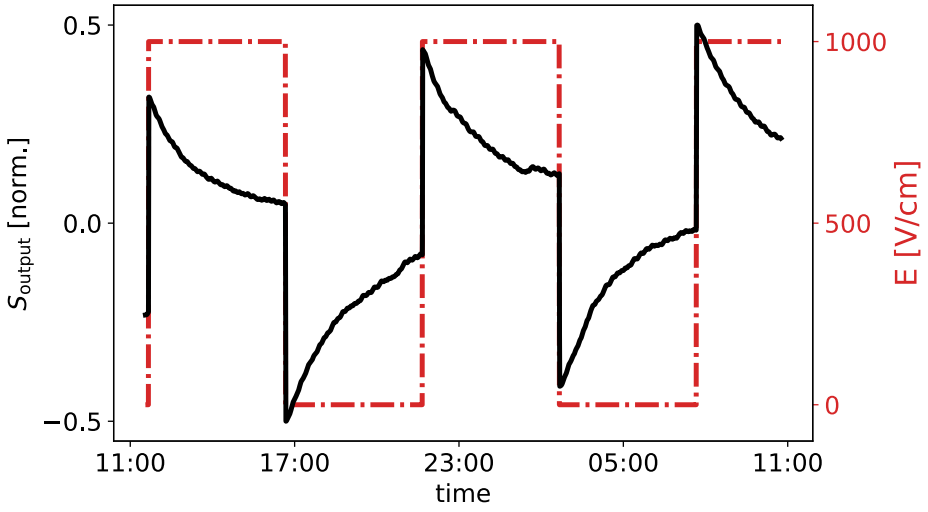

(a)

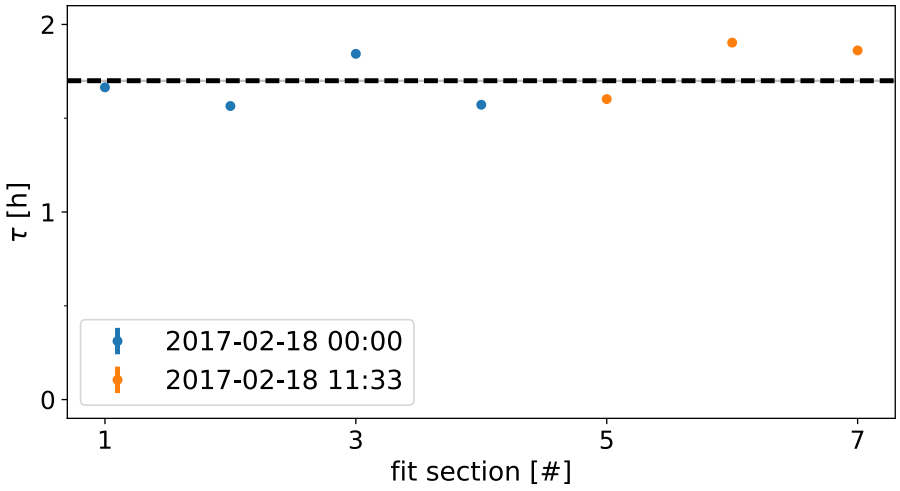

(b)

Figure 3.9.: Measurements on the integrated electro-optic electric field sensor described in Sec. 3.3. A Lithium-Niobate electro-optic crystal is used in the integrated sensor. The electric field was switched on/off every 5 hours. (a) S_{output} (Eq. 3.14). (b) τ_c extracted from recorded electric field stepwise changes resulting in $\tau_c = 1.7(1)$ h, indicated by the dashed black line. (Data from measurements 2017_02_18-00_00_39 and 2017_02_18-11_33_08.)

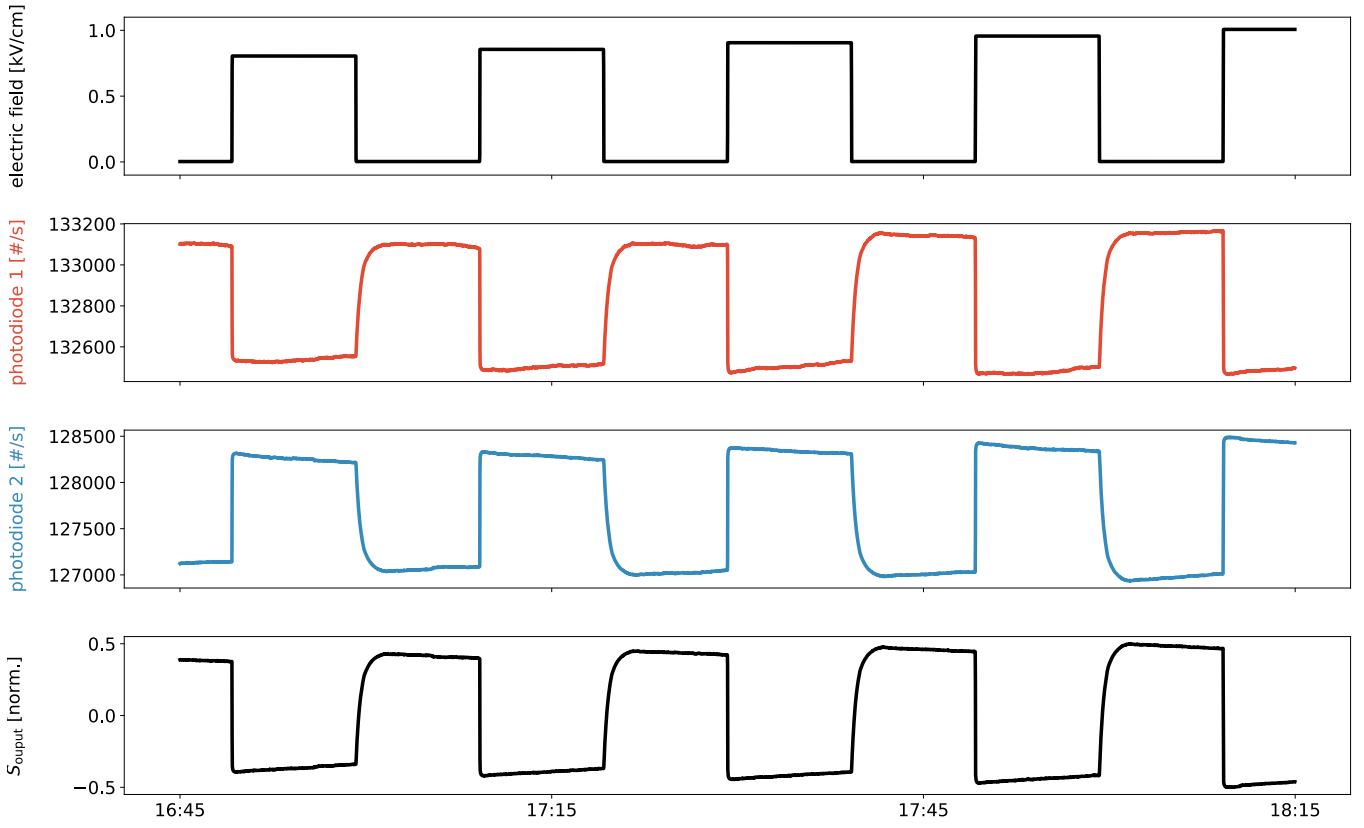

Figure 3.10.: Measurement of the electric field exploiting a Lithium Niobate electro-optic crystal. The measurement was performed over the course of an hour, using the setup in Figure 3.2. The top graph gives the electric field, the two center graphs are the photodiode response of two orthogonal polarization directions and the bottom graph is the normalized sensor output given by Eq. 3.14. The electric field switching was performed with 10 minutes period. The slow response when setting the field to zero is caused by the HV PSU, discharging slower than charging.

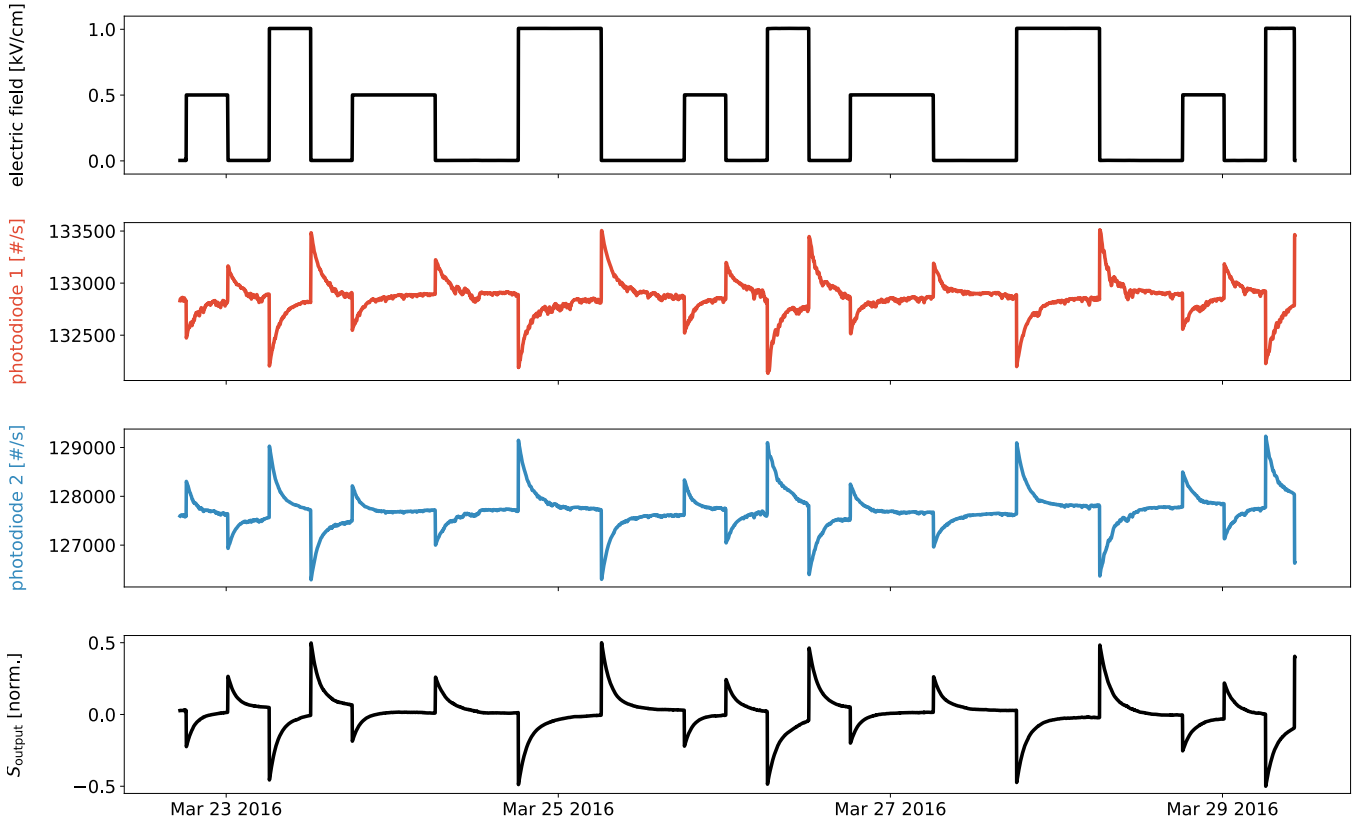

Figure 3.11.: Measurement of the electric field exploiting a Lithium Niobate electro-optic crystal. The measurement was performed over the course of several days, using the setup shown in Figure 3.2. The top graph is the electric field, the two center graphs are the photodiode response of two orthogonal polarization directions and the bottom graph is the normalized sensor output given by Eq. 3.14. The electric field was intermittently switched on and off for 6 and 12 hours, resulting in a time constant of 1.4(1) h.

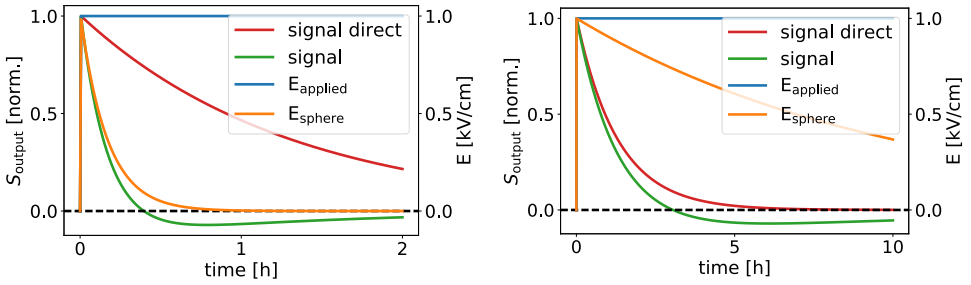

Figure 3.12.: Simulated S_{output} (Eq. 3.14) of the polarization change in an electro-optic crystal with characteristic time constant $\tau_c = 1.3$ h inside a glass bulb with a characteristic time constant τ_s. *Signal direct* indicates the signal without a glass bulb, *signal* indicates the signal with a glass bulb, $E_{applied}$ the applied electric field and E_{sphere} the electric field inside the glass volume. (a) signal for $\tau_s = 10$ m, (b) signal for $\tau_s = 10$ h.

3.5. Electric Field Inside a Spherical Glass Bulb

Charges can accumulate at different locations on the outer or inner surfaces of a glass bulb when put inside of an electric field. These charges travel over the surface and can, over time, diminish the electric field inside of the glass volume. The magnitude of the charges and travel are depending on the cleanliness of the glass surfaces.

In order to measure the electric dipole moment of ^{129}Xe, the presence of an electric field is required. Under the assumption that the mechanism with which the charges travel over the surface of the glass bulb causes an exponential decay of the electric field inside the bulb, a time constant τ_s in excess of the switching time of the electric field polarity is required. The electric field inside a glass bulb can be measured using an electro-optic crystal, as described in Section 3.2. Circular polarized light passes through an electro-optic crystal, where birefringence induced by an external electric field rotates the light polarization. A polarizing beamsplitter splits the light beam into two orthogonal polarizations, converting a polarization rotation into a light intensity change. The change in light intensity is measured with two photodiodes.

The electro-optic crystal also has a characteristic time constant associated with the decay of the electric field inside the crystal, τ_c. The decay of the field inside the bulb influences the decay of the field inside the crystal, and thus the signal. This is similar to two high pass filters in series, where the first high pass is the glass sphere and the second the

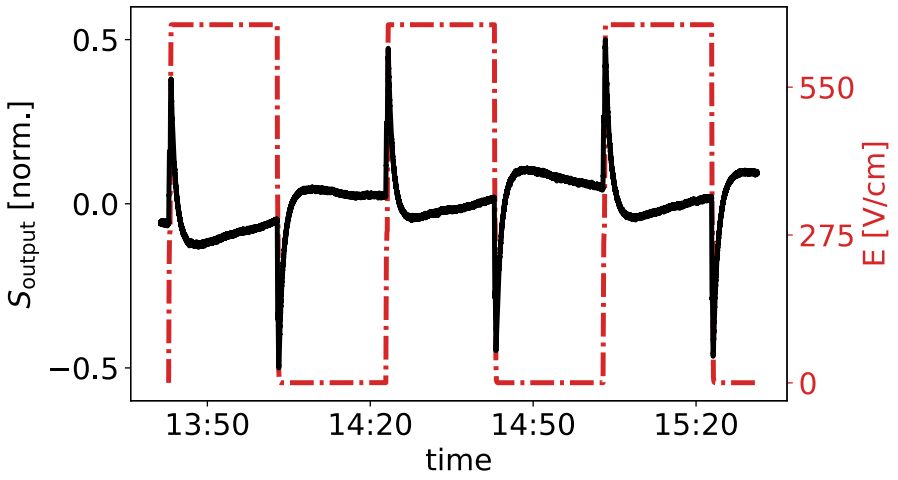

Figure 3.13.: S_{output} (Eq. 3.14) from a $LiNbO_3$ electro-optic crystal (see Sec. 3.2) inside a spherical glass bulb which has not been properly cleaned. Glass bulb was open to air. The electric field was switched on/off every 500 seconds. (Data from measurement 2017_12_22-13_41_22.) Cleaning the glass container removes the effect of fast declining signal.

crystal. Figure 3.12 shows a simulated sensor response for an electro-optic crystal inside a glass bulb. For $\tau_s < \tau_c$, the signal quickly overshoots zero and then slowly returns back to zero with the time constant of the crystal, τ_c, after the electric field inside the glass bulb has reached zero magnitude. When $\tau_s > \tau_c$ the signal still overshoots zero, but now as a result of the exponential decay of the crystal electric field reaching zero magnitude. The return of the overshoot to zero is now governed by the time constant of the glass bulb, and thus follows τ_s.

From measurements of a Lithium Niobate electro-optic crystal, on glass and plexiglass plates between bare electrodes, τ_c is extracted. τ_c is used in the analysis of the crystal response inside a glass bulb in order to get an estimate on τ_s. For our particular crystal the extracted time constant is $\tau_c = 1.3(1)$ h. The setup described in Section 3.2 was employed to extract τ_c.

Subsequently the crystal was placed inside a spherical glass bulb on a glass or a plexiglass plate, with circularly polarized LED light passing through the crystal from outside the bulb. The experimental setup was similar to Figure 3.2, with addition of a glass bulb encasing the electro-optic crystal. The electric field was generated by two electrodes separated by 12 cm, with neither electrode touching the glass bulb. The setup was in air.

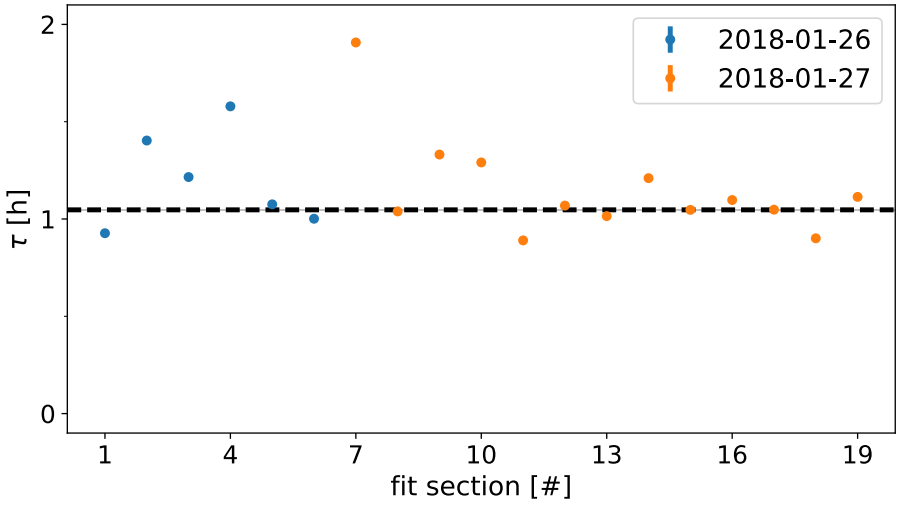

Figure 3.14.: Measurements of the characteristic time constant τ_c of a Lithium Niobate electro-optic crystal (see Sec. 3.2) on a glass plate inside a spherical glass bulb filled with xenon between two electrodes. Extracted from electric field changes $\tau_c = 1.1(1)$ h, indicated by the dashed black line. Measurement 2018_01_26 with 118.8(6) mbar Xe and measurement 2018_01_27 with 96.3(6) mbar Xe.

The goal of these measurements is to assure that an electric field is present inside a glass bulb, if placed inside an electric field. Specifically to be certain that there is an electric field applied to the spin polarized ^{3}He and ^{129}Xe atoms during the EDM measurements. Thus it is required to have similar environmental conditions during the electric field measurements, in this case the presence of gas inside the measurement bulb. The EDM measurements had a mixture of helium and xenon with roughly 25 mbar and 100 mbar, respectively.

The glass bulb was first cleaned extensively with soap, distilled water and finally acetone and ethanol. Before filling with xenon at $\sim$ 100 mbar pressure, the bulb was pumped to a residual gas pressure of $\sim 10^{-3}$ mbar. Figure 3.15 shows the signals from the electro-optic crystal inside the glass bulb for two separate measurements with xenon. Figure 3.14 shows the resulting τ for each successive electric field switch, resulting in $\tau = 1.0(1)$ h. The signal has not yet reached zero, i.e the starting value for zero electric field strength. Neither has it overshot zero, which has occurred in Figure 3.13. τ_s is sufficiently large to

prevent an overshoot in the first three hours after switching the electric field on/off.

Figure 3.12 shows the simulated response of the crystal inside a glass bulb for $\tau_c = 1.3$ h. From a qualitative comparison of the simulated result to the signals from Figure 3.15 $\tau_s \geq 20$ h is found, given that the signal has not overshot or reached zero.

The effect of the He Xe gas mixture on the lifetime off the bulb was also checked, with 37.0(6) mbar He and 155.0(6) Xe partial pressures, respectively. A lifetime $\tau = 1.1(1)$ h was found. The signal from the electro-optic crystal is shown in Figure 3.16. Again the signal has not reached or overshot zero, yielding also from qualitative comparison $\tau_s \geq 20$ h.

The electric field polarity reversal time used during the EDM measurements was at maximum 9000 s. We conclude that for $\tau_s \geq 20$ h, the electric field magnitude over the fiducial volume has decreased by less than 12% after 9000 s. This causes no problem for the EDM measurements and the electric field strength within the EDM glass cell was on average larger than the 95% of the external applied electric field.

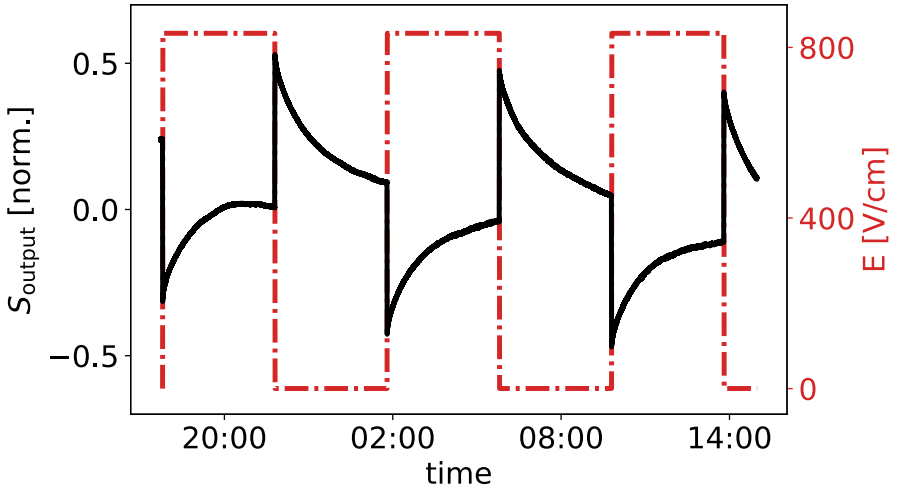

(a)

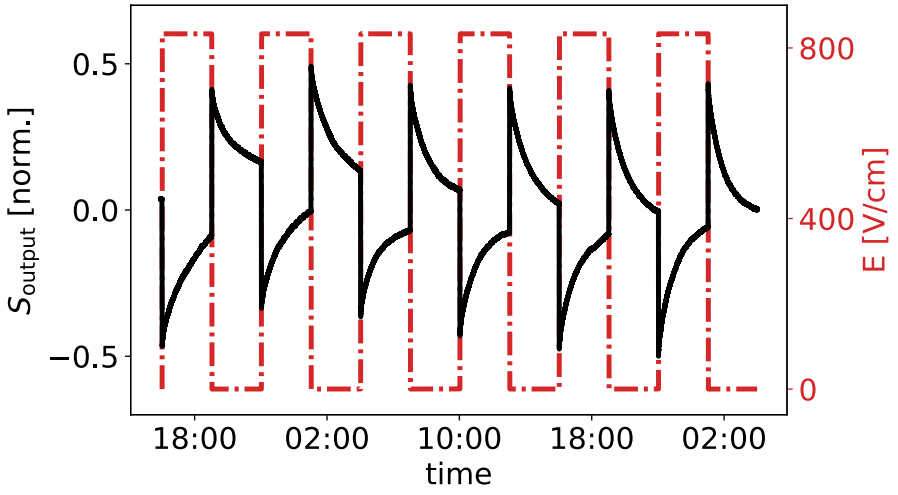

(b)

Figure 3.15.: S_{output} (Eq. 3.14) of a $LiNbO_3$ electro-optic crystal (see Sec. 3.2) inside a spherical glass bulb filled with xenon gas. The electric field was switched on/off every 3 hours. (a) measurement 2018_01_26 with 118.8(6) mbar Xe. (b) measurement 2018_01_27 with 96.3(6) mbar Xe.

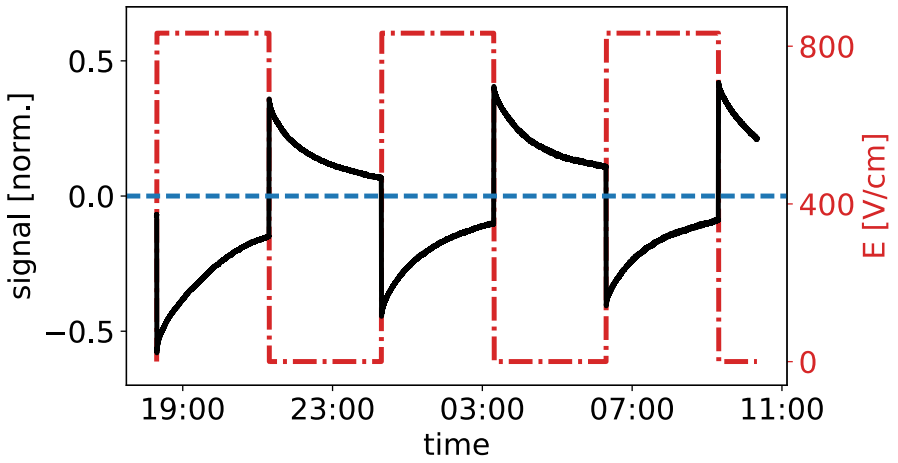

(a)

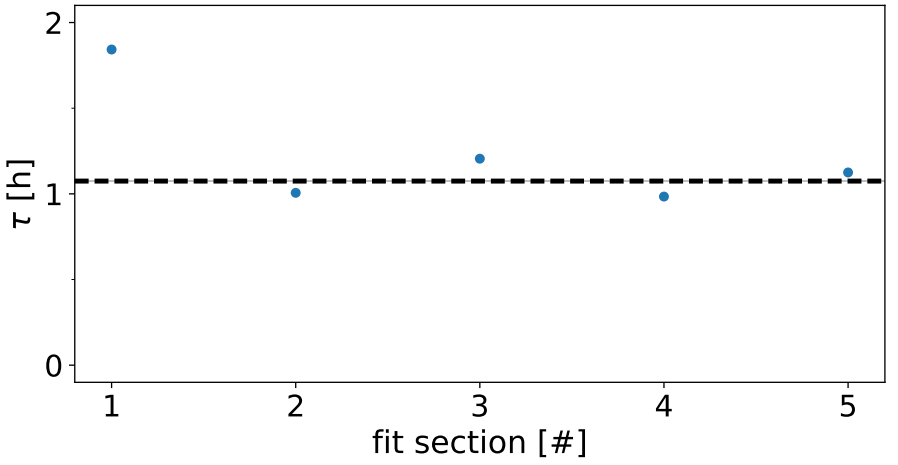

(b)

Figure 3.16.: S_{output} (Eq. 3.14) of a $LiNbO_3$ electro-optic crystal (see Sec. 3.2) inside a glass bulb filled with xenon and helium gas at (155±0.6) mbar and (37±0.6) mbar partial pressures, respectively. The electric field was switched on/off every 3 hours. (a) signal and electric field strength (b) measurements of the time constant τ, a combination of τ_s and τ_c. Extracted from electric field changes $\tau = 1.1(1)$ h, indicated by the dashed black line. (Data from measurement `2018_01_29-18_17_51`.)

4. The MiXeD Experiment

The MiXeD experiment aims to set a new limit on the electric dipole moment (EDM) of ^{129}Xe. To achieve this a ^{3}He/^{129}Xe spin clock is employed using ^{3}He as co-magnetometer (Sec. 2.4). The polarized gases are pumped into the measurement cell, where free spin precession in a magnetic and electric field is monitored using SQUIDs. In this chapter the experimental setup is discussed, with some separate components reviewed in more detail. Finally the measurement procedure is described.

4.1. Experimental Setup

The MiXeD experiment is performed inside of a magnetically shielded room (MSR), located at the Peter Grünberg Institute (PGI-8) at the Forschungszentrum Jülich. The room has inner dimensions (3 x 2.5 x 2.4) m^3 and consists of two μ-metal layers and one aluminum layer. μ-metal is a high-permeability nickel-iron alloy capable of providing low reluctance paths for magnetic flux, shielding the enclosing volume. An additional μ-metal cylinder, with 85 cm diameter and 1.5 mm wall thickness, is placed upright in the center of the MSR to provide additional magnetic shielding of the fiducial volume. The cylinder is attached to a fiberglass (GFK) cylinder of 75 cm outer diameter, 1 cm wall thickness and 210 cm length.

Outside access during operation consists of a filling station outside of the magnetically shielded room, providing access for the polarized gases to the measurement cell via a series of coil systems running from outside the MSR to the μ-metal shielding cylinder inside the MSR. The filling station and fill line are shown in Figure 4.4. The fill line continues on towards the measurement cell, a spherical cell constructed from GE180 glass, with a pneumatic valve attached for filling and pumping the cell. The cell is placed between two silicon wavers connected to high voltage for generating the electric field.

The magnetic holding field facilitating free spin precession has a magnitude of 400 nT and is generated by a cosine theta coil and the spin flip field is generated with a solenoid, discussed in more detail in Sections 4.2.1 and 4.2.2, respectively. Additional magnetic shim coil systems serve to minimize magnetic field gradients over the fiducial volume, discussed in more detail in Section 4.2.3. All coil systems are mounted to the GFK cylinder.

The spin precession signals are read out using superconducting magnetometers (SQUIDs), devices capable of measuring flux quanta.

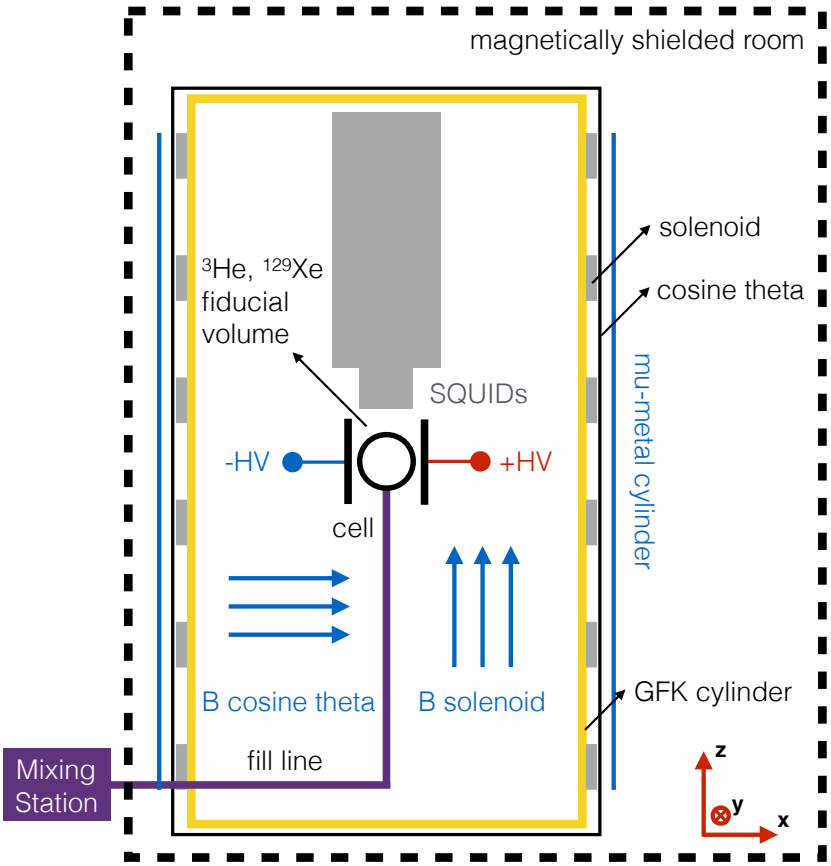

Figure 4.1.: Conceptual view of the experimental setup (not to scale) for measuring ^{3}He and ^{129}Xe spin precession. This setup is located inside a magnetically shielded room (MSR) at FZ Jülich.

A xenon polarizer built in Mainz [61] and transported to the PGI-8 provides polarized ^{129}Xe for each measurement run. Polarized ^{3}He is produced in Mainz and transported every three days in transport boxes with large homogeneous magnetic fields, capable of sustaining sufficient polarization for several days. The polarized gases are mixed at a mixing station with a homogeneous magnetic field generated with two Helmholtz coils. The possibility for adding buffer gases also exists at the mixing station. The mixing station is shown in Figure 4.2.

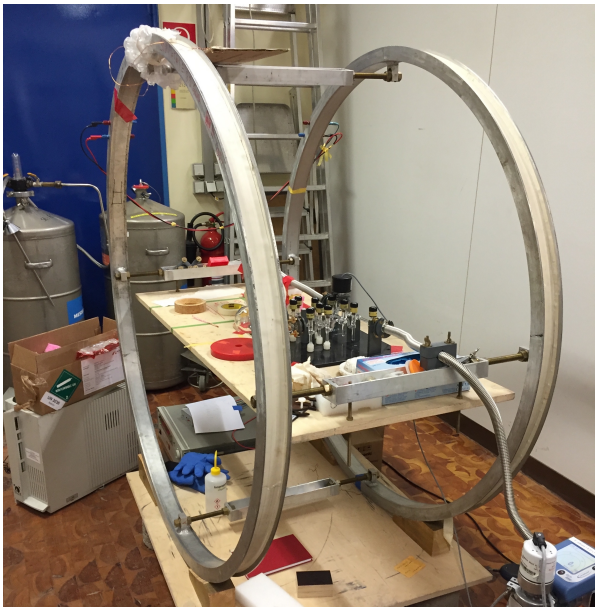

Figure 4.2.: Photograph of the mixing station. Polarized helium and Xenon are mixed here, with the possibility of adding buffer gases.

4.1.1. Magnetic Fields

The MiXeD experiment requires a magnetic holding field to measure spin precession. The magnetic holding field is produced by a cosine theta coil generating a field in the x direction as shown in Figure 4.1, either pointing away or towards the door permitting access to the magnetically shielded room. A solenoid generates the magnetic field along the z axis, inducing a 90° spin flip. Several magnetic shim coil systems serve to compensate magnetic field gradients over the fiducial volume to first order. The magnetic holding field, spin flip and shim coil systems are discussed in detail in Section 4.2.

Several coil systems surrounding the fill line serve to generate a homogeneous magnetic holding field during filling of the measurement cell. The magnetic field orientation of the fill coil systems are equivalent to the magnetic holding field direction.

A battery powered coil system serves to transport the polarized gases, specifically polarized ^{129}Xe from the polarizer to the mixing station and the mixed polarized gases from the mixing station to the filling station. Both the transport coil and the coil systems surrounding the fill line were developed by Michael Doll as part of a Bachelor research at the University of Mainz.

4.1.2. Generation of Electric Field

The electric field over the fiducial volume is generated by applying a voltage differential between two circular silicon wafers of 10.6 cm diameter. An ISEG high voltage power supply unit (HV PSU) is used to generate the required voltages. The NHQ 246L was chosen due to having two channels with selectable polarity and being a a high precision, low noise PSU, capable of generating from 0 kV to ±6 kV. The polarity of each channel can only be set manually, requiring the experiment to use digitally switchable relays in order to switch the electric field polarity [55].

The ISEG HV PSU is capable of remote operation via a serial interface. A Raspberry Pi, accessible via an optical serial interface, is used to control the PSU, as well as the relays.

The HV PSU is battery powered, as are the control electronics. It was found that the NHQ 246L generates a excessive high frequency noise, and to combat this the entire HV generating assembly was placed inside a copper box to shield the SQUIDs and SQUID electronics. Initially the copper box was situated inside of the MSR, but the HV PSU noise was still noticeable in the SQUID signals. The copper box was thus moved outside of the MSR, with the HV being transferred inside of the MSR with a high resistance cable to prevent noise from coupling into the MSR. This noticeably reduced the visible HV PSU noise. The copper box is also flooded with SF_6 gas to further decrease noise by preventing HV sparking.

4.1.3. SQUIDs

In the MiXeD experiment the SQUIDs are operated as current detectors in flux-locked loop configuration (FLL) (Sec. 2.6). Low-temperature DC-SQUID magnetometers are used in order to achieve low noise levels. The SQUID system, including the electronics, was manufactured by Magnicon. It consists of three SQUID modules in a niob shield configured as three gradiometers. The SQUID modules are controlled and read out with a three-channel FLL module on top of the cryostat. The liquid helium cryostat is manufactured by Cryoton (Model LH-16.4-NTE). It is manufactured with fiberglass and was tested for magnetizable materials. The cryostat has a total length of 900 mm and diameter of 307 mm. The bottom part of the cryostat has a smaller diameter, 127 mm, and is 200 mm in length. The volume of the cryostat is about 16 L, and can last around 6 days before a refill is required.

4.1.4. Data Acquisition

The SQUID signals are output as an analog voltage between -10 V and 10 V. These are read out with a 24-bit ADS1299 analog-to-digital converter (ADC) from Texas Instruments. The ADS1299 has 8 available differential channels, which are capable of simultaneous readout. The ADS1299 is capable of sampling at frequencies running from 250 Hz to 16

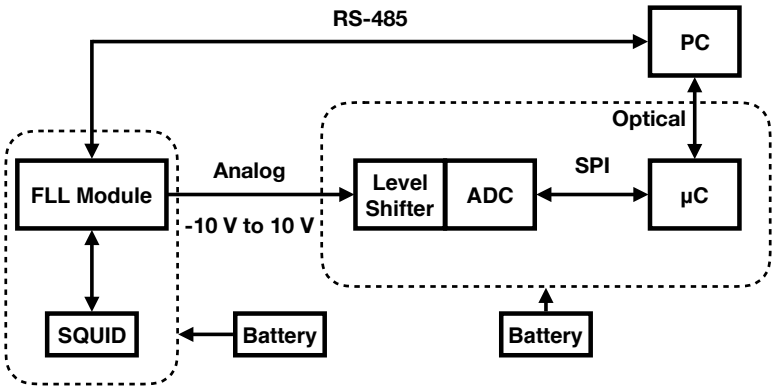

Figure 4.3.: Schematic overview of the data acquisition. The analog SQUID outputs are digitized by an ADS1299 ADC controlled by a XMEGA 32 A4 micro-controller. The micro-controller is read out and controlled via a serial over optical interface with a measurement computer situated outside of the magnetic shielding. The SQUIDs can be controlled via a RS-485 serial interface. Figure adapted from [55].

kHz, and can measure signals between 0 V and 5 V. Given that the SQUID signals are output between -10 V and +10 V, a level shifter is required to bring the signals to the ADC input range. For this purpose an AD8275 from Analog Devices is used. The sampling rate is set to 250 Hz, giving the lowest noise levels and is sufficient for the spin precession signals, which are around 5 Hz and 13 Hz for xenon and helium.

The ADC is controlled and read out with an Atmel XMEGA 32 A4 micro-controller, connected via an optical serial interface to a computer situated outside of the magnetically shielded room. The data acquisition inside the MSR is battery powered. A National Instruments LabVIEW program subsequently reads out the serial interface, saves the data to disk and displays it. Some preliminary analysis is run in the LabVIEW program, the amplitude and frequency of the precessing spins fitted online and an FFT is plotted for noise estimation.

The data acquisition system is discussed in more detail in [55].

4.1.5. Leakage Current Detection

Currents running in neighborhood of the measurement cell give rise to systematic effects (see Sec. 5.3), necessitating monitoring of the currents flowing near or through the measurement cell. To determine these currents a picoampere meter is used; designed and

constructed in Heidelberg by Fabian Allmendinger [55]. The carrier wire carries the high voltage towards the electrodes, and is enclosed by double shielding, with the innermost shielding at the same potential as the carrier wire and the outermost shielding at ground potential. The picoampere meter is located inside the MSR.

To prevent measuring currents running from the carrier wire to the shielding, only the current running through the carrier wire is measured. The current is measured via a integrator (IVC102 from Texas Instruments), a low bias-current operational amplifier with selectable integration capacitors (10 pF, 30 pF or 60 pF). Two methods for determining the current are possible. The first method reads out the integrator voltage, given by $V = -Q\frac{1}{C_{\text{int}}}$. To determine the current, take the derivative of the voltage in time: $I = \frac{dQ}{dt} = -C_{\text{int}}\frac{dV}{dt}$. The voltage is sampled at 10 Hz by a 12 bit ADC , the ADS7835 from Texas Instruments, read out by an Atmel XMEGA 32 A4 micro-controller and transmitted via a serial optical interface to the measurement computer outside the MSR.

The second method uses four comparators to process the integrator voltage. The comparator thresholds are adjustable individually, with two comparators per carrier wire. One comparator has a low threshold while the other has a high threshold, and when triggered trigger a timer on the micro-controller. The timespan Δt between the threshold triggers is transmitted to the measurement pc, making it possible to extract the current using $I = -C_{\text{int}}\frac{V_{\text{high}}-V_{\text{low}}}{\Delta t}$.

The first method is used for currents below 100 pA and the second method is used for larger currents. This is due to required integrator resets required when the integrator voltage reaches the supply voltage; for current larger than 100 pA 10 Hz sampling is not enough to resolve voltage changes.

4.1.6. Mixing and Filling stations

The polarized gases come from two polarizers. The helium polarizer is situated in Mainz, where polarized helium is produced every three days and transported to Jülich by means of a car. This is possible due to the long longitudinal relaxation time of helium in large GE-180 glass bulbs combined with a large homogeneous magnetic field produced by a carrying box with permanent magnets.

The xenon polarizer is situated in Jülich and polarized xenon is produced for every measurement run. The xenon polarizer is located in a different room than the MSR, requiring transport of the polarized xenon bulb in a mobile, battery powered, transport coil towards the mixing station.

Both the helium and xenon bulbs are attached to the mixing station, where room exist for addition of a bulb with buffer gas and a transport cell for transporting the mixed gases towards the filling station attached to the MSR. The mixing station has three intermediary volumes of differing size, enabling filling the transport cell with several millibar precision. An attached pressure sensor serves for monitoring the pressure in the measurement cell.

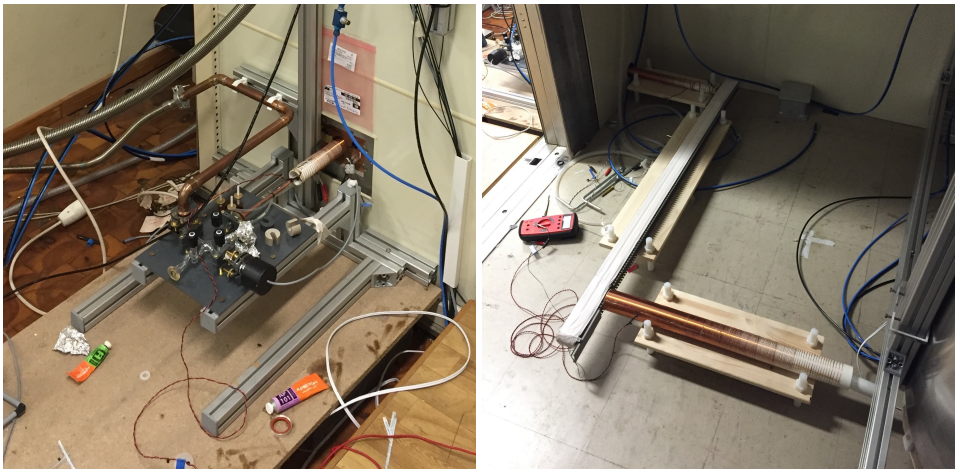

(a) (b)

Figure 4.4.: Photographs of the filling station and fill line. (a) Filling station outside of the magnetically shielded room. (b) Filling gas line, surrounded by coil systems generating a homogeneous magnetic field to allow for transport of hyperpolarized gases to the measurement cell.

Two Helmholtz coils generate a large homogeneous magnetic field for maintaining polarization, with a battery backup in case of power failure.

The mobile, battery powered, transport coil used for transporting polarized xenon towards the mixing station is also used for moving the transport cell, filled with the mixed polarized gases, towards the filling station. The filling station consists of a four-way intersection with valves at every end. Attached to the ends are the vacuum pump, transport cell, fill line and a pressure sensor. The fill line leads towards the measurement cell, enclosed until the magnetic shielding cylinder in coil systems generating a homogeneous magnetic field for transporting polarized gases.

4.1.7. Measurement Cell

The measurement cell is a GE-180 glass spherical cell of 10 cm diameter with a pneumatic valve attached allowing for opening and closing the cell towards the fill line. The cell is surrounded by a glass hull coated in carbon paint, setting the hull to the high voltage power supply ground to prevent sparking. The volume between the glass hull and spherical cell is filled with SF_6 to further suppress sparking and leakage currents caused by the

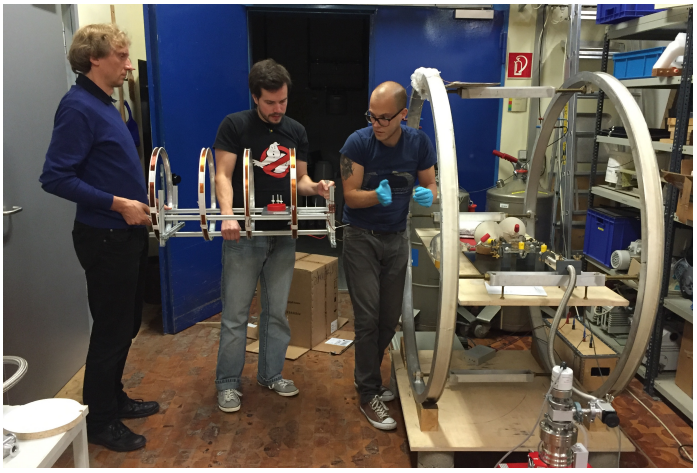

Figure 4.5.: Photograph of the transport coil for transporting polarized gases. Used for transporting polarized xenon from the xenon polarizer to the mixing station and mixed polarized gases from the mixing station to the filling station. Shown here at the mixing station, ready for transport of a bulb of mixed gases towards the filling station.

application of high voltage.

The measurement cell is placed in between two silicon wafers of diameter 10.6 cm and 10 cm apart, which are attached to the high voltage leads. Figure 4.6 shows the conductive hull surrounding the measurement cell, with high voltage leads attached. The fill line is not yet attached.

4.2. Magnetic Coil Systems

The magnetic field coils were simulated and designed using the COMSOL software package. The coils consist of 3 different subsystems; namely the magnetic holding field coil, an adiabatic spin flip coil and four gradient compensation coils. The magnetic holding field is generated with a cosine theta coil [62], the adiabatic spin flip field is generated with a solenoid and the gradient compensation fields are generated with three anti-Helmholtz configuration coil systems and one Helmholtz configuration coil system . All coil systems are mounted on a fiberglass (GFK) cylinder of 75 cm outer diameter, 1 cm wall thickness and 210 cm length. The solenoid and shim coils are mounted directly on the GFK cylinder, whereas the cosine theta coil is offset by 1.5 cm from the outer diameter of the GFK cylin-

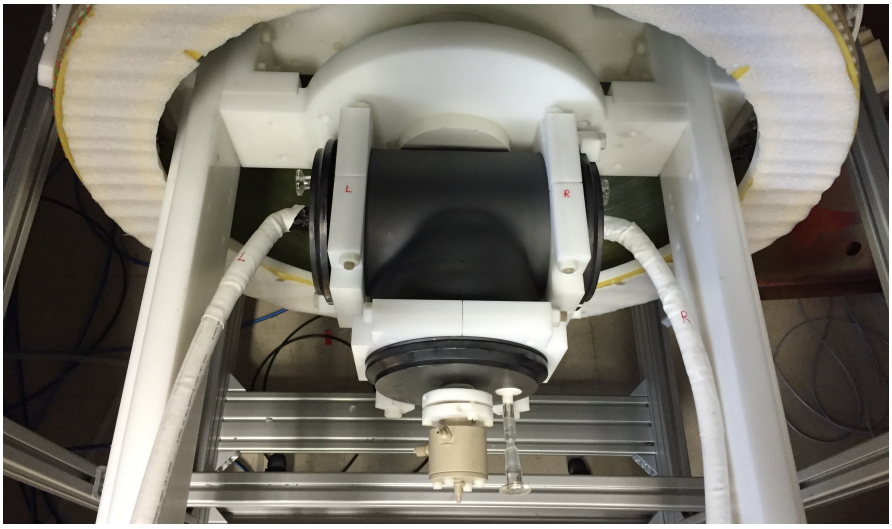

Figure 4.6.: Photograph of the measurement cell enclosed by the conductive hull preventing sparking caused by the application of high voltage. High voltage leads are attached, but the fill line has not yet been attached.

der. A picture of the coil systems mounted on the GFK cylinder is shown in Figure 4.7.

4.2.1. Magnetic Holding Field

The magnetic holding field is generated with a cosine theta coil: a coil on a cylinder with the current carrying wires are arranged in a cosine distribution, resulting in a current density that has a cosine theta dependence over the cylinder surface. The angle of each wire is determined by

$$\theta_j = \arctan\left(\frac{1}{\sqrt{N^2/(2j-1)^2 - 1}}\right), \tag{4.1}$$

where j runs from 1 to $N/2$ and N is the number of wire loops. This equation only covers the upper right quadrant of the unit circle, but two additional reflections result in the angles of all wires. Figure 4.8 shows a graphic overview of a cut-through of a cosine theta coil with 20 wire loops. The resulting magnetic field direction is also plotted.

Normally a cosine theta coil is fully closed, only permitting access through the gaps between the wires. This precludes easy service access, making a regular cosine coil not

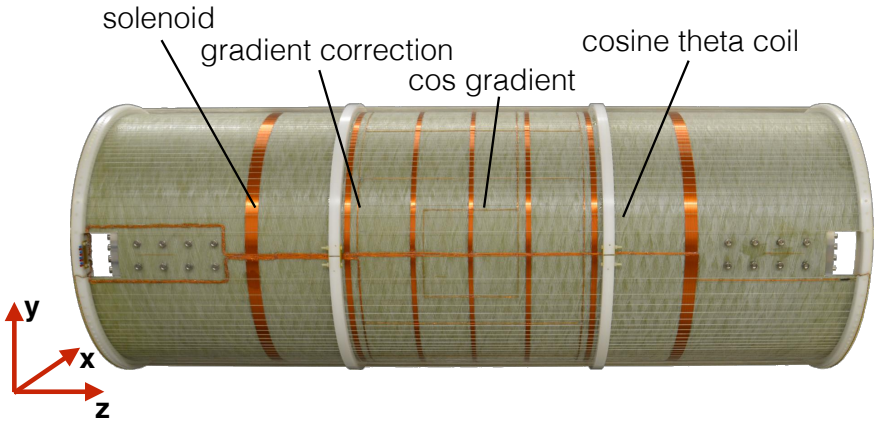

Figure 4.7.: Photograph of the coil setup used to generate the magnetic fields for the MiXeD experiment. The cosine theta coil, solenoid and four gradient correction coils are visible. Photographed by S. Zimmer.

suitable for the purposes of this experiment. In order to facilitate access, the cosine coil was split into three parts, the main coil on the GFK cylinder and two removable end-caps.

The main coil consists of 156 wires (78 wire loops) arranged in a cosine theta distribution at 1.5 cm distance from the GFK cylinder, mounted through specially constructed polyoxymethylene (POM, a thermoplastic) rings with holes matching the cosine theta distribution pattern. At the outer edges of the cylinder a printed circuit board (PCB) is attached, connecting the opposing wires and closing the coil loop.

The end-caps are also constructed from a PCB, mounted to a POM circular disk which is easily removable for service access. The end-cap PCBs complete the cosine theta coil loops, and are constructed to cancel out the magnetic field generated by the traces required to connect the opposing wires on the edges of the GFK cylinder.

Figure 4.9 shows a picture of the completed cosine theta coil, with dismounted the end-caps, and Figure 4.10 shows the cosine theta coil with mounted end-caps and cylindrical μ-metal shield.

4.2.2. Spin Flip Field

A solenoid generates the magnetic field used to perform the non-adiabatic spin flip of the spin polarized atoms. The solenoid has a length of 120 cm and consists of 7 rings, centered around the fiducial volume. The ring diameter is 75 cm, corresponding to the outer diameter of the GFK cylinder. The position and number of windings for each ring

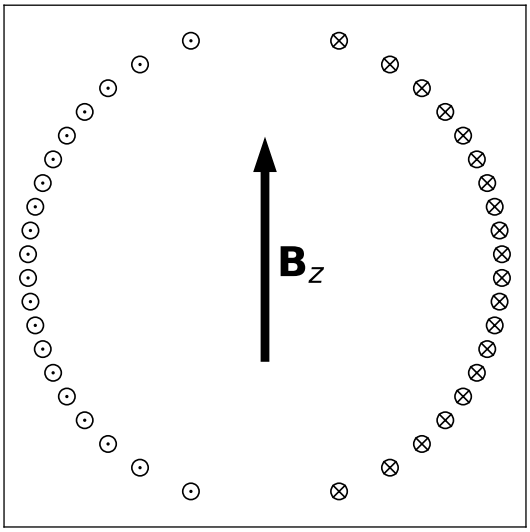

Figure 4.8.: Cut-through of a cosine theta coil for 20 wire loops. The current on the right hand side is flowing into the page and on the left hand side the current is flowing out of the page, resulting in a generated magnetic field direction indicated by the arrow.

was optimized to provide for small magnetic field gradients over the fiducial volume. The ring positions are at z = [-60, -32.7, -15.3, 0, 15.3, 32.7, 60] cm, where 0 cm corresponds to the center of the GFK cylinder. The number of windings per ring are [33, 15, 13, 12, 13, 15, 33], corresponding to the positions given in the previous sentence. The solenoid produces a magnetic field in the z direction, perpendicular to the field of the cosine theta coil. It serves for achieving the atomic spin flip, necessary to enable spin precession for this experiment.

The solenoid was constructed by mounting the GFK cylinder on a rotating axis, and winding the required number of windings at each ring position.

4.2.3. Gradient Compensation Coil Systems

The aim of the gradient compensation coil systems was to compensate constant gradients throughout the fiducial volume. Due to space constraints the coils needed to be constructed such that they can reside on the outer surface of the GFK cylinder. In order

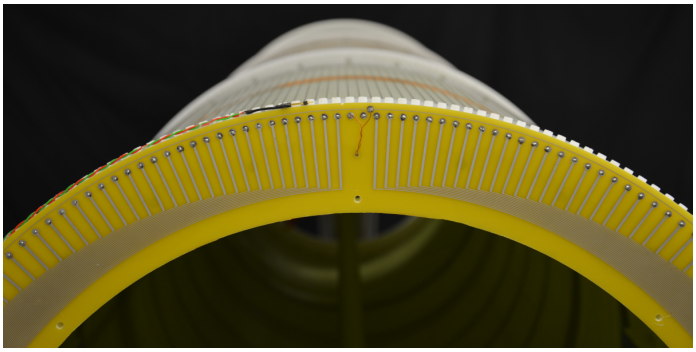

Figure 4.9.: Photograph of the cosine theta coil with mounted PCB to connect opposing wires while maintaining ease of accessibility. The end-caps have been dismounted in this photograph. Photographed by S. Zimmer.

Figure 4.10.: Photograph of the cosine theta coil with mounted end-cap, completing the cosine theta coil loops. The cylindrical μ-metal shield is mounted, as is a carton layer, serving to protect the coil systems. Photographed by S. Zimmer.

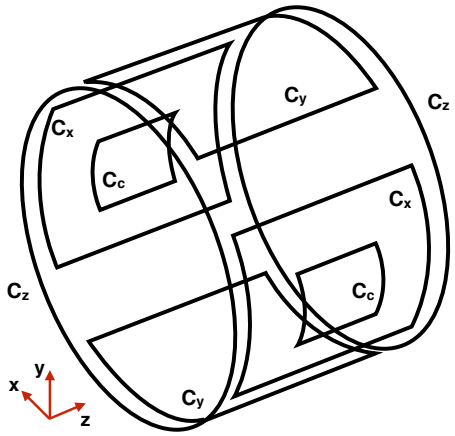

Figure 4.11.: Coil configuration to compensate magnetic field gradients. The coil system consists of two saddle coil systems (C_x and C_y) in anti-Helmholtz configuration and one anti-Helmholtz coil system (C_z) to compensate constant gradients in three Cartesian directions. In addition a saddle coil system in Helmholtz configuration (C_c) provides for compensation of the magnetic field gradient created by the cosine coil.

to generate constant gradients in three Cartesian directions, the anti-Helmholtz coil system C_z and the two saddle coil systems in anti-Helmholtz configuration C_x and C_y were designed. An additional saddle coil system C_c compensates the magnetic field gradients created by the cosine coil over the fiducial volume. In Figure 4.11 all respective coil configurations are visible.

When designing the anti-Helmholtz coil set C_z only the separation of the two coils could be varied. For the saddle coil systems C_x and C_y both their length and their arc length on the cylinder could be varied.

From simulations it was found that for the saddle coils along the z axis a length of $l_z = 60$ cm and an arc length of $\theta_r = 0.35\pi$ rad was sufficient to result in constant gradients across the volume of our measurement cell. The anti-Helmholtz coil set produces sufficiently constant gradients across the volume if the two coils were separated by 60cm along the z axis.

Simulation yields to 1st order the magnetic fields generated by the constant gradient

coils

$$\begin{bmatrix} B_x \\ B_y \\ B_z \end{bmatrix} = \alpha \begin{bmatrix} -8.7I_x + 5.9I_y - 4.0I_z & 0 & 0 \\ 0 & 5.9I_x - 8.7I_y - 4.0I_z & 0 \\ 0 & 0 & 2.8I_x + 2.8I_y + 8.1I_z \end{bmatrix} \begin{bmatrix} x \\ y \\ z \end{bmatrix} \tag{4.2}$$

with $\alpha = 10^{-9}\,\frac{\mathrm{T}}{\mathrm{mA}}$. The gradients corresponding to these fields are

$$\vec{\nabla}\vec{\mathrm{B}} = \beta \begin{bmatrix} -8.7 & 5.9 & -4.0 \\ 5.9 & -8.7 & -4.0 \\ 2.8 & 2.8 & 8.1 \end{bmatrix} \begin{bmatrix} I_x \\ I_y \\ I_z \end{bmatrix}, \tag{4.3}$$

where $\beta = 10^{-9}\,\frac{\mathrm{T}}{\mathrm{m\cdot mA}}$ and $I_x,\ I_y,\ I_z$ are the currents through the x, y and z coils respectively.

A fourth gradient compensation coil system was constructed to compensate the magnetic field gradient created with the cosine theta coil generating the magnetic holding field. By constructing an additional saddle coil system in Helmholtz configuration the magnetic field gradient generated by the cosine theta coil is compensated.

The magnetic field gradient of the cosine theta coil is calculated using COMSOL simulations, and the resulting magnetic field was used to tune the coil length and arc length. A coil length of $l_z = 25$ cm and an arc length of $\theta_r = 0.2\pi$ rad resulted in optimal compensation of the magnetic field gradients. To 2nd order the field generated by the by the cosine gradient coil is

$$\begin{bmatrix} B_x \\ B_y \\ B_z \end{bmatrix} = I_c \cdot \beta \begin{bmatrix} 0.6 + 18x^2 - 9.3y^2 - 8z^2 \\ -19xy \\ -17xz \end{bmatrix} \tag{4.4}$$

where I_c is the current through the cosine gradient coil.

4.3. Gradient Optimization

The sensitivity of an EDM measurement depends, among other things, inversely on the coherence time. The coherence time in the EDM experiment discussed in this thesis is a function of spin relaxation. Maximal sensitivity therefore requires maximizing the coherence time. In section 2.3 the effects causing spin relaxation are discussed. For this experiment the magnetic field gradients are mainly responsible for spin relaxation, as shown in equation 2.29. Minimizing the magnetic field gradients therefore decreases the spin relaxation rate, in turn increasing the coherence time of the experiment.

With the gradient coil systems discussed in section 4.2.3, arbitrary constant gradients in all three Cartesian axes can be created, thereby compensating the existing magnetic

field gradients over the fiducial volume. Usually the magnetic fields are mapped using systems with flux-gate magnetic field probes. From the recorded 3 dimensional field maps the magnetic field gradients can be extracted, and they can be compensated by applying appropriate currents to gradient correction coil systems.

We have devised a method, which is based on nuclear polarized atoms to obtain a quantitative measure of the magnetic field homogeneity over the entire fiducial volume. Equation 2.29 expresses a correlation between the magnetic field homogeneity and the transverse relaxation time. In particular the transverse relaxation time grows, if the magnetic field gradients decrease. By monitoring the spin precession and the spin relaxation of spin polarized atoms, an estimate is possible of the absolute magnetic field gradients across the volume in which the spins precess.

In addition to providing an estimate of the magnetic field homogeneity, the spin polarized atoms can also be exploited for compensating magnetic field gradients. Since T_2^* gives information about absolute values of magnetic field gradients, its value can serve as an indicator for the reduction of field gradients. This can be exploited for field shimming by varying the currents in the various gradient correction coils and subsequently observing the effect of such variations on T_2^*. A maximum T_2^* value corresponds to minimized magnetic field gradients over the entire volume in which the observed spins precess. It is a particular advantage of this new method that mapping of the entire magnetic field volume of interest is not required for minimizing gradients. This method is efficient, fast and in situ.

For minimizing the gradients the transverse relaxation time T_2^* needs to be measured. This is achieved with polarized gas, in this case ^{3}He, which is loaded into the measurement cell. The spin precession signal is picked up by SQUID gradiometers, from which T_2^* is extracted. Subsequently T_2^* can be maximized by adjusting the currents I_x, I_y, I_z, I_c through the magnetic gradient coil systems (see Sec. 4.2.3). With T_1 constant maximization of T_2^* results in a minimization of the magnetic field gradients (see Eq. 2.29).

The currents through the coils are adjusted automatically using the Nelder-Mead method [63]: a set of initial values is chosen for the coil currents and T_2^* is measured for these conditions. The currents are adjusted then according to the downhill-simplex algorithm. The algorithm finds the minimum of a function $f(\vec{x})$ where $\vec{x}$ is an n-dimensional set of parameters. In this experiment the alog maximize T_2^* as a function of the gradient coil systems currents I_x, I_y, I_z, I_c. The algorithm as applied to maximize T_2^* is shown graphically in Figure 4.12.

4.4. Measurement Procedure

Before starting a measurement run, the SQUIDs need to be cooled, requiring opening the magnetically shielded room (MSR) in PGI-8 at Forschungszentrum Jülich. The entire

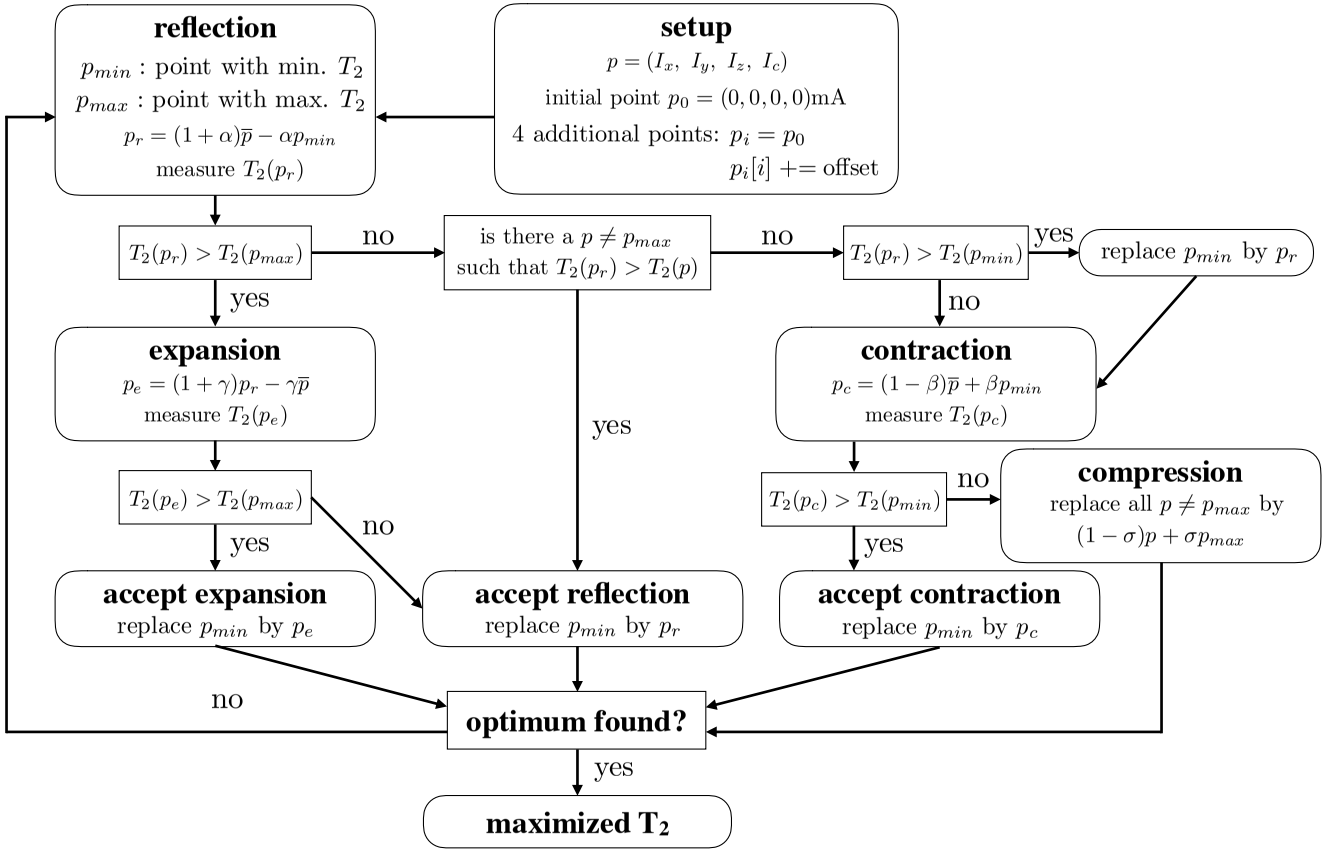

Figure 4.12.: Overview of the downhill-simplex algorithm as applied to maximize T_2^*. Each point p is a set of current combinations (I_x, I_y, I_z, I_c; currents through the coils mentioned in section 4.2.3) and 5 initial points are chosen in the first step. α, β, γ and σ are scale parameters for the reflection, expansion, contraction and compression steps respectively. $T_2(p)$ corresponds to T_2 at point p.

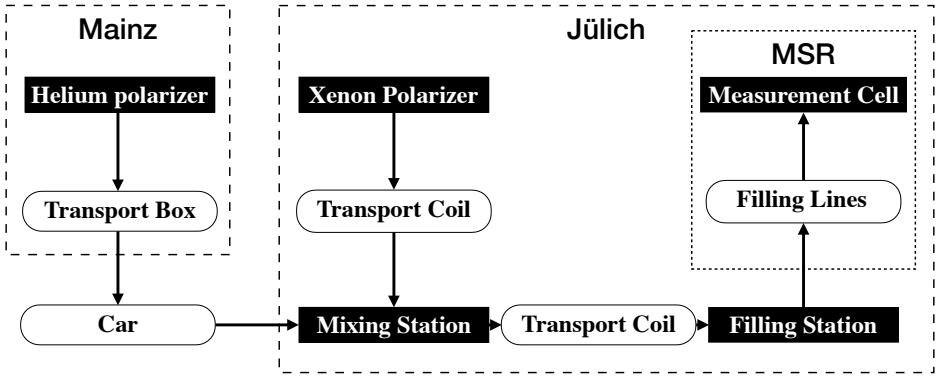

Figure 4.13.: Schematic overview of the polarized gas filling procedure. Polarized ^{3}He is polarized every three days in Mainz and transported via car to the FZ Jülich, where the polarized ^{3}He cell is attached to the mixing station. ^{129}Xe is polarized for every measurement run and transported to the mixing station with a battery powered transport coil. ^{3}He and ^{129}Xe are mixed into a smaller cell and transported to the filling station attached to the magnetically shielded room (MSR), again with the transport coil. Via filling lines surrounded by coils generating a homogeneous magnetic field in the same direction as the magnetic holding field, the measurement cell is filled with polarized gases.

filling procedure with liquid helium takes around 2 hours, before the MSR can be closed again. When opening and closing the MSR, the μ-metal of the room and the shielding cylinder can become magnetized. To demagnetize the MSR and cylinder, both are degaussed every time access to the MSR is required. The degaussing procedure is performed with an oscillating sinusoidal signal in an exponential decay envelope. First the MSR is degaussed, for 5 minutes at 3 Hz and again 5 minutes at 1 Hz. The procedure is repeated for the μ-metal cylinder.

In order to perform measurements polarized gas is required. Helium is polarized in Mainz and transported every 3 days to the PGI-8. Xenon is polarized at the PGI-8 using the compact xenon polarizer [61]. The polarized gases are mixed into a small transport cell at the mixing station, in a homogeneous magnetic field generated by two large Helmholtz coils. The mixing station allows for addition of a buffer gas into the transport cell. A battery powered transport coil is used to transport the mixed polarized gases from the mixing station to the magnetically shielded room (MSR). A series of coils, starting outside of the MSR and leading to the magnetically shielded cylinder inside of the MSR are used to fill the measurement cell. These coils are only switched on during the filling procedure.

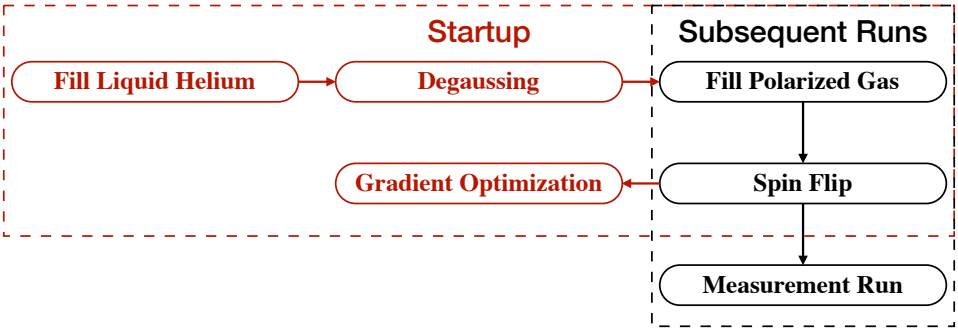

Figure 4.14.: Schematic overview of the measurement procedure. Starting measurements requires filling liquid helium first, necessitating access to the magnetically shielded room (MSR). After filling liquid helium the MSR and magnetically shielding cylinder need to be degaussed. Following degaussing a gradient optimization run is required, where the measurement cell is filled with either polarized ^{3}He or ^{129}Xe, a non-adiabatic spin flip is performed, and the gradient optimization procedure is started. Subsequent runs require only filling with polarized gases, performing a non-adiabatic spin flip and starting the desired measurement, either an EDM or systematics run. Note that entry into the MSR requires again degaussing and gradient optimization, for example when replacing the batteries powering the electronics inside the MSR.

The measurement cell is filled by pumping all lines and with the overpressure in the transport cell the measurement cell is automatically filled.

After the measurement cell is filled the filling lines are pumped and a 90° non-adiabatic spin flip is performed by slowly rotating the magnetic field from the cosine theta coil to the solenoid enabling the spins to follow adiabatically. A non-adiabatic flip is induced by suddenly switching off the solenoid while simultaneously switching on the cosine theta coil. The precessing spins are then picked up by the SQUIDs.

Following a degaussing of the setup, the magnetic field gradients have changed, requiring running the gradient optimization procedure, which can be performed with solely ^{3}He or ^{129}Xe. Usually ^{3}He is used, due to a longer T_2^* and larger signal-to-noise ratio, allowing the optimization to run longer without refilling. The optimization procedure is described in detail in Section 4.3.

The SQUID signals are measured using an ADC and transmitted via an optical serial interface to a measurement computer outside of the MSR. From here the spin precession signals and noise can be monitored, as can the leakage current. All coil currents are also

controlled via an optical serial interface on the same computer.

The electric field required for an EDM measurement is controlled via the same computer, via an optical serial interface connected to a Raspberry Pi controlling an ISEG HV PSU capable of generating ±6 kV. Digitally switchable relays are used to switch the electric field polarity during a measurement, in a python script on the Raspberry Pi the timing and amplitude of the electric field switches can be set.

5. Systematic Effects

We discuss here the systematic effects affecting the co-magnetometer measurement system used for the MIXed experiment. For estimation of the effects the species specific and environmental conditions as shown in Tables 5.1, 5.2 are assumed. To calculate the diffusion coefficients for helium and xenon the equation was used

$$\frac{1}{D_{\mathrm{He}}} = \frac{p_{\mathrm{He}}}{D^0_{\mathrm{He}}} + \frac{p_{\mathrm{Xe}}}{D^0_{\mathrm{He\ in\ Xe}}}\ [64], \tag{5.1}$$

where D_{He} is the total He diffusion coefficient, p_{He}, p_{Xe} are the partial pressures of He, Xe respectively, D^0_{He} is the pure diffusion coefficient for He and $D^0_{\mathrm{He\ in\ Xe}}$ is the pure diffusion coefficient for He in Xe. For xenon the equation becomes

$$\frac{1}{D_{\mathrm{Xe}}} = \frac{p_{\mathrm{Xe}}}{D^0_{\mathrm{Xe}}} + \frac{p_{\mathrm{He}}}{D^0_{\mathrm{Xe\ in\ He}}}\ [64]. \tag{5.2}$$

The pure diffusion coefficients used are

$$D^0_{\mathrm{He}} = 1.92 \text{ bar cm}^2 \text{ s } [65],$$
$$D^0_{\mathrm{Xe}} = 0.058 \text{ bar cm}^2 \text{ s } [66],$$
$$D^0_{\mathrm{He\ in\ Xe}} = 0.610 \text{ bar cm}^2 \text{ s } [66],$$
$$D^0_{\mathrm{Xe\ in\ He}} = 0.548 \text{ bar cm}^2 \text{ s } [66].$$

The partial pressures used are $p_{\mathrm{He}} = 26.6$ mbar and $p_{\mathrm{Xe}} = 90.7$ mbar, for a total pressure of $p = 117.3$ mbar. The total diffusion coefficients then are

$$D_{\mathrm{He}} = 6.15 \text{ cm}^2 \text{ s},$$
$$D_{\mathrm{Xe}} = 0.62 \text{ cm}^2 \text{ s}.$$

Table 5.1.: Species specific parameters used in calculations of systematic effects.

	γ [rad/s/Tesla]	M [u]	p [mbar]	D [cm^2 s]	T_2^* [h]	$\bar{l}$ [m]
^{3}He	-32.434×10^6	3.016	26.6	6.15	20.0	1.6×10^{-6}
^{129}Xe	-73.997×10^6	128.905	90.7	0.62	2.88	3.4×10^{-7}

The mean free path of He and Xe was estimated with

$$\bar{l} \cdot p = \frac{k_B T}{\sqrt{2}\pi d^2}, \tag{5.3}$$

where k_B is the Boltzmann constant, T the temperature and d the diameter of the particle. At 273.15 K the values for $\bar{l}p$ are

$$\left(\bar{l} \cdot p\right)_{\mathrm{He}} = 17.5 \times 10^{-5} \text{ m mbar [67]},$$
$$\left(\bar{l} \cdot p\right)_{\mathrm{Xe}} = 3.6 \times 10^{-5} \text{ m mbar [67]}.$$

With Eq. 5.3 and using $T = 300$ K, the mean free path of He and Xe is estimated

$$\bar{l}_{\mathrm{He}} = 1.6 \times 10^{-6} \text{ m},$$
$$\bar{l}_{\mathrm{Xe}} = 3.4 \times 10^{-7} \text{ m}.$$

To calculate the effect resulting from any of the discussed effects on the weighted frequency difference (See Sec. 2.4), the frequency shift is calculated separately for Xe and He, and subsequently the weighted frequency difference

$$\Delta\omega = \omega_{\mathrm{Xe}} - (\gamma_{\mathrm{Xe}}/\gamma_{\mathrm{He}})\,\omega_{\mathrm{He}}$$

is calculated, where γ_{Xe}, γ_{He} are the xenon and helium gyromagnetic ratios, respectively. The subsequent false edm d_f is then extracted with $\Delta\omega\hbar/(2E)$ (from Eq. 2.37), where correlation with the electric field switching is assumed.

5.1. Fields

Magnetic and electric fields are necessary to facilitate a measurement of an electric dipole moment. However, certain effects relating to the fields can mimic the presence of an electric dipole moment. Care has to be taken to prevent misclassification of these effects as an electric dipole moment.

Table 5.2.: Environmental conditions used in calculations of systematic effects.

T	p	B_0	E	$\frac{\partial B_0}{\partial z}$	$\frac{\partial B_0}{\partial r}$	r
300 K	117.3 mbar	400 nT	800 V/cm	30 pT/cm	10 pT/cm	5 cm

5.1.1. Magnetic Field Fluctuations

Changing magnetic fields also change the spin precession frequency. With co-magnetometry these fluctuations are traced by the co-magnetometer, in this case ^{3}He. However, because the SQUID system that is used in this experiment is a gradiometer, a changing magnetic field also shows up in the SQUID readout. Depending on the timescale and strength of these fluctuations they can interfere with the spin precession measurement. They can be classified into two distinct types of magnetic field fluctuations, namely fluctuations in field strength and fluctuations in field orientation.

Fluctuations in field strength are traced by the co-magnetometer. However, a change in magnetic field strength also changes the gradients, which in turn can generate frequency shifts due to effects that depend on the strength of the magnetic field gradients, such as the center of mass shift (COM) (Sec. 5.1.2), the magnetic field gradient shift (Sec. 5.1.4) and the geometric phase shift (Sec. 5.4.2). The geometric phase shift is suppressed sufficiently due to collisions, but the center of mass and magnetic field gradient shift are visible in the accumulated phase. They are compensated for by assuming the magnetic field gradients are sufficiently constant. Then these effects contribute linearly to the accumulated phase and are compensated for in the fit routine.

From simulations of the magnetic holding field, which is generated by the cosine theta coil (Sec. 4.2), the magnetic field gradient generated is $\sim$ 5 pT/cm at a holding field of 400 nT. From measurements of precessing spins, we know that the field experienced by the co-magnetometer during a night measurement fluctuates less than 0.1%, indicating that the magnetic field gradients stemming from the cosine theta coil fluctuate less than 5 fT/cm during a run, which is negligible. They fluctuate at $\sim 10^{-4}$ scale of the gradients present in the fiducial volume, which are $\sim$ 30 pT.

Fluctuations in field orientation can make the spin precession signal amplitude appear to decay more rapidly than is actually caused by T_2^*, by rotating the spin precession plane away from the SQUID direction. However, because multiple SQUIDs are present in our SQUID system, at different orientations, this can be monitored by looking at the change in decay time in all SQUID channels. A normal polarization decay would show up in all three channels, whereas a change in the field orientation would cause different spin precession signal amplitudes in all three SQUID channels. For instance in one channel the flux increases, while in another it decreases. See also Section 5.4.3 for an additional effect a rotation of the magnetic holding field has, due to the rotation of earth.

Note that cars and movement of the door to the laboratory in Jülich can influence the magnetic field inside the shielded volume, potentially changing its direction, albeit temporarily.

5.1.2. Center of Mass difference

The principle behind the use of co-magnetometry is that both species sample the magnetic field in the same volume at the same time. However, since the co-magnetometer is of a different species, and thus has a different mass, the center of mass of both differs between the species. Using the barometric height formula the difference in the center of mass can be calculated

$$p(z) = p_0 e^{-\frac{z}{c}} \text{ with } c = \frac{RT}{Mg}, \tag{5.4}$$

where p_0 is the pressure at the center of the measurement cell, z is the distance from the center of the measurement cell, R the gas constant, T the temperature, M the molar mass and finally g is the gravitational acceleration.

For a spherical cell with radius R the center of mass is given by

$$\bar{z} = \frac{\int_{-R}^{R} z p(z) \left(R^2 - z^2\right) dz}{\int_{-R}^{R} p(z) \left(R^2 - z^2\right) dz}. \tag{5.5}$$

At room temperature ($\sim$ 300 K) the shift in center of mass compared to the geometric center is

$$\bar{z}_{^3He} = -5.9 \times 10^{-9} \text{ m} \tag{5.6a}$$

$$\bar{z}_{^{129}Xe} = -2.5 \times 10^{-7} \text{ m} \tag{5.6b}$$

and

$$\Delta\bar{z} = \bar{z}_{^3He} - \bar{z}_{^{129}Xe} = 2.5 \times 10^{-7} \text{ m}. \tag{5.7}$$

The presence of a magnetic field gradient in combination with the difference in center of mass causes both species to experience slightly different magnetic fields

$$\begin{aligned} \delta\omega_{grav} &= \omega_{Xe} - \frac{\gamma_{Xe}}{\gamma_{He}}\omega_{He} = \gamma_{Xe}\left(B_{0,Xe} - \frac{\partial B_0}{\partial z}\Delta\bar{z}\right) - \gamma_{Xe}B_{0,Xe} \\ &= -\gamma_{Xe}\frac{\partial B_0}{\partial z}\Delta\bar{z}. \end{aligned} \tag{5.8}$$

A magnetic field gradient of $\frac{\partial B_0}{\partial z} = 30$ pT/cm results in a frequency shift of -5.5×10^{-8} rad/s. If the gradients remain constant during a measurement run, this contributes to the a linear phase increase in the weighted phase difference, which is fitted out. Since the EDM also contributes linearly to the weighted phase difference, care has to be taken to ensure the fluctuations are not on the same timescale with which the electric field is switched. For a 100% change in magnetic field gradients correlated to the electric field switching, the false EDM generated is 2.3×10^{-26} $e$cm. In order to reach 10^{-30} $e$cm sensitivity, the magnetic field gradient change correlated with the electric field switching has to be less than 1.3 fT.

5.1.3. Orientation B and E, Motional Magnetic Field and Degree of Field Reversal

Due to motional narrowing, we are not limited by the motional magnetic field and precision of electric field reversal. With the parameters of our experiment, the motional magnetic field generates a false EDM $d_{f,v} \sim 9.3 \times 10^{-35}$ e cm, orders of magnitude smaller than our intended limit, 10^{-29} $e$cm.

At temperature $T = 300$ K the average thermal velocities of both species are:

$$\bar{v}_T = \sqrt{\frac{3k_B T}{M}} = \begin{cases} 1600 \text{ m/s } [^3\text{He}] \\ 240 \text{ m/s } [^{129}\text{Xe}] \end{cases} . \tag{5.9}$$

The motion of atoms through an electric field causes the atoms to feel a motional magnetic field in addition to the holding magnetic field. Assuming an electric field of 800 V/cm, the motional magnetic field $\mathbf{B_v}$ has an amplitude of

$$|\mathbf{B}_v| = \left| \frac{\mathbf{v} \times \mathbf{E}}{c^2} \right| = \begin{cases} 1.4 \text{ nT } [^3\text{He}] \\ 0.2 \text{ nT } [^{129}\text{Xe}] \end{cases} \tag{5.10}$$

With an angle θ_{EB} between the magnetic field holding field B_0 and the electric field, the magnitude of the magnetic field seen on average by the spins is [68]

$$B = B_0 + \theta_{EB} B_v + \frac{B_v^2}{2B_0}. \tag{5.11}$$

The motional magnetic field is always perpendicular to the plane described by **v** and **E** , and by extension **E**. This means we can separate the motional magnetic field into two components, one aligned with the magnetic holding field $\mathbf{B}_0$ and another one in a plane perpendicular to $\mathbf{B}_0$.

The component parallel to $\mathbf{B}_0$ is $\sin(\theta_{EB}) B_v$, or $\theta_{EB} B_v$ for small angles. The component perpendicular to $\mathbf{B}_0$ is $\cos(\theta_{EB}) B_v$, or B_v for small angles.

The effective magnetic field experienced by the spins is then the magnitude of the two components, $B = \sqrt{(B_0 + \theta_{EB} B_v)^2 + B_v^2}$. Expanding for B_v (which is almost zero compared to B_0)

$$B = B_0 + \theta_{EB} B_v + \frac{B_v^2}{2(B_0 + \theta_{EB} B_v)}. \tag{5.12}$$

$B_0 + \theta_{EB} B_v$ reduces to B_0 for small angles, giving the effective magnetic field shown in Eq. 5.11.

A small angle between the electric and magnetic field then changes the effective field, and thus also the precession frequency. The second term, $\theta_{EB} B_v$, is linear in **E** and the sign depends on the orientation of **E**. Even for electric fields with exactly the same magnitude after field reversal this term mimics an EDM signal, due to the direct correlation with the

electric field switching. The B_v^2 term is quadratic in **E**, and does not depend on an angle between **E** and $\mathbf{B}_0$. It is present even for perfectly aligned magnetic and electric field. Due to the quadratic nature and presence under even perfectly aligned fields, care has to be taken that the electric field magnitude before and after a field reversal are sufficiently similar. A difference in magnitude results in a differing contribution to the accumulated phase under different electric field orientations, which mimics an EDM signal due to the direct correlation of the field switching.

Assuming the alignment between **E** and $\mathbf{B}_0$ is within 5° and the magnetic holding field B_0 is 400 nT, the frequency shifts are

$$\partial\omega_v = \begin{cases} \gamma\theta_{EB}B_v = \begin{cases} 2.5\times10^{-2}\ \text{rad/s}\ [^3\text{He}] \\ 1.3\times10^{-3}\ \text{rad/s}\ [^{129}\text{Xe}] \end{cases} \\ \gamma\frac{B_v^2}{2B_0} \quad = \begin{cases} 5.0\times10^{-4}\ \text{rad/s}\ [^3\text{He}] \\ 3.7\times10^{-6}\ \text{rad/s}\ [^{129}\text{Xe}] \end{cases} \end{cases} . \tag{5.13}$$

Taking the weighted frequency difference of these frequency shifts gives a total experimental frequency shift

$$\delta\omega_v = \begin{cases} \text{from } \theta_{EB}B_v \to -7.8\times10^{-3}\ \text{rad/s} \\ \text{from } \frac{B_v^2}{2B_0} \quad \to -1.8\times10^{-4}\ \text{rad/s} \end{cases} . \tag{5.14}$$

Not considering the averaging of the thermal velocity, if the magnitude of the electric field is not equal when it is reversed, both terms contribute to a false EDM signal. Note that for the $\frac{B_v^2}{2B_0}$ term this assumes a field reversal accuracy of 0%, essentially having 800 V/cm before and 0 V/cm after field reversal

$$d_{f,v} = \begin{cases} \text{from } \theta_{EB}B_v \to -3.2\times10^{-21}\ e\text{cm} \\ \text{from } \frac{B_v^2}{2B_0} \quad \to -7.4\times10^{-23}\ e\text{cm} \end{cases} . \tag{5.15}$$

In order to reach 10^{-29} $e$cm, with perfect magnetic and electric field aligned but without taking collisional averaging into account, a field reversal accuracy of at least 10^{-7} in magnitude of **E** is needed. Note that only the $\frac{B_v^2}{2B_0}$ term is strongly dependent on the field reversal accuracy due to the $\theta_{EB}B_v$ term being present even for perfect field reversal accuracy.

For particles in a vapor cell, the average atomic velocity is zero, e.g. the motional magnetic field on average is also zero (especially since we look at the ensemble signal of all polarized atoms). The θ_{EB} term then averages to zero. But the term with the square of the motional magnetic field does not average to zero [69, 70, 71].

Due to the pressure in the cell, the time between collisions is small ($\omega_L\tau_c \ll 1$). Then the total motional frequency shift is

$$\partial\omega_v = \frac{(2\pi)^3}{9}\left(\gamma vE/c^2\right)^2\gamma B_0\tau_c^2. \tag{5.16}$$

Here γ is the gyromagnetic ratio, v the particle velocity, E the electric field, B_0 the magnetic holding field and τ_c the time between collisions. Assuming a total pressure of 117 mbar, the mean free path is approximately μm scale and the time between collisions is ns scale. This largely suppresses the motional frequency shift, to $\delta\omega_v \sim -2.3\times10^{-16}$ rad/s, which equates to an EDM $d_{f,v}$ of 9.3×10^{-35} $e$cm.

5.1.4. Magnetic Field Gradient Shift

Apart from increasing the depolarization rate $\frac{1}{T_2}$, magnetic field gradients also cause a shift in the precession frequency of spins in a magnetic field [72]. The shift for a spherical cell is given by

$$\delta\omega_{grad} = R^2\gamma^3 B_0 \sum_n \frac{\left|\Delta B_{0,x}\right|^2 + \left|\Delta B_{0,y}\right|^2}{x_{1,n}^2\left(x_{1,n}^2-2\right)\left(D^2x_{1,n}^4R^{-4}+\gamma^2B_0^2\right)}, \tag{5.17}$$

where $x_{1,n}$ are the zero points of the derivative of the spherical Bessel function, γ is the gyromagnetic ratio, R is the radius of the cell, B_0 is the magnetic holding field and D is the diffusion constant. Assuming the gradients are constant during a measurement run, this frequency shift is constant during the run and thus adds a linear term to the phase accumulation over time.

For a spherical cell with our experimental parameters, e.g. 30 pT/cm magnetic field gradients, the weighted frequency shift $\delta\omega_{mfg} = 1.0\times10^{-16}$ rad/s, generating a false EDM of 4.2×10^{-35} $e$cm. Note that this false EDM is estimated assuming a 100% change in magnetic field gradients correlated with electric field switching, which would immediately be visible in T_2^* (See Sec. 2.3.2). Thus T_2^* can be employed to monitor the change in magnetic field gradients during a measurement, putting a limit on the contribution of the magnetic field gradient shift. The shim coils can be used to create a magnetic field gradient. Varying the gradient during a measurement puts a bound on the magnetic field gradient shift.

5.2. Hardware

5.2.1. SQUID Interaction

The SQUID system in the MIXed experiment uses SQUID gradiometers as current sensors (Sec. 2.6). This means the current in the pick-up loop is set to zero by a feedback mechanism. Thus a magnetic field field that could couple to the spins is not produced by the measurement method employed in this experiment.

5.2.2. Electronic Noise in Equipment

Two types of electronic noise can be classified for this experiment, namely magnetic noise generated by the electronics and noise that couples into the data acquisition system.

Extensive tests of the data acquisition system have been performed, from which it was found that the electronic noise of the data acquisition system is negligible compared to the measurement noise [55].

The magnetic noise of the cryostat is approximately 2 fT/$\sqrt{\text{Hz}}$, resulting in the same magnetic noise picked up in the SQUID system under ideal conditions. The scaling of the SQUID system is $\sim$ 20 mV/pT, so the input noise on the data acquisition system has to be below 40 μV/$\sqrt{\text{Hz}}$. With the use of 24-bit Texas Instruments ADS1299 ADCs, which have an input voltage of 0 to 5 V, the discretization of the ADCs is $\sim$ 0.3 μV, well below the required sensitivity. For $f_s = 250$ Hz, the average noise amplitude spectral density is 0.1 μV/$\sqrt{\text{Hz}}$, sufficiently small.

The electronics are partially shielded, negating some of the magnetic noise. It was found that the HV power supply increased the magnetic noise significantly while running, with a factor $\sim$ 5. A copper box was constructed to provided extra shielding for the HV power supply. From tests it is clear that this provides shielding, but the noise was still a factor 2 to 3 larger than without HV. Putting the copper box outside of the magnetically shielded room and running the HV line through the magnetic shielding with a set of large resistors in series dropped the SQUID noise back to levels without the HV PSU running, between 10 to 20 fT/$\sqrt{\text{Hz}}$.

5.2.3. Timing

Data acquisition is performed using a Texas Instruments ADS1299 (see Sec. 4.1.4) 24-bit ADC sampling at 250 Hz, coupled to a 2.048 MHz oscillator. The oscillator is a FXO-HC735-2.048 MHz, with 50 ppm frequency stability.

It is assumed that each successive data point acquired by the ADC is separated by 0.004 s, resulting from the 250 Hz sampling rate. Hence a change in clock frequency results in a changing time interval which is not visible in the recorded data, which can cause apparent phase shifts. Any effects which cause the same relative phase shift in xenon and helium (relative to their respective gyromagnetic ratios) are removed by employing co-magnetometry. For example for a constant magnetic holding field we have

$$\Delta\phi = \gamma_{\text{Xe}} \text{B} \Delta t' - \frac{\gamma_{\text{Xe}}}{\gamma_{\text{He}}} \gamma_{\text{He}} \text{B} \Delta t' = 0, \tag{5.18}$$

regardless of any change in sampling interval $\Delta t'$.

Effects that cause phase shifts while employing co-magnetometry are influenced by a changing clock frequency. For example, for a linear shift such as the chemical, center of mass or earth rotation a change in clock frequency correlating with the electric field

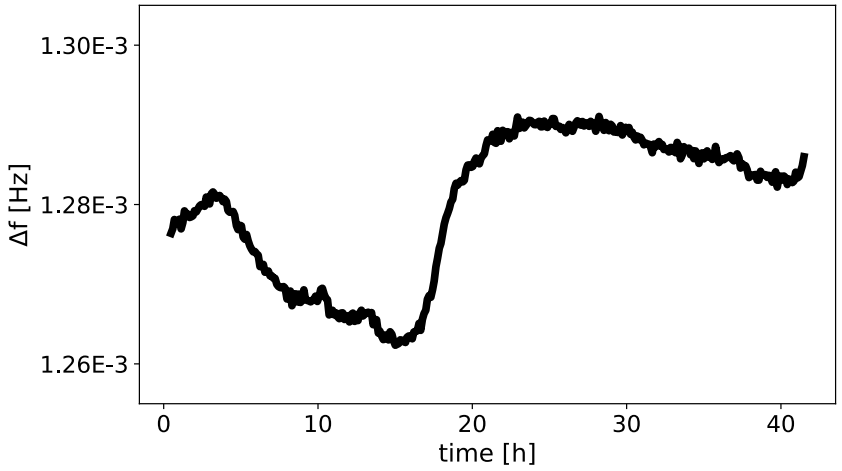

Figure 5.1.: Frequency fluctuations around 250 Hz for an ADS1299 ADC clock source, stepped down to 250 Hz. Determined using the principle described in Appendix B, with a 125 Hz square wave synced to a 10 MHz stabilized clock source.

switching can appear as a phase induced by an EDM. For the given clock stability of 5×10^{-5} (50 ppm), the maximum change in linear phase accumulation between switching times is then also given by 5×10^{-5}. The largest linear phase shift is a result of the earth rotation, resulting in a maximum false EDM of 5×10^{-24} $e$cm. A change in clock stability correlated perfectly with the electric field switching then gives a false EDM of 2.5×10^{-28} $e$cm.

Using a square wave at 125 Hz synced to a stabilized 10 MHz source, the long term stability of the ADC clock source was measured (see Appendix B), shown in Figure 5.1. The frequency stability is 2.9×10^{-5} Hz, assuming all frequency instability arises from the ADC clock source. Considering the external 10 MHz clock is stabilized, this is a safe assumption. Note that this only describes the long term stability, since the frequency difference corresponds to a period of 780 s. Any short term fluctuations will be averaged out over this time period. The relative long term frequency stability of the ADC is then 0.15 ppm, which is 2 orders of magnitude smaller than the specified frequency stability, corresponding to a maximum false EDM of 7.5×10^{-31} $e$cm.

5.2.4. Magnetic Shielding

The magnetic shielding for this experiment is μ-metal, a metal with high permeability for shielding static and low-frequency magnetic fields. It is comprised of a nickel-iron alloy and works by capturing the magnetic field and guiding it around the shielded volume.

In this experiment two different magnetic shields are used, both made of μ-metal. The first shielding layer is a multi-layered μ-metal shielded room, and the second shielding layer is a μ-metal cylinder, placed upright around the experiment.

The first layer of shielding, the shielded room, has a door, which causes less shielding locally than the rest of the room. The second layer of shielding compensates for this. Opening and closing the door changes the magnetization of the μ-metal, necessitating demagnetization of the shielded layers.

These layers significantly reduce the magnetic field inside of the room, and also the gradients from the external magnetic field. However, the μ-metal can also generate local gradients, due to magnetization of local parts of the μ-metal. This can be minimized by demagnetizing the μ-metal by a degaussing routine, using oscillating magnetic fields with a decaying amplitude to flush out any remnant magnetization. For example, during testing of the demagnetization routines, before degaussing gradients of 15 nT/cm were measured inside of the shielded volume, which were reduced to 50 pT/cm after degaussing. These gradients were measured using fluxgates mounted on a rotating measurement device, with the magnetometer mounted roughly at 20 cm from the center of the cylinder. The actual magnetic field gradients in our smaller fiducial volume are smaller.

After degaussing the remnant magnetization of the μ-metal needs time to relax to equilibrium, causing the magnetic field gradients to change over time. After degaussing some time has to be taken before starting a measurement run, in order to be sure that the gradients do not change appreciably during the run. After degaussing the magnetic field gradient optimization routine has to be run again (Sec. 4.3), which takes at least several hours, which is sufficient time for the μ-metal to relax.

5.2.5. Current Supply

The coil currents are generated by a high precision current supply manufactured in Heidelberg [55]. Fluctuations in the current output over time change change the magnetic field during an experimental run. The relative stability of the current supply used for the cosine theta coil and solenoid is at 10^{-5} level. This stability level is well below the observed magnetic field fluctuations during a measurement run, which are discussed in Section 5.1.1.

5.3. High Voltage

5.3.1. Leakage Current

During the experimental run, a leakage current may flow from one electrode to the other electrode. A current flowing near the measurement cell generates a magnetic field and gradient, disturbing the homogeneity of the magnetic holding field. The worst case scenario for a magnetic gradient caused by a leakage current is current flowing in a straight line from one electrode to the other. Assuming a leakage current of 10 pA, the magnetic gradient 2 mm from the current path is

$$\left|\frac{dB}{dr}\right| = \frac{\mu_0 I}{2\pi}\frac{1}{r^2} \simeq 3.2 \times 10^{-3}\ \text{pT/cm}, \tag{5.19}$$

where μ_0 is the vacuum permeability, I current and r distance from the wire. The influence of this magnetic field gradient on T_2^* is negligible, since the gradients caused by the magnetic field coils and μ-metal are much larger. The cosine theta coil gradient alone is ~ 5 pT/cm.

The difference in center-of-mass between He and Xe, combined with the gradient of the leakage current taken at the center of the spherical cell, also causes a frequency shift. With the calculated center-of-mass difference of 0.25 μm, this results in a frequency shift of $\delta\omega = 1.5 \times 10^{-14}$ rad/s. This would result in a false EDM signal of $d_{LC} = 6 \times 10^{-33}$ $e$cm, assuming the leakage current switches direction under electric field reversal.

Since the leakage current is being monitored, with 2% uncertainty at pA scale [55], the correlation between the leakage current and the phase accumulation can be checked. One would have to assume the current always travels over the same path during an experimental run, however.

Experimentally the effect of leakage currents on the experiment can also be determined by placing a wire near the cell, and running a current through the wire. By monitoring the weighted phase difference, an upper limit can be given on the frequency shift due to a leakage current.

5.3.2. Charging of Electrodes

During charging and discharging the electrodes, a current flows to and from the electrodes. The charging rate should be low enough such that the phase of the spins is not lost, i.e. that the magnetic field generated by the current is small enough

$$I_{\text{charge}} = A \cdot C\left[1 - e^{-t/\tau}\right], \tag{5.20}$$

$$I_{\text{discharge}} = A \cdot C\left[e^{-t/\tau} - 1\right], \tag{5.21}$$

where $\tau = RC$, A is the charging/discharging rate (assumed constant) and C capacitance. Because the capacitance is very small ($\sim 10^{-13}$ F), the exponential terms can be neglected.

Charging the electrodes to 5 kV and -5 kV in 60s generates a current of

$$I = C\frac{dV}{dt} \simeq 10^{-13}\ \text{F}\frac{10\ \text{kV}}{60\ \text{s}} = 1.7\times 10^{-11}\ \text{A}. \tag{5.22}$$

The magnetic field generated by this current, assuming a cell diameter of 10 cm

$$B = \frac{\mu_0 I}{2\pi}\frac{1}{r} \simeq 7\times 10^{-17}\ \text{T}, \tag{5.23}$$

and a magnetic field gradient of 1.4×10^{-5} pT/cm at the center of the cell. This is slightly larger than the leakage current, generating a frequency shift of $\delta\omega = 2.5\times 10^{-14}$ rad/s, resulting in a false EDM $d_{CC} = 1\times 10^{-32}$ $e$cm The charging current only appears during electric field reversal. When the required voltage differential is achieved, the charging current disappears, i.e. it is not a problem when the electric field is constant.

5.3.3. HV Ripple/Instability

If the HV PSU voltage is not constant in time, i.e. if there are ripples, it generates an AC current to the electrodes, $I = C\frac{dV}{dt}$. The ISEG NHQ 246L HV PSU has a ripple specification of 5mV. Assuming the ripple has a timescale of 0.1 s and the capacitance is $\sim 10^{-13}$ F, the generated current is 5×10^{-15} A. This current is approximately 4 orders of magnitude smaller than the current produced by charging the electrodes, and does not pose a problem. The HV PSU employed in the experimental setup has low pass filters attached, reducing the ripple current [55].

5.4. Spin Effects

5.4.1. Ramsey-Bloch-Siegert Shift

The Ramsey-Bloch-Siegert (RBS) shift is the shift in the spin precession frequency due to off-resonant oscillating fields [73, 74]. It is described by

$$\delta\omega_{BS} = \sqrt{(\omega_0-\omega_r)^2+(\gamma B_r)^2} - (\omega_0-\omega_r), \tag{5.24}$$

where B_r and ω_r are the magnitude and frequency of the rotating field, ω_0 is the spin precession frequency in the magnetic holding field and γ is the gyromagnetic ratio. The frequency shift as a function of ω_r is shown in Figure 5.2. Assuming $\gamma B_1 \ll \omega_0$, this expression can be simplified to

$$\delta\omega_{BS} = -\frac{(\gamma B_r)^2}{2(\omega_0-\omega_r)} = \pm\frac{(\gamma B_r)^2}{2\Delta\omega}, \tag{5.25}$$

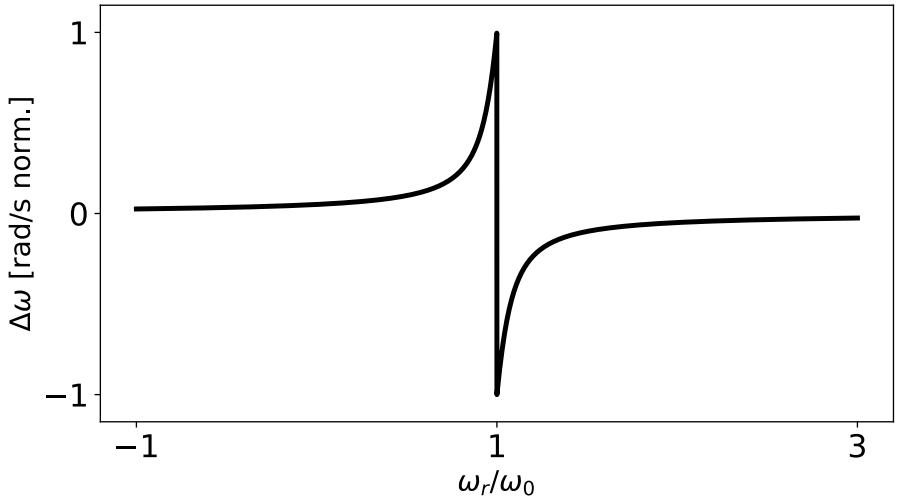

Figure 5.2.: Ramsey-Bloch-Siegert Shift generated by a rotating magnetic field perpendicular to the magnetic holding field. The frequency shift is plotted against the rotation frequency of the rotating magnetic field divided by the Larmor frequency.

where $\Delta\omega = |\omega_0 - \omega_r|$, and $\delta\omega_{BS} = +$ when $(\omega_0 - \omega_r) < 0$ and vice-versa.

In the EDM experiment two different atomic species are used, He and Xe, that precess at different frequencies. Spin precessing particles generate a field that rotates with the spin precession. Both species will then generate a rotating magnetic field that changes the precession frequency of the other. The shift in the Xe frequency is

$$\delta\omega_{RBS,Xe}(t) = \frac{\gamma_{Xe}^2 B_{1,He}(t)^2}{2\Delta\omega} = \frac{\gamma_{Xe}^2 B_{1,He}(0)^2}{2\Delta\omega} e^{-\frac{2t}{T_{2,He}^*}}, \tag{5.26}$$

whereas the shift in the He frequency is

$$\delta\omega_{RBS,He}(t) = -\frac{\gamma_{He}^2 B_{1,Xe}(t)^2}{2\Delta\omega} = -\frac{\gamma_{He}^2 B_{1,Xe}(0)^2}{2\Delta\omega} e^{-\frac{2t}{T_{2,Xe}^*}}. \tag{5.27}$$

The exponential term in both equations comes about due to the exponential decay of spin polarization both species undergo, with characteristic decay times $T_{2,\mathrm{Xe}}^*$ and $T_{2,\mathrm{He}}^*$. Note the differing sign between the two frequency shifts, arising from the $\Delta\omega$ term, which

is negative for Xenon (since $(\omega_{\mathrm{Xe}} - \omega_{\mathrm{He}}) < 0$, see Eq. 5.25) and positive for Helium $((\omega_{\mathrm{He}} - \omega_{\mathrm{Xe}}) > 0)$.

The inter-species thus depends on the gyromagnetic ratio (γ), internal magnetic field (B_1), frequency difference ($\Delta\omega$) and the relaxation time (T_2^*). Of these parameters, γ, $\Delta\omega$ and T_2^* are known with enough precision, but the internal magnetic field is not.

In addition to the interaction between the two species, there is also a frequency shift that arises from a single spin precessing species [55]. In an inhomogeneous magnetic field, spins at one location have a slightly different orientation from those at other locations. Assuming magnetic field gradients of $\sim$ 30 pT/cm, and given that the magnetic field produced by precessing spins is $10-100$ pT, generally $\Delta\omega < \gamma B_1$.

Expanding the Ramsey-Bloch-Siegert shift for self shifts gives

$$\delta\omega_{RBS,self} = \pm\left[\omega_1 - \Delta\omega + \frac{\Delta\omega^2}{2\omega_1} - \frac{\Delta\omega^4}{8\omega_1^3} + ...\right]. \tag{5.28}$$

To first order the self shift is then $\delta\omega_{RBS} \simeq \gamma B_1(t) = \gamma B_1(0)e^{-\frac{t}{T_2^*}}$.

However, this is not a proper estimate of the frequency shift due to the self shift. The actual frequency shift is an ensemble average over all atoms in the measurement cell, which are all precessing at slightly different frequencies. The distribution of precession frequencies depends on the magnitude of the magnetic field gradients. Diffusion over the measurement volume gives an averaging of the frequency shifts, and since some will be negative and some positive, the frequency shift is further dampened. To accurately estimate the frequency shift due to the self shift a precise description of the magnetic field gradients, cell geometry and diffusion is required.

Both contributions are fitted to the phase accumulation. Since T_2^* and ω_0 for both species can be found with high precision from the precession signals, these are fixed in the fit, leaving the other parameters free. During a single measurement run, experimental parameters such as the magnetic field gradients, cell geometry and diffusion are sufficiently constant, such that only accounting for the time dependence of the magnetization in the fit model is sufficient.

From measurements performed earlier and the recent Ramsey-Bloch-Siegert shift measurements performed in April 2016, it was found that the internal magnetic fields measured for Xe and He are $\sim$130 pT and $\sim$190 pT. The inter-species shifts resulting from these rotating field are $\sim -7 \times 10^{-6}$ rad/s for He and $\sim 2 \times 10^{-6}$ rad/s for Xe at maximum, from equations 5.26 and 5.27. The frequency shift as a result of the self shift cannot be estimated in a similar straightforward manner. It depends on the exact distribution of the magnetic field gradients, the geometry and the diffusion throughout the measurement volume. However, in previous measurements performed at the PTB in Berlin [75, 76] the following fit model was used on the weighted phase difference

$$\Phi(t) = \Phi_0 + \Delta\omega_{lin}t + E_{He}e^{-t/T^*_{2,He}} - E_{Xe}e^{-t/T^*_{2,Xe}} + F_{He}e^{-2t/T^*_{2,Xe}} - F_{Xe}e^{-2t/T^*_{2,He}}. \tag{5.29}$$

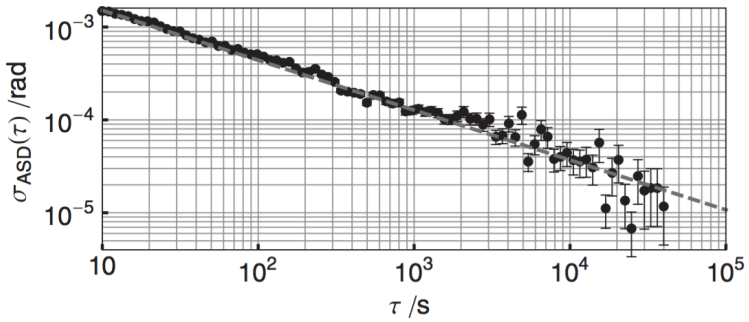

Figure 5.3.: Allan Standard Deviations plot of the residual phase noise of a single measurement run of T = 90000 s using the full fit model of equation 5.29 [75].

Here E_{He} and E_{Xe} are the magnitude of the contributions to the weighted phase difference from the self shift of He and Xe respectively, and F_{He} and F_{Xe} are the magnitude of the contributions from the inter-species shift.

From the Allan Standard Deviation plot of the residual phase in Figure 5.3, the uncertainty in the phase is approximately 10^{-5} rad after 90000 s. This is an uncertainty in the frequency of $\sim 1 \times 10^{-10}$ rad/s, or 8×10^{-30} $e$cm after 90000 s.

In conclusion, we are confident that contributions from the Ramsey-Bloch-Siegert shift to the accumulated phase are accounted for in the fitting routine

5.4.2. Geometric Phase Shift

The geometric phase shift [77] is an application of the Bloch-Siegert shift, with the rotating field generated by the movement of spin polarized atoms through an electric field generating a motional magnetic field and a radial magnetic field gradient from the magnetic holding field B_0. Because the experiment operates in the regime of motional narrowing, free movement of of particles throughout the cell is greatly suppressed.

The rotating field depends on the relative orientation of the magnetic and electric fields ($\uparrow\uparrow$ or $\uparrow\downarrow$), the magnitude of the radial magnetic field gradient and the direction of the orbit of the polarized atoms. Assuming the magnetic holding field, B_0, is in z direction

$$B_0 \uparrow\uparrow E,\ B_{xy+} = B_{0r} - |B_v|,\ B_{xy-} = B_{0r} + |B_v|, \tag{5.30a}$$

$$B_0 \uparrow\downarrow E,\ B_{xy+} = B_{0r} + |B_v|,\ B_{xy-} = B_{0r} - |B_v|, \tag{5.30b}$$

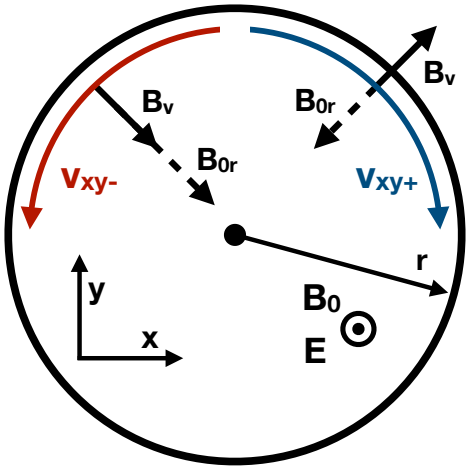

Figure 5.4.: Slice of the xy plane of the cell. Two paths for a particle undergoing circular orbit are shown, v_{xy+} and v_{xy-}, for clockwise and anti-clockwise, respectively. $\mathbf{B}_{0r}$ always points inwards, whereas $\mathbf{B}_v$ depends on the orbital direction. $\mathbf{B_0}$ and $\mathbf{E}$ point towards the reader. Figure adapted from [77].

with $B_v = \frac{|v_{xy}||E|}{c^2}$ and B_{0r} is the radial component of the holding field. This manifests as an effective rotating magnetic field shown schematically in Figure 5.4. The rotating magnetic field results in a frequency shift similar to the Bloch-Siegert shift 5.4.1

$$\delta\omega_{geo} = \frac{\left(\gamma B_{xy+}\right)^2}{4(\omega_0 - |\omega_r|)} + \frac{\left(\gamma B_{xy-}\right)^2}{4(\omega_0 + |\omega_r|)}, \tag{5.31}$$

where ω_r is, in the worst case, the frequency of clockwise or counterclockwise movement through the cell ($\omega_r = \frac{v_t}{r}$ rad/s), assuming an infinite mean free path length. The frequency shifts differ for parallel and anti-parallel fields

$$\begin{aligned}\delta\omega_{geo,\uparrow\uparrow} = &\frac{\gamma^2\left(B_{0r}^2 + B_v^2\right)}{4}\left[\frac{1}{(\omega_0 - |\omega_r|)} + \frac{1}{(\omega_0 + |\omega_r|)}\right] \\ &- \frac{\gamma^2\left(B_{0r}\,|B_v|\right)}{2}\left[\frac{1}{(\omega_0 - |\omega_r|)} - \frac{1}{(\omega_0 + |\omega_r|)}\right],\end{aligned} \tag{5.32a}$$

$$\begin{aligned}\delta\omega_{geo,\uparrow\downarrow} = &\frac{\gamma^2\left(B_{0r}^2+B_v^2\right)}{4}\left[\frac{1}{(\omega_0-|\omega_r|)}+\frac{1}{(\omega_0+|\omega_r|)}\right]\\ &+\frac{\gamma^2\left(B_{0r}\,|B_v|\right)}{2}\left[\frac{1}{(\omega_0-|\omega_r|)}-\frac{1}{(\omega_0+|\omega_r|)}\right].\end{aligned} \tag{5.32b}$$

Taking the difference in frequency shift between parallel and anti-parallel fields yields

$$\begin{aligned}\left(\delta\omega_{geo,\uparrow\uparrow}-\delta\omega_{geo,\uparrow\downarrow}\right) &= -\gamma^2 B_{0r}\,|B_v|\left[\frac{1}{(\omega_0-|\omega_r|)}-\frac{1}{(\omega_0+|\omega_r|)}\right]\\ &= -2\gamma^2 B_{0r}\,|B_v|\,\frac{|\omega_r|}{\left(\omega_0^2-\omega_r^2\right)}\end{aligned} \tag{5.33}$$

Assuming a temperature of 300 K, a spherical cell with 5 cm radius and a magnetic holding field of 400 nT, the weighted frequency difference with helium as a co-magnetometer and xenon, results in a frequency shift of

$$\delta\omega_{geo,WFD} = 2.6\times10^{-9}\ \text{rad/s} \tag{5.34}$$

Without any collisional damping the false EDM is $d_{f,geo} = 1.1\times10^{-27}\ e\text{cm}$. However, this assumes the particles essentially travel in circles around the outer perimeter of the spherical cell indefinitely. In reality collisions prohibit this and suppress the geometric phase shift significantly. The suppression of a false EDM due to collisions can be estimated [77]

$$d_{f,<geo>} = d_{f,geo}\left[\frac{\pi v_{xy}\lambda}{2R^2\omega_0}\right]^2, \tag{5.35}$$

Here v_{xy} is the velocity, R the radius of the cell, ω_0 the Larmor precession frequency and λ is the mean free path (see also Eq. 5.3)

$$\lambda = \frac{k_B T}{\sqrt{2}\pi d^2 p}, \tag{5.36}$$

with k_B the Boltzman constant, T the temperature, πd^2 the cross-section and p the pressure. The suppression is given by the term between the brackets on the right hand side of Eq. 5.35. For typical experimental parameters it is approximately 3×10^{-4}, pushing $d_{f,<geo>}$ to $-3.8\times10^{-31}\ e\text{cm}$.

5.4.3. Earth Rotation

The rotation of earth influences the apparent spin precession frequency. Earth rotates with the sidereal frequency of

$$\Omega_E = 7.29\times10^{-5}\ \text{rad/s}\ [78]. \tag{5.37}$$

This means the laboratory frame is not an inertial frame of reference, and the SQUIDs rotate with a frequency with respect to the precessing spins, shifting the measured frequencies from the true frequencies by ω_{SQ} The contribution of this frequency shift in the weighted frequency difference is

$$\begin{aligned}\delta\omega_E &= \left(\gamma_{Xe}B_0 - \omega_{SQ} - \frac{\gamma_{Xe}}{\gamma_{He}}\left(\gamma_{He}B_0 - \omega_{SQ}\right)\right) \\ &= \left(1 - \frac{\gamma_{Xe}}{\gamma_{He}}\right)\omega_{SQ}.\end{aligned} \tag{5.38}$$

The frequency shift ω_{SQ} depends on the orientation of the magnetic holding field and the earth rotation axis. For a magnetic holding field parallel to the Earth's surface it can be expressed in terms of the angle between the magnetic holding field and north, α, and the latitude of the experiment, Θ

$$\omega_{SQ} = \Omega_E \cos(\alpha)\cos(\Theta). \tag{5.39}$$

Θ can be determined with enough accuracy, but we are limited by α, which can be determined to $\sim 1^\circ$ accuracy [55].

Taking the latitude of Jülich for Θ, 0.8889 radians, and using an α generating the largest possible shift ($\alpha = 0^\circ$) , the SQUID frequency is $\omega_{SQ} = 4.6 \times 10^{-5}$ rad/s and the weighted frequency shift is $\delta\omega_E = 2.9 \times 10^{-5}$ rad/s. Provided the angle of the magnetic field does not change, this is a linear contribution to the phase accumulation, unchanging over duration of the measurement run. This is incorporated in the fitting routine with a linear term.

In the MIXed experiment the magnetic field is at an angle of $\sim 45^\circ$ with respect to north, generating a frequency shift $\Delta\omega_E = 2.1 \times 10^{-5}$ rad/s.

A change in the magnetic holding field angle during a measurement run correlated with electric field switching can mimic an EDM signal. The effect on the weighted phase difference depends on the angle of the magnetic holding field with respect to the earth rotation axis:

$$\frac{d\delta\omega_E}{d\alpha} = -\left(1 - \frac{\gamma_{Xe}}{\gamma_{He}}\right)\Omega_E \sin(\alpha)\cos(\Theta). \tag{5.40}$$

The effect of a change in magnetic holding field angle is largest for $\alpha = 90^\circ$ (east-west) and smallest for $\alpha = 0^\circ$ (south-north). At $\alpha = 90^\circ$ rad the required angular stability, i.e. the difference in magnetic field angle α before and after electric field reversal, is $\Delta\alpha = 8.3 \times 10^{-8}$ rad in order to reach 10^{-30} $e$cm. This assumes the angular change correlates with the electric field switching. At $\alpha = 0^\circ$ the required angular stability is $\Delta\alpha \leq 4.1 \times 10^{-4}$ rad to reach the same EDM sensitivity level, requiring four orders of magnitudes less angular stability. For the MIXed magnetic holding field, at $\alpha = 45^\circ$ degrees with respect to north, the required stability is $\Delta\alpha \leq 1.2 \times 10^{-7}$ rad. By changing the alignment significantly during experimental runs an upper limit on the required angular stability can be set.

5.4.4. Chemical Shift

The chemical shift is a shift in the spin precession frequency due to shielding of the external magnetic field from the nucleus by the electron shells, and formation of Xe and He dimers and He-Xe molecules. It depends on the partial pressures in the case of a ^{3}He-^{129}Xe co-magnetometer, causing the chemical shift to differ each time the measurement cell is refilled with polarized gasses. It gives a linear shift in the accumulated phase, which is fitted out.

The chemical shift is usually expressed as a relative shift of the frequency, and given in p.p.m. A relative shift of 10^{-6} results in a frequency shift of $\sim 10^{-5}$ rad/s, or $\sim 10^{-25}$ $e$cm. Provided the environmental conditions are sufficiently stable, this contribution is incorporated by the fit model as a linear shift.

As stated in Section 5.4.1, from Fig. 5.3 we know the uncertainty in the phase is approximately 10^{-5} rad after 90000 s. With this knowledge we can be confident that the environmental conditions are sufficiently stable to reach 10^{-30} $e$cm sensitivity in the ^{129}Xe EDM experiment.

5.4.5. Alignment Spin with Magnetic Field

Alignment of the spins with the magnetic field has influence on the spin precession signal amplitude in the SQUID system and also on the magnitude of the Bloch-Siegert shift .

Ideally the spins are perpendicular to the magnetic holding field. In that case, provided the magnetic holding field is also perpendicular to the SQUID system, the spin precession signal is maximal in the detector. This also provides for the maximal signal-to-noise ratio. If the spins are at an angle less than 90° to the magnetic holding field, the effective signal amplitude decreases with a factor $\sin\theta$, where θ is the angle between the magnetic field and the spin polarization direction, thereby causing the signal-to-noise ratio to decrease.

The magnitude Bloch-Siegert shift depends on the magnitude of the rotating field [See Section 5.4.1]. The magnetic field of spins can be decoupled into two components, one parallel and one perpendicular to the magnetic holding field. The component parallel to the magnetic holding field is experienced by both precessing species, which has the same effect as increasing the magnetic holding field. This is compensated for by co-magnetometry. The component perpendicular to the magnetic holding field causes the rotation frequency dependent shift, thus a change in the angle between the polarized spins and the holding field has differing Bloch-Siegert shifts as an effect, which is not compensated for by co-magnetometry.

5.5. Particularly Relevant Systematic Effects

The systematic effects that generate frequency shifts of a magnitude of concern for the EDM measurements are:

- Earth Rotation:
  Since the effect of the earth rotating is rather large ($\sim 2.9 \times 10^{-5}$ rad/s), and depends on $\cos(\alpha)$, where α is the angle between the magnetic holding field and the earth rotation axis, the required stability of the magnetic holding field direction is quite small. By varying the angle of the magnetic holding field during a measurement we can get a limit on the required angular stability.

- Effects dependent on magnetic field gradients:
  Several effects, such as the center of mass difference and the magnetic gradient shift, depend on magnetic field gradients. Since they result in a constant frequency shift, they are compensated linearly in the fit model. This however assumes that the magnetic field gradients are sufficiently constant during a single measurement run. By varying the magnetic field gradients during a measurement run, for instance by changing the magnetic field gradients using the magnetic gradients coils, a limit on the required magnetic field gradient stability can be obtained.

- External Magnetic Fields:
  By mounting several fluxgates outside of the magnetically shielded room external magnetic field fluctuations could be monitored in real time and correlated to magnetic field changes inside the shielded volume. We suggest at least 4 (better 6) probes mounted on each face of the magnetically shielded room.

Table 5.3.: Parameters to be constrained in order to reach $|d_{Xe}| < 10^{-30}$ $e$cm and the maximum amount each of the parameters may vary in order to correct for these effects during fitting. Only estimated for parameters which yielded a false edm above 10^{-30} $e$cm with our environmental conditions. The column *Max. Allowed Change* assumes the change occurs during an electric field reversal, causing a differing linear shift in the accumulated phase under differing electric field orientations, mimicking an EDM signal. Calculated assuming the environmental conditions shown in Table 5.2.

	Max. False EDM	Constraint	Max. Allowed Change
Earth Rotation [Sec. 5.4.3]	8.5×10^{-24} $e$cm	$B_0 \measuredangle$ w.r.t. rot. north	1.2×10^{-7} rad
Center of Mass [Sec. 5.1.2]	2.3×10^{-26} $e$cm	$\frac{\partial B}{\partial z}$	1.3×10^{-3} pT/cm

Table 5.4.: Overview of conservatively estimated systematic effects on spin precession phase accumulation. Worst case estimates, assuming the environmental conditions shown in Table 5.2. All calculated false edms, excluding the geometric phaseshift, are without flipping the electric field. Flipping of the electric field is integral to the geometric phaseshift, hence it is included there. The estimates for the Ramsey-Bloch-Siegert and chemical shift frequencies are an upper limit calculated from a measurement performed at the PTB in Berlin after using the fit model. Co-Magnetometry indicates if the co-magnetometer prevents this effect from playing a role, Flipping indiciates if an electric field reversal reverses the sign of this frequency and finally Fitting Routine specifies whether the effect is included either in $\Delta\omega_{\text{lin}}$ or the Ramsey-Bloch-Siegert terms in Eq. 5.29.

	Frequency Shift	Co-Magnetometry	Flipping	Fitting Routine	Max. False EDM at 800 V/cm
Earth Rotation [Sec. 5.4.3]	2.9×10^{-5} rad/s	No	Yes	Yes	1.2×10^{-23} $e$cm
Center of Mass [Sec. 5.1.2]	-5.5×10^{-8} rad/s	No	Yes	Yes	-2.3×10^{-26} $e$cm
Ramsey-Bloch-Siegert Shift [Sec. 5.4.1]	$< 1 \times 10^{-10}$ rad/s	No	No	Yes	$< 8 \times 10^{-30}$ $e$cm
Chemical Shift [Sec. 5.4.4]	$< 1 \times 10^{-10}$ rad/s	No	Yes	Yes	$< 8 \times 10^{-30}$ $e$cm
Geometric Phaseshift [Sec. 5.4.2]	9.4×10^{-13} rad/s	No	No	No	3.8×10^{-31} $e$cm
Leakage Current (10 pA) [Sec. 5.3.1]	1.5×10^{-14} rad/s	No	No	No	6×10^{-33} $e$cm
Motional Magnetic Field [Sec. 5.1.3]	2.3×10^{-16} rad/s	No	No	No	9.3×10^{-35} $e$cm
Magnetic Gradient Shift [Sec. 5.1.4]	1.0×10^{-16} rad/s	No	Yes	Yes	4.2×10^{-35} $e$cm

6. Extraction of EDM Limit

6.1. Data Analysis

During an experimental data taking period it is possible to measure the noise and amplitude of the xenon and helium signals captured by the SQUID gradiometers. However this is employed for diagnostics during the run. The actual analysis of the SQUID gradiometer data is performed later on off-line.

Off-line analysis first extracts the phase from chunks of the time series, then the EDM signal is extracted from the phase and finally the residuals are analyzed. This chapter gives a detailed description of this analysis procedure.

6.1.1. Phase Extraction

The signal captured by the gradiometers is a beat-note between the helium and xenon signals, at ∼5 Hz and ∼13 Hz, respectively, for a magnetic holding field of 400 nT. In addition to the signal noise is present, consisting mainly of pink noise (1/f noise), noise from power lines at 50 Hz frequency and some mechanical noise between 1 Hz and 4 Hz. The first step of the analysis is extracting the accumulated phase of the helium and xenon signals. This is achieved by splitting an experimental run, usually around 6 hours in length, into sub-cuts of 4 second duration. An example of such a sub-cut is shown in Figure 6.1, as is a FFT of the same data set. From these sub-cuts the frequencies and amplitudes of helium and xenon are extracted using as the fit function

$$f^i(t) = A^i_{\mathrm{He}} \sin\left(\omega^i_{\mathrm{He}} t\right) + B^i_{\mathrm{He}} \cos\left(\omega^i_{\mathrm{He}} t\right) + A^i_{\mathrm{Xe}} \sin\left(\omega^i_{\mathrm{Xe}} t\right) + B^i_{\mathrm{He}} \cos\left(\omega^i_{\mathrm{Xe}} t\right) + c^i_0 + c^i_1 \cdot t, \quad (6.1)$$

where i denotes the sub-cut number, the sine and cosine terms describe the helium and xenon Larmor precession, c_0 and c_1 are for a constant and a linear term, respectively, to compensate a constant offset and linear drift of the gradiometer offset. t is set symmetrically around zero for each sub-cut. The length of the sub-cuts was chosen such that the number of data points give sufficient statistics, while limiting the drift of the gradiometer offset such that it can be described by a linear term.

The fit is performed using χ^2 minimization (see Appendix D for a detailed explanation) implemented in the Minuit2 [79] minimization code. The fit parameters A_{He}, B_{He}, A_{Xe}, B_{Xe}, ω_{He}, ω_{Xe}, c_0 and c_1 are extracted for each sub-cut, including uncertainties. χ^2 for

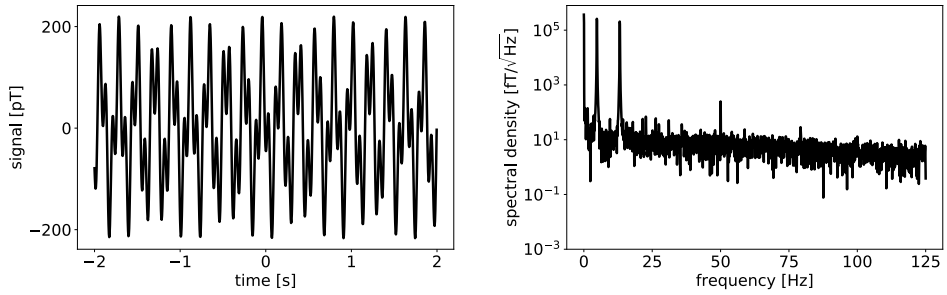

(a) (b)

Figure 6.1.: Sub-cut of raw data from a SQUID gradiometer displaying the beating of the ^{129}Xe and ^{3}He precession signals at Larmor frequencies of 5 Hz and 13 Hz. A magnetic holding field B_0 of 400 nT is applied. (b) displays a Fast Fourier Transform (FFT) of the same raw data, with two peaks at 5 Hz and 13 Hz, the helium and xenon signals. The characteristic 1/f noise is visible, as well as the noise peak at 50 Hz. With ∼143 fT noise, the signal-to-noise ratios for ^{129}Xe and ^{3}He are 863:1 and 672:1, respectively.

each sub-cut is used as a measure of the fit quality. χ^2 minimization minimizes the metric

$$\chi^2 = \sum_{i=0}^{N-1} \left(\frac{y_i - f(x_i; \boldsymbol{\theta})}{\sigma_i} \right)^2 . \tag{6.2}$$

where y_i are the observed values, $f(x_i; \boldsymbol{\theta})$ are the fit model values stemming from parameters $\boldsymbol{\theta}$ and σ_i are the errors for each measured data point o_j. Ideally χ^2 follows a χ^2 distribution

$$f_{\chi^2}(x; \nu) = \frac{e^{-x/2} x^{\nu/2-1}}{2^{\nu/2}\Gamma(\nu/2)}, \tag{6.3}$$

where ν is the number of degrees of freedom (d.o.f.), i.e. the number of data points N minus the number of fit parameters P, $\nu = N - P$. For the MiXeD experiment the sub-cuts have 1000 points and 8 parameters are fitted, yielding $\nu = 992$.

In this analysis the uncertainties for each data point are assumed to constant throughout the data taking period, independent of the data point, thus $\sigma_i = \sigma$. The value of σ first estimated by calculating the area underneath the FFT, excluding the ^{3}He and ^{129}Xe peaks. It is thereafter normalized by setting the mean of the resulting χ^2 distribution over all sub-cuts to 1 or $< \chi^2_\nu >_{\text{sub-cuts}} = 1$.

The phase and total amplitude for each individual sub-cut is determined by using $A\sin(\omega t) + B\cos(\omega t) = a\sin(\omega t + \phi)$, where $a = \sqrt{A^2 + B^2}$ and $\phi = \arctan(B/A)$. ϕ

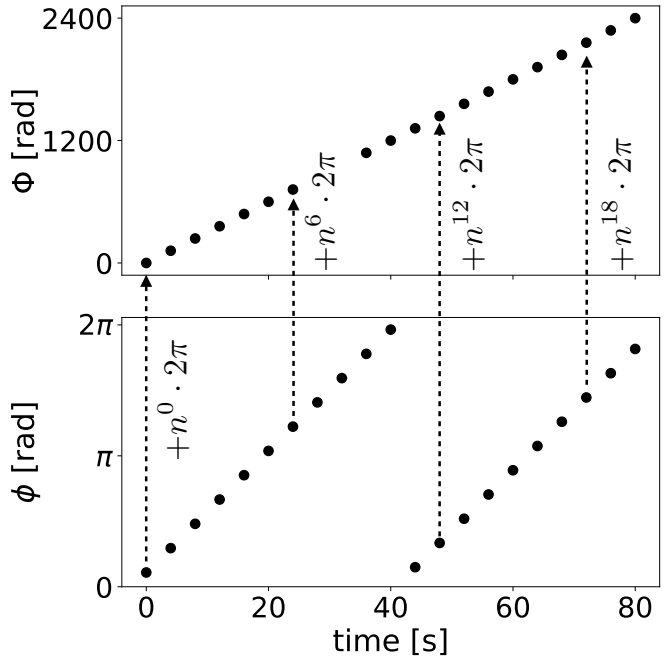

Figure 6.2.: Principle of determining the accumulated phases. Φ^i is determined by adding the appropriate multiples of 2π to ϕ^i. The multiples of 2π missed (n^i) are determined by calculating the missed complete spin rotations between each pair of neighboring sub-cut as shown in Eq. 6.7. Figure adapted from [55].

is the accumulated phase modulo 2π. This necessitates a determination of the number n_i of integer 2π missed. In the data analysis code $\arctan2(B,A)+\pi$ is used to ensure that ϕ is in the range $|0,\ 2\pi)$.

With this the phase for each sub-cut is then

$$\phi^i_{\mathrm{Xe/He}} = \arctan 2\left(B^i_{\mathrm{Xe/He}}, A^i_{\mathrm{Xe/He}}\right) + \pi, \tag{6.4}$$

which is the phase modulo 2π, at $t = (i-1/2)\cdot\Delta t$. To determine the total accumulated phase the appropriate multiples of 2π needs to be added (see Fig. 6.2)

$$\Phi^i_{\mathrm{Xe/He}} = n^i_{\mathrm{Xe/He}} \cdot 2\pi + \phi^i_{\mathrm{Xe/He}}. \tag{6.5}$$

Here $n^i_{\mathrm{Xe/He}}$ are the number of rotations of the ^{129}Xe and ^{3}He magnetization from the start of the measurement at $t = 0$ until t^i, the center of the i-th sub-cut. $n^i_{\mathrm{Xe/He}}$ is determined by

calculating the number of missed complete rotations between each neighboring sub-cut and summing them, e.g.

$$n^i_{\mathrm{Xe/He}} = \sum_{k=0}^{i} \Delta n^k_{\mathrm{Xe/He}}, \tag{6.6}$$

where $\Delta n^i_{\mathrm{Xe/He}}$, the number of missed rotations between each neighboring sub-cut is determined using

$$\Delta n^i_{\mathrm{Xe/He}} = \left[\frac{\omega^i_{\mathrm{Xe/He}} \cdot \Delta t - \left(\phi^i_{\mathrm{Xe/He}} - \phi^{i-1}_{\mathrm{Xe/He}} \right)}{2\pi} \right], \tag{6.7}$$

rounded to the nearest integer. The number of rotations depends on the Larmor frequency, which in turn depends on the magnetic field. This field is sufficiently stable to prevent false mappings. The mapping is shown in figure 6.2 schematically.

The weighted phase difference is determined using co-magnetometry, and is given by

$$\Delta\Phi^i = \Phi^i_{\mathrm{Xe}} - \gamma_{\mathrm{Xe}}/\gamma_{\mathrm{He}}\Phi^i_{\mathrm{He}}. \tag{6.8}$$

This removes the Larmor accumulated phase. In principle $\Delta\Phi^i$ is independent of the magnetic holding field B_0, and thus constant, in absence of any systematic effects or other interactions.

6.1.2. EDM Fit

With systematics included that can be compensated via the fit function and with the assumption of a zero EDM on ^{129}Xe, the differential accumulated phase follows (see Section 5.4.1, Eq. 5.29)

$$\Phi(t) = \Phi_0 + \Delta\omega_{\mathrm{lin}} t + E_{\mathrm{He}} e^{-t/T^*_{2,\mathrm{He}}} - E_{\mathrm{Xe}} e^{-t/T^*_{2,\mathrm{Xe}}} + F_{\mathrm{He}} e^{-2t/T^*_{2,\mathrm{Xe}}} - F_{\mathrm{Xe}} e^{-2t/T^*_{2,\mathrm{He}}}. \tag{6.9}$$

Here E_{He} and E_{Xe} are the magnitude of the contributions to the weighted phase difference from the self shift of He and Xe respectively, F_{He} and F_{Xe} are the magnitude of the contributions from the inter-species shift. The term $\Delta\omega_{\mathrm{lin}}$ contains the earth rotation and chemical shift contributions. Henceforth for ease of notation the fit function will have the form

$$\Phi(t) = a_0 + a_1 t + a_2 e^{-t/T^*_{2,\mathrm{He}}} + a_3 e^{-t/T^*_{2,\mathrm{Xe}}} + a_4 e^{-2t/T^*_{2,\mathrm{Xe}}} + a_5 e^{-2t/T^*_{2,\mathrm{He}}}. \tag{6.10}$$

These terms, especially the exponentials, result in highly correlated fit parameters. To prevent this the fit function is orthogonalized using Gram-Schmidt orthogonalization [80]. Defining a projection operator

$$\mathrm{proj}_{\mathrm{u}}(\mathbf{v}) = \frac{<\mathbf{u},\mathbf{v}>}{<\mathbf{u},\mathbf{u}>}\mathbf{u}, \tag{6.11}$$

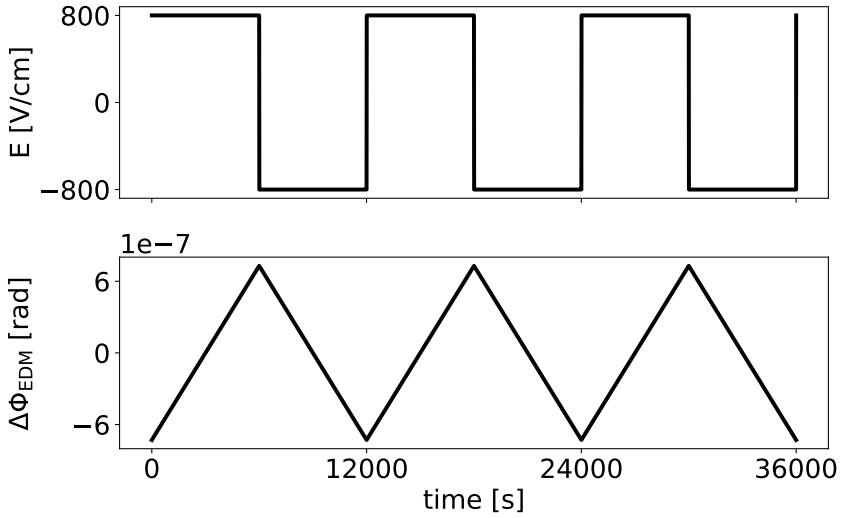

Figure 6.3.: Expected contribution evolution of the weighted phase difference under influence a periodically reversed electric field orientation of 800 V/cm and an EDM of $d_{\mathrm{Xe}} = 10^{-28}$ $e$cm. The electric field is shown in the top figure and the EDM contribution to the weighted phase difference in the bottom figure. The EDM under influence of a periodically reversed electric field generates a triangular contribution to $\Delta\Phi$. For this figure the switching time is set to 6000 s.

for a vector $\mathbf{v}$ the orthogonalized vector using the Gram-Schmidt process has form

$$\begin{aligned}
\mathbf{u}_1 &= \mathbf{v}_1, \\
\mathbf{u}_2 &= \mathbf{v}_2 - \mathrm{proj}_{\mathbf{u}_1}(\mathbf{v}_2), \\
\mathbf{u}_3 &= \mathbf{v}_3 - \mathrm{proj}_{\mathbf{u}_1}(\mathbf{v}_3) - \mathrm{proj}_{\mathbf{u}_2}(\mathbf{v}_3), \\
&\vdots \\
\mathbf{u}_k &= \mathbf{v}_k - \sum_{j=1}^{k-1} \mathrm{proj}_{\mathbf{u}_j}(\mathbf{v}_k).
\end{aligned} \tag{6.12}$$

To orthogonalize the fit function terms the inner product is defined as

$$< f(t), g(t) >= \int_{t_B}^{t_E} \exp(-2t/T^*_{2,Xe}) f(t) \cdot g(t) dt, \tag{6.13}$$

where t_B, t_E are the respective start and end time of the measurement, and the vectors $\mathbf{u}_i$ are the fit function terms 1, t, $e^{-t/T^*_{2,\mathrm{He}}}$, $e^{-t/T^*_{2,\mathrm{Xe}}}$, $e^{-2t/T^*_{2,\mathrm{Xe}}}$, $e^{-2t/T^*_{2,\mathrm{He}}}$. The orthogonalized fit function has form

$$\Phi_{\mathrm{ortho}}(t) = a_0\mathbf{u}_0(t) + a_1\mathbf{u}_1(t) + a_2\mathbf{u}_2(t) + a_3\mathbf{u}_3(t) + a_4\mathbf{u}_4(t) + a_5\mathbf{u}_5(t). \tag{6.14}$$

For ease of extracting the fitted EDM value, the term describing the EDM contribution to the weighted phase difference is added after orthogonalization.

As shown in Eq. 2.37, the contribution of the EDM to the weighted phase difference is $\frac{2d_{\mathrm{Xe}}E}{\hbar}t$. The EDM contribution to the weighted phase difference for a periodically reversed electric field orientation is then described by a triangular wave if the switching period is constant (See Fig. 6.3).

The triangular function $T(t, t_{\mathrm{switch}})$, where t_{switch} is the field reversal time, has amplitude 1 centered around 0 and is added to the orthogonalized fit function multiplied by a constant d

$$\Phi_{\mathrm{ortho,EDM}}(t) = a_0\mathbf{u}_0(t) + a_1\mathbf{u}_1(t) + a_2\mathbf{u}_2(t) + a_3\mathbf{u}_4 + a_4\mathbf{u}_4(t) + a_5\mathbf{u}_5(t) + dT(t, t_{\mathrm{switch}}). \tag{6.15}$$

The fitted parameter d then translates to the EDM on xenon d_{Xe} with

$$d_{\mathrm{Xe}} = \frac{\hbar}{2Et_{\mathrm{switch}}}d, \tag{6.16}$$

where E is the electric field strength. Multiplying the fitted value and 1 σ error for d with $\frac{\hbar}{2Et_{\mathrm{switch}}}$ results in the fitted xenon EDM value and 1 σ error. $\Phi_{\mathrm{ortho,EDM}}$ is fitted using the χ^2 minimization described in Section 6.1.1 and Appendix D, as used for the phase extraction.

6.1.3. Sub-cut Length

The number of data-points in a sub-cut was varied to check the dependence of the sub-cut length on the various fit parameters. The extracted EDM values and fit errors are shown in Figure 6.4. The extracted EDM for varying sub-cut lengths are compatible with each other. The increase in fit error after 500 data-points per sub-cut is caused by an increase in measurement error per data-point. The degree of polynomial terms in Eq. 6.1 is not sufficient to compensate the background for increased sub-cut length, necessitating an increase in measurement error in order to set the mean of χ^2_ν over all sub-cuts to 1. For sub-cuts with less than 500 data-points the amount of data-points used in the fit is limiting the fit accuracy.

6.1.4. Orthogonalizing EDM Phase Contribution

In Section 6.1.2 the fit function was orthogonalized (See Eqs. 6.12-6.15), before adding the EDM contribution to the weighed phase difference. Without an EDM contribution,

Table 6.1.: Table with correlation matrices for the phase fit. (a) shows the correlation matrix when adding the EDM contribution after orthogonalization, whereas (b) shows the correlation matrix with the EDM contribution included in orthogonalization. *Green* signifies minimal correlation whereas *red* indicates maximal correlation. Data from measurement L20170719_220808.

(a)

	a_0	a_1	a_2	a_3	a_4	a_5	d
a_0	1.00	-0.64	0.00	-0.69	0.71	-0.11	-0.87
a_1	-0.64	1.00	-0.03	0.56	-0.57	0.09	0.71
a_2	0.00	-0.03	1.00	0.04	-0.01	0.01	0.01
a_3	-0.69	0.56	0.04	1.00	-0.66	0.12	0.80
a_4	0.71	-0.57	-0.01	-0.66	1.00	-0.13	-0.81
a_5	-0.11	0.09	0.01	0.12	-0.13	1.00	0.13
d	-0.87	0.71	0.01	0.80	-0.81	0.13	1.00

(b)

	a_0	a_1	a_2	a_3	a_4	a_5	d
a_0	1.00	-0.05	0.02	0.01	-0.00	-0.00	-0.00
a_1	-0.05	1.00	-0.05	-0.02	0.01	-0.00	0.00
a_2	0.02	-0.05	1.00	0.05	-0.01	0.01	0.00
a_3	0.01	-0.02	0.05	1.00	-0.05	0.02	0.01
a_4	-0.00	0.01	-0.01	-0.05	1.00	-0.05	-0.01
a_5	-0.00	-0.00	0.01	0.02	-0.05	1.00	0.05
d	-0.00	0.00	0.00	0.01	-0.01	0.05	1.00

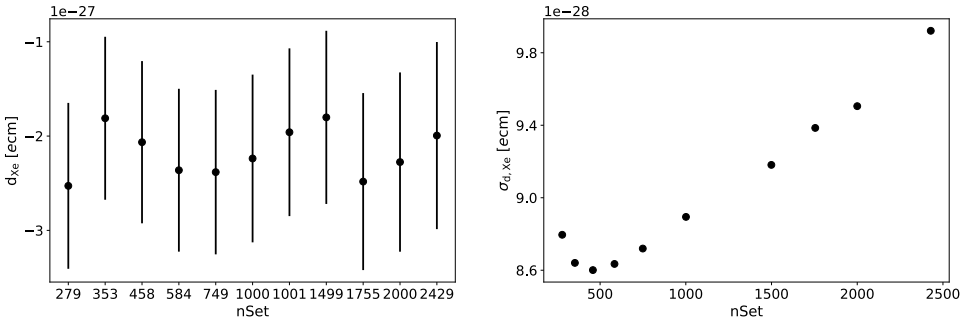

(a) (b)

Figure 6.4.: Effect of changing the number of datapoints (nSet) in a sub-cut on the phase fit parameters. Plotted are the extracted EDM (a) and the extracted EDM fit error (b). The extracted EDM values are compatible with each other. The increase in $\sigma_{\mathrm{d,Xe}}$ after nSet $\sim$ 500 is mostly caused by the increase in the measurement error per data-point, required to set $< \chi^2_\nu >_{\text{sub-cuts}}$ equal to 1. Additional polynomial background terms are needed in the oscillation fit to adequately compensate the background for increased sub-cut lengths. See Section 6.1.1 for more details regarding the measurement error. Data from run L20170719_220808.

the fit results in a diagonal correlation matrix. The addition of the EDM contribution increases the correlations again, but still less than without any orthogonalization.

The EDM contribution can be added to the orthogonalization as shown in Eq. 6.12. By setting the EDM contribution as the last term in $\mathbf{v}$, the last fit parameter of the orthogonalized function gives the fitted EDM. The resulting fit function is then

$$\Phi_{\text{ortho}}(t) = a_0\mathbf{u}_0(t) + a_1\mathbf{u}_1(t) + a_2\mathbf{u}_2(t) + a_3\mathbf{u}_3(t) + a_4\mathbf{u}_4(t) + a_5\mathbf{u}_5(t) + d\mathbf{u}_6(t). \quad (6.17)$$

The correlations with this fit function are greatly reduced, as shown in Table 6.1. Due to the increased correlations when using Eq. 6.15, the fit errors on the parameters a_0 through a_5 are increased in comparison to Eq. 6.17.

6.1.5. EDM Phase Contribution Function

The contribution of an EDM to the weighted phase difference is described by a triangular wave, as mentioned in Section 6.1.2. The triangular function described there assumes the electric field instantaneously switches polarity. In actuality the voltages creating the

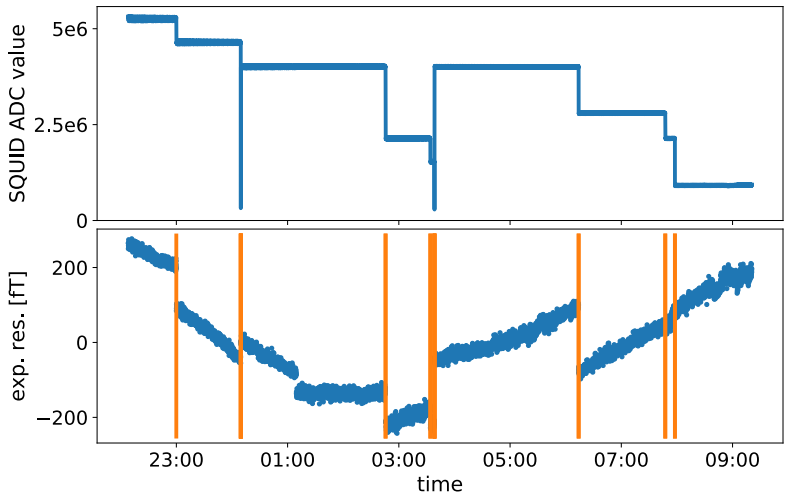

Figure 6.5.: SQUID jumps resulting in changing gain, seen here by plotting the residual of the exponential fit of the ^{3}He signal of run L20170719_220808. The vertical lines indicate moments where the SQUID offset changed significantly, as shown in the top graph.

electric field are ramped to zero before reversing the polarity, after which the voltages are ramped up again. This results in rounded peaks in $\Delta\Phi$. The ramp rate is 25 V/s for the EDM measurements, with ±4 kV on the electrodes. Full polarity reversal is achieved 320 seconds, which is negligible when compared to the field switching times which are at minimum 6000 s. The difference between fit parameters for an EDM contribution to the weighted phase difference taking into account the voltage ramping and a pure triangular EDM contribution is negligible, the fit parameters are compatible with each other well within the fit errors.

6.2. Properties of SQUID Data

Through analysis of the measurement data and correlation with external environmental events several experimental disturbances were identified and accounted for.

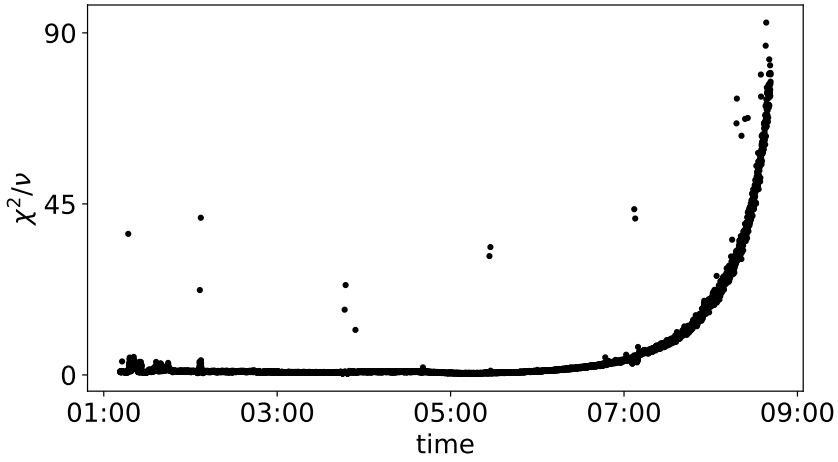

Figure 6.6.: χ^2/ν for each subcut of run L20161016_011117, showing the exponential increase of χ^2, and thus measurement noise, as a result of the SQUIDs heating up due to low liquid He levels. Normally distributed noise of constant amplitude is assumed for analysis, resulting in an increase in χ^2/ν when the noise amplitude increases.

6.2.1. SQUID Jumps

The SQUIDs have a working point (see Sec. 2.6), which may change during a measurement. The SQUIDs integrator is normally reset at the start of a measurement, resulting in measurement values centered around 0 V. However, when the working point changes, the value around which the measurement values are centered are modified. It was found that a modified SQUID offset also resulted in a change in the noise levels. A SQUID offset moving away from zero results in increased noise. Furthermore, the amplitude of the spin precession was observed to be modified, indicating change in gain for SQUID offset levels moving away from zero. Figure 6.5 shows this change in gain, by plotting the residual of the exponential fit of the ^{3}He signal. All discontinuous jumps but one in the residual are related to a change in SQUID offset, explained by a change in gain over the range of SQUID ADC values.

To combat this an automated reset of the integrator in the SQUID electronics is implemented. It is activated when the ADC values exceeded a set threshold level.

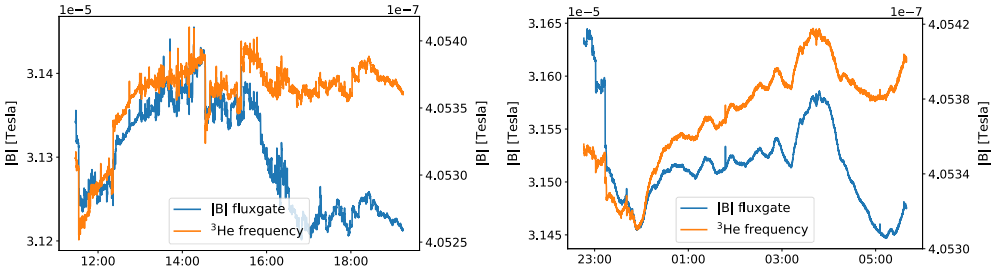

(a) (b)

Figure 6.7.: Normalized magnetic field as measured by a 3 axis fluxgate mounted outside of the MSR and the ^{3}He frequency. (a) uses data from measurement L20170720_112648 and (b) from measurement L20170720_224608. The fluxgate and the measured ^{3}He frequency reproduce the same qualitative features in the time dependence of the B field. This shows the influence of external field changes on the EDM measurement setup.

6.2.2. Low Liquid Helium Level

In order to function SQUIDs exploit superconductivity. Low T_c SQUIDs (T_c stands for critical temperature) used in the MiXeD experiment require liquid helium cooling. A Dewar containing the SQUIDs is filled with liquid helium for this purpose. Depleting liquid helium levels cause the SQUID noise to increase exponentially in time due to heating of the superconductive elements before the SQUIDs finally lose superconductivity. Hence an observed sudden exponential increase in SQUID noise indicates the need for refilling the liquid helium cooling reservoir, and it also signals the end of a data taking period. Figure 6.6 depicts a measurement during which superconductivity was lost. For cold SQUIDs the timescale for refilling is typically a week.

6.2.3. Magnetic Field Fluctuations

A 3 axis Stefan-Mayer fluxgate was mounted outside of the MSR to monitor the external magnetic fields. Figure 6.7 shows the ^{3}He frequency and the external magnetic field measured with the fluxgate. From the figure it is clear most fluctuations in ^{3}He frequency are directly correlated with the external magnetic field. The correlation is shown in Figure 6.8. From Fig. 6.8a there is some correlation, but with discontinuities. A software highpass filter, at 1/25 Hz, was applied to the fluxgate and frequency data. Figure 6.8b plots the correlation after applying the highpass filter, making the correlations more evident.

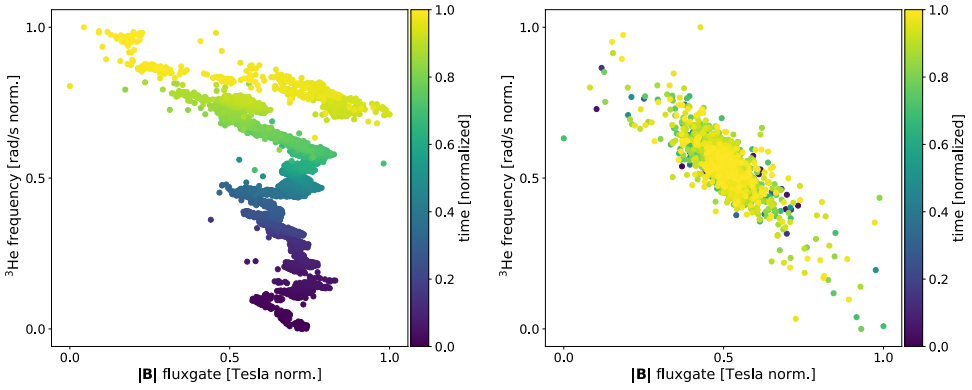

(a) (b)

Figure 6.8.: Correlation between the ^{3}He frequency and the magnetic field measured by a 3 axis fluxgate mounted outside of the MSR from measurement L20170719_220808. (a) Correlation of the raw data. (b) Correlation after a highpass filter set to 1/25 Hz.

A slow drift in the ^{3}He frequency is not present in the external magnetic field data. Because the magnitude of the drift decreases with time after the adiabatic spin flip it is assumed this is generated by relaxation of the magnetic fields inside the μ-metal cylinder surrounding the fiducial volume.

Figure 6.9 shows the effect of a magnet ramping in a nearby magnetic laboratory on the ^{3}He frequency. The ramping magnetic field generated by the magnet is visible with the ^{3}He and ^{129}Xe frequency. The corresponding magnetic field change inside the MSR is $\sim$ 2.6 nT. To prevent the ramping magnetic field from interfering with the EDM measurements the magnets were not ramped during measurement periods.

6.2.4. Residual Structure

The SQUID noise is expected to be normally distributed. With a correctly chosen fit model and properly determined measurement errors, the residuals are also expected to be normally distributed with a standard deviation equal to the measurement error. The residuals are calculated with

$$\mathbf{r} = \mathbf{y} - f(\mathbf{x}; \boldsymbol{\theta}), \tag{6.18}$$

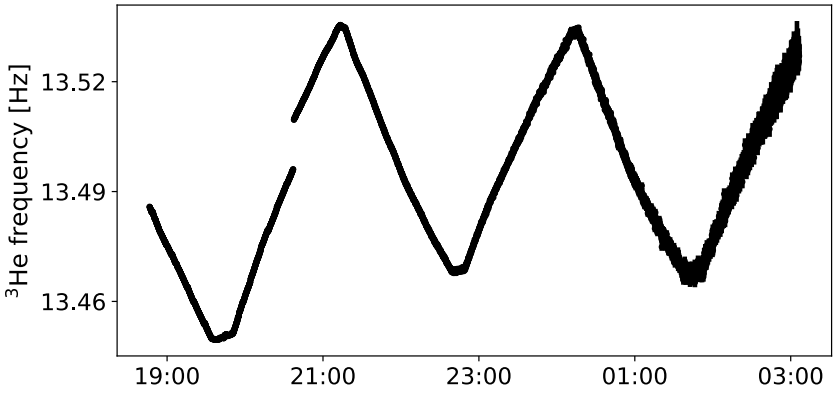

Figure 6.9.: Plot of the ^{3}He frequency showing the ramping of a 7 Tesla magnet in a nearby magnetic laboratory at distance $\sim$ 20 m. The change in frequency corresponds to a magnetic field change of $\sim$ 2.6 nT in the MSR over the fiducial volume. Data from measurement L20170321_184632.

where $\boldsymbol{\theta}$ are the minimal χ^2 fit parameters per sub-cut. Figure 6.10 show the residuals for a run taken in March of 2017. It appears the residuals are not normally distributed. The distribution of the residuals is less broad and some structure is hidden. It becomes visible when the difference between the normal and residual distribution is displayed. This is more evident when reviewing the distribution of χ^2 values for each sub-cut from the fit. From Eq. 6.3 the χ^2 values should follow a χ^2 distribution with 992 degrees of freedom, but from Figure 6.11 it is evident that this is not the case.

Under further investigation it was found that signals at 50 Hz and 100 Hz are present in the data, despite magnetic shielding and optical isolation of all electric and electronic connections. Additionally the linear background approximation was also found to be insufficient, generating outliers in the χ^2 values for sub-cuts with large background disturbances. To compensate, additional terms are added to the fit model, firstly oscillating terms for 50 Hz and 100 Hz, and secondly additional higher orders to the polynomial background. This is discussed in further detail in Section 6.3.

Figures 6.12 and 6.13 show the distribution of the residuals of the extended background fit model and the distribution of the χ^2 values of the sub-cuts. As a result of the additional fit parameters, the measurement noise, estimated by setting the mean of χ^2 sub-cut values over the number of d.o.f. to 1, has dropped to 131 fT. While the χ^2 values from the sub-cuts start approaching a χ^2 distribution, the residual distribution now shows the structure inside more clearly. due to the removal of more noise with the additional fit pa-

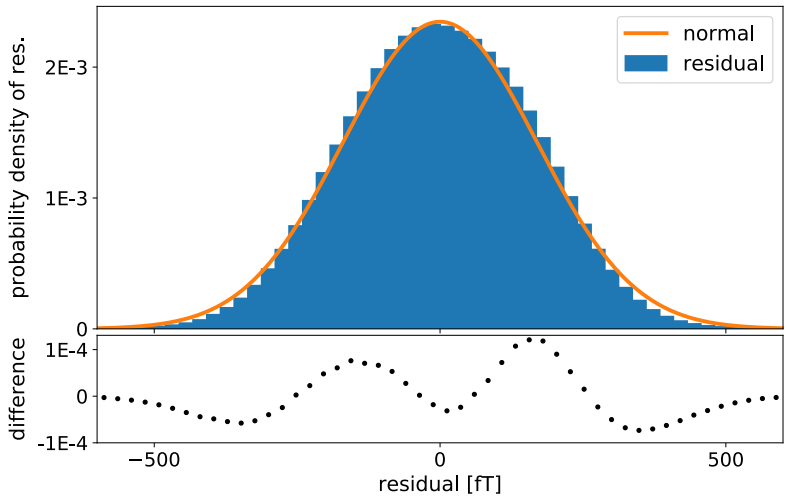

Figure 6.10.: Normalized histogram of the residuals of a run in March of 2017 (L20170328_202227), plotted with a normal distribution with standard deviation equal to the noise as used in the fit, 170 fT.

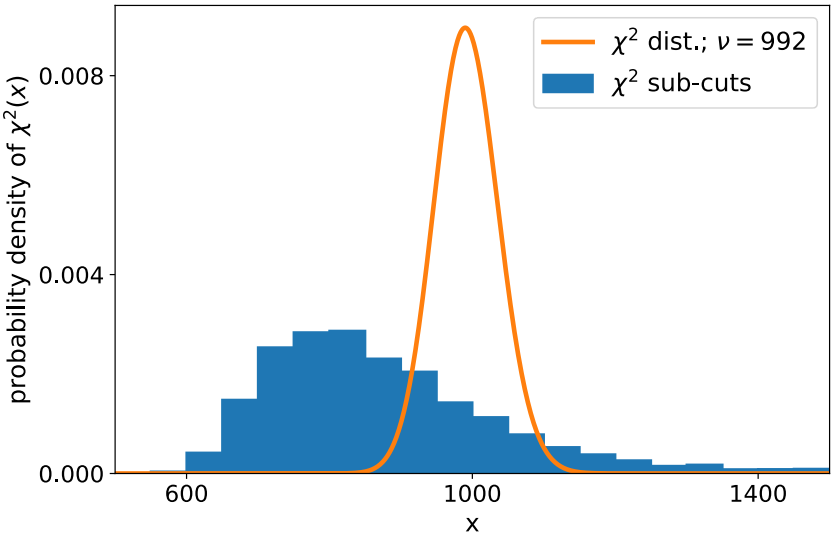

Figure 6.11.: Normalized histogram of χ^2 values from sub-cuts of a run in March 2017 (L20170328_202227), plotted with a χ^2 distribution for $\nu = 992$.

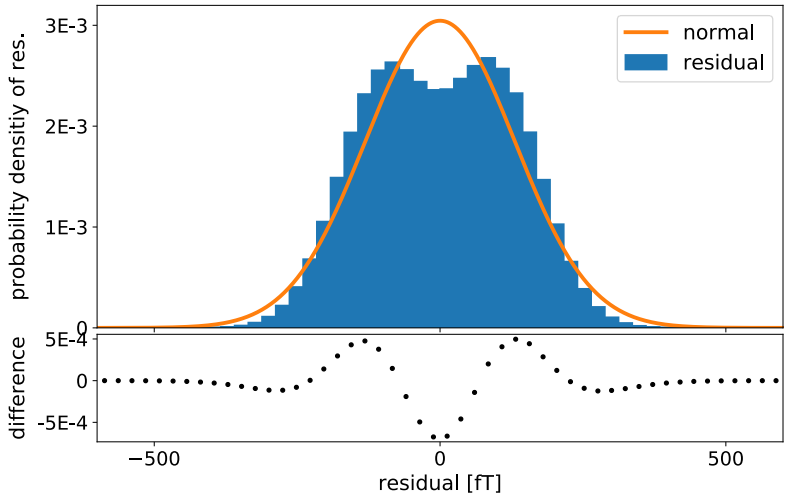

Figure 6.12.: Normalized histogram of the residuals of a run in March of 2017 (L20170328_202227) with additional fit parameters, plotted with a normal distribution with standard deviation equal to the noise as used in the fit, 131 fT.

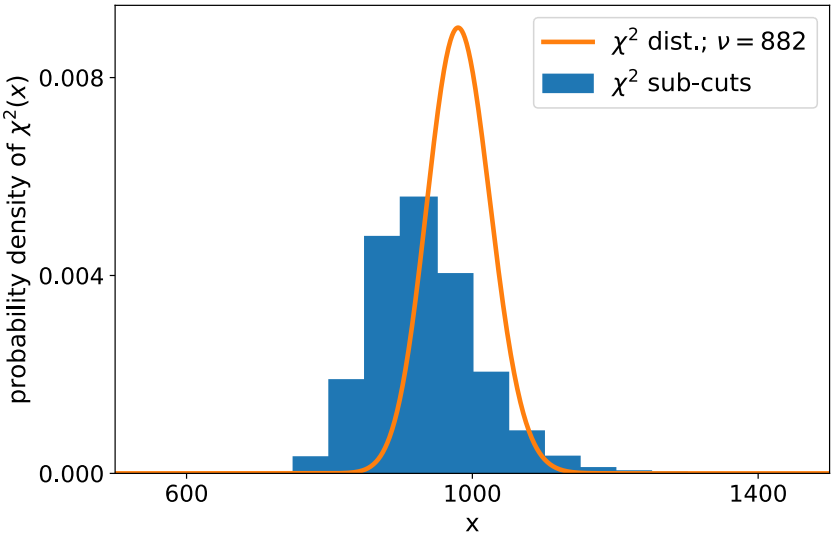

Figure 6.13.: Normalized histogram of χ^2 values from sub-cuts of a run in March 2017 (L20170328_202227) with additional fit parameters, plotted with a χ^2 distribution for $\nu = 882$.

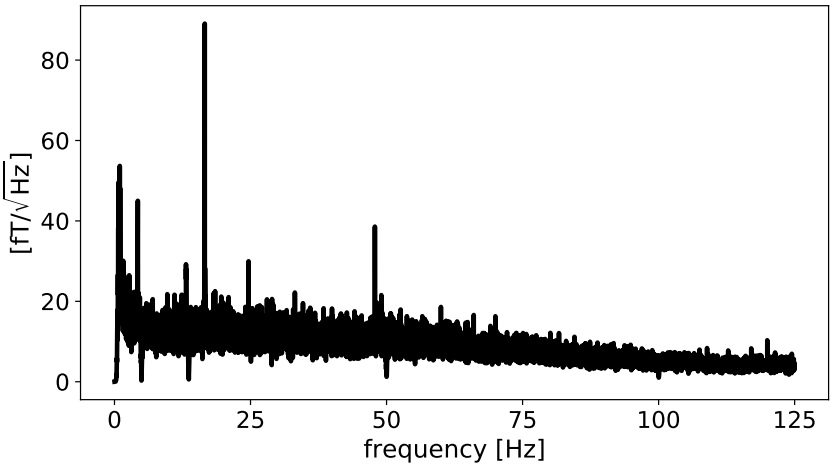

Figure 6.14.: FFT of the residuals from the fit with additional parameters, taken from a 10 minute section of a run in March 2017 (L20170328_202227).

rameters. There appear to be two peaks present, which is possible when some oscillation is still present in the residual. The FFT of the residuals from the fit with additional parameters is plotted in Fig. 6.14, where several peaks are visible, the largest at approximately 16.6 Hz. The issue is that while the peak is clear in the FFT, the amplitude is smaller than the measurement noise (which is the integrated FFT power), making it difficult for χ^2 minimization to fit the frequency, necessitating fixing the frequency for the fit. One common noise source around this frequency are the electrical railway systems, which operate at 16.7 Hz in Germany, which unfortunately does not match the FFT frequency.

Adding additional fit terms for the 16.6 Hz signal, with fixed frequency, did not resolve the double peaks in the residuals, nor did it appreciably improve the χ^2 distribution from the sub-cuts. The width of the peaks suggests that they are caused by oscillations at multiple frequencies, which would make them very difficult to completely resolve.

A possible straightforward solution would be to use a high pass and/or a low pass filter, removing all frequencies not in the band between the xenon and helium precession frequencies. A high pass, or low pass, filter essentially dampens all frequencies lower, respectively higher, than a specified frequency. Unfortunately due to the nature of such filters, the phases of signals passing through the filter are frequency dependently shifted. For high precision experiments tracking phase this prevents their use, but they can still be used for investigating which region in frequency space creates the residual structure.

Cutting off frequencies below the xenon precession frequency had no effect, but setting

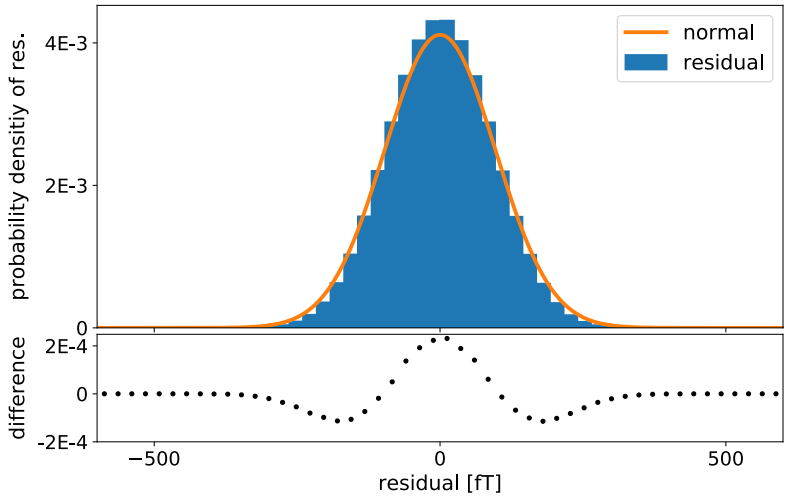

Figure 6.15.: Normalized histogram of the residuals of a run in March of 2017 (L20170328_202227) with additional fit parameters and a digital low pass filter, plotted with a normal distribution with standard deviation equal to the noise as used in the fit, 97 fT.

a frequency cut at 33.64 Hz, above the helium precession frequency, using a digital 5th order Butterworth filter did resolve the twin peaks in the residuals. Because the filter correlates all data points with each other, the distribution of χ^2 values from sub-cuts no longer follows a χ^2 distribution. Figure 6.15 shows the distribution of residuals compared with a normal distribution, suggesting that the structure in the residuals is caused by frequencies above 33.64 Hz. In the FFT in Fig. 6.14 there is a peak slightly below 50 Hz, but adding this oscillation to the fit model did not yet resolve the residual structure. This suggests that there is a wider band of frequencies which generate noise that is non-normally distributed, which is difficult to compensate for with a fit model.

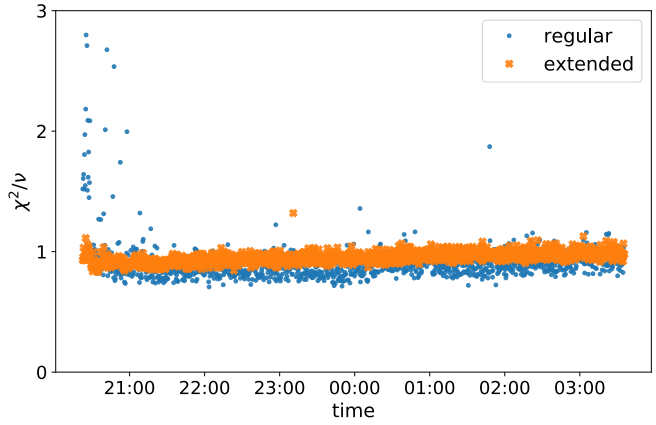

Figure 6.16.: Comparison of reduced χ^2 for the regular fit model and extended background fit model. The spread of χ^2/ν is greatly reduced as is the measurement error, from 170 fT to 131 fT, due to the nature of determining the measurement error (see Sections 6.1 and 6.3). Data from run L20170328_202227, averaged over every 5 sample points.

6.3. Extended Background Fit Model

The fit function to try and resolve the residual structure as discussed in Sec. 6.2.4 is

$$\begin{aligned} f^i(t) = {} & A^i_{\mathrm{He}} \sin\left(\omega^i_{\mathrm{He}} t\right) + B^i_{\mathrm{He}} \cos\left(\omega^i_{\mathrm{He}} t\right) + A^i_{\mathrm{Xe}} \sin\left(\omega^i_{\mathrm{Xe}} t\right) + B^i_{\mathrm{He}} \cos\left(\omega^i_{\mathrm{Xe}} t\right) \\ & + A^i_{50} \sin\left(\omega^i_{50} t\right) + B^i_{50} \cos\left(\omega^i_{50} t\right) + A^i_{100} \sin\left(2\omega^i_{50} t\right) + B^i_{100} \cos\left(2\omega^i_{50} t\right) \\ & + c^i_0 + c^i_1 \cdot t + c^i_2 \cdot t^2 + c^i_3 \cdot t^3 + c^i_4 \cdot t^4 + c^i_5 \cdot t^5 + c^i_6 \cdot t^6. \end{aligned} \tag{6.19}$$

The polynomial terms have been increased to 7th order, and terms fitting the 50 Hz and resulting 100 Hz harmonic are also fitted. The increased polynomial order of the background fit parameters result in lowered low frequency noise.

The extended background fit model results in lower χ^2 values, and given that the measurement noise is determined by setting the mean of the χ^2 values of the sub-cuts over the number of d.o.f. to 1, this also results in lower measurement noise. This in turn lowers the errors on the fit parameters determined by the χ^2 minimization, which in the end delivers lower phase noise. The spread of χ^2 values is reduced, see Figures 6.11, 6.13 and 6.16, approaching a χ^2 distribution. Figure 6.17 plots the reduction of weighted phase fit error resulting from the extended background fit model, reduced roughly by the ratio of measurement errors used as input for the χ^2 minimization. As with χ^2 the spread is greatly reduced.

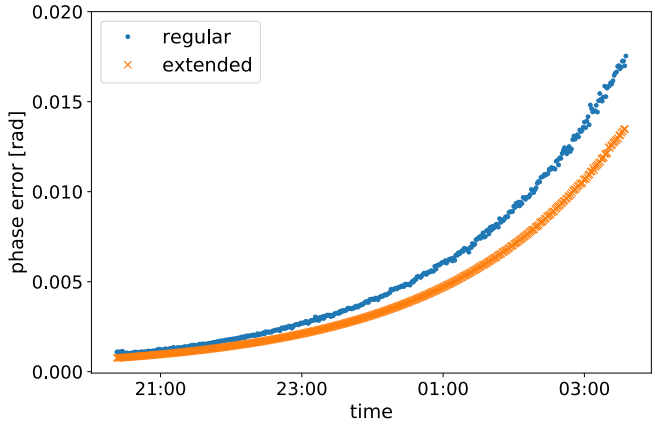

Figure 6.17.: Weighted phase difference $\Delta\varphi = \varphi_{\mathrm{Xe}} - \frac{\gamma_{\mathrm{Xe}}}{\gamma_{\mathrm{He}}}\varphi_{\mathrm{He}}$ fit error for the regular fit model and extended background fit model. The phase fit error is reduced by roughly the ratio of measurement errors used as input for the χ^2 minimization, 170 fT/131 fT ≈ 1.3. Data from run L20170328_202227.

For all fits a Gaussian distribution of errors is assumed, however a re-sampling technique such as bootstrapping can be employed such that the pdf is acquired from the data and the confidence levels on the fit parameters are thus reflective of the data.

The correlations between fit parameters are shown in Tables 6.3 and 6.4 for the old and new fit models, respectively. Important is that the correlations between the frequencies and amplitudes of the precession signals and additional background terms in the fit model do not increase appreciatively, since this introduces errors in the phase determination. From the tables it is clear that the polynomial terms have high correlation among themselves, as expected. The only increase in correlations between the frequency and amplitudes and the background fit terms are with the 6th and 7th order terms of the polynomial.

Table 6.3.: Correlation matrix of the regular fit model. The fit function is given in Eq. 6.1. *Green* signifies minimal correlation whereas *red* indicates maximal correlation.

	ω_{Xe}	ω_{He}	A_{Xe}	B_{Xe}	A_{He}	B_{He}	c_0	c_1
ω_{Xe}	1.00	0.02	0.01	0.01	-0.01	0.01	0.02	0.03
ω_{He}	0.02	1.00	-0.01	0.00	0.00	0.00	0.00	0.02
A_{Xe}	0.01	-0.01	1.00	-0.00	-0.00	0.00	-0.00	0.03
B_{Xe}	0.01	0.00	-0.00	1.00	0.00	-0.01	0.01	0.00
A_{He}	-0.01	0.00	-0.00	0.00	1.00	-0.00	0.00	-0.01
B_{He}	0.01	0.00	0.00	-0.01	-0.00	1.00	-0.01	-0.00
c_0	0.02	0.00	-0.00	0.01	0.00	-0.01	1.00	0.00
c_1	0.03	0.02	0.03	0.00	-0.01	-0.00	0.00	1.00

Table 6.4.: Correlation matrix of the new fit model. The only parameters with significant correlation are the even and odd coefficients of the polynomial background, which is inherent to a polynomial. The fit function is given in Eq. 6.19. *Green* signifies minimal correlation whereas *red* indicates maximal correlation.

	ω_{Xe}	ω_{He}	ω_{50}	A_{Xe}	B_{Xe}	A_{He}	B_{He}	A_{50}	B_{50}	A_{100}	B_{100}	c_0	c_1	c_2	c_3	c_4	c_5	c_6
ω_{Xe}	1.00	0.03	0.00	0.01	0.01	-0.01	0.00	0.00	0.00	0.00	0.00	-0.02	0.01	0.05	-0.02	-0.06	0.03	0.08
ω_{He}	0.03	1.00	0.00	-0.01	0.00	0.00	0.00	0.00	0.00	-0.00	0.00	-0.00	0.02	0.01	-0.03	-0.01	0.04	0.01
ω_{50}	0.00	0.00	1.00	0.00	-0.00	0.00	0.00	-0.02	-0.07	0.03	-0.08	0.00	0.00	-0.01	-0.00	0.01	0.00	-0.01
A_{Xe}	0.01	-0.01	0.00	1.00	-0.00	-0.00	0.00	-0.00	-0.00	-0.00	-0.00	0.00	0.04	-0.00	-0.06	0.00	0.07	-0.00
B_{Xe}	0.01	0.00	-0.00	-0.00	1.00	0.00	-0.01	0.00	-0.00	0.00	-0.00	-0.00	0.00	0.01	-0.00	-0.01	0.01	0.02
A_{He}	-0.01	0.00	0.00	-0.00	0.00	1.00	-0.00	0.00	0.00	0.00	0.00	-0.00	-0.01	0.00	0.01	-0.00	-0.01	0.00
B_{He}	0.00	0.00	0.00	0.00	-0.01	-0.00	1.00	-0.00	0.00	-0.00	0.00	0.01	-0.00	-0.02	0.00	0.02	-0.00	-0.03
A_{50}	0.00	0.00	-0.02	-0.00	0.00	0.00	-0.00	1.00	0.00	-0.00	0.00	-0.00	0.00	0.00	-0.00	-0.00	0.01	0.00
B_{50}	0.00	0.00	-0.07	-0.00	-0.00	0.00	0.00	0.00	1.00	-0.00	0.01	0.00	0.00	-0.00	-0.00	0.00	0.00	-0.00
A_{100}	0.00	-0.00	0.03	-0.00	0.00	0.00	-0.00	-0.00	-0.00	1.00	-0.00	-0.00	0.00	0.00	-0.00	-0.00	0.00	0.00
B_{100}	0.00	0.00	-0.08	-0.00	-0.00	0.00	0.00	0.00	0.01	-0.00	1.00	0.00	0.00	-0.00	-0.00	0.00	0.00	-0.00
c_0	-0.02	-0.00	0.00	0.00	-0.00	-0.00	0.01	-0.00	0.00	-0.00	0.00	1.00	-0.00	-0.75	0.00	0.60	-0.00	-0.51
c_1	0.01	0.02	0.00	0.04	0.00	-0.01	-0.00	0.00	0.00	0.00	0.00	-0.00	1.00	0.00	-0.92	-0.01	0.82	0.01
c_2	0.05	0.01	-0.01	-0.00	0.01	0.00	-0.02	0.00	-0.00	0.00	-0.00	-0.75	0.00	1.00	-0.01	-0.96	0.01	0.90
c_3	-0.02	-0.03	-0.00	-0.06	-0.00	0.01	0.00	-0.00	-0.00	-0.00	-0.00	0.00	-0.92	-0.01	1.00	0.01	-0.98	-0.01
c_4	-0.06	-0.01	0.01	0.00	-0.01	-0.00	0.02	-0.00	0.00	-0.00	0.00	0.60	-0.01	-0.96	0.01	1.00	-0.01	-0.98
c_5	0.03	0.04	0.00	0.07	0.01	-0.01	-0.00	0.01	0.00	0.00	0.00	-0.00	0.82	0.01	-0.98	-0.01	1.00	0.01
c_6	0.08	0.01	-0.01	-0.00	0.02	0.00	-0.03	0.00	-0.00	0.00	-0.00	-0.51	0.01	0.90	-0.01	-0.98	0.01	1.00

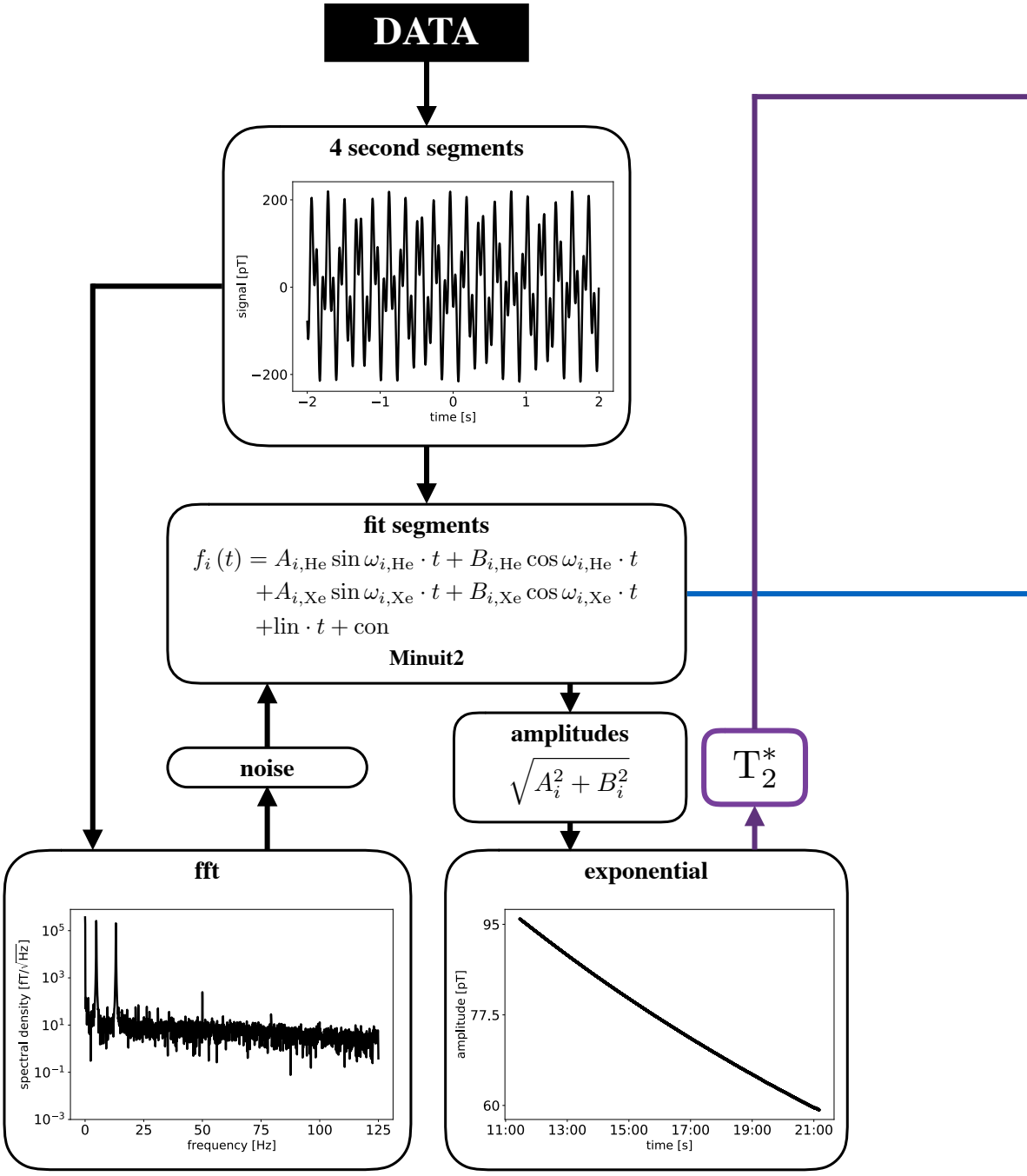

Figure 6.18.: Overview of the data analysis procedure starting from the SQUID gradiometer data to the weighted phase fit.

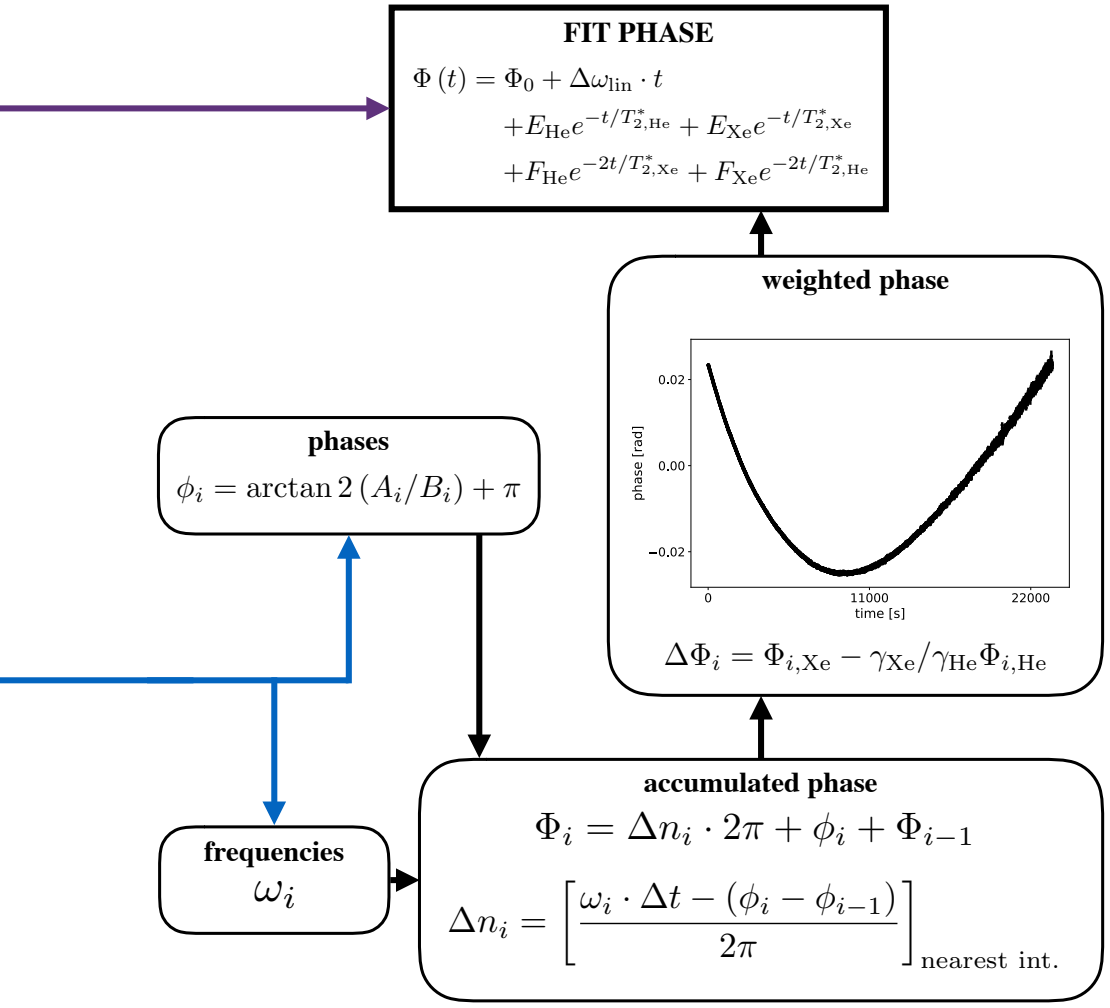
FIT PHASE
$\Phi(t) = \Phi_0 + \Delta\omega_{\mathrm{lin}} \cdot t$
$+E_{\mathrm{He}} e^{-t/T^*_{2,\mathrm{He}}} + E_{\mathrm{Xe}} e^{-t/T^*_{2,\mathrm{Xe}}}$
$+F_{\mathrm{He}} e^{-2t/T^*_{2,\mathrm{Xe}}} + F_{\mathrm{Xe}} e^{-2t/T^*_{2,\mathrm{He}}}$
weighted phase
0.02
0.00
−0.02
phase [rad]
0
11000
22000
time [s]
$\Delta\Phi_i = \Phi_{i,\mathrm{Xe}} - \gamma_{\mathrm{Xe}}/\gamma_{\mathrm{He}} \Phi_{i,\mathrm{He}}$
phases
$\phi_i = \arctan 2\,(A_i/B_i) + \pi$
frequencies
ω_i
accumulated phase
$\Phi_i = \Delta n_i \cdot 2\pi + \phi_i + \Phi_{i-1}$
$\Delta n_i = \left[\frac{\omega_i \cdot \Delta t - (\phi_i - \phi_{i-1})}{2\pi} \right]_{\text{nearest int.}}$

7. Results

Here the results of the analysis of the EDM precession measurements are compiled and discussed. The analysis techniques employed are described in Chapter 6. Based on this an outlook for future possible work will be given.

7.1. Analysis of EDM runs

The EDM limit was extracted from six runs performed in Jülich in July 2017, with run parameters as listed in Table 7.1. The applied electric field for all runs was 800 V/cm and the polarity switching time was varied between runs from 6000 s to 9000 s.

The fit procedure as described in Sections 6.1 and 6.3 is applied to the datasets, with the noise, range and electric field switching as described in Table 7.1.

The Figures shown in this section are from one measurement, `L20170719_220808`. These same figures for the other EDM measurements are shown in Appendix E. In Figure 7.1 the weighted phase (see Eq. 6.8) is shown, with the linear term subtracted. The remaining parabolic structure is a result of the Bloch Siegert shift (Sec. 5.4.1). Figures 7.2 and 7.3 show the residuals and normalized residuals, respectively, of the fit model to the weighted phase difference. For a statistically correct fit the residuals would be Gaussian distributed around zero with $\sigma = 1$. Some structure is visible in the normalized residuals but the origin of this structure has not yet been identified.

7.1.1. Allan Variance

The Allan Variance is a method to study the time stability of a phase or frequency signal due to noise processes [81, 82]. The classical method for calculating the variance does not converge for most common types of noise, whereas with the Allan Variance it is possible to distinguish between most common noise types.

A sample is split into S sections with each section consisting of n data points. Then

$$\bar{y}_s = \frac{1}{n} \sum_{j=n\cdot s}^{(n+1)s} y_j \tag{7.1}$$

is the sth average over the sample, corresponding to an average over $\tau = n \cdot \Delta t$, where s

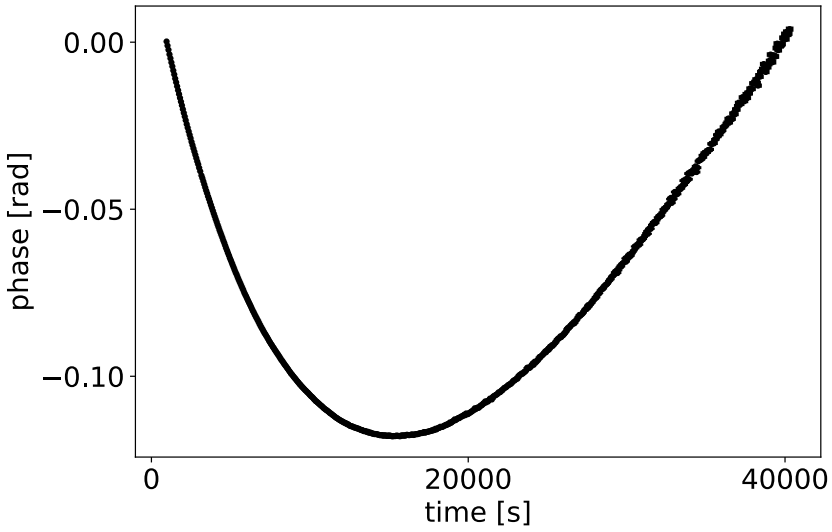

Figure 7.1.: Weighted phase difference for measurement L20170719_220808 with the linear term subtracted.

is the section number and y_j is the jth sample point. The Allan Variance is defined as

$$\sigma_y^2(\tau) = \frac{1}{2}\langle(\bar{y}_{s+1} - \bar{y}_s)^2\rangle, \tag{7.2}$$

resulting in an estimator

$$\sigma_y^2(\tau) = \frac{1}{2(S-1)}\sum_{s=0}^{S-2}(\bar{y}_{s+1} - \bar{y}_s)^2\,. \tag{7.3}$$

The Allan Standard Deviation is given by the square root of the Allan Variance, $\sigma_y(\tau)$.

Figures 7.4 and 7.5 show the Allan standard deviation of the phase and frequency, respectively. The phase ASD is calculated from the phase residuals of the fit model, shown in Figure 7.1 for the EDM measurements, with

$$\sigma_\Phi(\tau) = \sqrt{\frac{1}{2(S-1)}\sum_{s=0}^{S-2}\left(\bar{\Phi}_{s+1} - \bar{\Phi}_s\right)^2}. \tag{7.4}$$

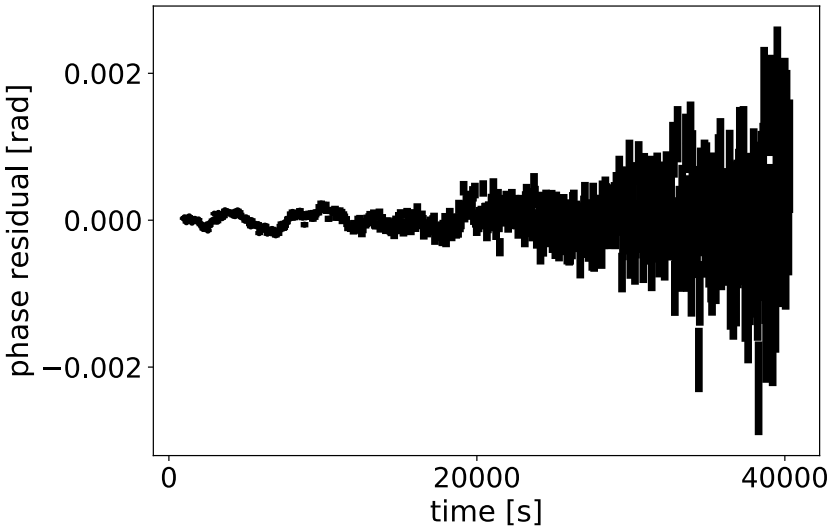

Figure 7.2.: Residuals of the weighted phase difference after applying the fit model from Eq. 6.15 to the data from measurement L20170719_220808.

The frequency ASD is calculated from the phase residuals divided by τ

$$\sigma_\omega(\tau) = \sigma_\Phi(\tau)/\tau. \tag{7.5}$$

For white noise $\sigma_\phi(\tau) \propto \tau^{-1/2}$ and $\sigma_\omega(\tau) \propto \tau^{-3/2}$. For the first ∼500 seconds the phase and frequency ASDs decreases proportional to these relations, after which it deviates from pure white noise. This indicates the fit model used to extract the phases and subsequently fit a model to the phase does not completely describe the data for longer timescales.

7.1.2. Extracted EDM

The resulting extracted ^{129}Xe EDM values are given in Tables 7.2. Table 7.2 shows the extracted values for the fit model given in Eq. 6.15. The values are also shown in Figure 7.7, together with a mean EDM value from all runs. From all six runs a *preliminary* value for the EDM on ^{129}Xe

$$d_{\mathrm{Xe}} = (-1.6 \pm 0.9) \times 10^{-27}\ e\mathrm{cm} \tag{7.6}$$

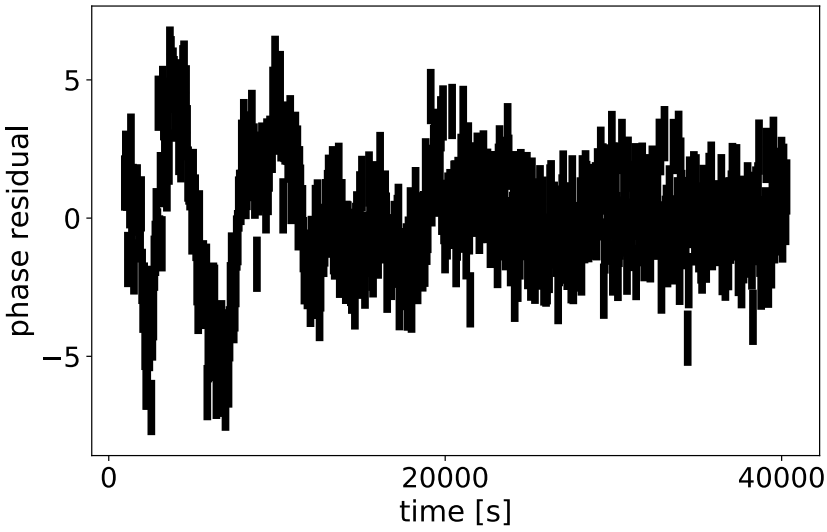

Figure 7.3.: Normalized residuals of the weighted phase difference after applying the fit model from Eq. 6.15 to measurement L20170719_220808. The residuals are divided by the phase error to facilitate detection of structures. A correct fit would result in normalized residuals distributed Gaussian around zero with $\sigma = 1$.

has been extracted. This corresponds to an upper limit of

$$|d_{\mathrm{Xe}}| < 3.1 \times 10^{-27}\ e\mathrm{cm}\ (90\%\ \mathrm{C.L.}), \tag{7.7}$$

obtained with the Feldman-Cousins method for constructing upper limits [83, 84], assuming a folded normal distribution.

From the six analyzed runs the last run (#6, L20170720_224608) deviates most from all other extracted EDMs. Upon further inspection it was found that the fit for this run has large correlations, approaching unity for some parameter combinations. The large correlations cause difficulty for the fit procedure to accurately find the best parameter estimates for the given fit model.

Most of the uncertainty is dominated by run #4, L20170719_220808. The last four runs, including run #4, have comparable SNR and T_2^* for both He and Xe. The major difference between these four runs is the measurement time, which is maximal for run #4. Run #5 has the second longest measurement time, but this alone is not sufficient

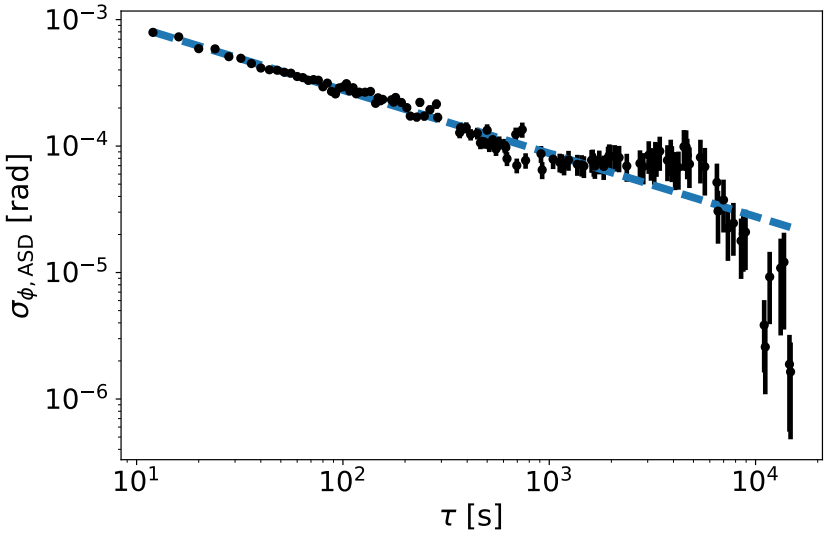

Figure 7.4.: Allan variance of the frequency for measurement of the phase L20170719_220808.

to explain the difference in uncertainty between run #4 and #5. The ASD Figures E.4 and E.5 in Appendix E show that run #4 has less deviation from white noise than run #5. This, in combination with the longer measurement time, could explain why run #4 has smaller uncertainty than run #5.

The consistency of the phase fit model can be checked by increasing the start time of the fit, essentially cutting of the first part of the data for each measurement run. The decrease in the number of data points would cause a decrease in fit sensitivity, and thus an increase in the sigma of the extracted EDM, but for a consistent fit the extracted EDMs should lie within a few sigma of each other.

For each individual cut time (the amount of time to cut away from the beginning of the measurement data) the fit model was fitted simultaneously to each measurement run, resulting in one extracted EDM for each cut time. For a cut time of zero seconds this leads to the result found by combining all individual fits, as is expected.

The results are shown in Figure 7.6, where a clear structure is visible, instead of the expected few sigma variation around the extracted value for a cut time of zero seconds. The cause of this structure is currently still being investigated and makes the extracted values shown in Eqs. 7.6 and 7.7 *preliminary* values.

Table 7.1.: Parameters for the EDM measurements. Noise indicates the measurement noise used for the fit procedure. nStart and nStop are the start and stop subcuts which the analysis was run over. E is the electric field strength and polarity indicates which start polarity was applied over the fiducial volume. tStart signifies the time the electric field was applied and tSwitch is the timescales for which the polarity was switched; the first always half a period. $T_{2,He}$, $T_{2,Xe}$ are the transverse relaxation times of helium and xenon during the measurement and A_{He}, A_{Xe} are the helium and xenon signal amplitudes at the start of the measurement.

	L20170718_120015	L20170718_195555	L20170719_151640	L20170719_220808	L20170720_112748	L20170720_224608
noise [fT]	163	150	173	132	143	149
nStart	1	1	1000	232	825	1500
nStop	5743	4500	5866	10090	8724	6235
E [v/cm]	800	800	800	800	800	800
polarity	-	-	-	+	+	-
tStart	12:10	20:02	15:32	22:20	11:42	23:02
tSwitch [s]	4000; 8000	3000; 6000	3000; 6000	4500; 9000	4500; 9000	4500; 9000
p_{He} [mbar]	12.1	25	45.2	19.7	26.6	31
p_{Xe} [mbar]	24.3	53	95.8	100	90.7	102.8
$p_{^4He}$ [mbar]	48.6	44	-	-	-	-
p_{SF^6} [mbar]	4.2	5	-	-	-	-
$T_{2,He}[h]$	4.7	3.2	18.8	20.8	20.0	18.0
$T_{2,Xe}[h]$	2.0	1.6	2.9	2.8	2.9	2.8
$A_{He}[pT]$	30.2	59.1	128.5	77.4	96.2	104.7
$A_{Xe}[pT]$	21.8	52.6	113.5	101.9	123.6	117.0

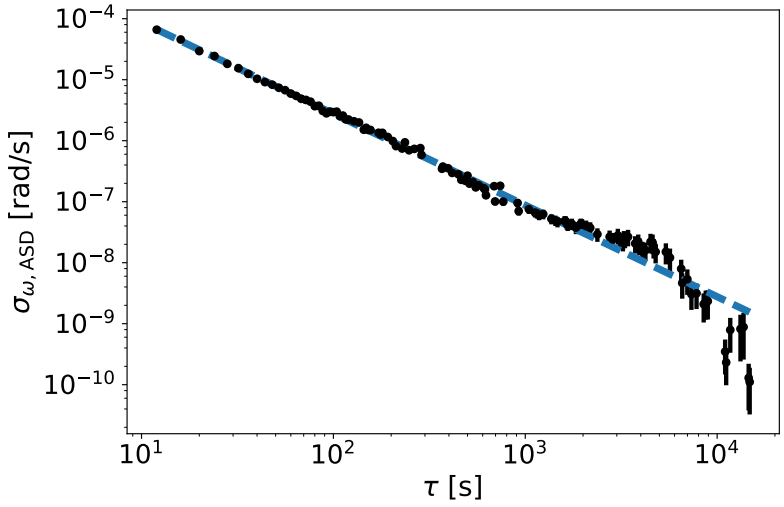

Figure 7.5.: Allan variance of the frequency for measurement L20170719_220808.

7.2. Outlook

In the coming years the goal is to improve the sensitivity of the experiment in order to achieve an improved limit on the EDM of ^{129}Xe. The sensitivity of an EDM measurement is given by the CRLB (see Eq. 2.43)

$$\sigma_{\mathrm{EDM}} \geq \frac{\sqrt{3}h}{2\pi \mathrm{SNR} E \sqrt{f_{\mathrm{BW}}} T^{3/2}} \sqrt{C(T; T_2^*)}. \tag{7.8}$$

The applied electric field E factors linearly into the EDM sensitivity. The applied field was 800 V/cm for the measurements discussed in this chapter. The challenge in increasing the applied electric field is minimizing the leakage currents over the cell, which generate magnetic field gradients disturbing the spin precession measurement.

The signal-to-noise ratio *SNR* also factors linearly into the sensitivity, and can be increased by decreasing the noise or increasing the precession signal. In Chapter 6 the presence of small signals at several frequencies is discussed, including those shrouded by noise at frequencies larger than 34 Hz. Currently designs for a new multi-layer magnetic shielding are being made and scouting for a new location is underway, which should reduce the noise over all frequencies. An alternative to shielding the signals is understanding where they come from, allowing them to be taken into account in the fit procedure.

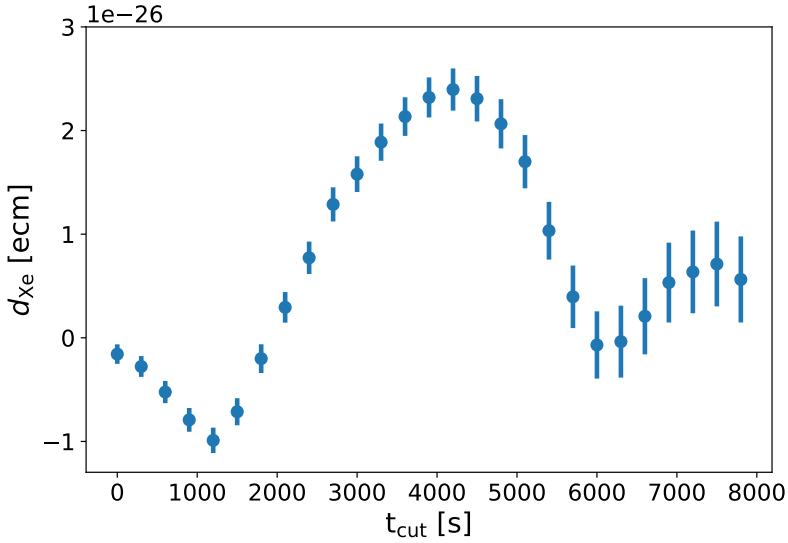

Figure 7.6.: Extracted EDM for a simultaneous fit to each measurement for varying cut times, the amount of time to cut away from the beginning of the measurement data. The sensitivity decreases with more data cut away, but the extracted EDM values should lie within a few sigma of each other for a consistent fit.

The sensitivity of the measurement scales as $1/T^{3/2}$. To increase the measurement time T_2^* has to be improved. The main limitation is T_2^* for ^{129}Xe, which was for the measurements described in this Chapter between 2 h and 3 h. Section 2.3 describes the mechanisms for spin relaxation. A decrease of magnetic field gradients or of wall relaxation improve T_2^* considerably. The magnetic field gradients should be reduced by the new multi-layer magnetic shielding.

The final improvement in sensitivity comes down to statistics. Repeating a measurement N times reduces the total sensitivity by $\sqrt{N}$. Taking into account that all other improvements mentioned here scale faster than $1/\sqrt{}$ it is recommended to try and achieve any other sensitivity improvements before resorting to many repeated EDM measurements in order to achieve a smaller sensitivity.

Table 7.2.: Extracted ^{129}Xe EDM values employing the fit procedure described in Sec. 6.1.2.

run #	measurement	d_{Xe} [10^{-28} $e$cm]	$\sigma_{d\mathrm{Xe}}$ [10^{-28} $e$cm]
1	L20170718_120015	-31.54	99.71
2	L20170718_195555	-70.83	53.75
3	L20170719_151640	-10.67	31.79
4	L20170719_220808	-16.21	11.38
5	L20170720_112748	16.37	22.87
6	L20170720_224608	-210.81	68.255

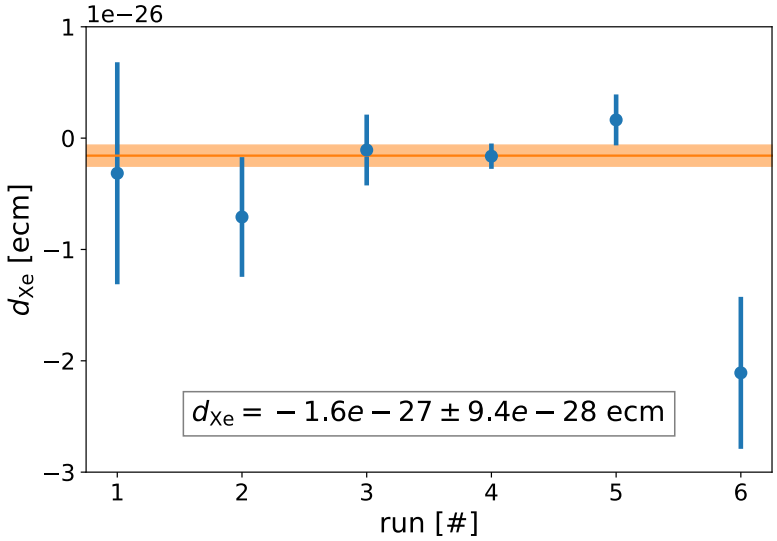

Figure 7.7.: Overview of the extracted ^{129}Xe values, given in Table 7.2. The mean $\mathrm{d_{Xe}}\left(-1.6 \times 10^{-27} \pm 9.4 \times 10^{-28}\right)$ $e$cm. Runs 1 and 2 have significantly larger σ as a result of the factor 2 to 3 lower SNR compared to other runs, in addition to smaller $\mathrm{T_2^*}$. The orange line indicates the mean EDM over all runs.

8. Summary

The Standard Model (SM) of particle physics describes all known fundamental forces in nature, with the exception of gravity. Together with General Relativity (GR), which describes gravity, it provides a framework for describing all experimental results to date and it provides for accurate predictions. The Standard Model and General Relativity have been tested to high precision on a wide range of energy scales. The fundamental forces are the electromagnetic, weak and strong interactions in the Standard Model, and gravity in General Relativity. The Standard Model also classifies all known elementary particles. The elementary particles are split into two distinct groups, 24 fundamental fermions and 13 bosons.

Fermions are half-integer spin particles that follow Fermi-Dirac statistics, in which no identical particles may occupy the same state. The 24 fundamental fermions are grouped into three generations of leptons (electron, muon and tau) and three generations of quarks (up/down, strange/charm and top/bottom). Bosons are integer spin particles that follow Bose-Einstein statistics, in which identical particles can occupy the same state. The 13 bosons fall into two groups, with 12 force-carrier gauge bosons and 1 scaler boson. The 12 gauge bosons are the photon, for the electromagnetic interaction, the Z^0 and $W^{\pm}$ bosons for the weak interaction and 8 gluons for the strong interaction. The scaler boson is the Higgs boson, which gives mass to fundamental particles.

From several observations it has been derived that the Standard Model and General Relativity together are not sufficient to explain certain findings, such as the matter-antimatter asymmetry found in the universe. In the Big Bang matter and antimatter are assumed to have been created in equal quantities. The cosmic microwave background is a relic of annihilations of matter and antimatter in photons and neutrinos. Only a small portion of matter $\left(10^{-9}\right)$ is still remaining today. The search for reasons for this assymmetry are the driving force between many ongoing projects in physics and astronomy. This search is mainly concentrated in two areas: high-energy physics at colliders, such as the LHC at CERN, or high-precision experiments at low energy, such as in atomic systems and astronomy.

The goal of the MIXed experiment is to measure the permanent electric dipole moment (EDM) of ^{129}Xe. An EDM quantifies the separation of charges in a system. A fundamental particle with an EDM implies a breakdown of parity (P) and time (T) symmetries, which together with charge conjugation symmetry form the CPT symmetry which is a fundamental symmetry of physics laws. In order for CPT symmetry to hold, a breakdown of P and T symmetries implies that charge-parity (CP) symmetry must also be broken. Additional

sources beyond the already established ones for CP violation in the SM could give rise to a sufficiently large imbalance between matter and antimatter in the universe.

Spin Precession

MIXed measures the EDM through differential free spin precession of ^{3}He and ^{129}Xe, co-occupying the same fiducial volume. Spin precession is the precession of particles around their spin. Spin is the intrinsic angular momentum of a particle, which is aligned along the spin axis. Spin precession occurs when, for example, a particle has a magnetic moment and is placed in a magnetic field. The magnetic moment is aligned along the spin axis, and exerts a torque on the particle when placed in a magnetic field, inducing a precession of the spin. Analogously a particle with an EDM experiences a torque when placed in an electric field, again inducing spin precession.

For an EDM measurement of ^{129}Xe the atoms are polarized and placed in a glass cell in a magnetic and electric field. The total induced spin precession is a sum of the magnetic moment and electric dipole moment spin precession. To extract the EDM the magnetic field needs to be known precisely in order to decouple the spin precession in electric and magnetic parts. During a measurement the magnetic field in the environment of the investigated sample fluctuates, which may severely limit the sensitivity to an EDM. To that end ^{3}He is employed as a co-magnetometer, tracking the magnetic field in-situ in real-time. The EDM of an atom scales with mass, hence the helium EDM can for all intents and purposes be considered to be negligable with respect to the xenon EDM. The spin precession of ^{3}He is to first order only dependent on the magnetic field, and can be employed to zero the magnetic field in subsequent analysis.

Even though a ^{3}He co-magnetometer is employed to track the magnetic field during a measurement, care has to be taken to minimize magnetic field fluctuations and maximize the magnetic field homogeneity, as well as shield stray magnetic fields. The sensitivity of a ^{129}Xe EDM follows the Cramer-Rao Lower Bound and is given by

$$\sigma_{\mathrm{EDM}} \geq \frac{\sqrt{3}h}{2\pi \mathrm{SNR} E \sqrt{f_{\mathrm{BW}}} T^{3/2}} \sqrt{C(T; T_2^*)}, \tag{8.1}$$

where C is a term accounting for the exponential decay of the signal, SNR is the signal-to-noise ratio, E the electric field strength, f_{BW} is the Nyquist frequency, T is the total measurement time and T_2^* is the transverse magnetic decay time constant. T_2^* is mainly limited by the magnetic field homogeneity, and determines the total feasible measurement time T.

To that end a magnetically shielded room is employed to minimize external magnetic fields. For additional shielding the glass cell with polarized atoms is placed inside an additional layer of shielding, a μ-metal cylinder placed in the center of the shielded room. This room is situated at the FZ Jülich, where the measurements were performed. Both the

Figure 8.1.: Photograph of the coil systems for the magnetic field holding field and gradient compensation. The outer metal cylinder is the cylindrical μ-metal shield. Photograph by S. Zimmer.

magnetically shielded room and the cylinder are constructed from μ-metal, a nickel-iron alloy with high magnetic permeability, trapping magnetic field lines inside the material, bending them around the enclosed volume. For additional homogeinity special coil systems were designed to compensate remaining magnetic field gradients in and around the fiducial volume. T_2^* depends directly on the magnetic field gradients, allowing for an automated routine employing the coil systems to minimize the magnetic field gradients. The coil systems and magnetic shielding cylinder are shown in Figure 8.1. In addition to shielding external magnetic field, care has to be take in order to minimize magnetic fields and noise emanating from equipment placed inside the magnetically shielded chamber in order to perform the measurement. To that end all materials close to the glass cell are non-magnetic, electronics inside the chamber are battery powered and a serial fiber-optic data connection is used to control electronics inside the chamber.

A typical measurement proceeds by filling the glass cell inside the chamber with polarized ^{3}He and ^{129}Xe. The precession due to a non-zero EDM is extremely small, requiring a magnetic field to maintain polarization during a measurement, the so-called magnetic holding field. An electric field which is applied parallel or anti-parallel along the magnetic field, which is periodically reversed in orientation. The precession frequency is modulated with a frequency corresponding to the electric field reversals by a non-zero ^{129}Xe EDM. Measuring this modulation of the frequency is achieved by tracking the phase during an entire spin-precession measurement, after which the magnetic field is zeroed by use of

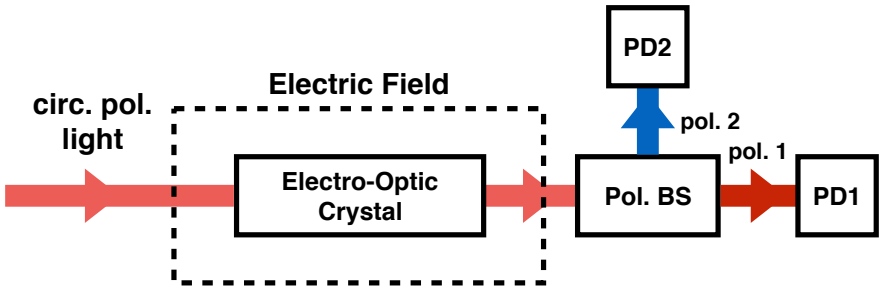

Figure 8.2.: Schematic overview of an electro-optic electric field sensor. Circular polarized light comes from a LED folowed by a linear polarizer and a quarter wave plate. The light enters the electro-optic crystal, which rotates the light polarization as a function of the applied electric field strength. The amount of polarization rotation is measured using a polarizing beamsplitter (the analyzer) in combination with two photodiodes (PD), which measure the intensities of the two light beams with orthogonal polarization.

^{3}He co-magnetometry. From this an EDM limit can be extracted.

Electric Field Measurement

The fiducial volume in the MIXed experiment is completely enclosed by magnetic field coil systems and magnetic shielding. The electric field is generated across the fiducial volume with two silicon wafers connected to a high voltage power supply residing outside of the magnetically shielded chamber. In order to verify the presence of an electric field inside the glass cell, an electro-optical device was developed with which the field could be measured and monitored sufficiently accurate.

In electro-optic crystals the polarization of light passing through the crystal depends on the applied electric field. This change in polarization can be determined by employing a polarizing beamsplitter as an analyzer and measuring the intensity of the two orthogonal components.

Figure 8.2 shows a schematic overview of the setup employed to measure the electric field inside a glass cell. From measurements with different gas mixtures and pressures, mimicking conditions in the EDM measurements, a decay constant of the electric field inside the glass cell of at least 20 h was found, sufficient for our purposes.

An electric field sensor employing an electro-optic crystal is also suitable for monitoring electric field in-situ during data taking when searching for an EDM. The optical components of our newly developed device, including the crystal and all components as well as the materials to mount them, are non-magnetic and generate no magnetic noise. Fiber

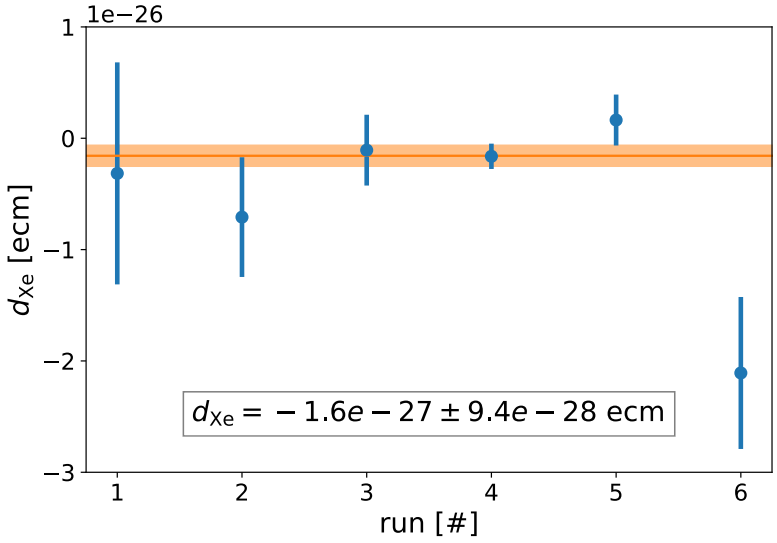

Figure 8.3.: The values extracted for an EDM on ^{129}Xe as given in Table 7.2. The mean $d_{Xe} = \left(-1.6 \times 10^{-27} \pm 9.4 \times 10^{-28}\right)$ $e$cm. The orange line indicates the mean EDM over all runs.

coupling the sensor to the light source and light detectors allows for placing the sensor next to the fiducial volume and tracking the electric field in real-time.

Results and Outlook

The EDM limit obtained in this thesis is extracted from six measurement runs performed in Jülich in July 2017. The applied electric field for all runs was 800 V/cm. The polarity switching time and the start polarity were varied between runs.

From this series of measurements of several hours length each, a *preliminary* value for the EDM of ^{129}Xe of $d_{Xe} = (-1.6 \pm 0.9) \times 10^{-27}$ $e$cm is extracted. This value corresponds to an upper limit of $|d_{Xe}| < 3.1 \times 10^{-27}$ $e$cm (90% C.L.). The extracted EDMs for each measurement run are shown in Figure 8.3.

In the coming years the goal is to improve the sensitivity of the experiment in order to achieve an improved limit on the EDM of ^{129}Xe. Several of the methods to improve the sensitivity include improving the signal-to-noise ratio, increasing the measurement time, taking more measurements to improve the statistics and finally gaining a better understanding of the noise present in the current measurements.

9. Nederlandse Samenvatting

Het standaardmodel van de deeltjesfysica beschrijft alle bekende fundamentele krachten in de natuur, met uitzondering van zwaartekracht, met hoge precisie. Samen met algemene relativiteitstheorie, de theorie van de zwaartekracht, biedt het een raamwerk voor het beschrijven van alle experimentele resultaten tot op heden en zorgt het voor nauwkeurige voorspellingen. Het standaardmodel en algemene relativiteitstheorie zijn met hoge precisie getest over een breed scala aan energieschalen. De fundamentele krachten zijn de elektromagnetische kracht, de zwakke kracht en de sterke kernkracht in het standaardmodel, en zwaartekracht in algemene relativiteitstheorie. Het standaardmodel classificeert ook alle bekende elementaire deeltjes. De elementaire deeltjes kunnen worden onderscheiden in twee groepen, 24 fundamentele fermionen en 13 bosonen.

De 24 fundamentele fermionen zijn gegroepeerd in drie generaties leptonen (elektron, muon en tau) en drie generaties quarks (up/down, strange/charm and top/bottom). De 13 bosonen kunnen in twee groepen worden ondergebracht, één met 12 ijkbosonen die de fundamentele krachten van het standaardmodel dragen en het Higgs boson. De ijkbosonen zijn het foton voor de elektromagnetische kracht, de $W^{\pm}$ en Z^0 bosonen voor de zwakke kernkracht en 8 gluonen voor de sterke kernkracht. Het Higgsboson tenslotte, geeft massa aan alle fundamentele deeltjes.

Uit verschillende observaties is afgeleid dat het standaardmodel en algemene relativiteitstheorie samen niet afdoende zijn om bepaalde bevindingen afdoende te verklaren, zoals de materie-antimaterie asymmetrie in het heelal. Aangenomen wordt dat tijdens de Oerknal een gelijke hoeveelheid materie en antimaterie geproduceerd werd. Hierna volgde meteen massa-annihilatie, waardoor er nog maar een fractie $\left(10^{-9}\right)$ van de oorspronkelijke materie is vandaag nog aanwezig. De zoektocht naar de oorzaak van deze assymmetrie is een van de drijvende krachten achter vele lopende onderzoeken in de natuurkunde en sterrenkunde. Deze zoektocht is voornamelijk geconcentreerd in twee gebieden: deeltjesfysica, zoals bij de LHC in CERN, of hoge precisie experimenten bij lage energie, in bijvoorbeeld atomaire systemen of sterrenkunde.

Het doel van het MIXed experiment is om een meting te doen van het permanente elektrische dipoolmoment (EDM) van ^{129}Xe. Een EDM is een maat voor de scheiding van ladingen in een systeem. Een fundamenteel deeltje met een EDM impliceert een schending van de pariteit (P) en tijd (T) symmetrieën, die samen met ladingsconjugatie symmetrie (C) de CPT-symmetrie vormen, een fundamentele symmetrie van de natuurkunde. Om CPT-symmetrie in stand te houden impliceert een schending van P en T symmetrieën dat de ladingspariteit symmetrie (CP) ook geschonden wordt. Aanvullende bronnen bui-

ten de reeds bestaande schendingen van CP symmetrie kunnen aanleiding geven tot een voldoende grote onbalans tussen materie en antimaterie in het universum.

Spin Precessie Meting

In het MIXed experiment wordt differentiële vrije spin precessie tussen ^{3}He en ^{129}Xe, in hetzelfde volume, gebruikt om het EDM te meten. Spin precessie is de precessie van deeltjes om hun spin. Spin is het intrinsieke impulsmoment van een deeltje, dat is uitgelijnd langs de spin as. Spin-precessie vindt bijvoorbeeld plaats wanneer een deeltje een magnetisch moment heeft en in een magnetisch veld wordt geplaatst. Het magnetisch moment is uitgelijnd langs de spin as en oefent een koppel uit op het deeltje wanneer het in een magnetisch veld word geplaatst, wat een precessie van de spin veroorzaakt. Analoog hieraan ondergaat een deeltje met een EDM een koppel wanneer het in een elektrisch veld wordt geplaatst, wat wederom een spin-precessie veroorzaakt.

Voor een EDM-meting van ^{129}Xe worden de atomen gepolariseerd en in een glazen cel in een magnetisch en elektrisch veld geplaatst. De totale spin-precessie is een som van de contributies van het magnetisch moment en het EDM. Om een EDM te extraheren moet het magnetisch veld nauwkeurig bekent zijn tijdens de meting om de spin-precessie te ontkoppelen in een een elekrsich en magnetisch deel. Gedurende een meting fluctueert het magnetisch veld in de omgeving van het onderzochte monster, wat de sensitiviteit voor een EDM kan belemmeren. Daartoe wordt ^{3}He gebruikt als co-magnetometer om het magnetisch veld in situ te volgen. Het EDM van een atoom schaalt met de massa, waardoor het helium EDM verwaarloosbaar is met betrekking tot het xenon EDM. De spin-precessie van ^{3}He is op eerste orde alleen afhankelijk van het magneetveld en kan worden gebruikt om het magneetveld te nullen in de analyse van de data.

Ondanks het gebruik van een ^{3}He co-magnetometer om het magneetveld to volgen tijdens een meting dienen de magneetveld fluctuaties en gradiënten geminimaliseerd te worden. De sensitiviteit voor een ^{129}Xe EDM schaalt volgens de Cramer-Rao ondergrens (CRLB)

$$\sigma_{\mathrm{EDM}} \geq \frac{\sqrt{3}h}{2\pi \mathrm{SNR} E \sqrt{f_{\mathrm{BW}}} T^{3/2}} \sqrt{C(T; T_2^*)}, \tag{9.1}$$

waar de C het exponentiële verval van het signaal beschrijft, SNR de signaal-ruis verhouding is, E het elektrisch veld, f_{BW} de Nyquist-frequentie, T de totale meettijd en T_2^* de magnetische spin relaxatie tijdsconstante. T_2^* is voornamelijk gelimiteerd door magneetveld gradiënten en bepaald de totaal haalbare meettijd T.

Daartoe wordt een magnetisch afgeschermde kamer gebruikt, geconstrueerd uit μ-metaal en alumium om externe magneetvelden te minimaliseren. μ-metaal is een nikkelijzerlegering met hoge magnetische permeabiliteit. Magneetveld lijnen worden binnen het μ-metaal opgesloten en om het ingesloten volume geleid, resulterend in afscherming van externe magneetvelden. De glazen cel met gepolariseerde atomen wordt voor extra

Figuur 9.1.: Foto van de spoelsystemen voor het magnetisch houdveld en gradiënten compensatie. De buitenste metalen cilinder is de cilindrische μ-metalen afscherming. Foto door S. Zimmer.

afscherming in een μ-metalen cilinder geplaatst in het midden van de magnetisch afgeschermde kamer. Deze kamer staat op het FZ in Jülich, waar de metingen worden uitgevoerd. Om het magneetveld nog homogener te maken zijn magneetveld spoelsystemen ontworpen om de resterende velden in en rondom het interactievolume te compenseren. T_2^* is direct afhankelijk van de magneetveld gradiënten, waardoor een automatisch routine mogelijk is om de magneetveld gradiënten te minimaliseren. De magneetveld spoelen en magnetische afscherm cilinder zijn zichtbaar in Figuur 9.1. Naast het afschermen van externe magneetvelden moet er zorgvuldig worden bekeken welke materialen binnen de afgeschermde kamer worden geplaatst, om magnetische ruis en magneetvelden te minimaliseren. Daartoe zijn alle materialen in de buurt van de glazen cel niet-magnetisch, wordt de elektronica binnen de afgeschermde kamer door batterijen aangedreven en zorgt een seriële glasvezel dataverbinding vor communicatie met de elektronica binnen de kamer.

Een typische meting vindt plaats door een glazen cell binnen de μ-metalen cilinder in het midden van de afgeschermde kamer te vullen met gepolariseerd ^{3}He en ^{129}Xe. De precessie ten gevolge van een EDM ongelijk aan nul is extreem klein, waardoor een magneetveld nodig is om polarisatie tijdens een meting te handhaven, het zogeheten houdveld. Een elektrisch veld dat parallel of anti-parallel wordt aangelegd langs het magneetveld wordt periodiek omgekeerd. De precessie frequentie wordt gemoduleerd met een frequentie die overeenkomt met de omkeringen van het elektrisch veld ten gevolge van

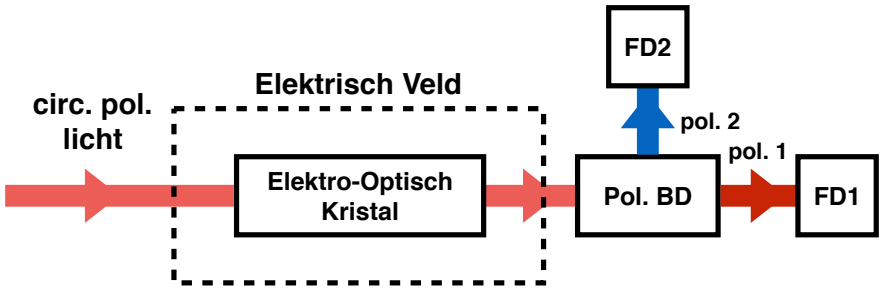

Figuur 9.2.: Schematisch overzicht van een electro-optische veldsensor. Circulair gepolariseerd licht komt van een LED, gevolgd door een lineaire polarisator en een kwart golfplaat. Het licht komt het electro-optische kristal binnen, dat lichpolarisatie roteert als functie van de toegepaste elektrische veldsterkte. De hoeveelheid rotatie wordt gemeten met behulp van een polariserende bundelsplitser in combinatie met twee fotodiodes (FD), die de intensiteit van de twee lichtbundels met orthogonale polarisatie meet.

een niet-nul ^{129}Xe EDM. Het meten van deze frequentie modulatie wordt bereikt door de fase tijdens een volledige spin-precessie meting te volgen, waarna het magneetveld wordt verwijderd met gebruik van ^{3}He co-magnetometrie. Hieruit kan een EDM limiet worden geëxtraheerd.

Elektrische Veld Meting

Het precessie volume in het MIXed experiment is volledig omsloten door magneetveld spoelsystemen en magnetische afscherming. Het elektrisch veld wordt gegenereerd over het precessie volume met twee silicium wafels verbonden met een hoogspanningsvoeding die zich buiten de magnetisch afgeschermde kamer bevindt. Om de aanwezigheid van een elektrisch veld binnen de glazen cel te verificiëren is een electro-optisch apparaat ontwikkeld waarmee het veld met voldoende precisie kan worden gemeten.

In elektro-optische kristallen is de polarisatie van licht dat door het kristal gaat afhankelijk van het aangelegde veld. Deze verandering van polarisatie kan worden bepaald door een polariserende bundelsplitser te gebruiken als analysator en de intensiteit van de twee orthogonale polarisatie componenten te meten.

In Figuur 9.2 wordt een schematisch overzicht gegeven van de gebruikte opstelling om het elektrisch veld binnen een glazen cel te meten. Uit metingen met verscheidene gasmengels en gasdrukken die de omstandigheden van de EDM metingen nabootsen volgt een vervalconstante van minsten 20 uur voor het veld binnen de glazen cel, voldoende

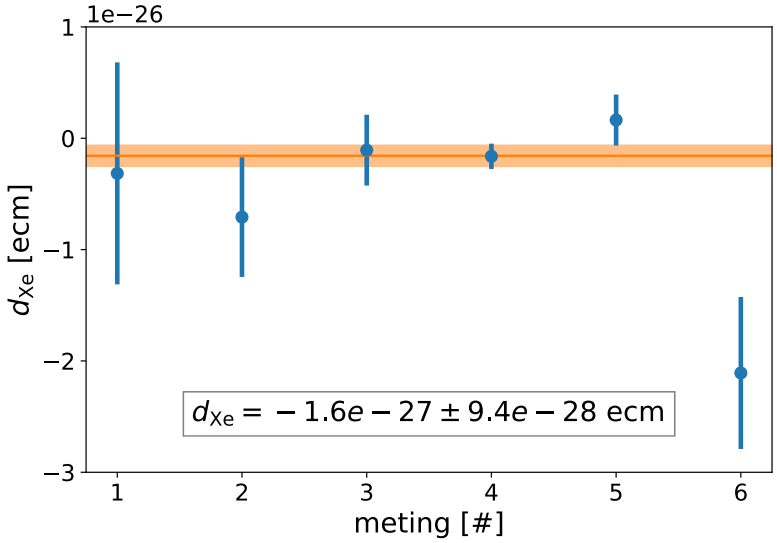

Figuur 9.3.: De geëxtraheerde EDM waardes voor ^{129}Xe als gegeven in Tabel 7.2. De gemiddelde $d_{Xe} = \left(-1.6 \times 10^{-27} \pm 9.4 \times 10^{-28}\right)$ $e$cm. De oranje lijn duidt de gemiddelde elektrische dipoolmoment waarde aan van alle metingen.

voor onze doeleinden.

Een elektrische veldsensor die een electro-optisch kristal gebruikt is ook geschikt voor het in-situ volgen van een elektrisch veld tijden het nemen van data voor een EDM meting. De optische componenten van ons ontwikkelde apparaat, inclusief het kristal en alle componenten om deze op te monteren, zijn niet-magnetisch en genereren weinig magnetisch ruis. Glasvezelkoppeling van de sensor aan de lichtbron en lichtdetectoren maakt het mogelijk om de sensor naast het precessie volume te plaatsen. De EDM limiet verkregen uit het onderzoek beschreven in dit proefschrift is ontleend aan zes metingen uitgevoerd in Jülich in juli 2017. Het aangelegde elektrische veld was 800 V/cm voor alle metingen. De elektrische veld polarisatieschakeltijd en startpolariteit werden gevarieerd tussen metingen.

Resultaten en Vooruitblik

Uit deze serie metingen, elk enkele uren lang, is een *voorlopige* waarde voor het EDM van ^{129}Xe, $d_{Xe} = (-1.6 \pm 0.9) \times 10^{-27}$ $e$cm, geëxtraheerd. Deze waarde komt overeen met een

bovenlimiet van $|d_{\mathrm{Xe}}| < 3.1 \times 10^{-27}$ $e$cm (90% vertrouwensniveau). De geëxtraheerde EDMs voor elke meting zijn te zien in Figuur 9.3.

De komende jaren is het doel om de sensitiviteit van het experiment te verhogen om een verbeterde limiet op het EDM van ^{129}Xe te verkrijgen. Enkele methoden voor het verhogen van de sensitiviteit zijn het verbeteren van de signaal-ruis verhouding, het verlengen van de meettijd, meer metingen doen om de statistiek te verbeteren en tenslotte een beter begrip te krijgen van de ruis die aanwezig is bij de huidige metingen.

A. Electro-Optic Crystals

In this section we collect basic properties of Electro-optic crystals such as they were employed as electric field measuring devices for DC fields.

A.1. Wave Propagation in Anisotropic Media

The polarization of a material expresses the density of permanent or induced electric dipole moments in a dielectric medium. In isotropic media, the polarization vector is parallel to the electric field vector, related by the susceptibility of the medium χ, a scaler in this case. In anisotropic media the polarization is dependent on the direction of the electric field vector. Thus, written in Einstein notation, the polarization vector is related to the electric field vector by the electric susceptibility tensor, χ_{ij} [56]

$$P_i = \epsilon_0 \chi_{ij} E_j, \quad i,j = 1,2,3 \tag{A.1}$$

where ϵ_0 is the permittivity of vacuum.

The susceptibility tensor is related to the permittivity tensor ϵ_{ij}

$$\epsilon_{ij} = \epsilon_0 \left(1 + \chi_{ij}\right). \tag{A.2}$$

The permittivity sensor is a second-rank tensor that can be represented geometrically by a quadratic surface:

$$\sum_{ij} \epsilon_{ij} x_i x_j. \tag{A.3}$$

With the electric impermeability tensor $\eta = \epsilon_0 \epsilon^{-1}$, this transforms to the index ellipsoid

$$\sum_{ij} \eta_{ij} x_i x_j = 1. \tag{A.4}$$

In the principal coordinates, the permittivity tensor, and thus also the impermeability tensor, are diagonal. Using the principal coordinate systems, the index ellipsoid becomes

$$\frac{x_1^2}{n_1^2} + \frac{x_2^2}{n_2^2} + \frac{x_3^2}{n_3^2} = 1, \tag{A.5}$$

where n_i are the refractive indices of the principal axes. Media can be classified into three different types using the principal axes

- Isotropic ($n_1 = n_2 = n_3$)
- Uniaxial ($n_1 = n_2 = n_0$, $n_3 = n_e$)
- Biaxial ($n_1 \neq n_2 \neq n_3$)

Propagation along principal axes has two distinct modes, namely polarization along a principal axis and polarization along an arbitrary direction.

With the polarization along a principal axis, the phase velocity is modified, but the polarization direction is not changed. These are the so-called normal modes of a crystal.

With an arbitrary polarization direction, the crystal acts as a wave retarder. An arbitrary polarization direction can be broken down into a super position of polarization on the two principal axes perpendicular to the propagation direction. For differing principal indices of refraction, the two components have differing phase velocities, causing a change in polarization. For example, for a wave propagating along x_3, the phase velocities are given by the refractive indices n_1 and n_2. The birefringence is the difference between the two indices of refraction, $n_2 - n_1$, and a measure of the retardance of a wave retarder.

For propagation in an arbitrary direction $\mathbf{u}$ the normal modes for a plane wave need to be determined. With

$$D_i = \epsilon_{ij} E_j \tag{A.6}$$

and the plane wave $\exp(-j\mathbf{j} \cdot \mathbf{k})$, where $\mathbf{k} = k\mathbf{u}$. Maxwell's equation reduce to [56]

$$\mathbf{k} \times \mathbf{H} = -\omega \mathbf{D}, \tag{A.7}$$

$$\mathbf{E} \times \mathbf{E} = \omega \mu_0 \mathbf{H}, \tag{A.8}$$

where $\mathbf{k}$ is the wavevector, ω the radian frequency of the light and μ is the permeability of the medium. Substituting A.7 into A.8 results in

$$\mathbf{k} \times (\mathbf{k} \times \mathbf{E}) + \omega^2 \mu \epsilon \mathbf{E} = 0. \tag{A.9}$$

From this equation the dispersion relation

$$\omega = \omega(k_1,\ k_2,\ k_3) \tag{A.10}$$

can be derived, an equation of a surface in $k_1,\ k_2,\ k_3$ space. The intersection of $\mathbf{u}$ with the $\mathbf{k}$-surface determines the normal mode. For each direction there are two intersections, corresponding to two normal modes [56].

An alternative representation of the problem can also be used

$$\mathbf{u} \times (\mathbf{u} \times \eta \mathbf{D}) + \frac{1}{n^2} \mathbf{D} = 0. \tag{A.11}$$

This is an eigenvalue problem (when $\mathbf{u}$ is filled in) where the eigenvectors are the normal modes of propagation, and the eigenvalues $1/n^2$ correspond to the indices of refraction along these two directions.

A.2. Electro-Optic Effect

In electro-optic media an electric field induces a change in the refractive indices, the so-called electro-optic effect. To describe the electro-optic effect with the index ellipsoid, the impermeability tensor, inverse of the relative permittivity tensor, is required (see also Eq. A.4)

$$\eta = \left(\frac{\epsilon}{\epsilon_0}\right)^{-1}. \tag{A.12}$$

Expanding the impermeability as a function of the electric field gives

$$\eta_{ij}(\mathbf{E}) = \eta_{ij}(0) + \left(\frac{\partial \eta_{ij}}{\partial \mathrm{E}_k}\right)_{\mathrm{E}=0} \mathrm{E}_k + \frac{1}{2}\left(\frac{\partial \eta_{ij}}{\partial \mathrm{E}_k \partial \mathrm{E}_l}\right)_{\mathrm{E}=0} \mathrm{E}_k \mathrm{E}_l + ..., \tag{A.13}$$

where the second term is the Pockels effect and the third term is the Kerr effect. The Pockels effect coefficients, $\left(\frac{\partial \eta_{ij}}{\partial \mathrm{E}_k}\right)_{\mathrm{E}=0}$, are usually expressed as r_{ijk}, a third rank tensor, where the k indicates the derivative to the kth field direction. A medium with dominating Pockels effects coefficients can distinguish between a positive and negative applied electric field.

Since η_{ij} is symmetric in i, j, Voigt's notation can be used. Then the index ellipsoid can be written using Eq. A.4 and Eq. A.13

$$\begin{aligned}\left(\frac{1}{n_x^2} + r_{1k}\mathrm{E}_k\right)x^2 + \left(\frac{1}{n_y^2} + r_{2k}\mathrm{E}_k\right)y^2 + \left(\frac{1}{n_z^2} + r_{3k}\mathrm{E}_k\right)z^2 \\ +2yzr_{4k}\mathrm{E}_k + 2xzr_{5k}E_k + 2xyr_{6k}\mathrm{E}_k = 1,\end{aligned} \tag{A.14}$$

neglecting any nonlinear electric field terms. The equation shows that an applied electric field changes the index ellipsoid, changing the polarization direction and refractive indices of the two eigenwaves. For electro-optic sensors the directions of normal modes should not change, only the principal refractive indices, causing a dependence of the birefringence on the applied electric field. This occurs when the electro-optic coefficients r_{4k}, r_{5k} or r_{6k} are zero.

An externally applied electric field can modify the orientation of the principal axes. The notation in which the optical axes are defined as the principal axes without an electric field is used.

A.3. Lithium Niobate Crystal ($LiNbO_3$)

$LiNbO_3$ is an electro-optic crystal with a low inherent inductance and low thermal coefficients for a well chosen orientation. The electro-optic coefficients r_{ij} can be expressed

as

$$\begin{bmatrix} 0 & -r_{22} & r_{13} \\ 0 & r_{22} & r_{13} \\ 0 & 0 & r_{33} \\ 0 & r_{51} & 0 \\ r_{51} & 0 & 0 \\ -r_{22} & 0 & 0 \end{bmatrix}, \tag{A.15}$$

Using the electro-optic coefficients and equation A.14, the index ellipsoid of a $LiNbO_3$ crystal can be calculated

$$\begin{aligned} \left(\frac{1}{n_0^2} - r_{22}\mathrm{E}_2 + r_{13}\mathrm{E}_3\right)x_1^2 + \left(\frac{1}{n_0^2} + r_{22}\mathrm{E}_2 + r_{13}\mathrm{E}_3\right)x_2^2 + \left(\frac{1}{n_e^2} + r_{33}\mathrm{E}_3\right)x_3^2 \\ +2x_2x_3r_{51}\mathrm{E}_2 + 2x_1x_3r_{51}E_1 - 2x_1x_2r_{22}\mathrm{E}_1 = 1, \end{aligned} \tag{A.16}$$

where n_0 and n_e are the ordinary and extraordinary refractive indices, respectively, and also the optical axes.

The index ellipsoid for light traveling along x_3 is

$$\left(\frac{1}{n_0^2} - r_{22}\mathrm{E}_2 + r_{13}\mathrm{E}_3\right)x_1^2 + \left(\frac{1}{n_0^2} + r_{22}\mathrm{E}_2 + r_{13}\mathrm{E}_3\right)x_2^2 - 2x_1x_2r_{22}\mathrm{E}_1 = 1. \tag{A.17}$$

It represents an equation of an ellipsoid whose major and minor axes correspond to the refractive indices. To find the eigenaxes of the equation a coordinate transformation is required

$$\begin{bmatrix} x_1' \\ x_2' \end{bmatrix} = \begin{bmatrix} \cos\theta & \sin\theta \\ -\sin\theta & \cos\theta \end{bmatrix}\begin{bmatrix} x_1 \\ x_2 \end{bmatrix}, \tag{A.18}$$

also shown in Figure A.1. The transformed coordinates result in the equation for the index ellipsoid for the new coordinates

$$\begin{aligned} \left(\frac{1}{n_0^2} - r_{22}E_2 + r_{13}E_3\right)\left(x_1'^2\cos^2\theta + x_2'^2\sin^2\theta - 2x_1'x_2'\cos\theta\sin\theta\right) \\ +\left(\frac{1}{n_0^2} + r_{22}E_2 + r_{13}E_3\right)\left(x_1'^2\sin^2\theta + x_2'^2\cos^2\theta + 2x_1'x_2'\cos\theta\sin\theta\right) \\ -2r_{22}E_1\left(x_1'^2\cos\theta\sin\theta + x_1'x_2'\cos^2\theta - x_1'x_2'\sin^2\theta - x_2'^2\sin\theta\cos\theta\right) = 1. \end{aligned} \tag{A.19}$$

When the mixed terms vanish the primed coordinates give the principal axes. Using the fact that E_1 and E_2 can be written as $E_{12}\sin\phi$ and $E_{12}\cos\phi$ respectively, where ϕ is the angle of electric field orientation in the x_1x_2 plane, leads to the requirement that

$$2\sin\phi\cos\theta\sin\theta - \cos\phi\left(\cos^2\theta - \sin^2\theta\right) = 0, \tag{A.20}$$

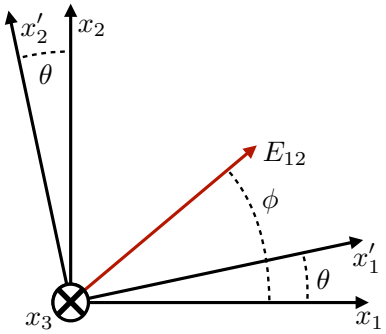

Figure A.1.: Transformation of the coordinate system of the principal axes of $LiNbO_3$ around x_3 optical axis. The normal modes without any applied electric field (optical axes) are given by x_1, x_2, which rotate to x_1', x_2' (principal axes) under influence of an applied electric field in the x_1x_2 plane at an angle ϕ. The dependence is shown in Eq. A.22.

which can be simplified to

$$\phi + 2\theta = \pi/2 \tag{A.21}$$

where θ gives the rotation of the principal axis with respect to the optical axes. Then

$$\theta = \frac{\pi/2 - \phi}{2} \tag{A.22}$$

meaning a rotation of the electric field vector in the x_1x_2 plane rotates the principal axes in opposite direction and twice as slow. The optical axes x_1', x_2' are rotated by 45° along x_3 with respect to x_1 for an electric field along x_1 and coincide with the x_1 and x_2 axes for an electric field along x_2. The refractive indices of the principal axes are

$$\frac{1}{n_1'^2} = \frac{1}{n_0^2} + r_{13}E_z - r_{22}E_2\cos 2\theta - r_{22}E_1\sin 2\theta, \tag{A.23}$$

$$\frac{1}{n_2'^2} = \frac{1}{n_0^2} + r_{13}E_z + r_{22}E_2\cos 2\theta + r_{22}E_1\sin 2\theta. \tag{A.24}$$

Since the electric field vector $\mathbf{E}$ can be written in the x_1x_2 plane as E_{12}, with $E_1 = E_{12}\cos\phi$ and $E_y = E_{12}\sin\phi$, the refractive indices become

$$n_1' = n_0\left[1 - n_0^2/2\,(r_{13}E_3 - r_{22}E_{12})\right], \tag{A.25}$$

$$n_2' = n_0\left[1 - n_0^2/2\,(r_{13}E_3 + r_{22}E_{12})\right]. \tag{A.26}$$

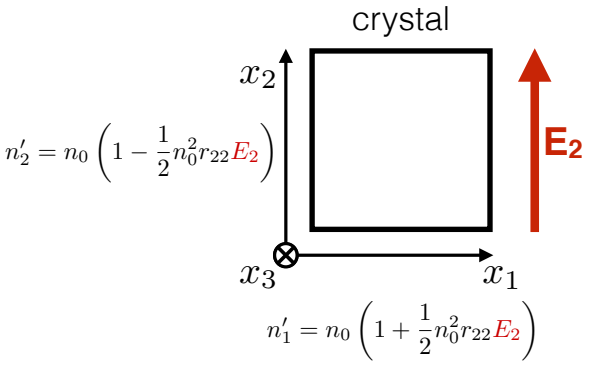

Figure A.2.: Schematic overview of the two principal axes of the electro-optic Lithium Niobate crystal for an electric field applied along x_2, assuming a light wave propagating along x_3. The principal axes then coincide with x_1, x_2, the optical axes. The birefringence of such a configuration as a function of the applied electric field is $\Delta n = -n_0^3 r_{22} E_2$.

This is shown schematically in Figure A.2 for an electric field along x_2, causing the principal axes to coincide with the x_1 and x_2 optical axes.

The induced birefringence (Δn) as a function of the applied electric field is then

$$\Delta n = \left(n_2' - n_1'\right) = -n_0^3 r_{22} E_{12} \tag{A.27}$$

and the resulting phase retardation Γ is given by

$$\Gamma = \frac{2\pi \Delta n L}{\lambda}, \tag{A.28}$$

where L is the path length the light travels through the electro-optic medium and λ is the light wavelength.

Another method of calculating the principal axes and corresponding refractive induces is by using equation A.11

$$\mathbf{u} \times (\mathbf{u} \times \eta \mathbf{D}) + \frac{1}{n^2}\mathbf{D} = 0, \tag{A.29}$$

where $\mathbf{n}$ is the normalized wave propagation direction. With an electric field vector $\mathbf{E}$ the electric impermeability tensor becomes

$$\eta = \begin{bmatrix} \frac{1}{n_0^2} - E_2 r_{22} + E_3 r_{13} & -E_1 r_{22} & E_1 r_{51} \\ -E_1 r_{22} & \frac{1}{n_0^2} + E_2 r_{22} & E_1 r_{51} \\ E_1 r_{51} & E_2 r_{51} & \frac{1}{n_e^2} + E_3 r_{33} \end{bmatrix}. \tag{A.30}$$

Table A.1.: Birefringence $(n_2 - n_1)$ resulting from combinations of **k** direction and **E** direction along the ordinary and extraordinary axes of a $LiNbO_3$ electro-optic crystal. n_0, n_e are the ordinary and extraordinary refractive indices and r_{ij} are the electro-optic coefficients

	E_1	E_2	E_3
u_1	$(n_e - n_0)$	$-\frac{n_0^3 r_{22} E_2}{2} + (n_e - n_0)$	$\frac{E_3}{2}\left(n_0^3 r_{13} - n_e^3 r_{33}\right) + (n_e - n_0)$
u_2		$\frac{n_0^3 r_{22} E_2}{2} + (n_e - n_0)$	$\frac{E_3}{2}\left(n_0^3 r_{13} - n_e^3 r_{33}\right) + (n_e - n_0)$
u_3	$E_1 n_0^3 r_{22}$	$-E_2 n_0^3 r_{22}$	0

For light propagating along x_3, equation A.29 becomes

$$\left(\begin{bmatrix} \frac{1}{n_0^2} - E_2 r_{22} - E_3 r_{31} & -E_x r_{22} \\ -E_1 r_{22} & \frac{1}{n_0^2} + E_2 r_{22} + E_3 r_{13} \end{bmatrix} - \frac{1}{n^2} I\right)\mathbf{D} = 0, \tag{A.31}$$

an eigensystem problem. Solving for the eigenvalues and eigenvectors gives

$$\frac{1 + E_3 n_0^2 r_{13} - n_0^2 r_{22}\sqrt{E_1^2 + E_2^2}}{n_0^2}, \frac{1 + E_3 n_0^2 r_{13} + n_0^2 r_{22}\sqrt{E_1^2 + E_2^2}}{n_0^2}, \tag{A.32}$$

for the eigenvalues and

$$\begin{bmatrix} \frac{E_2 + \sqrt{E_1^2 + E_2^2}}{E_1} \\ 1 \end{bmatrix}, \begin{bmatrix} \frac{E_2 - \sqrt{E_1^2 + E_2^2}}{E_1} \\ 1 \end{bmatrix}. \tag{A.33}$$

for the eigenvectors. $\sqrt{E_1^2 + E_2^2}$ is simply the magnitude of the electric field vector in the $x_1 x_2$ plane, which can also be written as E_{12}. The resulting eigenvalues are the same as for the method used in equations A.23 and A.24. The advantage is that this method makes it easier to calculate the birefringence of the combinations of wave propagation directions **u** and electric field orientation. Several combinations are shown in Table A.1.

B. ADC Timing

The timing of an ADC is given by the clock signal coupled to the ADC triggering when the ADC takes data. As a result, the stability of the timing of an ADC is given by the stability of the clock signal. The stability is usually given in terms of ppm (parts per million), in general terms this means that a clock of frequency f has a frequency stability of $f \cdot \text{ppm}$. For instance, a 2.048 MHz clock with 50 ppm stability has a frequency stability of $f \cdot \text{ppm} = 1.024 \times 10^{-4}$ MHz $= 10.24$ Hz.

A shifting frequency of the clock source results in varying time intervals between successive ADC samples, which can introduce errors when determining for instance frequencies of the measured signals. The stability of the clock source is usually given in the specifications, but it is also possible to obtain an estimate on the timing stability of an ADC using a signal generator coupled to a stabilized clock source.

Assuming an integrating ADC, imagine a square wave at 5 Hz sampled by an ADC running at exactly 10 Hz. Then, as shown in Fig. B.1, each successive time interval integrates exactly a half-period of the square wave, resulting in ADC values switching only in sign. Now imagine the same square wave sampled by an ADC running at 11.11 Hz, shown in Fig. B.2. Each successive time interval sampled is shifting left compared to the square wave, resulting in ADC values becoming slightly smaller, or larger, when starting above, or below, zero. Eventually the overlap will be such that the ADC sample is zero, before continuing on to a complete reversal of the initial configuration.

The time between zero crossings of the ADC values is when the ADC sampling interval has shifted a half-period of the square wave. Alternative the time difference between the maxima, or minima, can also be used. The difference in frequency between the square wave and the ADC sampling frequency is then given by

$$\Delta f = \frac{1}{2\Delta t_{\text{cross}}}. \tag{B.1}$$

A change in frequency of either the ADC clock source or the signal generator clock source then changes Δt_{cross}, giving information about the frequency stability of the combined signal generator and ADC clock source system. However when the signal generator is coupled to a stabilized 10 MHz source it is safe to assume the change in frequency stability is wholly resulting from the ADC clock source. From measuring many zero crossings an estimate can be made on the stability of the ADC clock source.

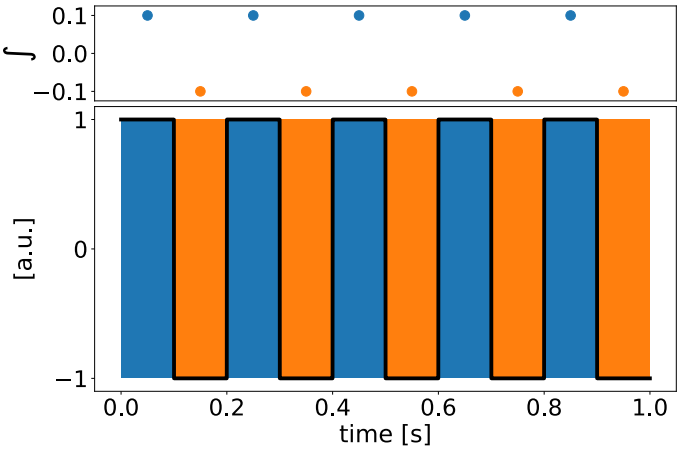

Figure B.1.: Square wave at 5 Hz sampled by an integrating ADC operating at 10 Hz. The bottom figure shows the square wave, where the patches alternating in color represent the integration sections of the ADC operating at 10 Hz. The top figure shows the ADC values, alternating between -0.1 and 0.1.

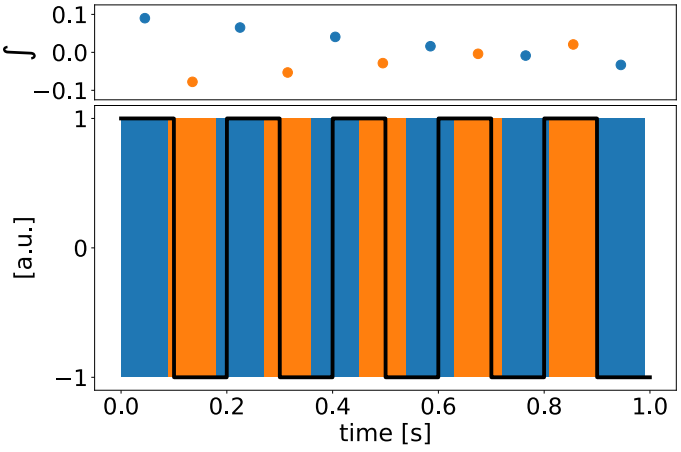

Figure B.2.: Square wave at 5 Hz sampled by an integrating ADC operating at 11.11 Hz. The bottom figure shows the square wave, where the patches alternating in color represent the integration sections of the ADC operating at 11.11 Hz. The patches are slowly moving left with respect to the square wave, resulting in the integrated values shown in the top figure moving in opposite direction as well.

C. Cramer-Rao Lower Bound

The Cramer-Rao Lower Bound theorem [85] states that for a probability distribution function (PDF) $p(\mathbf{x};\theta)$ satisfying the regularity condition

$$E\left[\frac{\delta \ln p(\mathbf{x};\theta)}{\delta\theta}\right] = 0 \text{ for all } \theta, \tag{C.1}$$

where E is the expectation with respect to $p(\mathbf{x};\theta)$, the variance of any unbiased estimator $\hat{\theta}$ must satisfy

$$\text{var}\left(\hat{\theta}\right) \geq \frac{1}{-E\left[\frac{\delta^2 \ln p(\mathbf{x};\theta)}{\delta\theta^2}\right]}. \tag{C.2}$$

The derivative is evaluated at the true value of theta and again the expectation is taken with respect to $p(\mathbf{x};\theta)$. Furthermore an unbiased estimator may be found that reaches the bound for all θ if

$$\frac{\delta \ln p(\mathbf{x};\theta)}{\delta\theta} = I(\theta)(g(\mathbf{x}) - \theta), \tag{C.3}$$

for some functions I and g. This estimator is the minimum variance unbiased (MVU) estimator, with $\hat{\theta} = g(\mathbf{x})$ and minimum variance $1/I(\theta)$. The expectation in Eq. C.2 can be written as

$$E\left[\frac{\delta^2 \ln p\,(\mathbf{x};\theta)}{\delta\theta^2}\right] = \int \frac{\delta^2 \ln p\,(\mathbf{x};\theta)}{\delta\theta^2} p(\mathbf{x};\theta) d\mathbf{x}. \tag{C.4}$$

A signal with a unknown parameter θ, including white noise, has form

$$x[n] = s[n;\theta] + w[n] \text{ for } n = 0, 1, ..., N-1. \tag{C.5}$$

The likelihood function is given by

$$p\,(\mathbf{x};\theta) = \frac{1}{(2\pi\sigma^2)^{\frac{N}{2}}} \exp\left(-\frac{1}{2\sigma^2}\sum_{n=0}^{N-1}(x[n] - s[n;\theta])^2\right), \tag{C.6}$$

and taking the derivative twice of the log likelihood function gives

$$\frac{\delta^2 \ln p(\mathbf{x};\theta}{\delta\theta^2} = \frac{1}{\sigma^2}\sum_{n=0}^{N-1}\left((x[n] - s[n;\theta])\frac{\delta^2 s[n;\theta]}{\delta\theta^2} - \left(\frac{\delta s[n;\theta]}{\delta\theta}\right)^2\right). \tag{C.7}$$

The expectation value results in

$$-\frac{1}{\sigma^2}\sum_{n=0}^{N-1}\left(\frac{\delta s[n;\theta]}{\delta\theta}\right)^2, \tag{C.8}$$

resulting in

$$\mathrm{var}\left(\hat{\theta}\right) \geq \frac{\sigma^2}{\sum_{n=0}^{N-1}\left(\frac{\delta s[n;\theta]}{\delta\theta}\right)^2}, \tag{C.9}$$

a general solution for signals with white noise.

For vector parameters, i.e. multiple unknown parameters in a signal, it is also possible take the Cramer-Rao Lower Bound [85]. Assuming an unbiased estimator $\hat{\theta}$, the CRLBs are then the diagonal elements of the inverse of the Fisher information matrix, defined by

$$[\mathbf{I}(\boldsymbol{\theta})]_{ij} = -E\left[\frac{\delta^2 \ln p(\mathbf{x};\boldsymbol{\theta})}{\delta\theta_i \delta\theta_j}\right], \tag{C.10}$$

with i, j the number of parameters. Then the CRLB is given by

$$\mathrm{var}\left(\hat{\theta}_i\right) \geq \left[\mathbf{I}^{-1}(\boldsymbol{\theta})\right]_{ii}. \tag{C.11}$$

For a signal with white noise the Fisher Information matrix generalizes to

$$[\mathbf{I}(\boldsymbol{\theta})]_{ij} = \frac{1}{\sigma^2}\sum_{n=0}^{N-1}\frac{\delta s[n;\boldsymbol{\theta}]}{\delta\theta_i}\frac{\delta s[n;\boldsymbol{\theta}]}{\delta\theta_j} \tag{C.12}$$

In the MiXeD experiment estimates of parameters of a sinusoidal are made. Assuming a simple model

$$x[n] = A\cos\left(2\pi\left(f/r_s\right)n + \phi\right) + w[n] \text{ for } n = 0, 1, ..., N-1, \tag{C.13}$$

where r_s is the sampling rate and n indicates the nth data point, the Fisher Information

matrix entries for (A, f, ϕ) are

$$\mathbf{I}_{11} = \frac{1}{\sigma^2}\sum_{n=0}^{N-1}\cos^2\alpha \approx \frac{N}{2\sigma^2} \tag{C.14a}$$

$$\mathbf{I}_{12} = -\frac{1}{\sigma^2}\sum_{n=0}^{N-1}2\pi A(n/r_s)\cos\alpha\sin\alpha \approx 0 \tag{C.14b}$$

$$\mathbf{I}_{13} = -\frac{1}{\sigma^2}\sum_{n=0}^{N-1}A\cos\alpha\sin\alpha \approx 0 \tag{C.14c}$$

$$\mathbf{I}_{22} = \frac{1}{\sigma^2}\sum_{n=0}^{N-1}A^2\left(2\pi\left(n/r_s\right)\right)^2\sin^2\alpha \approx \frac{(2\pi A)^2}{2r_s^2\sigma^2}\sum_{n=0}^{N-1}n^2 \tag{C.14d}$$

$$\mathbf{I}_{23} = \frac{1}{\sigma^2}\sum_{n=0}^{N-1}A^2 2\pi(n/r_s)\sin^2\alpha \approx \frac{\pi A^2}{r_s\sigma^2}\sum_{n=0}^{N-1}n \tag{C.14e}$$

$$\mathbf{I}_{33} = \frac{1}{\sigma^2}\sum_{n=0}^{N-1}A^2\sin^2\alpha \approx \frac{NA^2}{2\sigma^2} \tag{C.14f}$$

where $\alpha = 2\pi\left(f/r_s\right)n + \phi$, and the approximations

$$\frac{1}{N^{i+1}}\sum_{n=0}^{N-1}n^i\sin\left(2\alpha\right) \approx 0, \tag{C.15a}$$

$$\frac{1}{N^{i+1}}\sum_{n=0}^{N-1}n^i\cos\left(2\alpha\right) \approx 0, \tag{C.15b}$$

are used. With the following identities

$$\sum_{n=0}^{N-1}n = \frac{N(N-1)}{2}, \tag{C.16a}$$

$$\sum_{n=0}^{N-1}n^2 = \frac{N(N-1)(2N-1)}{6}, \tag{C.16b}$$

The inverted Fisher Information matrix then becomes

$$\mathbf{I}^{-1}(\boldsymbol{\theta}) = \sigma^2\begin{bmatrix} \frac{2}{N} & 0 & 0 \\ 0 & \frac{6r_s^2}{\pi^2A^2N(N^2-1)} & -\frac{6r_s}{\pi A^2N(N+1)} \\ 0 & -\frac{6r_s}{\pi A^2N(N+1)} & \frac{4(2N-1)}{A^2N(N+1))} \end{bmatrix}. \tag{C.17}$$

Given that $A^2/(2\sigma^2)$ is the signal-to-noise ratio squared (SNR^2), $\frac{N(N^2-1)}{r_s^3} < T^3$ (measurement time) and $r_s/2 = f_{\mathrm{BW}}$ is the Nyquist frequency (sampling rate limited bandwidth) the CRLB becomes for the frequency becomes

$$\mathbf{I}_{22}^{-1} = \mathrm{var}(\hat{f}) \geq \frac{12}{(2\pi)^2 \left(\frac{A^2}{2\sigma^2}\right)(r_s/2)\frac{N(N^2-1)}{r_s^3}} > \frac{12}{(2\pi)^2 \mathrm{SNR}^2 f_{\mathrm{BW}} T^3}. \tag{C.18}$$

For spin precession a decay term has to be taken into account, $e^{-\frac{n}{r_s T_2^*}}$. The signal then becomes [86]

$$x[n] = A\exp\left[-\frac{n}{r_s T_2^*}\right]\cos\left(2\pi\left(f/r_s\right)n + \phi\right) + w[n] \text{ for } n = 0, 1, ..., N-1. \tag{C.19}$$

Using $\beta = 1/(r_s T_2^*)$ the parameters for the Fisher Information matrix now become $\boldsymbol{\theta}(A, f, \phi, \beta)$. Using the same procedure as above, the matrix terms become

$$\mathbf{I}_{22} = \frac{(2\pi A)^2}{2r_s^2\sigma^2}\sum_{n=0}^{N-1} n^2 \exp[-2\beta n], \tag{C.20a}$$

$$\mathbf{I}_{23} = \frac{\pi A^2}{2r_s\sigma^2}\sum_{n=0}^{N-1} n \exp[-2\beta n], \tag{C.20b}$$

$$\mathbf{I}_{33} = \frac{A^2}{2\sigma^2}\sum_{n=0}^{N-1} \exp[-2\beta n]. \tag{C.20c}$$

To calculate $\mathrm{var}(f)$ the Fisher matrix needs to be inverted and $\mathbf{I}_{22}^{-1}$ is given by

$$\mathbf{I}_{22}^{-1} = \frac{\mathbf{I}_{33}}{\mathbf{I}_{22}\mathbf{I}_{33} - \mathbf{I}_{23}\mathbf{I}_{32}}. \tag{C.21}$$

With the identities

$$\sum_{n=0}^{N-1} n \exp[-2\beta n] = -\frac{1}{2}\frac{\delta}{\delta\beta}\left(\sum_{n=0}^{N-1}\exp[-2\beta n]\right), \tag{C.22a}$$

$$\sum_{n=0}^{N-1} n^2 \exp[-2\beta n] = -\frac{1}{4}\frac{\delta^2}{\delta\beta^2}\left(\sum_{n=0}^{N-1}\exp[-2\beta n]\right), \tag{C.22b}$$

$\mathrm{var}(\hat{f})$ becomes

$$\mathbf{I}_{22}^{-1} = \mathrm{var}(\hat{f}) \geq \frac{12}{(2\pi)^2 \mathrm{SNR}^2 f_{\mathrm{BW}} T^3} C(T; T_2^*) \tag{C.23}$$

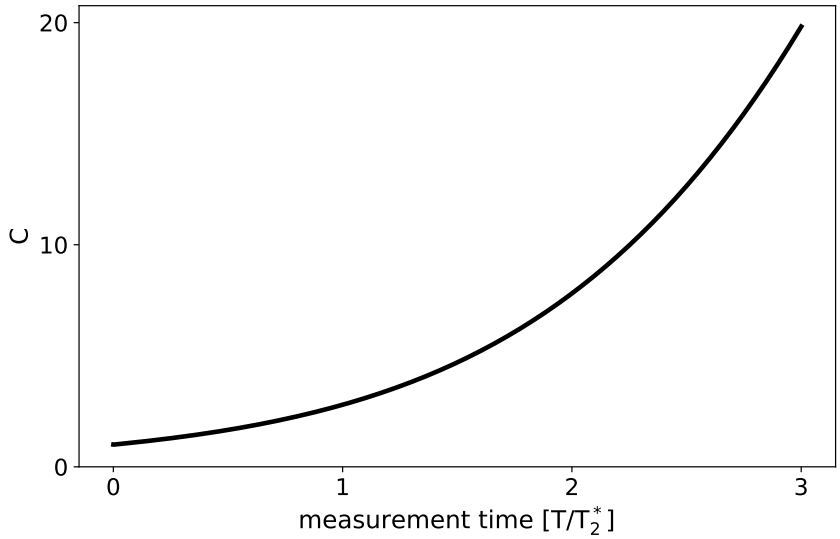

Figure C.1.: Exponential damping parameter C from the Cramer-Rao Lower Bound frequency estimator for a exponentially damped sinusoidal. Calculated for 20000 s T_2^* and 250 Hz sampling rate r_s.

where C gives the effect of exponential damping

$$C(T;T_2^*) = \frac{N^3}{12} \frac{\left(1-\exp[-\beta]^2\right)^3 \left(1-\exp[-\beta]^{2N}\right)}{\exp[-\beta]^2 \left(1-\exp[-\beta]^{2N}\right)^2 - N^2 \exp[-\beta]^{2N} \left(1-\exp[-\beta]^2\right)^2}. \quad \text{(C.24)}$$

N is the total number of data points, given by the integer $N = r_s T$. The parameter C is plotted in Fig. C.1 as a function of measurement time.

D. Chi-Square Fit

The aim of fitting a model to a set data points is to give the best possible fit parameters corresponding to the minimized difference between the fit model and the data points. Given data points (x_i, y_i) of length N the aim is to fit a function

$$f(\mathbf{x}) = f(\mathbf{x}; \boldsymbol{\theta}), \tag{D.1}$$

with P free parameters θ_j to the data points. A method for achieving this is maximum likelihood estimation (MLE). MLE finds the parameter values maximizing the likelihood of making observations given the parameters, resulting in the best-fit parameters. Most of this appendix is derived or taken from [87] and [88].

Assuming each data point has an independent, normally distributed error with standard deviation σ_i, the likelihood of the fit function matching the data points is

$$\mathscr{L}(\boldsymbol{\theta}; \mathbf{x}) = \frac{1}{\sqrt{2\pi}} \prod_{i=0}^{N-1} \frac{\exp\left[-\frac{1}{2}\left(\frac{y_i - f(x_i;\boldsymbol{\theta})}{\sigma_i}\right)^2\right]}{\sigma_i}. \tag{D.2}$$

To maximize Eq. D.2 one can minimize the negative logarithm

$$-\log \mathscr{L} = \frac{N}{2}\log 2\pi + \sum_{i=0}^{N-1} \log \sigma_i + \frac{1}{2}\sum_{i=0}^{N-1}\left(\frac{y_i - f(x_i;\boldsymbol{\theta})}{\sigma_i}\right)^2. \tag{D.3}$$

Given that N is constant, as is the sum over $\log \sigma_i$ for varying fit parameters, this is equivalent to minimizing chi-square

$$\chi^2 = \sum_{i=0}^{N-1}\left(\frac{y_i - f(x_i;\boldsymbol{\theta})}{\sigma_i}\right)^2. \tag{D.4}$$

With $\boldsymbol{\theta}$ known χ^2 is the sum of squares of N standard normal variables and has a $\chi^2(N)$ distribution, with probability density function (PDF)

$$f_{\chi^2}(x; \nu) = \frac{e^{-x/2} x^{\nu/2-1}}{2^{\nu/2}\Gamma(\nu/2)}, \tag{D.5}$$

where ν specifies the number of degrees of freedom (d.o.f.) and Γ is the gamma function. The mean of the χ^2 distribution is the number of d.o.f. ν and the variance is 2ν. The

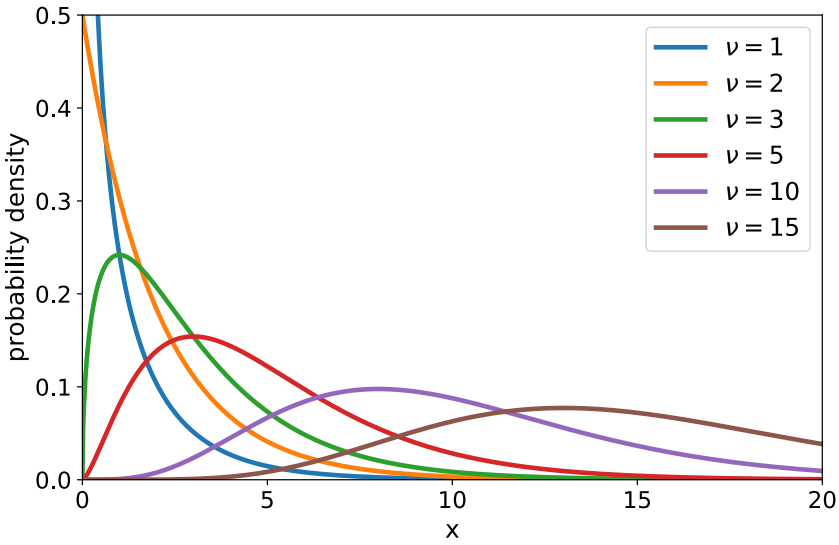

Figure D.1.: χ^2 distribution for varying degrees of freedom ν.

χ^2 distribution is plotted for several d.o.f. in Fig. D.1. For a sufficient number of d.o.f., generally $\nu > 30$, the χ^2 distribution approaches a normal distribution sufficiently to ignore the difference for practical applications (See Fig. D.2). As $\nu \to \infty$ the distribution

$$\frac{\chi^2 - \nu}{\sqrt{2\nu}} \tag{D.6}$$

tends to a standard normal distribution.

When $\boldsymbol{\theta}$ is estimated from minimizing Eq. D.4 it is the sum of squares of correlated, non-central random variables which are generally not normally distributed. However, for fit models linear in $\boldsymbol{\theta}$, Eq. D.4 follows a χ^2 probability distribution with $\nu = N - P$ d.o.f.. The goodness-of-fit of a model is determined by checking the probability that a computed value χ^2_{comp} occurs by chance. To compute this the value

$$Q = \int_{\chi^2_{\text{comp}}}^{\infty} f_{\chi^2}(x;\nu)dx \tag{D.7}$$

is calculated. A small Q value can have several causes, but generally means the fit does not have good agreement. The chosen fit model can be incorrect, or the measurement errors

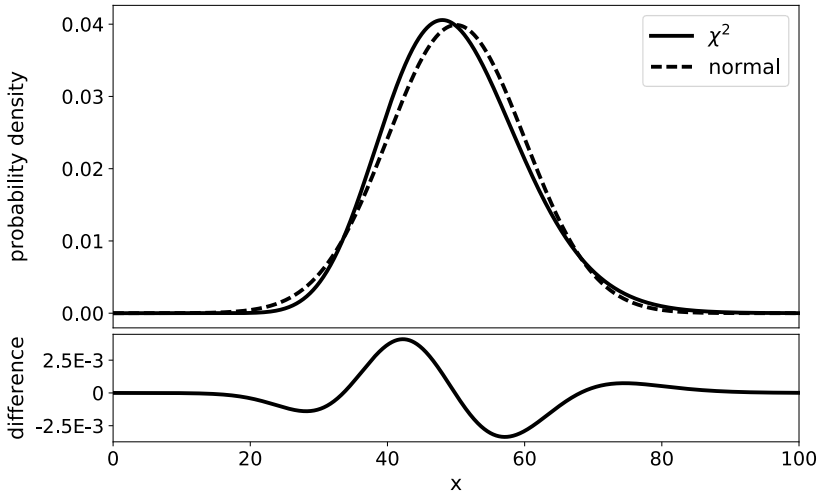

Figure D.2.: χ^2 distribution for $\nu = 50$ compared to a normal distribution with $\mu = \nu$ and $\sigma = \sqrt{2\nu}$.

are not normally distributed or even underestimated. Oppositely one can overestimate the measurement errors, resulting in Q values close to 1.

Often the measurement errors are not known in advance and are set during the χ^2 fit procedure, since the number of d.of. is known in advance. This is only valid if the measurement error is identical for each data point. The measurement error is then given by

$$\sigma^2 = \sum_{i=0}^{N-1} \frac{(y_i - f(x_i, \boldsymbol{\theta}))^2}{N - P}, \tag{D.8}$$

but this approach prohibits an independent goodness-of-fit test. However, when the data is split up into sections and the same fit model is applied to all sections, the resulting χ^2 values for each of the sections should follow a χ^2 distribution with mean value ν and standard deviation $\sqrt{2\nu}$, allowing for some goodness-of-fit test by means of comparing the two distributions.

E. Phase Analysis Measurements

The results of the analysis for the 6 data runs performed in July 2017 are compiled and presented as a set of graphs. The runs are labeled by the filenames L20170718_120015, L20170718_195555, L20170719_151640, L20170719_220808, L20170720_112748 and L20170720_224608.

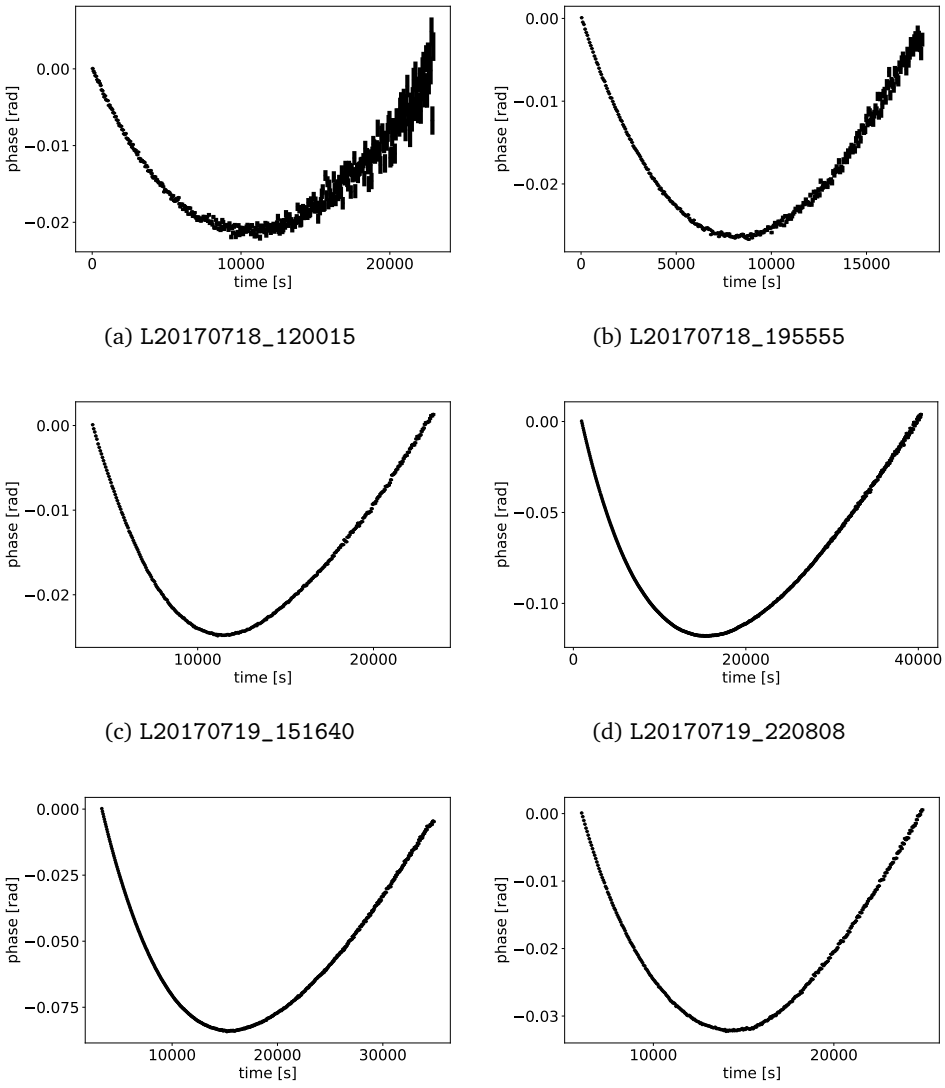

(a) L20170718_120015

(b) L20170718_195555

(c) L20170719_151640

(d) L20170719_220808

(e) L20170720_112748

(f) L20170720_224608

Figure E.1.: Weighted phase difference for all six runs with the linear term subtracted.

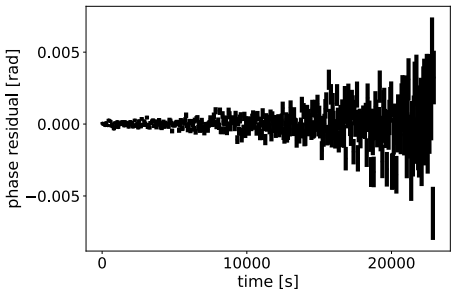

(a) L20170718_120015

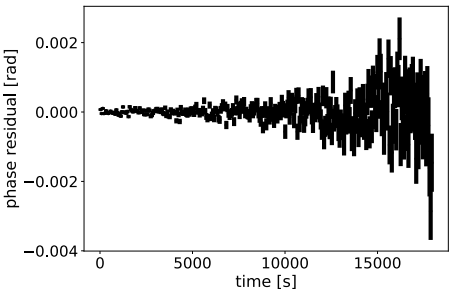

(b) L20170718_195555

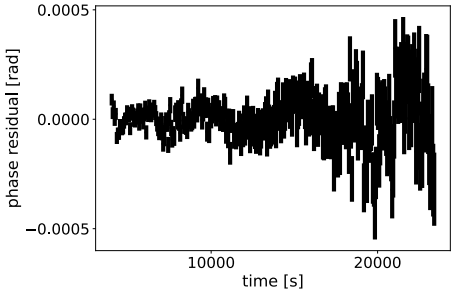

(c) L20170719_151640

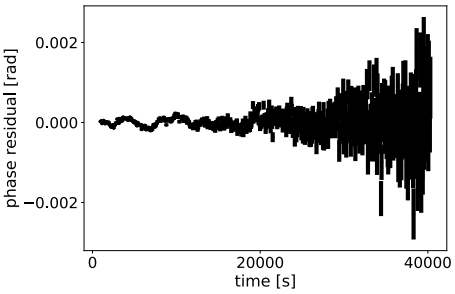

(d) L20170719_220808

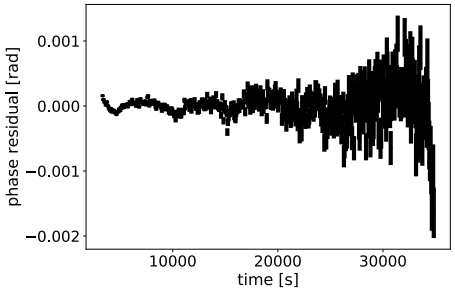

(e) L20170720_112748

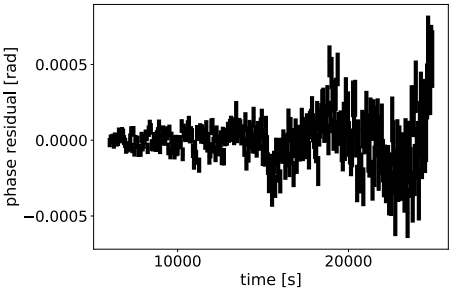

(f) L20170720_224608

Figure E.2.: Residuals of the weighted phase difference after applying the fit model from Eq. 6.15.

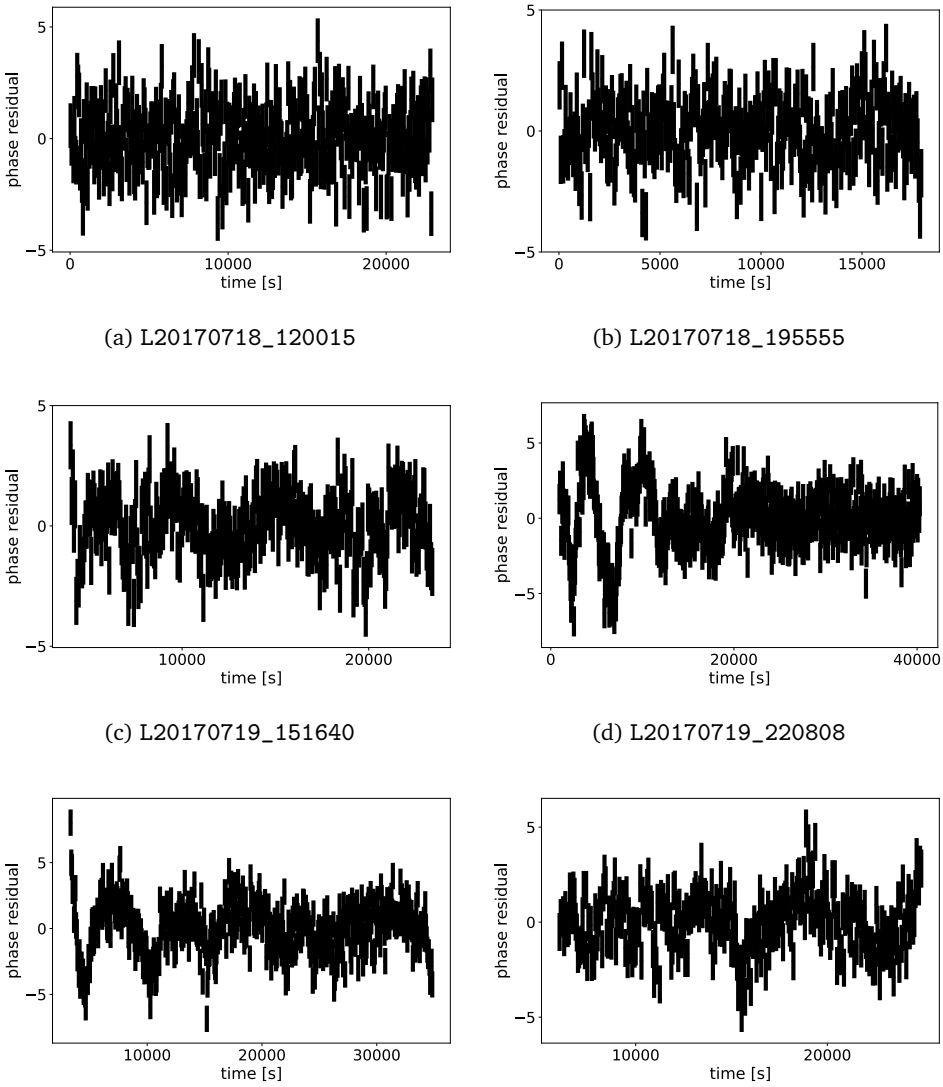

(a) L20170718_120015

(b) L20170718_195555

(c) L20170719_151640

(d) L20170719_220808

(e) L20170720_112748

(f) L20170720_224608

Figure E.3.: Normalized residuals of the weighted phase difference after applying the fit model from Eq. 6.15. The residuals are divided by the phase error to facilitate detection of structures. A correct fit would result in normalized residuals distributed Gaussian around zero with $\sigma = 1$.

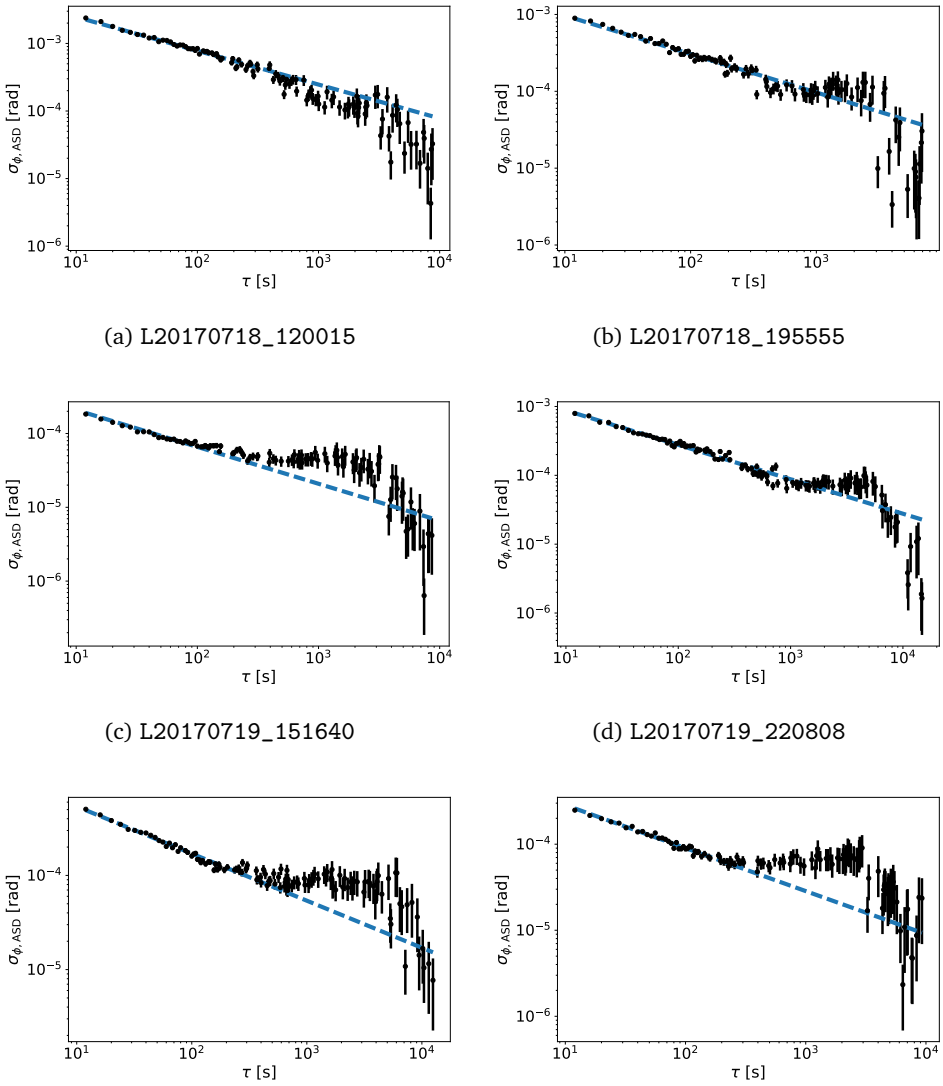

(a) L20170718_120015

(b) L20170718_195555

(c) L20170719_151640

(d) L20170719_220808

(e) L20170720_112748

(f) L20170720_224608

Figure E.4.: Allan variance of the phase residuals. For $\tau < \sim 5 \times 10^2$ s the decrease in phase uncertainty is proportional to $\tau^{-1/2}$, indicating white noise. For larger τ the ASD deviates from white noise, which is apparent as a structure in the phase residuals shown in Figures E.2, E.3.

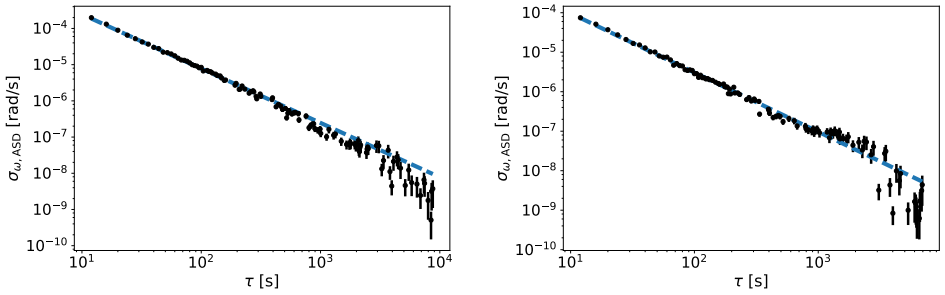

(a) L20170718_120015

(b) L20170718_195555

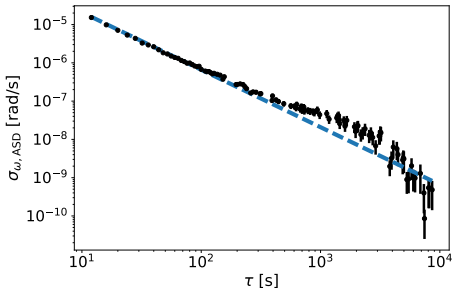

(c) L20170719_151640

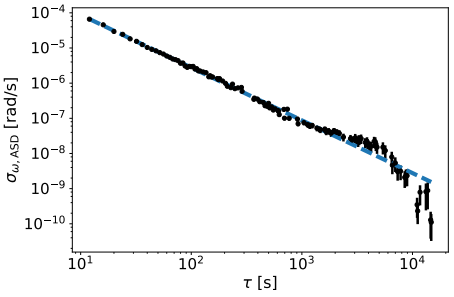

(d) L20170719_220808

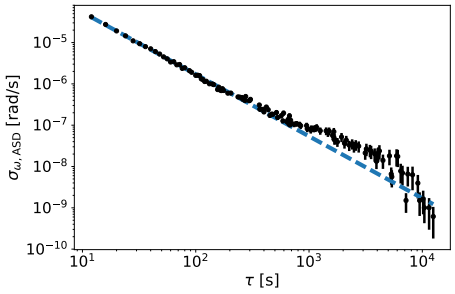

(e) L20170720_112748

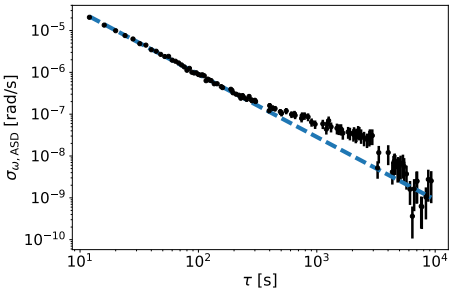

(f) L20170720_224608

Figure E.5.: Allan variance of the frequency. For $\tau < \sim 5 \times 10^2$ s the decrease in phase uncertainty is proportional to $\tau^{-3/2}$, indicating white noise. For larger τ the ASD deviates from white noise, which is apparent as a structure in the phase residuals shown in Figures E.2, E.3.

Table E.1.: Fit parameters and errors for the fit model described in Eq. 6.15 applied to the EDM measurements.

run #	measurement	a_0	σ_{a_0}	a_1	σ_{a_1}	a_2	σ_{a_2}	a_3	σ_{a_3}
1	L20170718_120015	3.30e+00	3.43e-05	-1.71e-06	4.73e-09	1.70e-01	1.14e-03	-1.12e-03	3.84e-03
2	L20170718_195555	-1.55e+00	1.40e-05	-2.85e-06	2.59e-09	1.66e-01	3.78e-04	-1.71e-02	1.70e-03
3	L20170719_151640	5.39e-01	3.49e-06	8.27e-07	1.36e-09	3.44e+00	3.84e-03	3.04e-01	2.11e-03
4	L20170719_220808	-8.79e-01	4.98e-06	-5.46e-06	6.74e-10	6.33e+00	6.99e-04	2.83e-01	2.44e-04
5	L20170720_112748	5.12e+00	9.87e-06	-1.91e-06	1.89e-09	5.70e+00	2.22e-03	3.49e-01	3.05e-04
6	L20170720_224608	-1.14e+00	9.79e-06	2.27e-06	5.53e-09	4.14e+00	1.65e-02	2.59e-01	1.59e-03

run #	measurement	a_4	σ_{a_4}	a_5	σ_{a_5}	d	σ_d
1	L20170718_120015					-1.12e-03	3.84e-03
2	L20170718_195555					-1.71e-02	1.70e-03
3	L20170719_151640	-9.77e+00	3.41e-01	6.31e-01	2.58e-02	2.59e-09	7.73e-09
4	L20170719_220808	-7.15e-02	5.52e-02	-3.77e-02	1.06e-03	-3.94e-09	2.77e-09
5	L20170720_112748	-2.44e+00	1.74e-01	1.07e-01	3.89e-03	3.98e-09	5.56e-09
6	L20170720_224608	-2.05e-01	7.49e-01	-1.06e+00	3.86e-02	5.13e-08	1.66e-08

Bibliography

[1] G. Luders, "On the Equivalence of Invariance under Time Reversal and under Particle-Antiparticle Conjugation for Relativistic Field Theories," *Kong. Dan. Vid. Sel. Mat. Fys. Med.*, vol. 28N5, pp. 1–17, 1954.

[2] W. Pauli, L. Rosenfeld, and V. Weisskopf, *Niels Bohr and the Development of Physics*. 1955.

[3] C. S. Wu, E. Ambler, R. W. Hayward, D. D. Hoppes, and R. P. Hudson, "Experimental Test of Parity Conservation in Beta Decay," *Phys.Rev.*, vol. 105, pp. 1413–1414, 1957.

[4] J. H. Christenson, J. W. Cronin, V. L. Fitch, and R. Turlay, "Evidence for the 2 pi Decay of the k(2)0 Meson," *Physical Review Letters*, vol. 13, pp. 138–140, 1964.

[5] J. Charles, A. Höcker, H. Lacker, S. Laplace, F. R. Diberder, J. Malclés, J. Ocariz, M. Pivk, and L. Roos, "CP violation and the CKM matrix: assessing the impact of the asymmetric B factories," *The European Physical Journal C*, vol. 41, pp. 1–131, May 2005.

[6] A. D. Sakharov, "Violation of CP invariance, C asymmetry, and baryon asymmetry of the universe," *JETP Lett.*, vol. 5, no. 1, pp. 24–27, 1967.

[7] V. A. Kostelecky and R. Potting, "Cpt and strings," *Nuclear Physics B*, vol. 359, no. 2, pp. 545 – 570, 1991.

[8] M. Pospelov and A. Ritz, "Electric dipole moments as probes of new physics," *Annals of Physics*, vol. 318, no. 1, pp. 119 – 169, 2005. Special Issue.

[9] S. Dar, "The Neutron EDM in the SM : A Review," *arXiv*, Aug. 2000.

[10] J. Baron, W. C. Campbell, D. DeMille, J. M. Doyle, G. Gabrielse, Y. V. Gurevich, P. W. Hess, N. R. Hutzler, E. Kirilov, I. Kozyryev, B. R. O'Leary, C. D. Panda, M. F. Parsons, E. S. Petrik, B. Spaun, A. C. Vutha, and A. D. West, "Order of magnitude smaller limit on the electric dipole moment of the electron," *Science*, vol. 343, no. 6168, pp. 269–272, 2014.

[11] B. Yip, "Analysis of electric dipole moment experiments and their future prospects." Bachelor's thesis, University of Groningen, 2015.

[12] B. Roberts, V. Dzuba, and V. Flambaum, "Parity and time-reversal violation in atomic systems," *Annual Review of Nuclear and Particle Science*, vol. 65, no. 1, pp. 63–86, 2015.

[13] I. B. Khriplovich and S. K. Lamoreaux, *CP Violation Without Strangeness*. Springer, 1997.

[14] J. S. M. Ginges and V. V. Flambaum, "Violations of fundamental symmetries in atoms and tests of unification theories of elementary particles," *Physics Reports*, vol. 397, pp. 63–154, July 2004.

[15] V. Dzuba, V. Flambaum, J. Ginges, and M. Kozlov, "Electric dipole moments of Hg, Xe, Rn, Ra, Pu, and TlF induced by the nuclear Schiff moment and limits on time-reversal violating interactions," *Physical Review A*, vol. 66, p. 012111, July 2002.

[16] J. H. Smith, E. M. Purcell, and N. F. Ramsey, "Experimental limit to the electric dipole moment of the neutron," *Phys. Rev.*, vol. 108, pp. 120–122, Oct 1957.

[17] C. J. Foot, *Atomic Physics*. Oxford Master Series in Atomic, Optical and Laser Physics, Oxford: Oxford Univ. Press, 2005.

[18] C. A. Baker, D. D. Doyle, P. Geltenbort, K. Green, M. G. D. van der Grinten, P. G. Harris, P. Iaydjiev, S. N. Ivanov, D. J. R. May, J. M. Pendlebury, J. D. Richardson, D. Shiers, and K. F. Smith, "Improved experimental limit on the electric dipole moment of the neutron," *Phys. Rev. Lett.*, vol. 97, p. 131801, Sep 2006.

[19] C. A. Baker, D. D. Doyle, P. Geltenbort, K. Green, M. G. D. van der Grinten, P. G. Harris, P. Iaydjiev, S. N. Ivanov, D. J. R. May, J. M. Pendlebury, J. D. Richardson, D. Shiers, and K. F. Smith, "Baker et al. reply:," *Phys. Rev. Lett.*, vol. 98, p. 149102, Apr 2007.

[20] J. M. Pendlebury, S. Afach, N. J. Ayres, C. A. Baker, G. Ban, G. Bison, K. Bodek, M. Burghoff, P. Geltenbort, K. Green, W. C. Griffith, M. van der Grinten, Z. D. Grujić, P. G. Harris, V. Hélaine, P. Iaydjiev, S. N. Ivanov, M. Kasprzak, Y. Kermaidic, K. Kirch, H.-C. Koch, S. Komposch, A. Kozela, J. Krempel, B. Lauss, T. Lefort, Y. Lemière, D. J. R. May, M. Musgrave, O. Naviliat-Cuncic, F. M. Piegsa, G. Pignol, P. N. Prashanth, G. Quéméner, M. Rawlik, D. Rebreyend, J. D. Richardson, D. Ries, S. Roccia, D. Rozpedzik, A. Schnabel, P. Schmidt-Wellenburg, N. Severijns, D. Shiers, J. A. Thorne, A. Weis, O. J. Winston, E. Wursten, J. Zejma, and G. Zsigmond, "Revised experimental upper limit on the electric dipole moment of the neutron," *Phys. Rev. D*, vol. 92, p. 092003, Nov 2015.

[21] G. W. Bennett, B. Bousquet, H. N. Brown, G. Bunce, R. M. Carey, P. Cushman, G. T. Danby, P. T. Debevec, M. Deile, H. Deng, W. Deninger, S. K. Dhawan, V. P. Druzhinin,

L. Duong, E. Efstathiadis, F. J. M. Farley, G. V. Fedotovich, S. Giron, F. E. Gray, D. Grigoriev, M. Grosse-Perdekamp, A. Grossmann, M. F. Hare, D. W. Hertzog, X. Huang, V. W. Hughes, M. Iwasaki, K. Jungmann, D. Kawall, M. Kawamura, B. I. Khazin, J. Kindem, F. Krienen, I. Kronkvist, A. Lam, R. Larsen, Y. Y. Lee, I. Logashenko, R. McNabb, W. Meng, J. Mi, J. P. Miller, Y. Mizumachi, W. M. Morse, D. Nikas, C. J. G. Onderwater, Y. Orlov, C. S. Özben, J. M. Paley, Q. Peng, C. C. Polly, J. Pretz, R. Prigl, G. zu Putlitz, T. Qian, S. I. Redin, O. Rind, B. L. Roberts, N. Ryskulov, S. Sedykh, Y. K. Semertzidis, P. Shagin, Y. M. Shatunov, E. P. Sichtermann, E. Solodov, M. Sossong, A. Steinmetz, L. R. Sulak, C. Timmermans, A. Trofimov, D. Urner, P. von Walter, D. Warburton, D. Winn, A. Yamamoto, and D. Zimmerman, "Improved limit on the muon electric dipole moment," *Phys. Rev. D*, vol. 80, p. 052008, Sep 2009.

[22] G. W. Bennett, B. Bousquet, H. N. Brown, G. Bunce, R. M. Carey, P. Cushman, G. T. Danby, P. T. Debevec, M. Deile, H. Deng, W. Deninger, S. K. Dhawan, V. P. Druzhinin, L. Duong, E. Efstathiadis, F. J. M. Farley, G. V. Fedotovich, S. Giron, F. E. Gray, D. Grigoriev, M. Grosse-Perdekamp, A. Grossmann, M. F. Hare, D. W. Hertzog, X. Huang, V. W. Hughes, M. Iwasaki, K. Jungmann, D. Kawall, M. Kawamura, B. I. Khazin, J. Kindem, F. Krienen, I. Kronkvist, A. Lam, R. Larsen, Y. Y. Lee, I. Logashenko, R. McNabb, W. Meng, J. Mi, J. P. Miller, Y. Mizumachi, W. M. Morse, D. Nikas, C. J. G. Onderwater, Y. Orlov, C. S. Özben, J. M. Paley, Q. Peng, C. C. Polly, J. Pretz, R. Prigl, G. zu Putlitz, T. Qian, S. I. Redin, O. Rind, B. L. Roberts, N. Ryskulov, S. Sedykh, Y. K. Semertzidis, P. Shagin, Y. M. Shatunov, E. P. Sichtermann, E. Solodov, M. Sossong, A. Steinmetz, L. R. Sulak, C. Timmermans, A. Trofimov, D. Urner, P. von Walter, D. Warburton, D. Winn, A. Yamamoto, and D. Zimmerman, "Final report of the E821 muon anomalous magnetic moment measurement at BNL," *Phys. Rev. D*, vol. 73, p. 072003, Apr 2006.

[23] J. J. Hudson, D. M. Kara, I. J. Smallman, B. E. Sauer, M. R. Tarbutt, and E. A. Hinds, "Improved measurement of the shape of the electron," *Nature*, vol. 473, no. 7348, pp. 493–496, 2012.

[24] L. V. Skripnikov, "Combined 4-component and relativistic pseudopotential study of tho for the electron electric dipole moment search," *The Journal of Chemical Physics*, vol. 145, no. 21, p. 214301, 2016.

[25] C. D. Panda, B. R. O'Leary, A. D. West, J. Baron, P. W. Hess, C. Hoffman, E. Kirilov, C. B. Overstreet, E. P. West, D. DeMille, J. M. Doyle, and G. Gabrielse, "Stimulated raman adiabatic passage preparation of a coherent superposition of tho $H^3\Delta_1$ states for an improved electron electric-dipole-moment measurement," *Phys. Rev. A*, vol. 93, p. 052110, May 2016.

[26] The NL-eEDM collaboration: P. Aggarwal, H. L. Bethlem, A. Borschevsky, M. Denis, K. Esajas and P. A. B. Haase, Y. Hao, S. Hoekstra, K. H. K. J. Jungmann, T. B. Mei-

jknecht, M. C. Mooij, R. G. E. Timmermans, W. Ubachs, L. Willmann, A. Zapara, "Measuring the electric dipole moment of the electron in BaF," *arXiv*, Apr. 2018.

[27] W. B. Cairncross, D. N. Gresh, M. Grau, K. C. Cossel, T. S. Roussy, Y. Ni, Y. Zhou, J. Ye, and E. A. Cornell, "Precision measurement of the electron's electric dipole moment using trapped molecular ions," *Phys. Rev. Lett.*, vol. 119, p. 153001, Oct 2017.

[28] B. Graner, Y. Chen, E. G. Lindahl, and B. R. Heckel, "Reduced limit on the permanent electric dipole moment of ^{199}Hg," *Phys. Rev. Lett.*, vol. 116, p. 161601, Apr 2016.

[29] M. Rosenberry and T. Chupp, "Atomic Electric Dipole Moment Measurement Using Spin Exchange Pumped Masers of 129Xe and 3He," *Physical Review Letters*, vol. 86, pp. 22–25, Jan. 2001.

[30] M. Bishof, R. H. Parker, K. G. Bailey, J. P. Greene, R. J. Holt, M. R. Kalita, W. Korsch, N. D. Lemke, Z.-T. Lu, P. Mueller, T. P. O'Connor, J. T. Singh, and M. R. Dietrich, "Improved limit on the ^{225}Ra electric dipole moment," *Phys. Rev. C*, vol. 94, p. 025501, Aug 2016.

[31] B. M. Roberts, V. A. Dzuba, and V. V. Flambaum, "Strongly enhanced atomic parity violation due to close levels of opposite parity," *Phys. Rev. A*, vol. 89, p. 042509, Apr 2014.

[32] P. W. Graham and S. Rajendran, "Axion dark matter detection with cold molecules," *Phys. Rev. D*, vol. 84, p. 055013, Sep 2011.

[33] C. Abel, N. J. Ayres, G. Ban, G. Bison, K. Bodek, V. Bondar, M. Daum, M. Fairbairn, V. V. Flambaum, P. Geltenbort, K. Green, W. C. Griffith, M. van der Grinten, Z. D. Grujić, P. G. Harris, N. Hild, P. Iaydjiev, S. N. Ivanov, M. Kasprzak, Y. Kermaidic, K. Kirch, H.-C. Koch, S. Komposch, P. A. Koss, A. Kozela, J. Krempel, B. Lauss, T. Lefort, Y. Lemière, D. J. E. Marsh, P. Mohanmurthy, A. Mtchedlishvili, M. Musgrave, F. M. Piegsa, G. Pignol, M. Rawlik, D. Rebreyend, D. Ries, S. Roccia, D. Rozpędzik, P. Schmidt-Wellenburg, N. Severijns, D. Shiers, Y. V. Stadnik, A. Weis, E. Wursten, J. Zejma, and G. Zsigmond, "Search for axionlike dark matter through nuclear spin precession in electric and magnetic fields," *Phys. Rev. X*, vol. 7, p. 041034, Nov 2017.

[34] C. Patrignani and P. D. Group, "Review of particle physics," *Chinese Physics C*, vol. 40, no. 10, p. 100001, 2016.

[35] J. Clarke and A. I. Braginski, *The SQUID Handbook Fundamentals and Technology of SQUIDs and SQUID Systems*, vol. 1. Weinheim: Wiley, 2006.

[36] C. Gemmel, *Test of Lorentz symmetry with a ^{3}He/^{129}Xe clock-comparison experiment*. PhD thesis, Universität Mainz, 2011.

[37] T. G. Walker, "Fundamentals of spin-exchange optical pumping," *Journal of Physics: Conference Series*, vol. 294, no. 1, p. 012001, 2011.

[38] S. Appelt, A. B.-A. Baranga, C. J. Erickson, M. V. Romalis, A. R. Young, and W. Happer, "Theory of spin-exchange optical pumping of ^{3}He and ^{129}Xe," *Phys. Rev. A*, vol. 58, pp. 1412–1439, Aug 1998.

[39] F. D. Colegrove, L. D. Schearer, and G. K. Walters, "Polarization of He^3 Gas by Optical Pumping," *Physical Review*, vol. 132, no. 6, p. 2561, 1963.

[40] M. Batz, P. J. Nacher, and G. Tastevin, "Fundamentals of metastability exchange optical pumping in helium," *Journal of Physics: Conference Series*, vol. 294, p. 012002, June 2011.

[41] M. Wolf, *Erzeugung höchster 3He-Kernspinpolarisation durch Metastabiles Optisches Pumpen*. PhD thesis, Universität Mainz, 2004.

[42] C. Mrozik, *Konstruktion und Inbetriebnahme eines kompakten 3-He-Polarisators*. PhD thesis, Universität Mainz, 2014.

[43] I. Ruset, S. Ketel, and F. Hersman, "Optical Pumping System Design for Large Production of Hyperpolarized Xe129," *Physical Review Letters*, vol. 96, p. 053002, Feb. 2006.

[44] T. G. Walker and W. Happer, "Spin-exchange optical pumping of noble-gas nuclei," *Reviews of Modern Physics*, vol. 69, no. 2, p. 629, 1997.

[45] C. P. Slichter, *Principles of Magnetic resonance*. Springer, 3 ed., 1990.

[46] G. D. Cates, S. R. Schaefer, and W. Happer, "Relaxation of Spins Due to Field Inhomogeneities in Gaseous Samples at Low Magnetic-Fields and Low-Pressures," *Physical Review A*, vol. 37, no. 8, pp. 2877–2885, 1988.

[47] J. Schmiedeskamp, W. Heil, E. W. Otten, R. K. Kremer, A. Simon, and J. Zimmer, "Paramagnetic relaxation of spin polarized 3He at bare glass surfaces," *The European Physical Journal D*, vol. 38, no. 3, pp. 427–438, 2006.

[48] A. Deninger, W. Heil, E. W. Otten, M. Wolf, R. K. Kremer, and A. Simon, "Paramagnetic relaxation of spin polarized 3He at coated glass walls," *The European Physical Journal D*, vol. 38, no. 3, pp. 439–443, 2006.

[49] J. Schmiedeskamp, H. J. Elmers, W. Heil, E. W. Otten, Y. Sobolev, W. Kilian, H. Rinneberg, T. Sander-Thömmes, F. Seifert, and J. Zimmer, "Relaxation of spin polarized 3He by magnetized ferromagnetic contaminants," *The European Physical Journal D*, vol. 38, no. 3, pp. 445–454, 2006.

[50] N. Newbury, A. Barton, and G. Cates, "Gaseous He-He magnetic dipolar spin relaxation," *Physical Review A*, vol. 48, no. 6, 1993.

[51] I. L. Moudrakovski, S. R. Breeze, B. Simard, C. I. Ratcliffe, J. A. Ripmeester, T. Seideman, J. S. Tse, and G. Santyr, "Gas-phase nuclear magnetic relaxation in 129xe revisited," *The Journal of Chemical Physics*, vol. 114, no. 5, pp. 2173–2181, 2001.

[52] B. Chann, I. Nelson, L. Anderson, B. Driehuys, and T. Walker, "129Xe-Xe Molecular Spin Relaxation," *Physical Review Letters*, vol. 88, no. 11, p. 113201, 2002.

[53] D. D. McGregor, "Transverse Relaxation of Spin-Polarized He-3 Gas Due to a Magnetic-Field Gradient," *Physical Review A*, vol. 41, no. 5, pp. 2631–2635, 1990.

[54] J. Clarke and A. I. Braginski, *The SQUID Handbook: Applications of SQUIDs and SQUID systems*, vol. 2. Wiley, 2006.

[55] F. Allmendinger, *Precise Tests of Fundamental Symmetries at Low Energies using a 3He-129Xe Comagnetometer*. PhD thesis, Ruperto-Carola University of Heidelberg, 2015.

[56] B. E. A. Saleh and M. C. Teich, *Fundamentals of photonics*. Wiley series in pure and applied optics, Wiley, 2007.

[57] F. Cecelja, M. Bordovsky, and W. Balachandran, "Electro-optic sensor for measurement of dc fields in the presence of space charge," *IEEE Transactions on Instrumentation and Measurement*, vol. 51, pp. 282–286, Apr 2002.

[58] F. Cecelja and W. Balachandran, "Compensation of environmental effects in bulk optical sensors," *IEEE Transactions on Instrumentation and Measurement*, vol. 51, pp. 866–869, Aug 2002.

[59] K. Takizawa and L. Jin, "Electro-optic modulation analysis of a Y-cut Z-propagation LiNbO3 light modulator: Comparison with an X-cut Z-propagation LiNbO3 light modulator and a dual LiNbO3 crystal type modulator," *Optical Review*, vol. 18, pp. 203–211, Mar 2011.

[60] M. Bordovsky, *Electric Field Sensor for DC and Extra-Low-Frequency Measurement*. PhD thesis, Brunel University, 1998.

[61] M. T. Repetto, *Improvements in production and storage of HP-129 Xe*. PhD thesis, Universität Mainz, 2015.

[62] M. D. Swallows, T. H. Loftus, W. C. Griffith, B. R. Heckel, E. N. Fortson, and M. V. Romalis, "Techniques used to search for a permanent electric dipole moment of the ^{199}hg atom and the implications for *CP* violation," *Phys. Rev. A*, vol. 87, p. 012102, Jan 2013.

[63] J. A. Nelder and R. Mead, "A simplex method for function minimization," *The Computer Journal*, vol. 7, no. 4, pp. 308–313, 1965.

[64] R. W. Mair, D. Hoffmann, S. A. Sheth, G. P. Wong, J. P. Butler, S. Patz, G. P. Topulos, and R. L. Walsworth, "Reduced xenon diffusion for quantitative lung study—the role of SF6," *NMR in Biomedicine*, vol. 13, no. 4, pp. 229–233, 2000.

[65] R. Barbé, M. Leduc, and F. Laloë, "Résonance magnétique en champ de radiofréquence inhomogéne - 2 e partie : Vérifications expèrimentales ; mesure du coefficient de self-diffusion de 3He," *J. Phys. France*, vol. 35, no. 12, pp. 935–951, 1974.

[66] R. H. Acosta, L. Agulles-Pedros, S. Komin, D. Sebastiani, H. W. Spiess, and P. Blumler, "Diffusion in binary gas mixtures studied by nmr of hyperpolarized gases and molecular dynamics simulations," *Phys. Chem. Chem. Phys.*, vol. 8, pp. 4182–4188, 2006.

[67] K. Jousten, *Wutz Handbuch Vakuumtechnik*. Springer, 2012.

[68] S. K. Lamoreaux, "Additional motional-magnetic-field considerations for electric-dipole-moment experiments," *Physical Review A*, vol. 53, p. 3705, 1996.

[69] S. Lamoreaux and R. Golub, "Detailed discussion of a linear electric field frequency shift induced in confined gases by a magnetic field gradient: Implications for neutron electric-dipole-moment experiments," *Physical Review A*, vol. 71, no. 3, p. 32104, 2005.

[70] S. K. Lamoreaux and R. Golub, "Experimental searches for the neutron electric dipole moment," *Journal of Physics G: Nuclear and Particle Physics*, vol. 36, no. 10, p. 104002, 2009.

[71] G. Pignol and S. Roccia, "Electric dipole moment searches: reexamination of frequency shifts for particles in traps," *Arxiv*, vol. nucl-ex, 2012.

[72] G. Cates, D. White, T.-r. Chien, S. Schaefer, and W. Happer, "Spin relaxation in gases due to inhomogeneous static and oscillating magnetic fields," *Physical Review A*, vol. 38, no. 10, pp. 5092–5106, 1988.

[73] F. Bloch and A. Siegert, "Magnetic resonance for nonrotating fields," *Physical Review*, vol. 57, no. 6, p. 522, 1940.

[74] N. F. Ramsey, "Resonance transitions induced by perturbations at two or more different frequencies," *Physical Review*, vol. 100, no. 4, p. 1191, 1955.

[75] F. Allmendinger, W. Heil, S. Karpuk, W. Kilian, A. Scharth, U. Schmidt, A. Schnabel, Y. Sobolev, and K. Tullney, "New Limit on Lorentz-Invariance- and C P T -Violating Neutron Spin Interactions Using a Free-Spin-Precession He 3 - Xe 129 Comagnetometer," *Physical Review Letters*, vol. 112, no. 11, pp. 1–5, 2014.

[76] F. Allmendinger, U. Schmidt, W. Heil, S. Karpuk, A. Scharth, Y. Sobolev, and K. Tullney, "Allmendinger et al. reply," *Physical Review Letters*, vol. 113, no. 18, p. 188902, 2014.

[77] J. Pendlebury, W. Heil, Y. Sobolev, P. Harris, J. Richardson, R. Baskin, D. Doyle, P. Geltenbort, K. Green, M. van der Grinten, P. Iaydjiev, S. Ivanov, D. May, and K. Smith, "Geometric-phase-induced false electric dipole moment signals for particles in traps," *Physical Review A*, vol. 70, p. 32102, sep 2004.

[78] G. Petit and B. Luzum, "IERS Conventions," 2010.

[79] F. James and M. Winkler, "MINUIT User's Guide," 2004.

[80] S. J. Leaon, *Linear Algebra with Applications*. Pearson, 9 ed., 2015.

[81] D. W. Allan, "Statistics of atomic frequency standards," *Proceedings of the IEEE*, vol. 54, pp. 221–230, Feb 1966.

[82] J. A. Barnes, A. R. Chi, L. S. Cutler, D. J. Healey, D. B. Leeson, T. E. McGunigal, J. A. Mullen, W. L. Smith, R. L. Sydnor, R. F. C. Vessot, and G. M. R. Winkler, "Characterization of frequency stability," *IEEE Transactions on Instrumentation and Measurement*, vol. IM-20, pp. 105–120, May 1971.

[83] G. J. Feldman and R. D. Cousins, "Unified approach to the classical statistical analysis of small signals," *Phys. Rev. D*, vol. 57, pp. 3873–3889, Apr 1998.

[84] J. Baron, W. C. Campbell, D. DeMille, J. M. Doyle, G. Gabrielse, Y. V. Gurevich, P. W. Hess, N. R. Hutzler, E. Kirilov, I. Kozyryev, B. R. O'Leary, C. D. Panda, M. F. Parsons, B. Spaun, A. C. Vutha, A. D. West, E. P. West, and A. Collaboration, "Methods, analysis, and the treatment of systematic errors for the electron electric dipole moment search in thorium monoxide," *New Journal of Physics*, vol. 19, no. 7, p. 073029, 2017.

[85] S. M. Kay, *Fundamentals of Statistical Signal Processing: Estimation Theory*. Prentice-Hall, 1993.

[86] C. Gemmel, W. Heil, S. Karpuk, K. Lenz, C. Ludwig, Y. Sobolev, K. Tullney, M. Burghoff, W. Kilian, S. Knappe-Grüneberg, W. Müller, A. Schnabel, F. Seifert, L. Trahms, and S. Baeßler, "Ultra-sensitive magnetometry based on free precession of nuclear spins," *The European Physical Journal D*, vol. 57, pp. 303–320, Apr 2010.

[87] F. James, *Statistical methods in experimental physics*. World Scientific, 2 ed., 2006.

[88] W. H. Press, S. A. Teukolsky, W. T. Vetterling, and B. P. Flannery, *Numerical Recipes: The Art of Scientific Computing*. Cambridge University Press, 3 ed., 2007.

Acknowledgments

This thesis has been conducted in the framework of the FOM programme Broken Mirrors and Drifting Constants. This work was performed in context of the MIXed collaboration between the University of Mainz, University of Heidelberg, University of Groningen and the research Center FZ Jüelich. I am grateful to the leaders of the respective teams, Werner Heil, Ulrich Schmidt, Klaus Jungmann, Andreas Offenhäusser and Hans-Joachim Krause, for their active participation and stimulating discussions. My work in Groningen was conducted within the VSI Fundamental Interactions and Symmetries group with my direct supervisors Klaus Jungmann and Lorenz Willmann.

In particular I would like to thank Werner Heil for allowing a one year stay at Mainz, enabling me to work closely with Stefan Zimmer on designing and constructing the experimental apparatus.

Within the collaboration I would like to thank Fabian Allmendinger, Maricel Repetto and Stefan Zimmer. I would like to thank Fabian for his work on the data acquisition and analysis, and answering the many questions I had regarding the data acquisition and analysis when working on the data analysis myself. I am grateful to Stefan for all his work on designing and constructing the experimental apparatus. Maricel, thank you for all your work on operating and improving the xenon polarizer, allowing the measurements described in this thesis to be performed. I would like to thank all of you for making the many days and nights we spent in Jülich taking measurements the Forschungszentrum and playing games at Cafe Liebevoll very enjoyable. I would also like to thank Xiongfei Bai for his assistance in the last months of my time at the VSI with measurements on the electro-optic crystals.

I of course have to thank my promotor Klaus Jungmann and co-promotor Lorenz Willmann, without whose help and advice this work would not have been possible. Klaus, thank you for the invaluable lessons you gave me about physics and working in physics, and in particular also about operating in collaborations. Lorenz, thank you for the many discussions we had every time I had found something out of the ordinary in the data analysis. In addition you were alway a great sounding board when I had some idea regarding the data analysis or experimental setup, replying with questions which often nudged me in the right direction.

I would like express my gratitude the members of the assessment committee, Prof. Ben Sauer, Prof. Antonio Pellegrino and Prof. Rob Timmermans, for carefully reading this thesis and providing valuable feedback.

Within the Fundamental Interactions and Symmetries (FIS) group I am grateful to Hilde

van der Meer, whose administrative support of the Fundamental interactions and Symmetries group simplified my interaction with the university bureaucracy immensely. I would also like to acknowledge the technical support from Leo Huisman and Oliver Böll. Leo, thank you for all the help with high voltage systems and making technical drawings for the machine shop. Oliver, thanks for your help with optical components and random pieces of equipment I would often pester you about. I would like to acknowledge Gerco Onderwater for his advice regarding data analysis and statistics in general. I would like to express gratitude to the other senior staff of the FIS group, Steven Hoekstra and Hans Wilschut, for their work in the group and advice in general. Finally I have to thank my colleagues Amita, Artem, Auke, Bai, Corine, Elwin, Joost, Jordi, Keri, Kevin, Mayerlin, Nivedya, Parul, Sreekanth, Thomas and Wouter for any scientific advice and enjoyable time we spent together, either at or outside of work.

I would like to thank the mechanical and electrical workshop of KVI-CART for their work and support on multiple mechanical and electronic pieces. Furthermore I am also grateful to the mechanical workshop at the University of Mainz, who constructed a great many parts of our experimental setup. I am also thankful to all the support staff that made my work at VSI possible.

I am thankful to my fellow members of the Graduate School of Science and Engineering PhD council, with whom organizing social events for the PhD students was always a pleasure. Daniel, Christian, Frita, Kumar, Monique, Sabrina, Vincent, Yvonne and Zsofia, thank you.

I would also like to thank the members of the Tuesday ski-training group, with whom the Tuesday evening circuit training and unihockey was always very enjoyable and a welcome respite after sitting behind a computer or in a lab the entire day. On the subject of skiing I would be remiss not to thank all the people I would go skiing with in Hinterthal every February. Their company, as well as the skiing, always made that week my favorite vacation.

Many thanks go out the my hockey team, H10 Booze Brothers, with whom the last two years of my PhD were a blast on and off the hockey field.

I also owe thanks to the members of the Hobbyalcoholics chat group, with whom the Friday after-work drinks were a welcome respite to the working week. Christian, Daniel, Els, Elwin and Markus, thank you.

I would also like to thank the members of my jaarclub at R.K.S.V. Albertus Magnus, JC Cliche, for enriching my life greatly during my studies and PhD. Imre, Jan-Lucas, Ronald, Tom, Thomas, Thomas and Wouter, thank you.

Erik and Tom, thank you for your friendship and support during the course of my PhD. We met when we were 5 years old in elementary school, and still remain friends and hang out, even though we all live in different cities now. I hope this will remain so for the rest of our lives.

Second to last I would like to thank Tom and Ronald for agreeing to be my paranymphs. I have full confidence that with your support during and after the defense everything will

proceed smoothly.

Finally I would like to thank my family. My mother and father, Hanneke and Pieter, who gave me unwavering support during the course of my PhD, and of course also preceding my PhD. They always allowed and facilitated me to pursue any interest I had. My brother, Sebastiaan, with whom I often had dinner or hung out with after a day of hard work at the VSI. My aunt and uncle, Ida and Dick, and my uncle Jeroen, for their support during my PhD.

Als laatste wil ik graag mijn opa, Jan, bedanken. De laatste jaren ging ik met veel plezier om de anderhalve maand met de trein naar Hoogezand, om vervolgens bij de plaatselijke Chinees de rijsttafel af te halen en een avond bij opa te zitten.

Olivier Grasdijk
May 2018